Site C0012[1]

Expedition 322 Scientists[2]

Chapter contents

Background and objectives

Integrated Ocean Drilling Program (IODP) Site C0012 (proposed Site NT1-01) was the contingency site for IODP Expedition 322 (Saito et al., 2009). The site is located in the Shikoku Basin on the crest of a prominent basement high (Kashinosaki Knoll) that was constructed on the subducting Philippine Sea plate (Fig. **F1**). Because of premature destruction of the drill bit in IODP Hole C0011B, we failed to reach the total depth (TD) target, and the decision was made shortly thereafter to collect a full suite of cores and wireline logs at the contingency site. The primary purpose of drilling at this new location was to recover the entire succession of sedimentary strata and uppermost igneous basement, thereby characterizing the subduction inputs to the Nankai Trough. Analysis of seismic reflection data just prior to drilling indicated a depth to basement of ~515 meters below seafloor (mbsf), which is considerably less than the value used in the *Scientific Prospectus* (600 mbsf). The adjustment to TD at Site C0012 was made after refining the acoustic velocity model following successful acquisition of logging-while-drilling data in IODP Hole C0011A during the final days of IODP Expedition 319.

By recovering a complete suite of cores and wireline logs from Site C0012, the Expedition 322 scientists expected to demonstrate conclusively how depositional history varied between the flank and the crest of the subducting basement high. This spatial comparison between two reference sites (expanded section versus condensed section) was designed to help provide answers to the following questions:

1. How does the physical hydrogeology of the Shikoku Basin respond to variations in primary lithologic architecture and basement structure?
2. How do fluids in the igneous basement affect subduction processes?
3. How have system-wide patterns of sediment dispersal affected composition within the Shikoku Basin, particularly on the northeast side of the fossil spreading ridge (Kinan seamount chain)?
4. Which factor(s) inherited from the Shikoku Basin control(s) the décollement's position near the toe of the Nankai accretionary prism, as well as the location of ramps and flats and mechanical behavior throughout?
5. Does the plate boundary fault, near its updip limit of seismicity, shift its position from a sediment/sediment interface

[1] Expedition 322 Scientists, 2010. Site C0012. *In* Saito, S., Underwood, M.B., Kubo, Y., and the Expedition 322 Scientists, *Proc. IODP,* 322: Tokyo (Integrated Ocean Drilling Program Management International, Inc.). doi:10.2204/iodp.proc.322.104.2010
[2] **Expedition 322 Scientists' addresses.**

doi:10.2204/iodp.proc.322.104.2010

(stable sliding) to the sediment/basalt interface (stick-slip)? If so, what are the causes?

Answers to these questions will require data from multiple drilling sites and expeditions and will contribute to the success of the Nankai Trough Seismogenic Zone Experiment (NanTroSEIZE) in many important ways. The importance of the lower stratigraphic units with the Shikoku Basin cannot be overstated; those intervals yield information about initial conditions within presubduction equivalents of the seismogenic zone.

Operations

Hole C0012A

Five transponders were set, and calibration was completed at 0615 h on 25 September. We started running into the hole with a 10⅝ inch coring assembly at 0915 h, spudding Hole C0012A at 2103 h. We jetted to 60 mbsf with the inner barrel, and the seafloor was confirmed at 3539 m drilling depth below rig floor by weight on bit. We continued to jet-in to 60 m drilling depth below seafloor (DSF). Core 322-C0012A-1R was retrieved at 60 m DSF and was on deck at 0020 h on 26 September. The recovered 0.84 m of material was sediments pushed into the core barrel during the jet-in.

Regular rotary core barrel (RCB) coring started from 60 m DSF. Recovered cores were short and of poor quality to Core 322-C0012A-22R because sediments were too soft for RCB coring, but in general, core recovery and quality improved with depth. Ten RCB cores were recovered on 26 September, every 2–2.5 h. See Table **T1** for a breakdown of general coring operations. RCB coring continued without any major problems. Reduced pump rate and lower rotation (<30 rotations per minute) were used until Core 322-C0012A-15R (187 m DSF). Average recovery was >80% for Cores 322-C0012A-6R through 11R.

Steady coring operations continued to the end of September, recovering core every 2–3 h except for Cores 322-C0012A-33R and 37R, each of which took >2 h to cut. Every effort was made to optimize the drilling parameters for better core quality. Good quality cores were recovered from Cores 322-C0012A-40R and 45R. On 1 October, core recovery dropped after Core 322-C0012A-47R to <20%, probably due to increased tuffaceous beds. Red silty claystone appeared in addition to hemipelagic mud and tuffaceous beds.

On 2 October, we reached the sediment/basalt interface in Core 322-C0012A-53R. After that, short advances (<5 m) were used to improve recovery of basalt. Coring was suspended after Core 322-C0012A-57R at 560 m DSF, which was the approved maximum penetration depth at this site. Coring resumed at 2045 h after receiving approval for deepening the hole to 600 m DSF.

Core 322-C0012A-58R was on deck at 0100 h on 3 October and became the last core from this hole. Coring was terminated at this point to leave time to complete wireline logging operations before the arrival of an approaching typhoon. Core 322-C0012A-58R was cut by 16 m of advance to reach >30 m below sediment/basalt interface in order to make a space for the logging tool to sit within the basalt interval.

Hole C0012B

Following completion of coring, we started a wiper trip for hole cleaning, during which running back down failed several times at 72 m DSF. Attempts to ream the interval resulted in a probable side track. Efforts were made to return to the original hole, which probably deviated significantly from vertical, but we decided to drill down the side-track hole for wireline logging operations. Although the start of the side track, now Hole C0012B, is unclear, drilling with the center bit was started at 1415 h at 216 m DSF. Target depth was tentatively set at either 600 m DSF or 30 m below the probable sediment/basalt interface.

We stopped drilling at 561 m DSF at 0305 h on 4 October, as drilling parameters suggested this depth was likely to be >30 m below the sediment/basalt interface. We reamed up and down tight spots then drilled another 10 m because we could not clear the fills at the hole bottom. The center bit assembly was pulled out at 2230 h.

Drill bit release was confirmed at 1500 h on 5 October, and the drill string was pulled up to 100 m DSF at 0030 h on 6 October. Rig-up of the wireline logging tools started at 0045 h, and the tools were lowered through the drill pipe. Due to an approaching typhoon, we had <10 h for logging operations. We had only one run with the High-Resolution Laterolog Array (HRLA)–self potential (SP)–slim-Formation MicroScanner (FMS) resistivity image–gamma ray–casing collar locator (CCL). We started running into the hole at 0515 h and observed the seafloor at 3539 m wireline depth below rig floor (WRF) from gamma ray response during the down-logging at 0810 h. We observed a loss of wireline tension and stacking at 3648 m WRF at 0821 h, and we could advance no farther than 10 m into the open hole. After several attempts to pass the difficult interval 10 m below the drill pipe, we cancelled wireline logging operations at 1000 h. The tools were retrieved at 1200 h and rigged down at 1415 h.

Typhoon evacuation and transit

We started moving to south of Hachijo Island for typhoon evacuation at 0245 h on 7 October. We arrived at a safe point near Aoga-shima, 120 nmi southeast of the drilling sites, at 1800 h. Because of high winds and waves, the ship could not hold position in dynamic positioning mode at 2245 h. We continued waiting on weather in autohead mode. After recovery of sea conditions, we started moving to our drilling sites for retrieval of transponders. At 0100 h on 9 October, we attempted communication with a lost transponder at Site C0011, but there was no response. Retrieval of five transponders at Site C0012 was finished at 1410 h. We arrived at Shingu port, and the science party disembarked at 1130 h on 10 October.

Lithology

At Site C0012, seven lithologic units were identified on the basis of sediment composition, sediment texture, and sedimentary structures (Fig. F2, Table T2):

- Unit I: 0.0–150.86 m core depth below seafloor (CSF) (bottom = Section 322-C0012A-12R-2, 43 cm),
- Unit II: 150.86–219.81 m CSF (bottom = Section 322-C0012A-19R-4, 83 cm),
- Unit III: 219.81–331.81 m CSF (bottom = Section 322-C0012A-31R-4, 74 cm),
- Unit IV: 331.81–415.58 m CSF (bottom = Section 322-C0012A-40R-2, 27 cm),
- Unit V: 415.58–528.51 m CSF (bottom = Section 322-C0012A-52R-1, 50.5 cm),
- Unit VI: 528.51–537.81 m CSF (bottom = Section 322-C0012A-53R-1, 31 cm), and
- Unit VII: 537.81 m CSF to TD (bottom = Core 322-C0012A-58R-CC).

Lithologic Unit I (upper Shikoku Basin)

Interval: Sections 322-C0012A-1R-1, 0 cm, through 12R-2, 43 cm
Depth: 0.0–150.86 m CSF
Age: Pleistocene–late Miocene (0–7.8 Ma)

Lithologic Unit I is 150.86 m thick and extends from the seafloor (0.0 m CSF) to 150.86 m CSF, where the first volcaniclastic sandstone was recovered. Poor core recovery together with very intense core disturbance in this unit means that it is possible that the first sandstone occurrence is at a shallower depth. The dominant lithology is green-gray, intensely bioturbated silty clay to silty claystone with thin interbeds of volcanic ash. Most of the silty claystone is rich in nannofossils. Within the silty claystone intervals, dark green silty claystone layers are typically <0.5 cm thick. The uppermost 11 cm of Core 322-C0012A-1R, which was jetted into the formation, contains a poorly consolidated light brown–colored, oxidized clayey silt layer (interval 322-C0012A-1R-1, 0–11 cm). The uppermost fine- to coarse-grained ash layers range from light gray to olive-gray (to interval 322-C0012A-9R-1, 11–15 cm). In Core 322-C0012A-9R, the color and composition of the ash layers changes to black and mafic components, respectively (e.g., the first dark ash is at interval 322-C0012A-9R-1, 136.5–138 cm). Below interval 322-C0012A-9R-7, 48.5–57 cm, the color of the ash layers alternates between off white/olive-gray and black.

Lithologic Unit II (middle Shikoku Basin)

Interval: Sections 322-C0012A-12R-2, 43 cm, through 19R-4, 83 cm
Depth: 150.86–219.81 m CSF
Age: late Miocene (7.8–9.4 Ma)

Lithologic Unit II is 68.95 m thick and extends from 150.86 to 219.81 m CSF. Poor core recovery, together with very intense drilling disturbance, precludes any division of this unit. The dominant lithology is green-gray silty claystone, which alternates with medium- to thick-bedded tuffaceous/volcaniclastic sandstone interbedded with dark gray clayey siltstone. The silty claystone appears to be the "background sedimentation" and typically occurs as intensely bioturbated intervals from centimeters to several meters thick. Within the silty claystone intervals, dark green silty claystone layers are typically <0.5 cm thick and, where bioturbation has not obscured their presence to the naked eye, are commonly spaced 5–10 cm apart. The volcaniclastic sandstone beds range from granular to fine grained, are 5–50 cm thick, and are typically normally graded with planar-parallel lamination (Fig. F3). A minor lithology in Unit II is thin-bedded, dark gray clayey siltstone (e.g., intervals 322-C0012A-17R-1, 33–47.5 cm; 17R-1, 64–72 cm; and 18R-2, 54–57 cm). Unit II also contains chaotic deposits that are at least 0.31 and 3.1 m thick, extending from 150.86 to 151.17 m CSF (Section 322-C0012A-12R-2, 43 cm, through 12R-CC, 15 cm) and from 178 to 181.1 m CSF (Sections 322-C0012A-15R-1, 0 cm, through 15R-CC, 18.5 cm), respectively. These deposits are composed of disaggregated pieces of volcaniclastic sandstone and bioturbated silty claystone that show folding, thinning, and attenuation of original bedding (Fig. F4). Drilling-induced deformation throughout Unit II precludes an accurate assessment of the amount and thickness of other chaotic intervals that may be present.

Figure F5 (see also "Site C0012 smear slides" in "Core descriptions") shows the total volcaniclastic

components for Unit II, and Figure F6 shows representative photomicrographs from the smear slides. These results were obtained by point counting (200 points). The volcaniclastic sandstone lithology includes both volcaniclastic and terrigenous siliciclastic grains. Smear slides show an estimated >25% volcaniclastic grains and <25% pyroclastic grains. These sandstones have large amounts of minerals, with relative abundances of plagioclase > pyroxene > quartz > amphibole. The quartz content is estimated to be between 4% and 10%, most of which is polycrystalline. Additionally, there are large amounts of sedimentary lithic grains, mainly as reworked siltstone, sandstone, and chert grains. These sedimentary lithic grains increase in abundance toward the base of Unit II. Unit II differs from the units above and below by a higher total mineral content (on average), especially feldspar and heavy minerals, and an increase in the average ratio of volcanic lithic grains versus total lithic grains. Scatter among individual sample compositions, however, is considerable.

Lithologic Unit III (lower Shikoku Basin hemipelagites)

Interval: Sections 322-C0012A-19R-4, 83 cm, through 31R-4, 74 cm
Depth: 219.81–331.81 m CSF
Age: middle–late Miocene (9.4–12.7 Ma)

Lithologic Unit III is 112.0 m thick and extends from 219.81 to 331.81 m CSF. The top of Unit III is defined at the base of the last sandstone in Unit II. The base of Unit III is just above the first appearance of dark gray siltstone. Unit III contains an unusual interval of steeply inclined bedding, typically at 30°–45° (Sections 322-C0012A-22R-1, 73 cm, through 23R-CC, 17 cm) (Fig. F7) (see "Structural geology"). The lithology is characterized by bioturbated silty claystone. *Zoophycos* isp., *Phycosiphon incertum,* and *Chondrites* isp. are commonly observed in the silty claystone. The intensity of bioturbation mostly corresponds to ichnofabric Index 5 (see the "Methods" chapter). Minor lithologies in this unit are dark gray silty claystone, lime mudstone, and very thin ocher-colored calcareous claystone (-filled burrows). Unit III also contains dark green layers, typically <0.5 cm thick, which recur every ~5–10 cm. These dark green layers are intensely bioturbated and contain altered mafic glass, silica, and plagioclase. The off white–colored lime mudstone lithology is rich in altered nannofossils. A cemented, yellowish carbonate layer is present at interval 322-C0012A-20R-4, 115–122 cm. We note a similarity between this layer and a potentially correlative carbonate layer at Site C0011 (interval 322-C0011B-19R-5, 132–137 cm) (Fig. F8). Minor amounts of ocher-colored burrows occur throughout this unit. Although nannofossils are rare in parts of Unit III, some burrows tend to contain concentrations of nannofossils.

Smear slide data for Unit III show relatively low proportions of quartz, accessory minerals (i.e., all other minerals except clay minerals), and volcaniclastic components. Within Unit III in Hole C0012A are peaks in the amount of feldspar and sedimentary lithic grains at ~275 m CSF (Fig. F5; see "Site C0012 smear slides" in "Core descriptions").

Lithologic Unit IV (lower Shikoku Basin turbidites)

Interval: Sections 322-C0012A-31R-4, 74 cm, through 40R-5, 19 cm
Depth: 331.81–415.58 m CSF
Age: middle Miocene (12.7–13.5 Ma)

Lithologic Unit IV is 83.77 m thick and extends from 331.81 to 418.29 m CSF. The top of Unit IV was defined by the appearance of dark gray siltstone; the base of this unit was placed above a bed of tuff. Unit IV is characterized by alternations of silty claystone, clayey siltstone, and normally graded siltstone. The clay-bearing siltstone occurs in beds ~5–50 cm thick, but typically 5–20 cm thick, characterized mainly by sharp bases, diffuse plane-parallel lamination in the lower part, and normal grading into silty claystone. Bioturbation in the clayey siltstone is slight to moderate, compared with the intense bioturbation observed in the silty claystone. We interpret these deposits as muddy turbidites. The sharp-based, normally graded siltstones are 10–80 cm thick and typically show plane-parallel lamination. These are also interpreted as turbidites. Unit IV contains an 82 cm thick interval of steeply inclined bedding, typically at ~40° (Sections 322-C0012A-33R-5, 35 cm, through 33R-CC, 18.5 cm).

Smear slides show that the clayey siltstones have a larger terrigenous component than deposits in Unit III, with more detrital quartz (Fig. F5; "Site C0012 smear slides" in "Core descriptions"). Most grains show undulose extinction and polycrystalline quartz. Metamorphic rock fragments are also typical (i.e., sericite-quartz intergrowths, typical of low-grade metamorphic terranes).

Lithologic Unit V (volcaniclastic-rich)

Interval: Sections 322-C0012A-40R-2, 27 cm, through 52R-1, 50.5 cm
Depth: 415.58–528.51 m CSF
Age: early–middle Miocene (13.5 to ≥18.9 Ma)

Lithologic Unit V is 112.93 m thick and extends from 415.58 to 528.51 m CSF. The Unit IV/V boundary is defined by a bed of tuff. The Unit V/VI boundary is

defined by the first appearance of red calcareous claystone. The main lithologies in the upper part of Unit V are silty claystone alternating with tuff, and in the lower part volcaniclastic siltstone/sandstone beds alternate with siliciclastic sandstone/siltstone and rare tuff layers. This change occurs immediately beneath a tuff layer at 435.68 m CSF (Section 322-C0012A-42R-3, 102 cm). The sandstone and tuff beds typically show normal grading, plane-parallel lamination, and current-ripple lamination (Fig. F9A). The volcaniclastic deposits show load structures, flame structures, and current-ripple lamination (Fig. F9B, F9C). These laminated strata are involved in a 50.5 cm thick chaotic interval (Sections 322-C0012A-45R-1, 71 cm, through 45R-1, 121.5 cm), showing isoclinal folding, attenuation of beds, and sandstone injections (Fig. F9C). This chaotic interval contains at least three discrete zones, distinguished by sharp detachment surfaces with an abrupt change of bedding dip above them, with the uppermost zone having the most intense internal deformation. The volcaniclastic sandstones are characterized by abundant dark-colored glass shards up to several millimeters in *a*-axis, which are oriented parallel/subparallel to bedding (Fig. F9D, F9E). One of the very coarse grained volcaniclastic sandstones contains large (>6 cm) angular clasts of bioturbated, green-gray silty claystone (Fig. F9F). Disseminated and framboidal pyrite (as long as 2 cm) is common through Unit V. The larger pyrite nodules appear as the infill of burrows.

Smear slide analyses show background mud sedimentation with 5%–15% glass, and the tuffs contain an estimated 40%–80% glass, juvenile minerals, and minor amounts of pelagic sediments (claystone, chert, and siltstone grains). Within Unit V, there is a marked increase in the feldspar content (Fig. F5; see "Site C0012 smear slides" in "Core descriptions"). In the upper part of Unit V, the glass components appear to be derived from highly evolved explosive volcanism. However, the sandstones in the lower part of Unit V have high amounts of fresh, dark brown, blocky, and vesicle-free glass shards, suggesting a hyaloclastic origin. The sandstones in Unit V appear to have two separate detrital provenances: a source with fresh volcanic glass, together with relatively large amounts of feldspar, and a source enriched in sedimentary lithic grains, quartz, and heavy minerals (including pyroxene, zircon, and amphibole) (Fig. F10; "Site C0012 smear slides" in "Core descriptions").

Lithologic Unit VI (pelagic claystone)

Interval: Sections 322-C0012A-52R-1, 50.5 cm, through 53R-1, 31 cm
Depth: 528.51–537.81 m CSF
Age: early Miocene (≥18.9 Ma)

Lithologic Unit VI is 9.3 m thick and extends from 528.51 to 537.81 m CSF. Unit VI is characterized by red calcareous claystone and is rich in nannofossils with minor amounts of radiolarian spines. Locally, particularly in the tens of centimeters overlying the basaltic basement of Unit VII, the claystones have a mottled red-green coloration, probably due to iron reduction. Immediately above the basalt, the red calcareous claystone appears much more indurated than in the overlying part of Unit VI (Fig. F11).

Lithologic Unit VII (Kashinosaki Knoll basement)

Interval: Sections 322-C0012A-53R-1, 31 cm, through 58R-CC
Depth: 537.81–576 m CSF
Age: early Miocene (>18.9 Ma)

Basement is composed of (1) pillow lava basalt, (2) basalt, (3) basaltic hyaloclastite breccia, and (4) mixed rubble pieces of basalt caused by drilling disturbance (Fig. F12). Successful recovery of volcanic basement in Hole C0012A defined lithologic Unit VII. On the basis of the nannofossils in the overlying red claystone, the volcanic rock is older than 18.9 Ma. The cored interval extends from 537.81 to 576 m CSF, and a sharp contact between red claystone and basalt is well preserved in Core 322-C0012A-53R (Fig. F11). The 38.2 m of basement coring resulted in 18% recovery. Pillow lavas were identified by their curved, chilled margins oriented oblique to the vertical axis of the core. Where such margins were absent, identification of pillow lavas was made by their variolitic textures, curved fractures, and microcrystalline or cryptocrystalline grain size. The name "basalt" was assigned to rocks that did not present these features, even though some pieces may be too small to be representative of the rock morphology.

Basalts and pillow basalts have aphanitic to porphyritic textures (Fig. F13). Phenocryst abundance is highly variable, from slightly to highly phyric textures. This variability is not restricted to separate intervals but is also observed across diffuse boundaries between highly phyric and sparsely phyric basalts (Fig. F14). Phenocrysts are composed mostly of plagioclase, pyroxene, Fe-Ti oxides, and sparse altered olivine. Orthopyroxene is dominant compared to clinopyroxene, suggesting low CaO content in the parent magma. Pyrite is present as an accessory mineral in some basalt. Vesicularity is highly heterogeneous. In a single unit, basalts can have sparse (1%–5%) to high (>20%) vesicle content. Visual core

description and thin section analyses show that two different types of basalts with different color, vesicle content, and phenocryst proportion are present. The boundaries between the two types of basalt are diffuse. This may be due to either magma mixing within the magmatic chamber or lava reworking during the emplacement of the basalts (Fig. F14).

Alteration ranges from moderate to very high, with a large proportion of basalt being highly altered (Fig. F15). Alteration styles include interstitial groundmass replacement, vesicle fill, vein formation (with associated alteration halos), and complete replacement of pillow lava glass rims by alteration materials. Phenocrysts are well preserved. Phyllosilicates are among the main products of alteration and occur as saponite, celadonite, and mixtures of these two phases (Fig. F16). Other secondary mineralogical phases include zeolite (fibrous and isometric), pyrite, iddingsite, quartz, and calcite (Fig. F17). Therefore, basalts from Site C0012 exhibit the effects of several stages of alteration from relatively high temperature facies (>200°C for zeolite and saponite) to low-temperature facies (<30°C for celadonite). One thin layer of basaltic hyaloclastite breccia was also recovered. Additionally, many fractures were filled with brecciated material. These breccias are composed of clasts that are similar to the surrounding basalts and are sealed with celadonite and saponite. Given the low recovery of these intervals, it is not possible to determine the relationship between the hyaloclastite portions and underlying lavas.

Major elements were measured postexpedition at University Joseph Fourier on 20 bulk rock samples of basalt (Fig. F18). The variable extent of alteration is confirmed by loss on ignition values, which range from 3.1 to 18.0 wt%. SiO_2 content ranges from 45.5 to 53.3 wt%, and MgO content ranges from 6.6 to 9.0 wt%. Alkaline content is high with $Na_2O + K_2O$ ranging from 3.6 to 6.9 wt%. Na_2O increases with depth while K_2O decreases with depth. This may be related to interactions between the basalts, the overlying sediments, and any pore fluids from other sources. Further study of trace element contents is necessary to explain these characteristics.

X-ray diffraction analyses

For Site C0012, the results of X-ray diffraction (XRD) analysis of bulk sediment samples are shown in Figure F19 and Table T3. In Unit I, quartz values range from 14% to 24% (average = 17%), with a slight decrease toward the bottom. Total clay mineral content increases from 51% to 72%, with an average of 65%. Feldspar content ranges from 10% to 33%, with a positive excursion at ~90 m CSF and high values (~33%) in the lower part of Unit I. The feldspar and clay mineral content are inversely correlated. Calcite content is a relatively high in the lower part of Unit I (up to 12%), with an average of 3%.

In Unit II, XRD analyses of bulk samples show that calcite is low throughout (typically <0.5%, but with one value as high as ~32%). Quartz values are somewhat scattered without a significant trend and an average value of 16%. Clay mineral content ranges from 43% to 77% but with a slight increase downhole. Feldspar content, however, appears fairly uniform (~17%) throughout Unit II.

Throughout Units III and IV, there are no significant mineralogical variations with depth. The average values are 71% total clay minerals, 15% quartz, 11% feldspar, and 2% calcite for Unit III and 69% total clay minerals, 18% quartz, 11% feldspar, and 2% calcite for Unit IV. Four samples contain unusually high concentrations of total clay minerals and are probably bentonites.

Unit V has the most scatter in mineral values throughout Hole C0012A, possibly due to a grain-size effect. Quartz values range from 3% to 37%, with an average of 15%. Feldspar content varies between 1% and 31%, with an average of 16%. Quartz and feldspar show similar variations but show an inverse relation with total clay mineral content. Clay mineral content ranges from 20% to 91%, with an average of 64%. Calcite values are low (typically <0.5), except for several outlying samples of calcareous claystone (up to 74%).

X-ray fluorescence analyses

In order to characterize compositional trends with depth and/or lithologic characteristics of the sediments in Hole C0012A, X-ray fluorescence (XRF) analysis was undertaken for 83 sediment samples from all of the cored units (Fig. F20; Table T4). The analyzed sediments span a relatively small range of major element composition, compatible with a dominant crustal composition (both high SiO_2 and Al_2O_3, with average of 62.51 and 16.17 wt%, respectively) (Taylor and McLennan, 1985).

Throughout Units I, II, III, and IV, Al_2O_3, SiO_2, Fe_2O_3, MgO, CaO, and K_2O content show no significant variations, with an average of 16.17 wt% Al_2O_3, 62.51 wt% SiO_2, 6.27 wt% Fe_2O_3, 2.26 wt% MgO, 4.66 wt% CaO, and 2.88 wt% K_2O. These variations are consistent with those uniform values for total clay minerals, quartz, feldspar, and calcite in the XRD analyses (Fig. F20). Several outlying samples of calcareous claystone have high CaO content and low Al_2O_3 and SiO_2. At 332.12 m CSF (Section 322-C0012A-31R-4, 105 cm), the samples have high CaO values (up to 47.49 wt%) together with high P_2O_5

and MnO concentrations (up to 19.87 and 4.57 wt%, respectively) (Table T4). The high P_2O_5 content in the calcareous claystone samples is probably related to the presence of authigenic apatite ($Ca_5[PO_4]_3[F,Cl,OH]$). The MnO content can be explained by the presence of rhodochrosite ($MnCO_3$). Rhodochrosite is typical of anoxic environments and is indicative of geochemical conditions where ferric iron oxides usually dissolve (Canfield et al., 1992). Sodium content shows a gradually decreasing trend (from 4.09 to 1.43 wt%) from Unit I to Unit IV.

In Unit V, all major element concentrations show considerable scatter, and their values range from 8.25 to 19.15 wt% (Al_2O_3), 30.87 to 76.25 wt% (SiO_2), 2.19 to 10.55 wt% (Fe_2O_3), 0.86 to 4.2 wt% (MgO), 1.24 to 50.32 wt% (CaO), 0.9 to 2.64 wt% (Na_2O), and 0.5 to 3.31 wt% (K_2O). The average values are 14.72 wt% for Al_2O_3, 63.24 wt% for SiO_2, 6.03 wt% for Fe_2O_3, 2.01 wt% for MgO, 7.09 wt% for CaO, 1.94 wt% for Na_2O, and 2.55 wt% for K_2O (Table T4).

Lithofacies at Site C0012

At Site C0012, eight major lithologies are recognized (silty claystone, clayey siltstone, siltstone, tuffaceous sandstone, volcaniclastic sandstone, sandstone, red calcareous claystone, and basalt). Several minor lithologies such as volcanic ash/tuff, tuffaceous siltstone, calcareous claystone, lime mudstone, and chaotic deposits also occur (Table T2). These lithologies are grouped into six broad "lithofacies:" pelagic, hemipelagic, turbidite, chaotic deposits, tuff, and igneous rocks.

The hemipelagic lithofacies is mostly composed of green-gray silty claystone, the dominant lithology throughout deposition at Site C0012. This lithology is intensely bioturbated and commonly intercalated with green silty claystone layers (<1 cm thick). It is interpreted to represent the "background" fallout from suspended sediment. The approximately constant sediment accumulation rate supports this view (see **"Sediment accumulation rates at Site C0012"**). Some minor lithologies, such as calcareous claystone and lime mudstone, contributed as nannofossils are mixed with hemipelagic sediment influx, although some carbonates may also be produced by diagenesis.

Coarser grained lithologies (clayey siltstone, siltstone, tuffaceous sandstone, volcaniclastic sandstone, and sandstone) all show sharp-based beds, normal grading, and plane-parallel lamination. Such features are typical in turbidites, and, therefore, we interpret these deposits as the products of sediment gravity flows, mostly from turbidity currents. Together, we group these lithologies into the turbidite lithofacies. The volcaniclastic and siliciclastic sandstones in the lower part of Unit V, together with ash in Unit I, are interpreted as the deposits from various sediment gravity flows and belong to the turbidite lithofacies.

Chaotic deposits occur in Units II, III, IV, and V. Throughout Cores 322-C0012A-1R through 22R there is severe drilling-induced deformation, which precludes any accurate assessment of the actual amount and thickness of the chaotic deposits. These chaotic deposits formed either during long-distance transport in cohesive debris flows or more locally as sediment slides (e.g., along the inner margins of submarine channels) or in response to essentially in situ deformation liked to seismicity on the normal fault flanking Kashinosaki Knoll (Fig. F21; see **"Logging and core-log-seismic integration"**). The steeply dipping beds in Unit III were probably formed by rotational normal faulting (see **"Structural geology"**). Together, these deposits constitute the chaotic lithofacies.

The tuffs in the upper part of Unit V are interpreted as fallout pyroclastic deposits because they are estimated to contain >75% glass shards, show normal grading, and are texturally well sorted. These deposits form the tuff lithofacies.

The red calcareous claystone in Unit VI is interpreted as pelagic deposition and is, therefore, the sole constituent of the pelagic lithofacies. The basalt in Unit VII belongs to the igneous oceanic crust, including pillow lavas from effusive eruptions and hyaloclastic breccias.

Sediment accumulation rates at Site C0012

An analysis of the sediment accumulation rates for the hemipelagites and turbidites show differences among lithologic units. For sedimentation accumulation analysis, the thickness ratio between the hemipelagites (silty claystone, calcareous mudstone, and lime mudstone) and turbidites (sandstone, tuffaceous sandstone, volcaniclastic sandstone, and clayey siltstone) was measured in each core (Fig. F22A). Then, the cumulative thickness of the hemipelagic and turbiditic deposits was calculated on the basis of the thickness ratio and core length. Next, the cumulative thickness of the turbidites was plotted against that of the hemipelagites (Fig. F22B). Although the recovery rate of most cores was considerably <100%, as an approximation, the thickness ratio between two lithofacies was assumed to be constant within each core. Cores showing low recovery rates (<15%) were excluded from this analysis, and their data were linearly interpolated with respect to data in adjacent cores. There are two likely hiatuses at this site (see **"Biostratigraphy"** and **"Paleomag-**

netism"). On the basis of the integrated age model, the youngest of the two hiatuses occurs (1.35 m.y.) within the uppermost interval of Unit III. In our analysis of the sediment accumulation rate, we followed the age model of the biostratigraphy because it is more consistent with the lithologic and structural observations of the inclined bedding (as described for Unit III). A large hiatus (up to ~4 m.y.) probably exists within the basal part of Unit V, and, therefore, we excluded the data obtained from the lower part of Unit V from our analysis. In addition, core recovery at this site was low (average = 43%) as compared with Site C0011 (average = 71%). Therefore, this analysis is less reliable than that for Site C0011, although both sets of results for the sediment accumulation rates show concordant trends.

The sediment accumulation rates for the hemipelagites and turbidites were calculated on the basis of paleontologic and magnetostratigraphic data (see "Paleomagnetism"), using a least-squares fit and a central difference method with a length of two cores (Fig. F22B). The results of this analysis suggest that the sediment accumulation rate for the hemipelagic deposits was constant (4.5 cm/k.y.) from Unit V to the lower part of Unit III, but in the middle part of Unit III, there appears to have been a significant decrease to 2.6 cm/k.y. (Fig. F22B). This change coincides with a shift in magnetic susceptibility (see "Physical properties"). The sediment accumulation rate was also constant throughout Unit II and into Unit I. The significant decrease in the sediment accumulation rate for the hemipelagites in Unit III at ~11–12 Ma suggests the possibility of some fundamental paleoenvironmental change at Sites C0011 and C0012. Our analysis shows that the sediment accumulation rate for the turbidites in Units II and IV averaged ~0.5–1.0 m per 1 m of deposition for the hemipelagites. The sediment accumulation rate of the turbidites, therefore, was ~1.3–2.6 cm/k.y., for a hemipelagic sediment accumulation rate of ~2.6 cm/k.y. At the Unit IV/III boundary, the sediment accumulation rate for the turbidites shows a substantial decrease (Fig. F22C), followed by a marked increase at the Unit III/II boundary. These trends are all similar to those observed at Site C0011.

Paleogeography and sediment provenance at Site C0012

Site C0012 is located 10 km south of Site C0011, and, therefore, the paleogeography and many of the related discussions are similar to those described for that site (see the "Site C0011" chapter). However, Hole C0012A reached basalt basement and allows us to interpret two lithologic units not previously discussed. The basement rock beneath the Kashinosaki Knoll is basalt (Unit VII) covered by a thin veneer of red calcareous claystone (Unit VI) that represents both pelagic and hemipelagic deposits. The igneous age of the basement is unknown, but calcareous nannofossil assemblages obtained from red calcareous claystone (Unit VI) require an age >18.9 Ma (see "Biostratigraphy"). Following cessation of pelagic sedimentation, the overlying submarine fan system(s) includes coarse-grained sandy turbidites with air fall tuff (Units V and IV) at this site.

The lower part of Unit V is characterized by sandstone turbidites that show alternating compositional changes. Because these sandstones are either volcanic or terrigenous in composition, two discrete sediment sources can be assumed. One possibility is that such compositional differences may be related to separate feeder canyon and channel systems, originating from different parts of the Izu-Bonin arc (e.g., separated by a cross-chain in the Shikoku Basin). An alternative explanation is that the different sediment compositions reflect discrete contributions from both the Outer Zone of southwest Japan and the Izu-Bonin arc sources. Total organic carbon (TOC)/total nitrogen (TN) ratios in the fluid phase of the sediments in Unit V are consistent with a terrigenous component (Fig. F23; see "Organic geochemistry"). In contrast, the submarine fan system of Unit IV is composed mostly of terrigenous material, suggesting the possibility of a later change in the source area.

The turbidity current influx ceased in the middle Miocene (~12.5 Ma) and was replaced by hemipelagic deposition at Site C0012 (Unit III). During that hemipelagic phase of sedimentation, the accumulation rate slowed at ~11–12 Ma, which is coincident with the cessation of voluminous forearc volcanism of southwest Japan at ~ 11 Ma (the transition from Stage II to Stage III of Kimura et al., 2005).

After the deposition of hemipelagic Unit III, another turbidite system that contains abundant tuffaceous materials (Unit II) was activated during the late Miocene (~9 Ma). As discussed for Site C0011, we tentatively interpret this middle Shikoku Basin facies as the distal parts of a submarine fan that was sourced from the Izu-Bonin arc. This submarine fan system ceased during the late Miocene (~7.8 Ma), and hemipelagic sediment with air fall ash layers finally covered Site C0012 (Unit I).

Seismic depth Section ODKM-22 crosses the summit of the Kashinosaki Knoll in the vicinity of Sites C0011 and C0012 and shows thinning of the Shikoku Basin lithologic units onto the basement high (Ike et al., 2008). The upper part of Unit III contains a minimum ~15 m thick interval with steeply

inclined strata, typically at 40°–45° (Sections 322-C0012A-22R-1, 73 cm, through 23R-CC, 26 cm). This is interpreted as a rotational normal fault block on the flank of the Kashinosaki Knoll (see **"Structural geology"**). In the ~20 m above this interval of rotated strata, there appears to be a hiatus of ~1.35 m.y. (Sections 322-C0012A-21R-3, 7 cm, through 19R-1, 32–34 cm) (see **"Biostratigraphy"**). The occurrence of gravitational failure suggests that significant bathymetric relief existed on the Kashinosaki Knoll at the time. The older Units IV and V thin considerably toward the Kashinosaki Knoll (see **"Logging and core-log-seismic integration"**), which demonstrates considerable effects on seafloor bathymetry on the transport and deposition of the turbidites. Unit VI represents the thin veneer of pelagic sediments (~9.3 m thick) immediately overlying the basalt basement.

Comparison between Site C0012 and ODP/IODP sites

The seven lithologic units at Site C0012 tentatively correlate with lithostratigraphic units at Ocean Drilling Program (ODP) Sites 808, 1173, 1174, and 1177 (Table **T5**) (Taira, Hill, Firth, et al., 1991; Moore, Taira, Klaus, et al., 2001; Underwood and Steurer, 2003). On the basis of lithology and age, Unit I at Site C0012 correlates with the upper Shikoku Basin facies at Sites 808 (Subunit IVa), 1173 (Unit II), 1174 (Unit III), and 1177 (Unit I) (Table **T5**). These deposits are all composed of hemipelagic mudstone with intercalations of thin ash. Unit I is Pleistocene–late Miocene in age at Site C0012, which also overlaps with the age of the upper Shikoku Basin facies at the other sites (above).

At Sites C0011 and C0012, Unit II contains abundant tuffaceous and volcaniclastic turbidites and has no equivalent at any other ODP or IODP site (Table **T5**). No unequivocal ash fall deposit occurs in this unit. Unit II is assigned to the middle Shikoku Basin (see the **"Site C0011"** chapter for explanation) on the basis of age and lithology.

Unit III at Site C0012 is older than, but correlates lithologically with, the lower Shikoku Basin hemipelagic facies at Sites 808 (Subunit IVb), 1173 (Unit III), 1174 (Unit IV), and 1177 (Unit II) (Table **T5**). Unit III is characterized by hemipelagic deposits with thin dark green layers (color banding), which is a common lithology in the lower Shikoku Basin facies of all correlative ODP sites in the Nankai Trough and surrounding deep-marine basins. Although ODP Leg 190 scientists did not interpret the origin of color banding, the dark gray to dark green claystone layers may be the alteration products of volcanic glass. Generally, the upper boundary of the lower Shikoku Basin facies is assigned to the bottom of the last distinct ash layer in the upper Shikoku Basin facies, although this transition is also affected by a diagenetic front for ash layers (Taira, Hill, Firth, et al., 1991; Moore, Taira, Klaus, et al., 2001).

Unit IV at Site C0012 roughly corresponds to the lower Shikoku Basin turbidite facies of Site 1177 (Unit III) (Table **T5**). Abundant muddy to sandy turbidites suggest that this unit was deposited in a submarine fan system. The lower Shikoku Basin turbidite facies of Site 1177 contains four packets of sandy turbidites, which contain abundant quartz, sedimentary and metasedimentary lithic fragments, and woody organic matter, all indicating a terrigenous origin. These features are similar to the composition of Unit IV at Site C0012, although the siltstone turbidites in Unit IV are finer grained.

Unit V at Site C0012 is composed of both volcaniclastic and siliciclastic deposits, including tuff and volcaniclastic sandstone, and it is tentatively correlated with the volcaniclastic facies observed at other ODP and IODP sites (i.e., Sites 808, 1174, 1173, 1177, C0011) (Table **T5**). However, at Site C0012 there is only a thin interval (~25 cm) of felsic tuffs (and a slightly thicker interval of >15 m at Site C0011), which contrasts with Site 808, where ~50 m of acidic volcaniclastic deposits occur (Taira, Hill, Firth, et al., 1991). Volcaniclastic facies are widely distributed as deposits covering the basement rocks in the Nankai Trough, with ages increasing away from the axis of the Kinan Seamounts (Unit V at Sites 808, 1174, and C0011; Unit IV of Sites 1173 and 1177). Unit V at Site C0012 is ~14–19 Ma, which also overlaps the age of volcaniclastic deposits at previous ODP sites. Sites 808, 1173, and 1177 penetrated the basalt basement. Thus, the basalt basement rock (Unit VII), together with its thin veneer of red calcareous claystone (Unit VI) recovered at Site C0012, correlates with Unit VI of Site 808 and Unit V of Sites 1173 and 1177; basement ages increase with distance from the axis of the Kinan Seamounts.

Structural geology

Most of the recovered cores at Site C0012 are relatively good quality for the observation of structures; however, poor recovery and highly bioturbated hemipelagic sediments limited the amount of data. Structural data measured on cores are given in C0012_STRUCT_DATA.XLS in STRUCTUR in **"Supplementary material."** The correction of planar structure orientation using shipboard paleomagnetic data was performed the same as at Site C0011 for as long as possible. The distribution of

planar structures and lithologic units with depth are shown in Figure F24.

Bedding

From Cores 322-C0012A-1R through 7R, bedding planes could not be defined because of heavy bioturbation and drilling disturbance. Bedding planes generally dip <25° in lithologic Units I, II, IV, and V. On the other hand, from Cores 322-C0012A-22R through 24R in the upper part of Unit III, bedding shows anomalously steep inclination with a maximum dip of 45°. Although no bedding could be measured in Cores 322-C0012A-25R through 29R because of bioturbation, core surface lineaments, such as *Zoophycos* burrows, are apparently steep. Thus, Unit III is apparently characterized throughout by steep-dipping bedding planes. The bottom of the steep-bedding interval is expected to be between Sections 322-C0012A-29R-4 and 31R-1 (which is not clear in Section 29R-CC and there was no recovery for Core 30R). A similar bedding-angle variation is also identified in Unit III at Site C0011, though the variation is faint. Small-scale chaotic deposits are observed in Sections 322-C0012A-12R-CC and 49R-1 (Fig. F24).

Figure F25 shows the reoriented plot of the planar structures to the geographic coordinate system using paleomagnetic data listed in Table T6. Dominant bedding planes concentrate around the subhorizontal inclination dipping northward. Data from a steeply inclined interval in Unit III show girdle distribution trending north-northwest–south-southeast (Fig. F25). From these data we infer that although bedding planes at this site are tilted to the north, bedding planes in Unit III show large block rotation possibly because of northward sliding.

Deformation structures

Faults

Three types of faults were described at Site C0011 (layer-parallel faults, high-angle faults, and bioturbated dark deformation bands), and they are all observed at Site C0012. Layer-parallel faults are distributed from Units III to V (Fig. F26). High-angle faults/fractures that strike north-northwest–south-southeast are common throughout Hole C0012A from Units I to V (Fig. F27), whereas they develop only in Unit III and deeper at Site C0011. The high-angle faults commonly accompany slickenlines on the fault surface, indicating dip-slip movement. Displacement markers are occasionally identified, and all indicate normal fault sense (e.g., Fig. F27).

Dark deformation bands with bioturbation are also observed at Site C0012 (Fig. F28). Similar to those at Site C0011, finer material fills layer-subparallel bands. The bands occur from Units II to V, whereas we only observed them in Unit III at Site C0011.

Veins

A mineral-filled vein ~5 mm thick is observed in Unit IV (Section 322-C0012A-33R-4), and we observed similar veins in Unit IV at Site C0011. This type of vein is apparently composed of calcite (Fig. F29A). Another type of vein that occurs in Unit V is a layer-parallel vein (Fig. F29B, F29C). Layer-parallel veins appear to develop along former parallel laminae in a thin turbidite package. In interval 322-C0012A-46R-3, 10–12 cm, a layer with thin veins accompanies kinklike folding (Fig. F29B). This may result from coarser grain size with some fluid flow and associated shear concentration.

Sheath folds

Small-scale flow folds with interlimb angles <20° are well developed in laminated sandstone in interval 322-C0012A-45R-1, 80–96 cm (Fig. F30). Although the fold axes are oriented horizontally, the trends of axes curve and exhibit sheath folds. Muddy material injected into the sandy part and the saw-shaped boundary indicate that these structures were formed soon after sedimentation. The sheath fold is a common structure in mass transport deposits (e.g., sediment slides); however, no such structures were reported from Sites 1173 and 1177 (reference sites off Cape Muroto and Cape Ashizuri in the Nankai Trough, respectively).

Interpretation

In general, the deformation structures observed in Hole C0012A correspond with lateral extension and vertical compaction. High-angle bedding that is characteristic in Unit III likely formed because of large block sliding on the northward-tilted seafloor. The upper boundary of this inclined block was not recognized in the cores; however, it is expected to be between Section 322-C0012A-21R-CC and 22R-1. Biostratigraphy data show a possible hiatus in interval 322-C0012A-19R-1, 32–34 cm, through 21R-3, 7 cm (see Table T7), which does not overlap with the slide-induced unconformity. This slight incompatibility in the possible unconformity can be explained by two distinct events. However, we propose a model to interpret this discrepancy with one event because the evidence lies very close together in depth. During block rotation by submarine sliding, the surface sediments may have been soft enough to be suspended and redeposited, followed by further fine-grained sedimentation to attempt to smooth any residual seafloor topography

(Fig. F31). In this case, the hiatus apparently shifts upward. In addition, Unit III consists almost entirely of hemipelagic claystone, which makes structural features hard to detect from the seismic profile. The lower boundary or sliding surface is expected to be between Sections 322-C0012A-29R-4 and 31R-1, which is above the top of Unit IV (Section 31R-4, 74 cm).

High-angle faults/fractures strike north-northwest–south-southeast, and the poles show girdle distribution trending east-northeast–west-southwest. Because most of the slickenlines on the fault surfaces exhibit dip-slip movement, the intermediate principal stress (σ_2) apparently trends north-northwest–south-southeast, perpendicular to the trench, which is similar to the stress trend at Site C0011. Documentation of the structures in Hole C0012A provides a further important structural datum against which we can compare more highly deformed sites within the nearby accretionary prism.

Biostratigraphy

Preliminary shipboard analysis of the core catcher and additional samples from Cores 322-C0012A-1R through 52R reveals assemblages of calcareous nannofossils and planktonic foraminifers (Tables T7, T8). The nannofossil and planktonic foraminifer events recognized in Hole C0012A are reported in Tables T9 and T10. Biostratigraphic datums were mainly derived from calcareous nannofossils (Fig. F32; Table T9). According to these datum events, the composite of Hole C0012A has a Pleistocene age in Core 322-C0012A-1R and an age range of early Pliocene to early Miocene below Core 2R.

Floral and faunal assemblages of planktonic organisms provide some insight into paleoceanographic conditions. Species abundance is generally common to rare. The sediments throughout the sequence contain warm-water genera such as the calcareous nannofossil genus *Discoaster.*

Calcareous nannofossils

Preliminary examination of all core catcher samples from Hole C0012A obtains moderately to poorly preserved nannofossils, which occur in common abundance in most of the samples; species diversity is comparatively high. However, severe dissolution occurred, leading to barren or very poor occurrence of coccoliths in some intervals (Table T7). Most of the zonal markers of Martini's zonation (1971) and Raffi et al. (2006) have been identified in the sedimentary sequence. The nannofossils that occurred in Hole C0012A are listed in Table T7, and the correlations between the hole and the biostratigraphy are shown in Figure F32.

The youngest assemblages in this hole belong to the lower part of the *Ceratolithus cristatus* Zone NN13 and are present in Samples 322-C0012A-2R-4, 15 cm, through 4R-CC, 14–19 cm, where *Amaurolithus* spp. occurred together. The first occurrence (FO) of *C. cristatus*, which defines the bottom of Zone NN13, is observed between Samples 322-C0012A-4R-CC, 14–19 cm, and 5R-CC, 17.5–22.5 cm.

Discoaster quinqueramus and *Discoaster berggrenii,* which indicate upper Miocene Zone NN11 (5.59–8.52 Ma), were found in Samples 322-C0012A-5R-CC, 17.5–22.5 cm, through 17R-CC, 41–43 cm. The paracme end (Raffi et al., 2006) of *Reticulofenestra pseudoumbilicus* was recorded between Samples 322-C0012A-7R-5, 40–42 cm, and 8R-4, 45 cm. The bottom of Zone NN11, marked by the FO of *D. berggrenii,* was observed between Samples 322-C0012A-17R-1, 41–43 cm, and 17R-CC, 10.5–15.5 cm. The paracme beginning (Raffi et al., 2006) of *Reticulofenestra pseudoumbilicus* (8.78 Ma) was also identified between Samples 322-C0012A-17R-CC, 10.5–15.5 cm, and 18R-1, 40–41 cm. Zones NN9 and NN8 are defined by the presence of *Discoaster hamatus* and *Catinaster coalitus,* which were not found in core catcher and additional samples. Therefore, nannofossils indicate a Zone NN9–NN8 hiatus or condensed section in this hole. Samples 322-C0012A-21R-3, 7 cm, through 26R-CC, 4–9 cm, are characterized by the occurrence of *Discoaster kugleri* and *Coccolithus miopelagicus,* which reveals that the intervals are assigned to Zone NN7 (between 10.88 and 11.90 Ma). The last occurrence (LO) of *Cyclicargolithus floridanus* indicates the upper part of Zone NN6 (12.037 Ma), and it was found between Samples 322-C0012A-26R-CC, 4–9 cm, and 27R-3, 67 cm. Therefore, the middle Miocene/upper Miocene boundary is situated between Samples 322-C0012A-21R-3, 7 cm, and 26R-CC, 4–9 cm. *Sphenolithus heteromorphus* occurred continuously in Samples 322-C0012A-40R-5, 16 cm, through 48R-CC, 11–16 cm, and disappeared at the Zone NN5/NN6 boundary (13.532–13.654 Ma) in the middle part of the middle Miocene, which lies between Samples 40R-2, 61 cm, and 40R-5, 16 cm. The assemblages in Samples 322-C0012A-52R-1, 67 cm, through 52R-CC, 7–12 cm, are characterized by the occurrences of *Helicosphaera ampliaperta, Discoaster druggii, Sphenolithus disbelemnos,* and *Sphenolithus dissimilis* and the absence of *S. heteromorphus* and *Sphenolithus belemnos,* which places these samples in the upper part of Zone NN2 (18.921–20.393 Ma). Zones NN4 (*H. ampliaperta* Zone) and NN3 (*S. belemnos* Zone) are missing. However, a middle–lower Miocene hiatus or condensed section occurs at this site. Therefore, Unit

VI is characterized as early Miocene from 18.921 to 20.393 Ma, which corresponds to the deposition of sediments from 528.67 to 530.325 m CSF.

The assemblages are characterized by the occurrence of warmer water species. In particular, the assemblages found in all samples are characterized by high species diversity throughout the hole.

Planktonic foraminifers

Preliminary analysis of all core catcher samples from Cores 322-C0012A-1R through 52R and a few additional samples were examined on board the ship. Planktonic foraminifer fossils occurred at rare (or even barren) to common abundances with good to poor preservation. Hole C0012A sediment samples showed the planktonic foraminifer assemblages are barren to rare in abundance in an almost consecutive number of intervals (Tables **T8, T10**).

Five biohorizons and datum events were noted in Hole C0012A (Table **T8**). The first biohorizon occurred in the middle part of Unit I and was recognized by the FO of *Globigerinoides conglobatus* between Samples 322-C0012A-6R-CC, 10.5–15.5 cm, and 7R-CC, 10–15 cm. The upper part of Unit II is characterized by three biohorizons between Samples 322-C0012A-12R-CC, 15–20 cm, and 13R-CC, 10–15 cm, due to the FO of *Globorotalia plesiotumida*. The FO of *Globoturborotalita nepenthes* is situated between Samples 322-C0012A-13R-CC, 11–16 cm, and 14R-CC, 16–21 cm. The LO of *Paragloborotalia mayeri* between Samples 322-C0012A-17R-CC, 10.5–15.5 cm, and 19R-CC, 10–15 cm, is also situated in Unit II. The fifth and last biohorizon occurred in Unit IV and was recognized by the FO of *Orbulina universa* between Samples 322-C0012A-36R-CC, 0–1 cm, and 37R-CC, 0–5 cm (Table **T8**). However, some planktonic foraminifer shells show deformation in their structure, as observed in the core catcher samples from Samples 322-C0012A-38R-CC, 14.5–19.5 cm, 48R-CC, 11–16 cm, 49R-CC, 8.5–13.5 cm, and 52R-CC, 7–12 cm (Fig. **F33**). For the better explanation of rare availability and correct position of datum events, postcruise studies are required on the additional samples from the core sections.

Sedimentation rates based on biostratigraphy

The changes in sedimentation rate in Hole C0012A, based on calcareous nannofossils, are shown in Figure **F34.** The sedimentation rate was 1.59 cm/k.y. between 5.56 and 7.12 Ma (86.92 and 111.67 m CSF), which corresponds to the middle part of Unit I. In continuation, the sedimentation rate of 5.58 cm/k.y. between 7.12 and 8.40 Ma (111.67 and 199.02 m CSF) corresponds from the middle part of Unit I to the middle part of Unit II. The lower part of Unit II shows a slow sedimentation rate of 2.65 cm/k.y. from 8.40 to 9.60 Ma (199.02 to 225.89 m CSF). Interestingly, a consistent sedimentation rate of 6.93 cm/k.y. from 10.80 to 14.91 Ma (225.89 to 510.55 m CSF) corresponds to the upper part of Unit III to the lower part of Unit V. However, Unit VI sediment deposition is characterized by the time interval from 18.921 to 20.393 Ma (528.67 to 530.325 m CSF). Hence, error bars have been plotted for all the datums (Fig. **F34;** Table **T9**), and the possible error on the oldest sediment from this site is ±0.736 m.y., which may be considered the age of the oldest sediment at this site, between 18.921 and 20.393 Ma.

The sedimentation rates based on calcareous nannofossil datum events indicate a possible time gap of ~2.1 m.y. in Unit III during the late Miocene (LO of *Discoaster hamatus,* 8.78 Ma, to the FO of *Catinaster coalitus,* 10.88 Ma) and of ~4 m.y. at the Unit V/VI boundary during the early Miocene (FO of *Sphenolithus belemnos,* 14.91 Ma, to the FO of *Sphenolithus belemnos,* 18.921 Ma).

Paleomagnetism

We completed natural remanent magnetization (NRM) measurements and alternating-field (AF) demagnetization on a total of 269 discrete samples from Hole C0012A. We analyzed the results in Zijderveld diagrams (Zijderveld, 1967) and calculated the characteristic remanent magnetization (ChRM) direction using principal component analysis (Kirschvink, 1980). Volume magnetic susceptibility of these discrete samples was measured after AF demagnetization with the Kappabridge KLY 35, except for 96 discrete samples from Cores 322-C0012A-4R through 20R, which were measured for anisotropy of magnetic susceptibility (AMS) with the Kappabridge KLY 35 before the AF demagnetization experiments. The Königsberger (*Q*) ratio was also determined for all measured samples. Because of a malfunction of the spinner magnetometer toward the end of the expedition, only two samples from basaltic basement yielded measurements of remanent magnetization on board the ship. Additional postcruise measurements with a cryogenic magnetometer at Geological Survey of Japan, National Institute of Advanced Industrial Science and Technology, made it possible to characterize the remanent magnetization of basaltic samples collected for shipboard study.

NRM, magnetic susceptibility, and Königsberger ratio

Downhole variations of paleomagnetic data obtained from Hole C0012A are shown in Figure **F35.**

Variations of magnetic properties among various lithologies are similar to those observed at Site C0011. Overall, silty claystones in the lower part of Unit III and siltstone in Unit IV and the upper part of Unit V have relatively low NRM intensity (averaging ~2 mA/m) compared to those of sandstones in Unit II (average ~9 mA/m) and volcaniclastic sandstones in the lower part of Unit V (~80 mA/m). In lithologic Unit II, NRM intensity also shows two extremely high peaks of the order of 1 A/m at 161 and 172 m CSF, corresponding to the presence of volcaniclastic sandstones. In lithologic Unit III, both NRM intensity and magnetic susceptibility show a stepwise decrease downhole. The mean NRM intensity value decreases from ~30 mA/m above 270 m CSF to ~7 mA/m below 270 m CSF, indicating a possible change in the depositional environment and perhaps associated with the observed sulfate reduction (see **"Biogeochemical processes"** in "Inorganic geochemistry") and production of methane (see **"Organic geochemistry"**) below 270 m CSF. In contrast, NRM shows a stepwise increase in Unit V from 10 mA/m of the upper sandstone to 80 mA/m of the lower part of the sediments at 480 m CSF, which is the strongest NRM in Hole C0012A.

Magnetic susceptibility and NRM intensity variations through sedimentary units are closely correlated. Magnetic susceptibility values are generally ~2×10^{-4} to ~4×10^{-4} SI in lithologic Units II–IV but are significantly higher (>7×10^{-4} SI) for volcaniclastic sandstones in the lower part of lithologic Unit V. Like the NRM record, two sharp increases in magnetic susceptibility are present at 161 and 172 m CSF in Unit II, corresponding to tuffaceous sandstone and volcaniclastic sandstone at these depths, respectively. Magnetic susceptibility is ~2×10^{-4} SI throughout lithologic Unit I and gradually increases to ~5×10^{-4} SI at the bottom of lithologic Unit II. In lithologic Unit III, magnetic susceptibility shows a stepwise decrease from ~5×10^{-4} to ~2×10^{-4} SI at around 270 m CSF, which is synchronous with the change in intensity of magnetization. Magnetic susceptibility stays around 2×10^{-4} SI through lithologic Unit IV down to the middle of lithologic Unit V, where magnetic susceptibility abruptly increases associated with tuffaceous sandstone and volcaniclastic sandstone. The *Q* ratio for NRM after AF demagnetization at 10 mT (NRM_{10mT}) for the majority of samples (except for the sediments in Unit I) is <1, suggesting that the total magnetization of the sediments contain dominantly induced magnetization. As shown in Figure **F35** (last column), the disappearance of several high peaks and large decrease in *Q* ratios between NRM before demagnetization (NRM_{0mT}) minus NRM_{10mT} (blue symbols) and NRM_{10mT} (red symbols) reveal the existence of the pervasive drilling-induced remanent magnetization (DIRM). The *Q* ratio peaks of various sandstones (triangle and square data points) in Figure **F35** are the results of DIRM because *Q* ratio values after AF demagnetization at 10 mT (red symbols) fall in the same range as those for muddy sediments (Fig. **F35**). This observation suggests that the low-coercivity magnetic minerals in various sandstones carry an unstable remanence that is more susceptible to an external magnetic field.

Paleomagnetic stability tests

Remanent magnetization of discrete samples was investigated using stepwise AF demagnetization techniques in order to extract the primary component of magnetizations acquired at the time of deposition. Because of time constraints and because AF demagnetization appears to be more effective in removing the DIRM as seen in the shipboard paleomagnetic investigation for Site C0011, AF demagnetization was preferred over the thermal technique for sediments and rocks in Hole C0012A. A histogram of inclinations isolated from the 269 discrete samples is shown in Figure **F36.** Inclinations from these discrete samples are mostly concentrated at ±60° (Fig. **F36;** positive and negative peaks). These values are slightly higher but more or less close to the theoretically predicted value for the latitude of this site (±52.1°). Furthermore, the two polarity inclinations are not statistically different from each other, indicating that ChRM is a record of the paleomagnetic field close to the time of formation of the recovered sediments.

Figure **F37** illustrates the magnetic stability behavior of several representative samples from various lithologic units. Figure **F37A, F37B, F37C,** and **F37D** shows examples of normal and reversed polarity intervals giving reliable results for polarity determination. The behavior demonstrates the removal of nearly vertical downward DIRM remanence after AF demagnetization at 10 mT and the isolation of a stable magnetization component that univectorially decays toward the origin of the vector plots (Zijderveld, 1967). As at Site C0011, we also noted that several samples from Hole C0012A display higher remanent magnetization stability (Fig. **F37E, F37F**), indicating the presence of a higher coercivity component, which cannot be completely demagnetized by AF demagnetization at 60 mT. Overall, the quality of paleomagnetic data throughout Hole C0012A is much higher than that at Site C0011, enabling the correlation between magnetostratigraphic data with the standard geomagnetic polarity timescale (GPTS) more confidently (see **"Integrated age model and sediment accumulation rates"**).

Polarity sequence and magnetostratigraphy

We used ChRM inclinations from discrete measurements to define magnetic polarity sequences for Site C0012. Similar to the magnetic records at Site C0011, several relatively well defined polarity intervals have been identified in downhole magnetostratigraphic records. As with most applications of magnetostratigraphy, one of the greatest problems is correctly matching the observed sequence of magnetic polarity zones with the appropriate part of the GPTS. The polarity interval between 7.5 and 8.5 Ma could be well correlated with the standard GPTS unambiguously. For instance, shipboard biostratigraphic data suggest that sediments within 107.17–200.63 m CSF are older than 7.07 Ma but younger than 8.78 Ma (see **"Biostratigraphy"**). This information suggests that the observed normal polarity interval between 142.11 and 169.39 m CSF (Sections 322-C0012A-11R-2, 86 cm, through 14R-1, 88 cm) should correspond to the normal polarity Chron C4n.2n (7.695–8.108 Ma).

For the other part of Hole C0012A, the interpretation of the paleomagnetic polarity record is less straightforward. However, available biostratigraphic data from this site assisted in deciding which observed magnetic polarity zone or set of zones can be correlated with which magnetic chron on the GPTS (Tables **T11, T6**).

Integrated age model and sediment accumulation rates

Magnetostratigraphic and biostratigraphic (calcareous nannofossil) datum events are summarized in Tables **T11** (Model A) and **T6** (Model B), and the main features of the magnetostratigraphic interpretation along with the inferred biostratigraphic zones at Site C0012 are presented in Figure **F38.** The age determinations based on magnetostratigraphy are modeled in two ways. Although both of the models rely on biostratigraphy (nannofossil datum; blue curve), Model A (green curve) stresses on internal consistency of magnetozone sequences, whereas Model B (purple curve) follows the nannofossil datum as faithfully as possible.

From these age models we infer that a significant increase in sediment accumulation rate occurred in Unit I at ~130 m CSF from ~2 to ~6 cm/k.y. for Model A (green curve) or at ~110 m CSF from ~1 to ~6 cm/k.y. for Model B (purple curve). For both of these models, the lithologic Unit I/II boundary can be assigned an age of 7.8 Ma. These sedimentation rate values are not corrected for compaction.

For Unit II, the two age models (A and B) are the same to 175 m CSF (~8.3 Ma). Model A suggests successive changes in sediment accumulation rates from ~6 to ~1 cm/k.y. at ~180 m CSF, from ~1 to ~7 cm/k.y. at ~190 m CSF, and from ~7 to ~3 cm/k.y. at ~210 m CSF. Model A gives a Unit II/III boundary age of 10.2 Ma (Fig. **F38A**). The interpretation of Model A strongly relies on the recognition of an apparently long normal interval between 216.84 and 238.04 m CSF as long normal Chron C5n.2n (9.987–11.040 Ma), although there are considerable breaks between cores. This model correlates the successive sequence of relatively short polarity intervals found in the magnetostratigraphic record between 180 and 195 m CSF to Chrons C4Ar.2r through C4r.1r, which forms a straight line. A drawback of Model A might be the correlation of the dominantly reversed polarity interval between 197 and 207 m CSF with successive chrons between Chrons C4Ar.3r and C5n.1r, where polarity is dominantly normal in the middle and only the margins are reversed. This can be compromised by attributing the normal chron (C5n.1n) to the breaks of the core.

On the contrary, the discrepancy between Model A (green) and the nannofossil age model (blue) can be compromised by Model B (purple), which mostly follows nannofossil datum events with less emphasis on the consistency of the magnetic polarity zonations in the middle part of Unit II. Model B imposes the normal sequence between 213 and 240 m CSF to between polarity Chrons C4An and C5n.2n. The two relatively long reversed Chrons C4Ar.1r and C4Ar.2r could be imposed on the possible hiatus close to the base of Unit II (~220 m CSF) suggested by nannofossil (see **"Biostratigraphy"**) and sedimentological features (see **"Lithology"**). Only the hiatus can explain the absence of reversed polarity intervals and relatively slow sedimentation rate of ~1.3 cm/k.y. for this period. One advantage of this model is the fairly uniform sedimentation rate of ~6 cm/k.y. between 111 and 213 m CSF. Model B gives a Unit II/III boundary age of 9.4 Ma.

For Model A, in the middle part of Unit III, the sedimentation rate increases slightly from ~3 to 4 cm/k.y. at ~250 m CSF and increases further to ~6 cm/k.y. at ~280 m CSF (Fig. **F38B**). The Unit III/IV boundary age can be estimated as 12.8 Ma according to the magnetostratigraphy, which is also consistent with the age model based on nannofossil datum. Model B merges to Model A at ~240 m CSF and both models are mostly consistent to the bottom of Unit III. The Unit III/IV boundary age for Model B is 12.7 Ma, which is slightly younger than Model A.

The age models for Units IV and V are less certain, especially for the lower part of the hole where core recovery was rather poor. Although there is a considerably reliable nannofossil datum at 417 m CSF

(Zone NN6/NN5 boundary; Table T11), we seek for the age model (Model A) away from the control point trying to follow a straight line from Unit III down to the upper part of Unit V (430 m CSF) with a sedimentation rate of ~6 cm/k.y. Model A requires a significant increase in sedimentation rate to ~46 cm/k.y. below ~430 m CSF down to ~470 m CSF, which can be justified by imposing on the possible rapid deposition expected for the thick sandstones recovered for the interval (see "Lithology"). The age model infers a Unit IV/V boundary age of 14.4 Ma. The sedimentation rate decreases to ~8 cm/k.y. below 470 m CSF to 500 m CSF. Below 500 m CSF, the age model is less definite because of low recovery and a suspected hiatus inferred from nannofossil data.

Model B departs from Model A (green curve) from 270 m CSF downward. Model B favors an age of 13.5 Ma for the Unit IV/V boundary (Fig. F38B; purple text). Model B also infers a smoother sedimentation rate for the base of Unit V but a significantly increased sedimentation rate from Unit III (6.8 cm/k.y.) to Unit IV (10 cm/k.y.). According to these age models, the age of the thick sandstone units in the upper part of Unit V (430~470 m CSF) is estimated at 14.8 Ma (green curve, Model A) and 13.9 Ma (purple curve, Model B).

We emphasize that although there are options for the selection of age models, the ChRM of rocks from Hole C0012A is stable and of high quality as mentioned above. Thus, the possibility of misinterpretation of the polarity of the magnetozone is small compared with Hole C0011B, where interpretation of the magnetic polarity pattern itself was very difficult for the lower part of the hole. The missing intervals due to poor core recovery and a possible hiatus leave room for the possibility of several interpretations such as Models A and B for Site C0012. With the stability of ChRM, it is clear that possible future continuous piston coring at the site should unify the age model.

Paleomagnetic reorientation of the cores

Paleomagnetic declinations were used extensively for reorienting cored material. Table T12 lists the paleomagnetic directions used for reorienting coherent blocks cored by RCB for structural parameters relative to the geographic coordinate system (see "Structural geology"). Although clockwise rotation of ~30° is expected for the Shikoku Basin between 5 and 15 Ma according to Sdrolias et al. (2004), we assumed that the cored material did not experience significant rotation relative to the geographic coordinate system after the deposition. Further analysis to detect reliable magnetization components by distinguishing both viscous remanent magnetization and primary remanent magnetization could be conducted by using a superconducting quantum interference device magnetometer in combination with AF and thermal demagnetizations in shore-based studies.

Paleomagnetic characterization of basement rocks

Toward the end of Expedition 322, we collected four basaltic samples from lithologic Unit VII and measured them with detailed AF demagnetization experiments. Reversed polarity magnetization was observed on two of these basaltic samples (Samples 322-C0012A-53R-2, 35–37 cm, and 54R-1, 77–79 cm) after removal of the DIRM at 5 mT or less. Figure F39 shows examples of the demagnetization behavior of these samples. At least three components of magnetization are revealed by the AF demagnetization (Fig. F39A). DIRM is removed after AF demagnetization at 5 mT and shows a stable magnetization component (declination = 41.4°, inclination = –30°, and maximum angular deviation = 0.7°) decreasing toward the origin. However, after 15 mT AF demagnetization, the magnetization direction shows complicated behavior and starts to radiate out after 25 mT AF demagnetization. After 35 mT AF demagnetization, the magnetization turns around and moves toward origin with the magnetization direction antiparallel to the direction observed from 7.5–15 mT AF demagnetization (declination = –142.8°, inclination = –34.7°, and maximum angular deviation = 4.7°). The magnetization intensity at 5 mT is 15 A/m after removal of DIRM, whereas after 35 mT it is 52 A/m, which is unusually strong. Similarly, Sample 322-C0012A-54R-1, 77–79 cm, showed complex behavior through AF demagnetization (Fig. F39C, F39D).

Remanent magnetization measurements were conducted after the cruise with a cryogenic magnetometer in combination with an AF demagnetizer on sister specimens of Samples 322-C0012A-53R-2, 35–37 cm (Fig. F39B), and 54R-1, 77–79 cm (Fig. F39E). Neither specimen showed the complex demagnetization behavior with antiparallel magnetization observed during shipboard measurements. Sample 322-C0012A-53R-2, 35–37 cm (Fig. F39B), shows stable magnetization of reversed polarity decreasing toward the origin, which agrees with the magnetization component below 15 mT measured with the shipboard spinner magnetometer (Fig. F39A). The magnetization intensity shown in Figure F39B is much lower than that in Figure F39A. This may be explained by the fact that the sister specimen was taken from the outer rim of the minicore

(Sample 322-C0012A-53R-2, 35–37 cm), which shows altered color. Sample 322-C0012A-54R-2, 77–79 cm (Fig. F39E), shows normal polarity, which does not agree with the magnetization component of Sample 54R-1, 35–37 cm (Fig. F39B), measured with the shipboard spinner magnetometer. The relatively low coercivity component of Figure F39E and the position of the sister specimen (outer rim of the minicore) may indicate that the magnetization component is mainly composed of DIRM. Another sister specimen was taken between the above two specimens for Sample 322-C0012A-54R-1, 35–37 cm, and measured with a cryogenic magnetometer with stepwise thermal demagnetization up to 600°C (Fig. F39F). The magnetization shows reversed polarity, which agrees with the magnetization component below the AF demagnetization field of 23 mT (Fig. F39D). Specimens from two other samples taken as shipboard paleomagnetic samples were subjected to both AF and thermal demagnetizations and showed relatively stable maganetization of reversed polarity. In conclusion, the basaltic basement rocks taken below the sediment at this site may retain reversed polarity magnetization as the primary magnetization. Table T13 is the summary of the paleomagnetic directions obtained for basaltic samples measured on board the ship and onshore either with AF or thermal demagnetization.

Although the origin of the antiparallel magnetization observed only for the specimens measured with the shipboard spinner magnetometer cannot be understood completely at present, the significant increase in the magnetization intensity after AF demagnetization antiparallel to the original magnetization combined with unstable behavior in-between may suggest the presence of self-reversed remanent magnetization. This phenomenon may be explained as a special case for some magnetic minerals that were in the limited place of only two samples, which cannot even be observed in the sister samples from the same minicore. Another possibility may be that the phenomenon occurred only for the samples taken just after drilling. The magnetic mineral characteristic of the phenomenon disappeared several weeks after the cruise. This could possibly be attributed to self-reversal of pyrrhtite during AF demagnetization, which was already reported by Bina et al. (1999). A third possibility is that the phenomenon was caused by the malfunction of the spinner magnetometer that occurred on the same day basaltic basement rocks were measured. This may be justified by the noisy behavior during AF demagnetization measured with the shipboard spinner magnetometer for Samples 322-C0012A-55R-1, 23–25 cm, and 57R-1, 44–46 cm.

Anisotropy of magnetic susceptibility

We were able to measure AMS with the Kappabridge KLY 35 for minicore samples from Cores 322-C0012A-4R through 20R, with generous help provided by the shipboard scientific party. For the lower part of Hole C0012A, limited samples were taken from tuffaceous/volcaniclastic sandstone layers and sand/silty sandstone layers, and AMS measurements on these samples were performed after AF demagnetization. As stated in the "Site C0011" chapter, based on the results of the comparison experiment, AMS after AF demagnetization could be used for sandstones, although it was recommended that AMS should be measured before AF demagnetization (e.g., Jordanova et al., 2007).

Figure F40 shows the AMS parameters measured for various lithologies in Hole C0012A. K_{min} inclinations (Fig. F40A) are dominantly steeper than 60° except for a few horizons. For example, four samples at 90 m CSF (from Sections 322-C0012A-5R-1 through 5R-4) have K_{min} inclinations ~0. Shape parameter (T) also indicates prolate ellipsoid (Fig. F40C). This observation may indicate possible vertical stretching of the core because of RCB coring of soft sediments, which was also visually observed as vertical striations (see "Lithology"). An interesting feature is that a shallower K_{min} inclination (~15°) is present at the Unit I/II boundary at ~150 m CSF (Fig. F40A). The anisotropy degree parameter (P′) increases at the base of Unit II from ~1.02 to ~1.10 and also at bottom of the Unit V (Fig. F40B). These increases in anisotropy degree may be related to the change in the sedimentary depositional environment.

The K_{min} inclination values for the four basaltic rock samples of lithologic Unit VII are close to zero, and shape parameter is negative (i.e., prolate). The characteristics of these AMS parameters could indicate the presence of linear fabric caused by basaltic flow during the basalt emplacement or by late-stage extensions of the seafloor.

Physical properties

The goal of physical property measurements was to define bulk physical properties and their downhole variations in Hole C0012A. Measurements included natural gamma radiation, gamma ray attenuation (GRA) density, electrical resistivity, magnetic susceptibility, thermal conductivity, moisture and density (MAD) properties (bulk and grain density, porosity, and water content), and *P*-wave velocity (see "Physical properties" in the "Methods" chapter). All physical property measurements were made after cores had been imaged by X-ray computed tomography

and equilibrated to room temperature (~20°C). Whole-round multisensor core logger (MSCL-W) data were collected on whole-round sections to define natural gamma radiation, GRA density, noncontact resistivity, magnetic susceptibility, and *P*-wave velocity. Thermal conductivity was measured using either a full-space needle probe method on whole-round cores or a half-space line source method on working halves of cores. The half-space method was used on sediments below 130 m CSF where the needle probe could not be inserted into whole-round cores. MAD analyses were performed on discrete samples collected from the working halves and cluster samples taken adjacent to whole-round samples. Undrained shear strength measurements were made above 95 m CSF. Below 115 m CSF, where sediment was competent enough to cut samples from working halves, *P*-wave velocity and electrical resistivity were measured in the *x*-, *y*-, and *z*-directions (see Fig. **F17** in the "Methods" chapter) on discrete cube samples.

MSCL-W

Electrical resistivity

Electrical resistivity increases downhole in Units I–V (Fig. **F41**). Average values are 0.85 Ωm in Unit I, 1.46 Ωm in Unit II, 1.92 Ωm in Unit III, 2.70 Ωm in Unit IV, and 4.13 Ωm in Unit V. Electrical resistivity then decreases abruptly to an average of 3.85 Ωm in Unit VI. The increasing resistivity through Units I–IV is likely controlled by porosity loss (Fig. **F42**) during burial and consolidation. Maximum resistivity values of 59.7 Ωm are nearly identical to those observed in Hole C0011B.

Natural gamma radiation

Natural gamma radiation also increases downhole through Unit IV, averaging 27.3 counts per second (cps) in Unit I, 32.2 cps in Unit II, 36.9 cps in Unit III, and 39.3 cps in Unit IV (Fig. **F41**). Natural gamma radiation then decreases to average values of 35.1 cps in Unit V and 29.3 cps in Unit VI. The shift to lower natural gamma radiation within Unit V occurs at ~480 m CSF. This corresponds to an increase in magnetic susceptibility (Fig. **F41**), suggesting a bulk compositional change. Natural gamma radiation again decreases in Unit VII.

Magnetic susceptibility

Magnetic susceptibility averages 33.8×10^{-5} corrected volume magnetic susceptibility (CMS) in Unit I, then increases within Unit II, with an average of 101.6×10^{-5} CMS with peaks reaching 1445×10^{-5} CMS. Local high magnetic susceptibility values occur within volcaniclastic sandstones (see **"Lithology,"** Fig. **F2**). Magnetic susceptibility increases with depth in Unit III until ~270 m CSF, below which it decreases to an average of 14.7×10^{-5} CMS. A similar decrease within Unit III was observed in Hole C0011B at 575 m CSF, providing a surface within Unit III for correlation between sites. Magnetic susceptibility is constant in Unit IV and the upper half of Unit V. At ~480 m CSF, average magnetic susceptibility increases to 59.2×10^{-5} CMS for the lower section of Unit V and Unit VI. This correlates with a decrease in natural gamma radiation (Fig. **F41**), and both of these changes correlate with the appearance of sandstone beds containing abundant iron-rich minerals (see **"Lithology"**). The basalt of Unit VII is characterized by high magnetic susceptibility.

GRA density

GRA density is relatively uniform over Units I–VI and ranges from 0.82 to 0.97 g/cm³, with an average of 0.94 g/cm³ (Fig. **F41**). As observed in Hole C0011B, the presence of air between cores and core liners resulted in anomalously low values of both GRA density and *P*-wave velocity.

MAD measurements

MAD measurements of discrete samples from Hole C0012A provide a detailed characterization of grain density, bulk density, porosity, void ratio, and water content. All MAD data are provided in Tables **T14** and **T15** and are summarized below.

Bulk and grain density

Bulk density in Hole C0012A increases downhole from 1.45 g/cm³ at the seafloor to 2.10 g/cm³ by 530 m CSF (Fig. **F42A**). Within lithologic Unit I, bulk density shows a minor increase from 100 to 136 m CSF. Bulk density then increases consistently through Units II, III, and IV. The Unit IV/V boundary has a notable decrease (~0.12 g/cm³) in bulk density. Bulk density then continues to increase with depth through Unit V. Grain density throughout the sedimentary section (lithologic Units I–VI) has high variability ranging between 2.1 and 3.0 g/cm³ with few outliers. Some of this scatter could be due to inaccurate pycnometer measurements. Some of the bulk density scatter was likely the result of coring disturbance.

Porosity

MAD-determined porosity decreases downhole through the sedimentary section in Hole C0012A (lithologic Units I–VI) (Fig. **F42B**). Seafloor porosity is 0.70, and porosity decreases to 0.35 by 530 m CSF. Similar to bulk density, small deviations from the overall trend are present. For example, the lithologic

Unit IV/V boundary (418 m CSF) displays an increase in porosity from 0.38 to 0.45. A subtle porosity increase may also exist near 125 m CSF, but there are scatter in the data.

To characterize the general porosity behavior, we employ a porosity-effective stress model (e.g., Rubey and Hubbert, 1959):

$$\phi = \phi_o e^{-\beta \sigma'_v},$$

where

ϕ_o = reference porosity,
β = bulk compressibility, and
σ'_v = effective vertical stress determined by integrating the bulk density data and assuming hydrostatic fluid pressure.

A regression of the mudstone porosity-effective stress data yields bulk compressibility of 0.15 1/MPa and reference porosity of 0.65. This bulk compressibility is twice that observed in Hole C0011A (see **"Physical properties"** in the "Site C0011" chapter). The source of the difference in compressibility requires future analyses. The hemipelagic mudstones from the two sites are similar in bulk mineral composition (see **"Lithology"**), and thus, they should have similar compression behavior.

The porosity model provides a baseline behavior for sediments in Hole C0012A. Deviations from the model can provide insights to lithologic variation, mineralogy, or grain fabric differences. Our model trend predicts slightly lower porosity than observed in Unit I (Fig. **F42B**). This mismatch is most pronounced from ~120 to 136 m CSF, which may indicate greater stiffness in these sediments. This stiffness could be controlled by grain shape, sediment composition, or the presence of intergranular cement. Lithologic Unit III generally has slightly lower porosity than predicted; these sediments may have been exposed to higher stresses (e.g., erosion of previous overburden) and are mildly overconsolidated or they may have greater compressibility than the bounding sediments. A thin interval of strata near the top of the Unit V boundary has higher porosity than the background trend. This high-porosity zone correlates with a zone of decreased compressional velocity and lower thermal conductivity (Fig. **F42**). This interval could represent an in situ high-porosity zone within the volcaniclastic-rich deposits. Further shore-based analyses are required to establish the origin of this high-porosity/low-velocity/low-thermal conductivity zone.

Shear strength

Vane shear and penetrometer measurements constrain undrained shear strength in lithologic Unit I above 95 m CSF (Fig. **F43;** Table **T16**). In this interval, plastic deformation was observed during shear strength measurements; below 95 m CSF, brittle deformation occurred when shear strength measurements were attempted, so no data were recorded. The observed shear strength was low (21–30 kPa) near the seafloor. From 50 to 95 m CSF, shear strength was highly variable, ranging from values similar to observations at the seafloor to ~100 kPa. The scatter in the data does not indicate any trend with depth or lithology.

Anisotropy of *P*-wave velocity and electrical resistivity

P-wave velocity and electrical resistivity were measured on discrete cube samples cut from working halves. Sample cubes were cut once the sediment was competent enough for cutting, which occurred at 115 m CSF. Measurements were made in three directions orthogonal to the *x*-, *y*-, and *z*-axes of the core reference (see Fig. **F17** in the "Methods" chapter), allowing determination of the horizontal-plane anisotropy (a_{VPhor}, a_{phor}) and vertical-plane anisotropy (a_{VPvert}, a_{pvert}) of *P*-wave velocity and electrical resistivity (see **"Physical properties"** in the "Methods" chapter).

Compressional wave velocity (V_P) increases downhole consistent with the increase in bulk density and the decrease in porosity (Fig. **F42**). Average compressional velocity is 1600 m/s near the base of lithologic Unit I and increases to 2100 m/s in Unit V. From 500 m CSF into lithologic Unit VI, average velocity decreases. Two samples had V_P that exceeded 2200 m/s; these samples were collected in proximity to densely lithified calcareous claystones (see **"Lithology"**). Velocity in lithologic Unit VII (basalt) greatly exceeds the overlying sedimentary section (Fig. **F42C**). *P*-wave velocities of basalt samples ranged from 3083 to 4767 m/s (Table **T17**). Within these data, one sample (322-C0012A-54R-2, 24.0 cm) was distinctly faster than the others.

Vertical-plane anisotropy (a_{VPvert}) has significant scatter in Hole C0012A that may be related to sample disturbance; however, general trends are discernable. Sediment velocity is slightly positive at the base of lithologic Unit I, from which point anisotropy increases (horizontal velocity greater than vertical velocity) with depth through Units II–VI (Fig. **F44;** Table **T17**). This increase correlates with increasing bulk density and decreasing porosity and thus likely reflects preferential grain orientation and enhanced grain contacts from consolidation. At ~450 m CSF, a cluster of samples has vertical velocity exceeding horizontal (negative V_P anisotropy). These samples

are from sandstone layers or fine-grained sediment adjacent to sandstone layers. Variable grain shape and structure may have influenced grain orientation and reorientation during burial, producing this response. Alternately, a change in depositional process (e.g., turbidity current versus hemipelagic settling) could have produced a different initial fabric. *P*-wave velocity anisotropy in the basalt was generally positive with a maximum of 5.84%. The fastest specimen (Sample 322-C0012A-54R-2, 24.0 cm) was the only basalt specimen with a negative vertical-plane anisotropy of velocity (Fig. **F44**).

A velocity-porosity relation is developed with measured *P*-wave velocity and nearest neighbor (<66 cm offset) porosity data (Fig. **F45**). For comparison to the observations, empirical relations for *P*-wave velocity versus porosity from (1) global compilations for "normal" and "high" consolidation sediment (Erickson and Jarrard, 1998) and (2) Shikoku Basin sediments (Hoffman and Tobin, 2004) are plotted (Fig. **F45**). The global compilations provide loose upper and lower bounds for the expected relationship between velocity and porosity. The curve reported for Shikoku Basin sediments is

$$V_P = 0.746 + 0.532\phi + \{0.305/[(\phi + 0.124)^2 + 0.051]\} + 0.61(v_{sh} - 1.123)X_1,$$

where

V_P = *P*-wave velocity,
ϕ = porosity,
v_{sh} = shale fraction (0.32), and
X_1 = $\tanh[40(\phi - \phi_c)] - |\tanh[40(\phi - \phi_c)]|$,

where critical porosity (ϕ_c) is 0.295 (Hoffman and Tobin, 2004). Most of the velocity observations in Hole C0012A lie above the Shikoku Basin trend but within the bounds of the global compilation (Fig. **F45**). This trend suggests that for a given porosity, sediments in Hole C0012A are faster than those at Site 1173. This is similar to our observations of data from Hole C0011B (Fig. **F44**) and suggests that the bulk and/or shear moduli of the sediments is higher at Sites C0011 and C0012 in comparison to Site 1173. The nature of grain contacts and fabric could contribute to these differences between Shikoku Basin sites.

Electrical resistivity measured on cube samples varies from 2.0 to 8.0 Ωm (Table **T18;** Fig. **F46**). In most cases, vertical resistivity is greater than horizontal (negative anisotropy), with anisotropy becoming more negative downhole. The increase in resistivity with depth through Units I and II is steeper than in the underlying units. The increase in anisotropy with depth appears fairly constant through all lithologic units. Scatter in the data (likely resulting from variability in the number and orientation of drilling-induced, fluid-filled microfractures) obscures any definitive trend in resistivity anisotropy.

Thermal conductivity

Thermal conductivity measurements were conducted on whole-round cores (<105 m CSF) with the full-space needle probe and on split core samples (>130 m CSF) with the half-space method. Thermal conductivity values vary between 0.98 and 1.47 W/(m·K) in mud(stone) and between 1.19 and 2.10 W/(m·K) in sand(stone) (Table **T19;** Fig. **F42D**). Units I and II have increasing thermal conductivity with depth. Thermal conductivity in Unit III increases until 290 m CSF, where a step decrease occurs. This decrease coincides with a marked decrease in core quality (smaller biscuits and more fractures below 290 m CSF). The change in core quality may reflect a lithologic change; the rate of porosity loss may also change at 290 m CSF, potentially suggesting a change in compression and/or pore structure. Thermal conductivity then increases to the base of Unit IV. The top of Unit V is marked by a second decrease in thermal conductivity, which correlates with a porosity increase (Fig. **F42**). Sand(stone) in Unit V has a higher thermal conductivity than mud(stone). The correlation between thermal conductivity and porosity is shown in Fig. **F47.** The relationship is consistent with thermal conductivity of the sediment grains ranging from 2.1 to 3.4 W/(m·K) and centered at 2.6 W/(m·K).

Comparison with Site C0011 and Sites 1173 and 1177

We compare some of the general trends in sediment physical properties between Sites C0012, C0011, 1173, and 1177. Site C0012 has an interval where porosity may not decrease steadily with depth. Similar trends existed at Sites 1173, 1177, and C0011 (Figs. **F47, F42B**). This zone is shallower (<136 m CSF) at Site C0012 than it is at the other sites. Below this zone, porosity decreases along a normal consolidation trend at each site. The interval of near-constant porosity and the transition to normal consolidation are much more pronounced (i.e., larger porosity shifts) at Sites 1173 and 1177. The trends are less obvious at Sites C0011 and C0012. Each of the sites has increasing *P*-wave velocity and *P*-wave anisotropy with depth through the normal consolidation zone (Figs. **F47, F44**). With the exception of a small region in lithologic Unit V in Hole C0012A, all sites have positive velocity anisotropy, indicating *P*-waves travel faster in the horizontal direction than in the vertical direction. Overall, these general porosity and velocity trends are indicative of

shallow sediments having an open framework of randomly oriented particles. As consolidation progresses during burial, porosity loss occurs, platey, clay-sized particles align, and preferential fabrics develop. While the general consolidation trends of mudstones between sites are similar, there are distinct differences in compressibility. Specifically, the sediments at Sites C0012 and 1173 are more compressible than sediments at Site C0011. These differences, for what appear to be similar hemipelagic mudstones, are difficult to explain. They could be influenced by minor changes in depositional environment and processes, variations in stress history, and/or bias and distribution in sampling or disturbance. These differences could prove important for pore shape changes and flow pathways, and thus warrant further research, which will be facilitated by shore-based geotechnical experiments.

Core quality and physical properties

Multiple drilling and coring processes affected core quality in a negative way, which had adverse effects on data quality from bulk physical property measurements. Hole C0012A suffered from many of the same problems observed in Hole C0011A (see **"Core quality and physical properties"** in "Physical properties" in the "Site C0011" chapter): decreased core diameter from overwashing, microscale cracks and fractures, decreasing thermal conductivity with decreasing porosity, large scatter in MAD measurements, and scatter in velocity and velocity anisotropy (Figs. **F47, F41, F42, F44**). Although disturbance existed, Hole C0012A had intervals of good core recovery where data trends are cleaner than those observed in Hole C0011A. With depth, however, core quality degraded and disturbance artifacts increased. These disturbance effects do not preclude interpretation of general trends in the physical properties; however, they should be carefully considered as additional research, including shore-based geotechnical experiments, continues.

Inorganic geochemistry

The main objective of the inorganic geochemistry program at Site C0012 was to document the geochemical properties of subduction inputs at a site located at a basement high, near the crest of the Kashinosaki Knoll. Such data will increase our understanding of how basement topography and concomitant changes in temperature regime and stratigraphy may control fluid composition, fluid and chemical transport, and water-rock interactions in the presubduction equivalent of the seismogenic zone. A total of 42 pore fluid samples were squeezed from selected whole-round sections for chemical and isotopic analyses. Sample depths ranged from 89.4 to 529.2 m CSF. One sample per core was collected when possible. Because of poor core recovery, no pore fluids were recovered from Cores 322-C0012B-1R, 2R, 3R, 4R, 12R, 22R, 26R, 30R, 38R, and 51R.

Fluid recovery

To obtain enough interstitial water for shipboard and shore-based analyses, 19–48 cm long sections were squeezed. Interstitial water volumes recovered from whole-round sections by squeezing at a maximum pressure of 25,000 psi are presented as a function of depth in Figure **F48.** Interstitial water volume shows a general decrease with depth, from 28 to 3 mL. In contrast to the distribution observed in Hole C0011B, there is no correlation between water volume and lithologic units or sand content of the samples.

Even though the strata at Site C0012 are moderately lithified, core quality was significantly better than that at Site C0011; thus, contamination with drilling fluid at this site was minimal. The dissolved sulfate profile (Fig. **F49**) shows quite a bit of structure, which is consistent with biogeochemical processes at this site (see **"Biogeochemical processes"**). The observed distribution precludes any correction for potential contamination because a total depletion of sulfate in the formation fluids could not be assumed. The interstitial water data collected at Site C0012 are listed in Table **T20** and illustrated in Figures **F49, F50,** and **F51.** These distributions reflect the balance between reactions in the sediment section, reactions with underlying oceanic crust, and possibly diffusive interaction with seawater-like fluid within basaltic basement.

Biogeochemical processes

The dissolved sulfate profile indicates continued depletion with depth to ~300 m CSF. There is a small amount of ammonium at this site (<1 mM), which reflects the production of this metabolite during organic matter degradation. However, the actual production and consumption pathways cannot be fully constrained because of a lack of samples shallower than 89 m CSF. Alkalinity is also probably produced in the shallower section, and the observed low values throughout the hole reflect low carbon cycling rates at this site, superimposed on the consumption of bicarbonate ions by ash alteration and carbonate formation (Fig. **F49**).

The sulfate profile clearly documents a sulfate reduction zone that is significantly deeper than that recovered at other sites in this margin (Fig. **F52**). Other sites have rapid deposition and burial of sediment by

turbidites, with TOC content ranging from 0.3 to 1 wt% (see "Organic geochemistry" in the "Site C0011" chapter and Shipboard Scientific Party, 2001). Sedimentation rates ranging from 6 to 11 cm/k.y. at ODP Sites 1173, 1175, and 1176 lead to sulfate consumption in the upper 20 m CSF because of a lessening resupply by diffusion from overlying water. Site C0012 sits on a bathymetric high; here a lower sedimentation rate (see "Biostratigraphy") and the generally low organic matter content of the sediment (TOC 0.2 wt%, see "Organic geochemistry") lead to extremely slow sulfate consumption. Thus, the topography of Site C0012 provides an end-member system to study processes associated with metabolic carbon pathways. It is worth noting that sulfate depletion at ~300 m CSF coincides with a marked increase in methane concentration (see "Organic geochemistry"). It is possible that the sulfate profile at Site C0012 is driven by anaerobic oxidation of this methane. This reaction leads to the production of hydrogen sulfide (Fig. F52), as manifested by a marked increase in concentration concomitant with the methane peak. Sulfide produced by this process is removed as a variety of iron sulfide minerals, with pyrite being its most stable phase. Pyrite is commonly observed in sediments from this depth range (see "Lithology").

Another interesting aspect of the observed sulfate profile is the increase in concentration in the lower strata below ~450 m CSF, which also feed the anaerobic methane oxidation (AMO). Detailed sampling of the expanded sulfate–methane transition zone at this site and postcruise analyses of organic metabolites and their isotopic composition will enhance our understanding of the operating microbial pathways (see "Microbiology" and "Organic geochemistry").

Halogen concentration (Cl and Br)

The chlorinity profile at Site C0012 increases by 12% from ~560 mM to a maximum value of 627 mM at 509 m CSF. The probable cause is hydration reactions during alteration of volcanic sand, dispersed volcanic glass, and basement. At Site C0012, there is no indication of any of the freshening patterns observed at Site C0011 and at sites drilled seaward of the deformation front during ODP Legs 131 and 190 (Gieskes et al., 1993; Shipboard Scientific Party, 2001). At Site 1177, where heat flow is relatively low, the freshened interstitial waters are thought to have originated from greater depth arcward and reflect fluid migration updip through high-permeability horizons (Steurer and Underwood, 2003; Saffer et al., 2008; Saffer and McKiernan, 2009). If this interpretation is correct, then the lack of a freshening pattern at Site C0012 indicates that a similar system of fluid flow might advance to Site C0011 but not reach the crest of the Kashinosaki Knoll. Although noteworthy when compared to results from Site C0011, these chlorinity data are not the highest observed along the transect defined by IODP Expeditions 315, 316, and 322. Along this transect, IODP Site C0004, located to access the shallow portion of the megasplay fault system, has even higher chlorinity values (Expedition 316 Scientists, 2009).

Chemical changes due to alteration of volcaniclastics

Changes in dissolved magnesium, potassium, and silica concentrations are driven by several processes, which are dominated at Site C0012 by alteration of volcanic ash, volcanic rock fragments, and underlying basement rock (e.g., Gieskes et al., 1990; Lawrence and Gieskes, 1981). Decreasing magnesium, potassium, and silica concentrations in the upper 220 m CSF illustrates the importance of Mg and K uptake by clay formation during volcanic ash alteration. Rubidium, zinc, and uranium also show a marked decrease in concentration, suggesting uptake of these minerals during smectite formation (Fig. F51). As shown for Site C0011, first-order equilibrium thermodynamic calculations indicate that the distribution of magnesium, potassium, and silica below 250 m CSF is controlled by formation of montmorillonite phases (Fig. F53).

For calcium, the predicted increase because of ash alteration is overprinted by carbonate precipitation and by deep-seated reactions within the lower sediment section. The high levels of dissolved calcium support carbonate precipitation, even at very low alkalinity (<2 mM), as shown by values above saturation for calcite and dolomite (Fig. F53). Carbonate was recovered throughout the cored section as vein filling, carbonate cements, and discrete layers up to 16 cm thick (see "Lithology"). Zeolite formation from volcanic glass alteration is also favored by high calcium concentration in the basal fluids. The decrease in dissolved Na in the lower sections sampled is consistent with the formation of these minerals, and the low dissolved potassium content in the fluids probably hinders formation of K-clinoptilolite (Fig. F53).

The increase in strontium in interstitial waters from reaction with volcanoclastic material is well established (e.g., Gieskes et al., 1990) and is likely the cause of the observed increase in dissolved Sr with depth at Site C0012 (Fig. F50). In contrast to observations at Site C0011, lithium distribution shows a decrease with depth below a maximum value of ~208 µM at 227.5 m CSF. Field and laboratory observations document remobilization of lithium at tem-

peratures >70°C and uptake at lower temperatures (Edmond et al., 1979; Seyfried et al., 1984; You et al., 1996). The causes for the unusual Li profiles at Site C0012 are not yet clear. Analyses of the distribution of this element among other sites drilled in this margin and isotopic data collected postcruise will help constrain the processes leading to the observed Li distributions.

Basal fluids

Profiles of most major cations and sulfate show an intriguing reversal to near-seawater values in Cores 322-C0012B-48R and 49R (between 490 and 500 m CSF). Similar reversals have been observed at the flanks of the Juan de Fuca Ridge (e.g., Elderfield et al., 1999; Wheat and Mottl, 1994) and in the equatorial Pacific (Baker et al., 1991; Oyun et al., 1995), which were cited as evidence for the presence of fluid flow in the underlying oceanic crust. To provide a preliminary evaluation of the nature of the anomalous pore fluid at Site C0012, we estimate the fraction of seawater needed to produce the reversal in the potassium profile to be ~20%. We then estimate major ion concentration in the fluids if no anomaly was present by interpolating data from above and below Cores 322-C0012B-48R and 49R and calculate the concentration that would be created by a 20% dilution of this signal with seawater. The results (shown in Table **T21**) show good consistency between the expected and observed values. We tentatively attributed the observed reversals to a seawater-like fluid migrating through the permeable basaltic basement. At this moment, the hydrology controlling this flow, including potential recharge and discharge zones, remains unidentified.

These results outline the intriguing possibility of two fluid regimes that alter the chemical composition of the interstitial water in the sediments seaward of the Nankai Trench. One regime is characterized by in situ dehydration of clay minerals in areas of high heat flow (Steurer and Underwood, 2003). At Site 1177, where heat flow is lower, there is evidence of local migration through high-permeability turbidite units in the incoming sediment section. Patterns of fluid freshening (negative chloride anomalies) (Saffer et al., 2008; Saffer and McKiernan, 2009) and the presence of methane and higher hydrocarbons are similar at Sites 1177 and C0012; the methane and ethane measured may indicate a very small contribution of fluid flow at this site, or alternatively, these hydrocarbons may be generated in situ by microbial processes. Identification of the hydrocarbon sources remains to be resolved by shore-based investigations, and high-quality borehole temperature data will allow better assessments of in situ reaction conditions.

Here, we postulate the presence of another flow regime driven by migration of a seawater-like flow through the upper basaltic crust, which modifies the chemical composition observed within the sediment pile. In particular, the observed increase in sulfate below 490 m CSF cannot be supplied by the methane-rich fluids that originate from greater depth arcward because those fluids are depleted in sulfate. Furthermore, the fact that we see an increase in hydrogen sulfide produced by AMO in the overlying sediments, argues for the sustained presence of sulfate in upper basaltic basement, which must be supplied by active flow within the basaltic crust. This fluid in basaltic basement is actively exchanging with the ocean and altering the interstitial fluid composition of the deep sediments by either diffusional exchange, or a via a hydrologic connection to the sandstone turbidites in lithologic Unit V.

Organic geochemistry

The organic geochemistry program during Expedition 322 aimed to characterize the composition of sediments entering the subduction system with respect to their role as a habitat for the deep subseafloor biosphere. The main objectives were to characterize (1) potential energy sources of the deep biosphere (i.e., amount and quality of organic matter within the sediment); (2) the availability of hydrogen (H_2), which represents an alternative energy source that results from the degradation of organic matter, mineral–water interactions, or radiolysis of water; (3) the presence of methane that could be exploited as an energy source in the process of AMO and which may lead to the formation of authigenic carbonate; and (4) sources of methane and other hydrocarbon gases that formed in the course of biogenic and thermogenic alteration of organic matter during sediment burial.

To achieve these objectives, we (1) measured the quantity and composition of hydrocarbon gases (C_1–C_4) by headspace technique, (2) determined the potential of the sediments to produce and consume hydrogen in incubation experiments, (3) characterized the composition of the particulate sedimentary organic matter by elemental analysis and Rock-Eval pyrolysis, and (4) measured total inorganic carbon concentration in the sediment.

Hydrocarbon gases

At Site C0012, no dissolved hydrocarbon gases were detected in the upper 189 m of sediment (Table **T22**). Below this depth, low methane (C_1) levels were observed in all cores. Methane concentration increases with depth to a maximum of 244 µM at 417 m CSF

(Fig. F54). In the depth range of the higher methane values (359.5–453.2 m CSF), ethane (C_2) was detected, reaching a concentration maximum of 3.9 µM at 417 m CSF. These concentrations are considerably lower than those at Site C0011. Propane (C_3) and butane (C_4) were not detected in any core. The occurrence of ethane below 359.5 m CSF results in low C_1/C_2 ratios (<100) that generally decrease with depth. The concentration maxima of methane and ethane occur in the same depth interval and are located at the interface of lithologic Units IV and V. These maxima correspond to a zone with locally elevated TOC contents in the solid phase of the sediment (Fig. F55).

The very low C_1/C_2 ratios at Site C0012 are unusual for sediment with low organic carbon contents, and data plot within the "abnormal" range in the context of safety considerations (Pimmel and Claypool, 2001; Fulthorpe and Blum, 1992; Shipboard Scientific Party, 1995) when plotted versus an estimated temperature (Fig. F56), assuming a geothermal gradient of 0.056°C/m and a bottom water temperature of 3°C. Operations continued despite the low C_1/C_2 ratio because the observed concentrations were much smaller than those at Site C0011. Potential sources of the hydrocarbon gases (i.e., in situ production and/or migration from deeper, hotter sources) remain to be determined by additional shore-based investigations.

Hydrogen gas

Because the analysis of H_2 using the extraction method at Site C0011 demonstrated the high potential for H_2 contamination with RCB drilling and coring, we only used the incubation method to investigate H_2 concentrations at Site C0012. For this approach, we subsampled nine whole-round cores that had been taken for shore-based analyses (biogeochemistry and deep biosphere studies), incubated the subsamples at estimated in situ temperatures, and monitored for the evolution of H_2 concentration in the headspace of the incubation vials until the expedition ended (i.e., over a period of 170–300 h) (see the "Methods" chapter). During this period, dissolved H_2 concentrations were uniformly low in all samples (Table T23; Fig. F57), with a maximum value of 3.26 nM in the deepest core (Section 322-C0012A-45R-3).

Carbon, nitrogen, and sulfur contents of the solid phase

In general, nitrogen and sulfur contents are low in the majority of cores retrieved from Site C0012 (Table T24). Inorganic carbon contents (0.4 ± 0.9 wt%) are of similar magnitude to organic carbon contents (0.3 ± 0.1 wt%) but show sporadic excursions toward higher values in all lithologic units (Fig. F55). Inorganic carbon contents correspond to a mean calcium carbonate content of 3.26 wt%, but elevated carbonate contents reach 63.6 wt% (Table T24). Total sulfur contents average 0.2 ± 0.5 wt% but show distinct excursions toward higher values at the Unit IV/V boundary and reach a maximum of 4.3 wt% in Unit V (Fig. F55). Except for one elevated value, nitrogen contents are nearly uniform in Units I–IV, where they averaged 0.05 ± 0.01 wt%, but they decrease with depth to 0.02 wt% in Unit V (Fig. F55). TOC/TN averaged ~7 ± 4, which indicates a predominantly marine origin of the sedimentary organic matter (Fig. F23), but ratios >25 indicate the presence of terrigenous organic matter in Unit V.

The trend toward higher TOC and sulfur contents in the solid phase of sediments in the upper part of Unit V occurs ~10 m deeper than the maxima of dissolved methane, ethane (Fig. F54), and sulfide (Fig. F23) at the lithologic Unit IV/V boundary. This observation gives rise to the question of whether or not the presence of terrigenous matter in Unit V supports the metabolic activity of deeply buried microorganisms that could produce methane and ethane in situ, whereas other microorganisms consume these dissolved gases by AMO where sulfate is available. The presence and metabolic activity of microorganisms and the origin of the hydrocarbon gases remain to be explored by shore-based investigations.

Characterization of the type and maturity of organic matter by Rock-Eval pyrolysis

At Site C0012, the type and maturity of the organic matter was characterized in seven samples using shipboard Rock-Eval pyrolysis. The amount of hydrocarbons generated through thermal cracking of nonvolatile organic matter (S_2) is <0.32 mg hydrocarbon (HC)/g sediment and the amount of CO_2 produced during pyrolysis of the kerogen (S_3) is <1.2 mg CO_2/g sediment (Table T25). S_2 and S_3 values show little variation throughout lithologic Units II, III, and IV (Fig. F58). The hydrogen index and oxygen index average 50 ± 10 mg HC/g TOC and 400 ± 200 mg CO_2/g TOC (Table T25; Fig. F58), respectively, and indicate that the sedimentary organic matter is a kerogen of Type III evolution. T_{max} values average 420° ± 10°C, which shows that organic matter in the samples is at a thermally immature stage (Table T25). T_{max} does not vary with depth (Fig. F58).

Microbiology

Fifteen 10 cm long whole-round cores were taken from Hole C0012A for molecular microbiology

(phylogenetic) studies and stored at –80°C. Where dedicated microbiology whole-round core sampling was not possible, thirteen 10 cm^3 "chips" were obtained from cleaned whole-round cores used for interstitial water analyses.

Fourteen 5 cm long whole-round cores were taken, sampled for fluorescence in situ hybridization (FISH) and cell counting studies, and stored anaerobically at 4°C for shore-based cultivation studies. Thirteen 2–3 cm^3 samples were also taken from these 5 cm long whole-round cores and two samples from the 10 cm long whole-round cores described above (prior to ultralow freezing). These samples were preserved for shore-based cell counting and FISH studies.

Sixteen samples were taken from the working-half split core containing the contact between the lowermost sedimentary unit, a red claystone, and the uppermost basement basalt (lithologic Units VI and VII, respectively). These samples were obtained 3 days after core collection from cores that were stored at 4°C during this time.

Thirty-nine 1–2 mL interstitial water samples were obtained for shipboard spectrophotometric analyses of ferrous iron and acid volatile sulfide. Data from these measurements are presented in **"Inorganic geochemistry."**

Table **T26** presents the depth and type distribution of the samples obtained from Hole C0012A described above.

Logging and core-log-seismic integration

Hole C0012 B logging data quality

No scientifically useful wireline logging data were obtained at Site C0012, on a side track of Hole C0012A (see **"Operations"**).

Seismic analysis

Seismic stratigraphy

We tried to consistently trace the seismic units identified at Site C0011 up to Site C0012 throughout the three dimensional (3-D) seismic data. In-line 95 and Cross-line 435 of the 3-D prestack depth migration (PSDM) across Site C0012 and their interpretations are shown in Figures **F21** and **F59,** respectively. Based on reflection characteristics, we identified six of the seven major seismic reflection units that were identified at Site C0011. Unit F is missing around this site. Units A and B both show several discontinuous and chaotic reflectors, and the Unit A/B boundary is more or less continuous along Cross-line 435 and ambiguous on In-line 95. Compared with Site C0011 seismic profiles, they represent a significant thickness decrease. On In-line 95, the upper boundary of Unit C, which is highly reflective, shows more or less continuous reflection, whereas the lower boundary is quite disrupted. The ~200 m thick Unit D is characterized by a transparent reflection character. Unit E, a series of strong reflectors just above Unit G, seems to show thickness changes and unconformably overlies the basement Unit G. We recognize a normal fault on the northwest flank of Unit E. Unit E appears to show northeast tilting on Cross-line 435, even though its upper and lower boundaries are limited to the central part of the profile because of a lack of sufficient common depth point coverage. Unit G is oceanic crust of the Philippine Sea plate.

Based on core-log-seismic integration at Site C0011 and lithologic/seismic correlation between Sites C0011 and C0012, seismic Units A–B, C, D, and E correspond to lithologic Units I, II, III–upper IV, and lower IV–V, respectively.

References

Baker, P.A., Stout, P.M., Kastner, M., and Elderfield, H., 1991. Large-scale lateral advection of seawater through oceanic crust in the central equatorial Pacific. *Earth Planet. Sci. Lett.,* 105(4):522–533. **doi:10.1016/0012-821X(91)90189-O**

Bina, M., Tanguy, J.C., Hoffmann, V., Prévot, M., Listanco, E.L., Keller, R., Fehr, K.Th., Goguitchaïchvili, A.T., and Punongbayan, R.S., 1999. A detailed magnetic and mineralogical study of self-reversed dacitic pumices from the 1991 Pinatubo eruption (Philippines). *Geophys. J. Int.,* 138(1):159–178. **doi:10.1046/j.1365-246x.1999.00865.x**

Canfield, D.E., Raiswell, R., and Bottrell, S., 1992. The reactivity of sedimentary iron minerals toward sulfide. *Am. J. Sci.,* 292:659–683.

Crozier, T.E., and Yamamoto, S., 1974. Solubility of hydrogen in water, sea water, and sodium chloride solutions. *J. Chem. Eng. Data,* 19(3):242–244. **doi:10.1021/je60062a007**

Edmond, J.M., Measures, C., McDuff, R.E., Chan, L.H., Collier, R., Grant, B., Gordon, L.I., and Corliss, J.B., 1979. Ridge crest hydrothermal activity and the balances of the major and minor elements in the ocean: the Galapagos data. *Earth Planet. Sci. Lett.,* 46(1):1–18. **doi:10.1016/0012-821X(79)90061-X**

Elderfield, H., Wheat, C.G., Mottl, M.J., Monnin, C., and Spiro, B., 1999. Fluid and geochemical transport through oceanic crust: a transect across the eastern flank of the Juan de Fuca Ridge. *Earth Planet. Sci. Lett.,* 172(1–2):151–165. **doi:10.1016/S0012-821X(99)00191-0**

Erickson, S.N., and Jarrard, R.D., 1998. Velocity-porosity relationships for water-saturated siliciclastic sediments.

J. Geophys. Res., 103(B12):30385–30406. doi:10.1029/98JB02128

Expedition 316 Scientists, 2009. Expedition 316 Site C0004. *In* Kinoshita, M., Tobin, H., Ashi, J., Kimura, G., Lallemant, S., Screaton, E.J., Curewitz, D., Masago, H., Moe, K.T., and the Expedition 314/315/316 Scientists, *Proc. IODP,* 314/315/316: Washington, DC (Integrated Ocean Drilling Program Management International, Inc.). doi:10.2204/iodp.proc.314315316.133.2009

Fulthorpe, C.S., and Blum, P. (Eds.), 1992. Ocean Drilling Program guidelines for pollution prevention and safety. *JOIDES J.,* 18(7). http://www.odplegacy.org/PDF/Admin/JOIDES_Journal/JJ_1992_V18_No7.pdf

Gieskes, J.M., Blanc, G., Vrolijk, P., Elderfield, H., and Barnes, R., 1990. Interstitial water chemistry—major constituents. *In* Moore, J.C., Mascle, A., et al., *Proc. ODP, Sci. Results,* 110: College Station, TX (Ocean Drilling Program), 155–178. doi:10.2973/odp.proc.sr.110.170.1990

Gieskes, J.M., Gamo, T., and Kastner, M., 1993. Major and minor element geochemistry of interstitial waters of Site 808, Nankai Trough: an overview. *In* Hill, I.A., Taira, A., Firth, J.V., et al., *Proc. ODP, Sci. Results,* 131: College Station, TX (Ocean Drilling Program), 387–396. doi:10.2973/odp.proc.sr.131.133.1993

Hoffman, N.W., and Tobin, H.J., 2004. An empirical relationship between velocity and porosity for underthrust sediments in the Nankai Trough accretionary prism. *In* Mikada, H., Moore, G.F., Taira, A., Becker, K., Moore, J.C., and Klaus, A. (Eds.), *Proc. ODP, Sci. Results,* 190/196: College Station, TX (Ocean Drilling Program), 1–23. doi:10.2973/odp.proc.sr.190196.355.2004

Ike, T., Moore, G.F., Kuramoto, S., Park, J-O., Kaneda, Y., and Taira, A., 2008. Tectonics and sedimentation around Kashinosaki Knoll: a subducting basement high in the eastern Nankai Trough. *Isl. Arc,* 17(3):358–375. doi:10.1111/j.1440-1738.2008.00625.x

Jordanova, D., Jordanova, N., Henry, B., Hus, J., Bascou, J., Funaki, M., and Dimov, D., 2007. Changes in mean magnetic susceptibility and its anisotropy of rock samples as a result of alternating field demagnetization. *Earth Planet. Sci. Lett.,* 255(3–4):390–401. doi:10.1016/j.epsl.2006.12.025

Kimura, J.-I., Stern, R.J., and Yoshida, T., 2005. Reinitiation of subduction and magmatic responses in SW Japan during Neogene time. *Geol. Soc. Am. Bull.,* 117(7–8):969–986. doi:10.1130/B25565.1

Kirschvink, J.L., 1980. The least-squares line and plane and the analysis of palaeomagnetic data. *Geophys. J. R. Astron. Soc.,* 62(3):699–718. doi:10.1111/j.1365-246X.1980.tb02601.x

Lawrence, J.R., and Gieskes, J.M., 1981. Constraints on water transport and alteration in the oceanic crust from the isotopic composition of pore water. *J. Geophys. Res.,* 86(B9):7924–7934. doi:10.1029/JB086iB09p07924

Lourens, L.J., Hilgen, F.J., Shackleton, N.J., Laskar, J., and Wilson, D., 2004. The Neogene period. *In* Gradstein, F.M., Ogg, J.G., and Smith, A.G. (Eds.), *A Geological Time Scale 2004*. Cambridge (Cambridge Univ. Press), 409–440.

Martini, E., 1971. Standard Tertiary and Quaternary calcareous nannoplankton zonation. *Proc. Int. Conf. Planktonic Microfossils,* 2:739–785.

Moore, G.F., Taira, A., Klaus, A., et al., 2001. *Proc. ODP, Init. Repts.,* 190: College Station, TX (Ocean Drilling Program). doi:10.2973/odp.proc.ir.190.2001

Oyun, S., Elderfield, H., and Klinkhammer, G.P., 1995. Strontium isotopes in pore waters of east equatorial Pacific sediments: indicators of seawater advection through oceanic crust and sediments. *In* Pisias, N.G., Mayer, L.A., Janecek, T.R., Palmer-Julson, A., and van Andel, T.H. (Eds.), *Proc. ODP, Sci. Results,* 138: College Station, TX (Ocean Drilling Program), 813–819. doi:10.2973/odp.proc.sr.138.156.1995

Parkhurst, D.L., and Appelo, C.A.J., 1999. User's guide to PHREEQC (version 2)—a computer program for speciation, batch-reaction, one-dimensional transport and inverse geochemical calculations. *USGS Water-Resour. Invest. Rep.,* 99–4259.

Pimmel, A., and Claypool, G., 2001. Introduction to shipboard organic geochemistry on the *JOIDES Resolution*. *ODP Tech. Note,* 30. doi:10.2973/odp.tn.30.2001

Raffi, I., Backman, J., Fornaciari, E., Pälike, H., Rio, D., Lourens, L., and Hilgen, F., 2006. A review of calcareous nannofossil astrobiochronology encompassing the past 25 million years. *Quat. Sci. Rev.,* 25(23–24):3113–3137. doi:10.1016/j.quascirev.2006.07.007

Rubey, W.W., and Hubbert, M.K., 1959. Role of fluid pressure in mechanics of overthrust faulting, Part 2. Overthrust belt in geosynclinal area of western Wyoming in light of fluid-pressure hypothesis. *Geol. Soc. Am. Bull.,* 70(2):167–206. doi:10.1130/0016-7606(1959)70[167:ROFPIM]2.0.CO;2

Saffer, D.M., and McKiernan, A.W., 2009. Evaluation of in situ smectite dehydration as a pore water freshening mechanism in the Nankai Trough, offshore southwest Japan. *Geochem., Geophys. Geosys.,* 10(2):Q02010. doi:10.1029/2008GC002226

Saffer, D.M., Underwood, M.B., and McKiernan, A.W., 2008. Evaluation of factors controlling smectite transformation and fluid production in subduction zones: application to the Nankai Trough. *Isl. Arc,* 17(2):208–230. doi:10.1111/j.1440-1738.2008.00614.x

Saito, S., Underwood, M.B., and Kubo, Y., 2009. NanTroSEIZE Stage 2: subduction inputs. *IODP Sci. Prosp.,* 322. doi:10.2204/iodp.sp.322.2009

Sdrolias, M., Roest, W.R., and Müller, R.D., 2004. An expression of Philippine Sea plate rotation: the Parece Vela and Shikoku basins. *Tectonophysics,* 394(1–2):69–86. doi:10.1016/j.tecto.2004.07.061

Seyfried, W.E., Jr., Janecky, D.R., and Mottl, M.J., 1984. Alteration of the oceanic crust: implications for geochemical cycles of lithium and boron. *Geochim. Cosmochim. Acta,* 48(3):557–569. doi:10.1016/0016-7037(84)90284-9

Shipboard Scientific Party, 1995. Site 909. *In* Myhre, A.M., Thiede, J., Firth, J.V., et al., *Proc. ODP, Init. Repts.,* 151: College Station, TX (Ocean Drilling Program), 159–220. doi:10.2973/odp.proc.ir.151.107.1995

Shipboard Scientific Party, 2001. Site 1177. *In* Moore, G.F., Taira, A., Klaus, A., et al., *Proc. ODP, Init. Repts.,* 190: College Station, TX (Ocean Drilling Program), 1–91. **doi:10.2973/odp.proc.ir.190.108.2001**

Steurer, J.F., and Underwood, M.B., 2003. Clay mineralogy of mudstones from the Nankai Trough reference Sites 1173 and 1177 and frontal accretionary prism Site 1174. *In* Mikada, H., Moore, G.F., Taira, A., Becker, K., Moore, J.C., and Klaus, A. (Eds.), *Proc. ODP, Sci. Results,* 190/196: College Station, TX (Ocean Drilling Program), 1–37. **doi:10.2973/odp.proc.sr.190196.211.2003**

Taira, A., Hill, I., Firth, J.V., et al., 1991. *Proc. ODP, Init. Repts.,* 131: College Station, TX (Ocean Drilling Program). **doi:10.2973/odp.proc.ir.131.1991**

Taylor, S.R., and McLennan, S.M., 1985. *The Continental Crust: Its Composition and Evolution:* Oxford (Blackwell Scientific).

Underwood, M.B., and Steurer, J.F., 2003. Composition and sources of clay from the trench slope and shallow accretionary prism of Nankai Trough. *In* Mikada, H., Moore, G.F., Taira, A., Becker, K., Moore, J.C., and Klaus, A. (Eds.), *Proc. ODP, Sci. Results,* 190/196: College Station, TX (Ocean Drilling Program), 1–28. **doi:10.2973/odp.proc.sr.190196.206.2003**

Wheat, C.G., and Mottl, M.J., 1994. Hydrothermal circulation, Juan de Fuca Ridge eastern flank: factors controlling basement water composition. *J. Geophys. Res.,* 99(B2):3067–3080. **doi:10.1029/93JB01612**

You, C.-F., Chan, L.H., Spivack, A.J., and Gieskes, J.M., 1995. Lithium, boron, and their isotopes in sediments and pore waters of Ocean Drilling Program Site 808, Nankai Trough: implications for fluid expulsion in accretionary prisms. *Geology,* 23(1):37–40. **doi:10.1130/0091-7613(1995)023<0037:LBATII>2.3.CO;2**

Zijderveld, J.D.A., 1967. AC demagnetization of rocks: analysis of results. *In* Collinson, D.W., Creer, K.M., and Runcorn, S.K. (Eds.), *Methods in Palaeomagnetism:* New York (Elsevier), 254–286.

Publication: 10 October 2010
MS 322-104

Figure F1. Portion of IFREE 3-D seismic reflection Line 95 showing Sites C0011 and C0012. VE = vertical exaggeration.

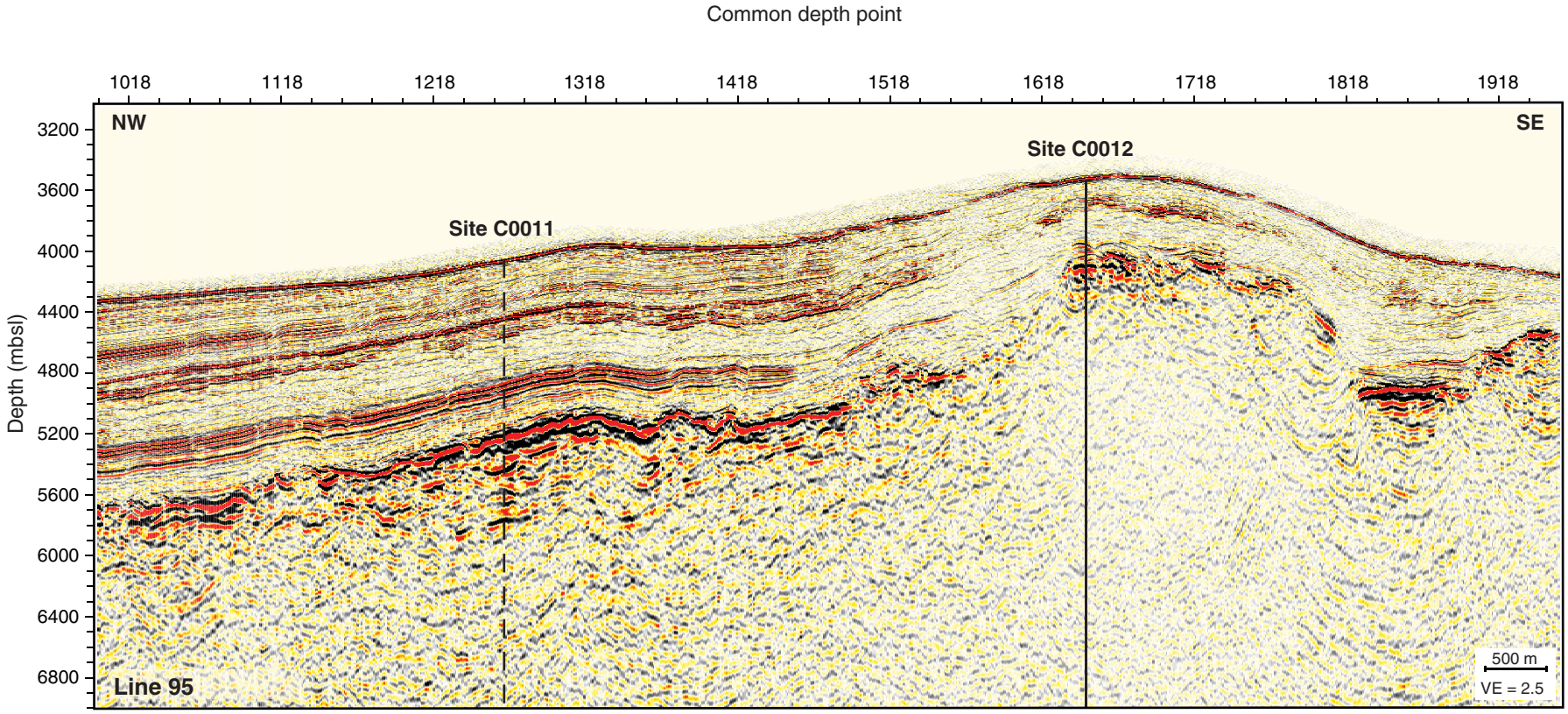

Figure F2. Summary lithology, Site C0012. TD = total depth.

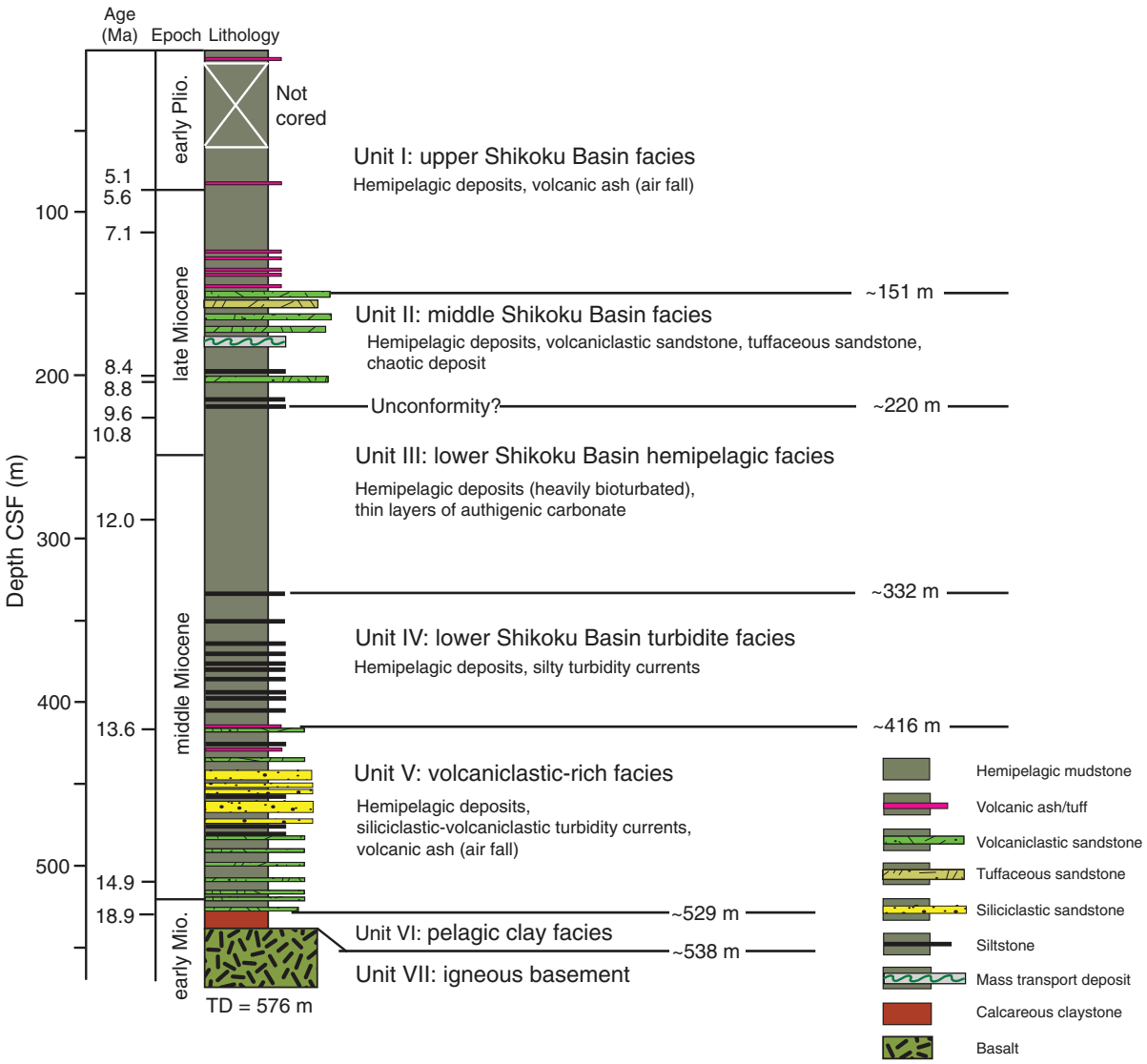

Figure F3. Thickness of turbidites (clayey siltstone, tuffaceous sandstone, volcaniclastic sandstone, and sandstone), Site C0012. Units II and IV characterized by thick turbidites (>60 cm thick).

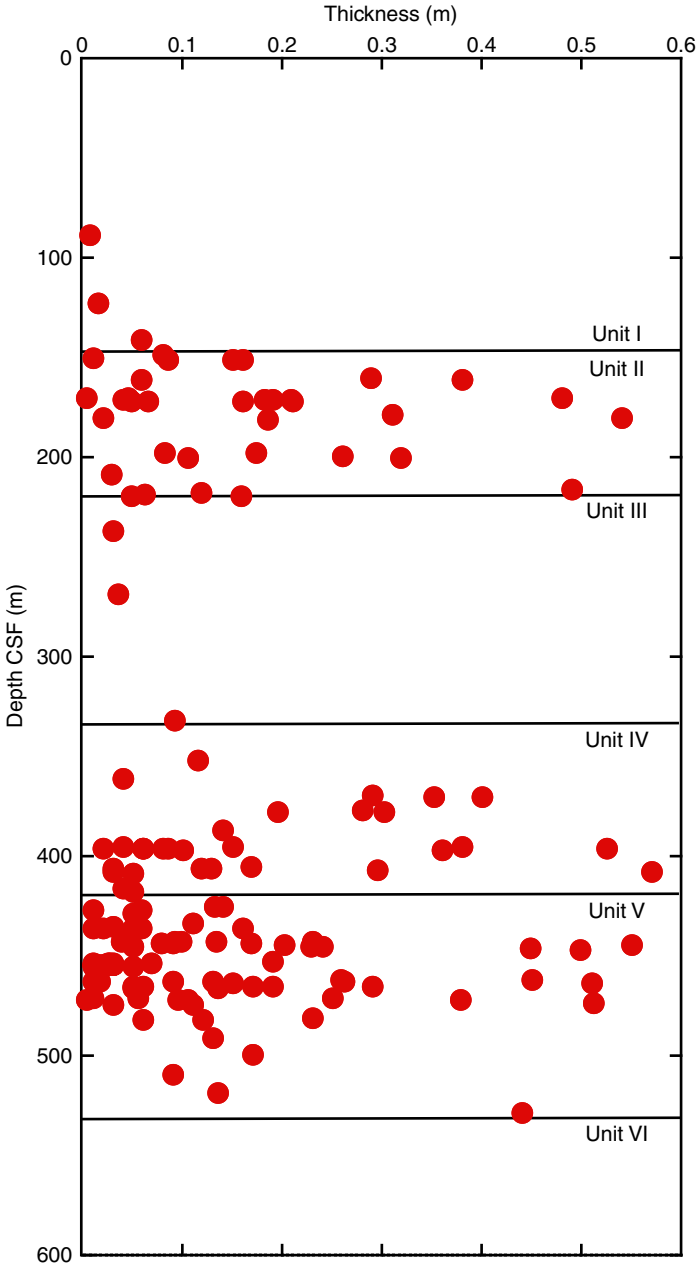

Figure F4. Example of chaotic deposit in Unit II (Sample 322-C0012A-14R-4, 27–43 cm). These deposits comprise disaggregated pieces of volcanic sandstone and bioturbated silty claystone that show folding, thinning, and attenuation of original bedding.

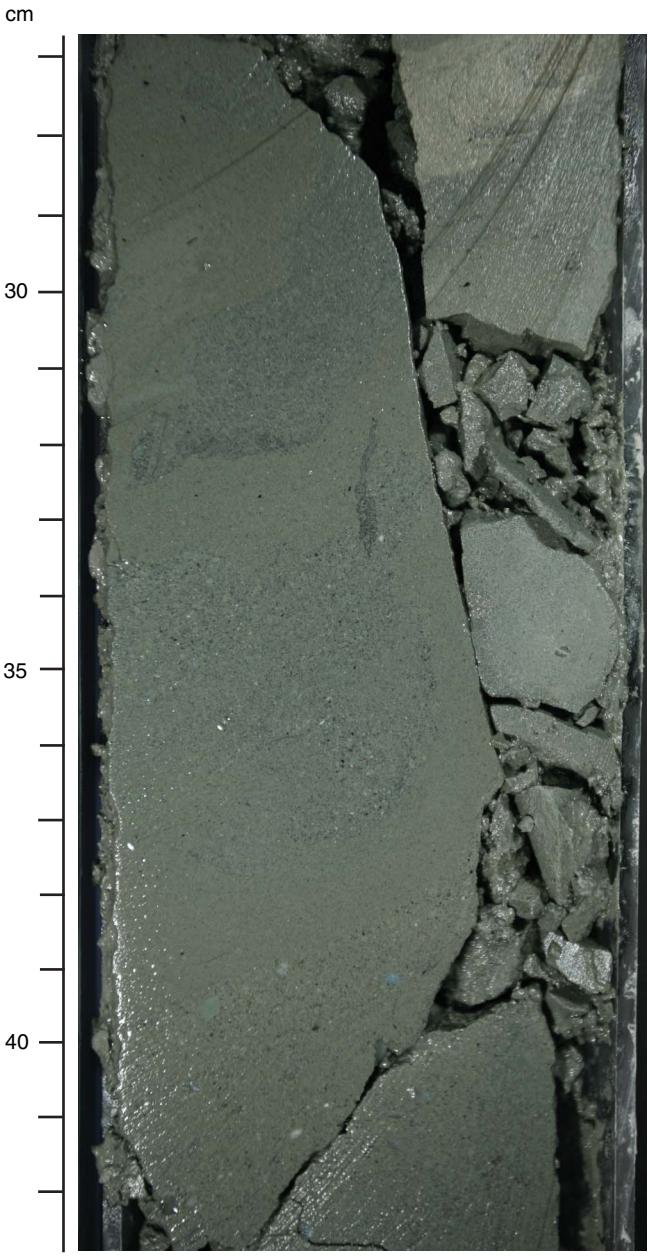

Figure F5. Smear slide data for Site C0012 versus depth (m CSF). **A.** Ratio of feldspar versus total mineral content. **B.** Quartz to total mineral ratio. **C.** Heavy minerals to total mineral ratio. **D.** Volcanic lithics to total lithic ratio. **E.** Total mineral content. **F.** Sedimentary lithics. **G.** Total volcaniclastic component. **H.** Total glass content.

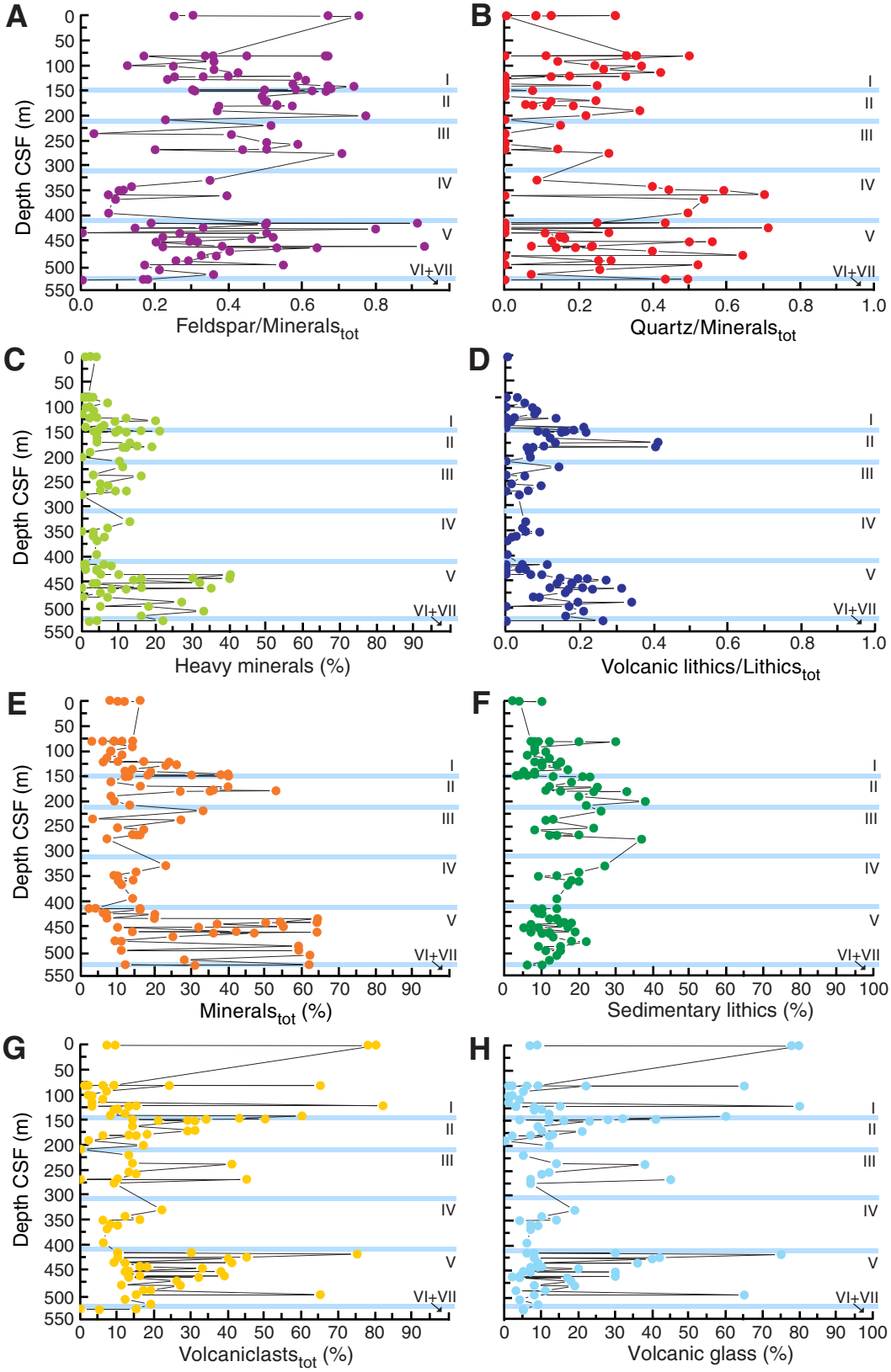

Figure F6. Photomicrographs of smear slides. **A.** Zircon in sandstone of Unit V (Section 322-C0012A-52R-1, 44 cm). **B.** Same as A under crossed nicols. **C.** Rounded quartz grain in Unit V, showing characteristic morphology associated with reworking (Section 322-C0012A-52R-1, 44 cm). **D.** Polycrystalline quartz grain under crossed nicols (Section 322-C0012A-45R-1, 45 cm). **E.** Same as D under plane-polarized light. **F.** Transparent, blocky, felsic glass shard from an ash layer deposited after a large explosive eruption, showing first signs of alteration (black dots) (Section 322-C0012A-1R-1, 48.5 cm). (**Continued on next page.**)

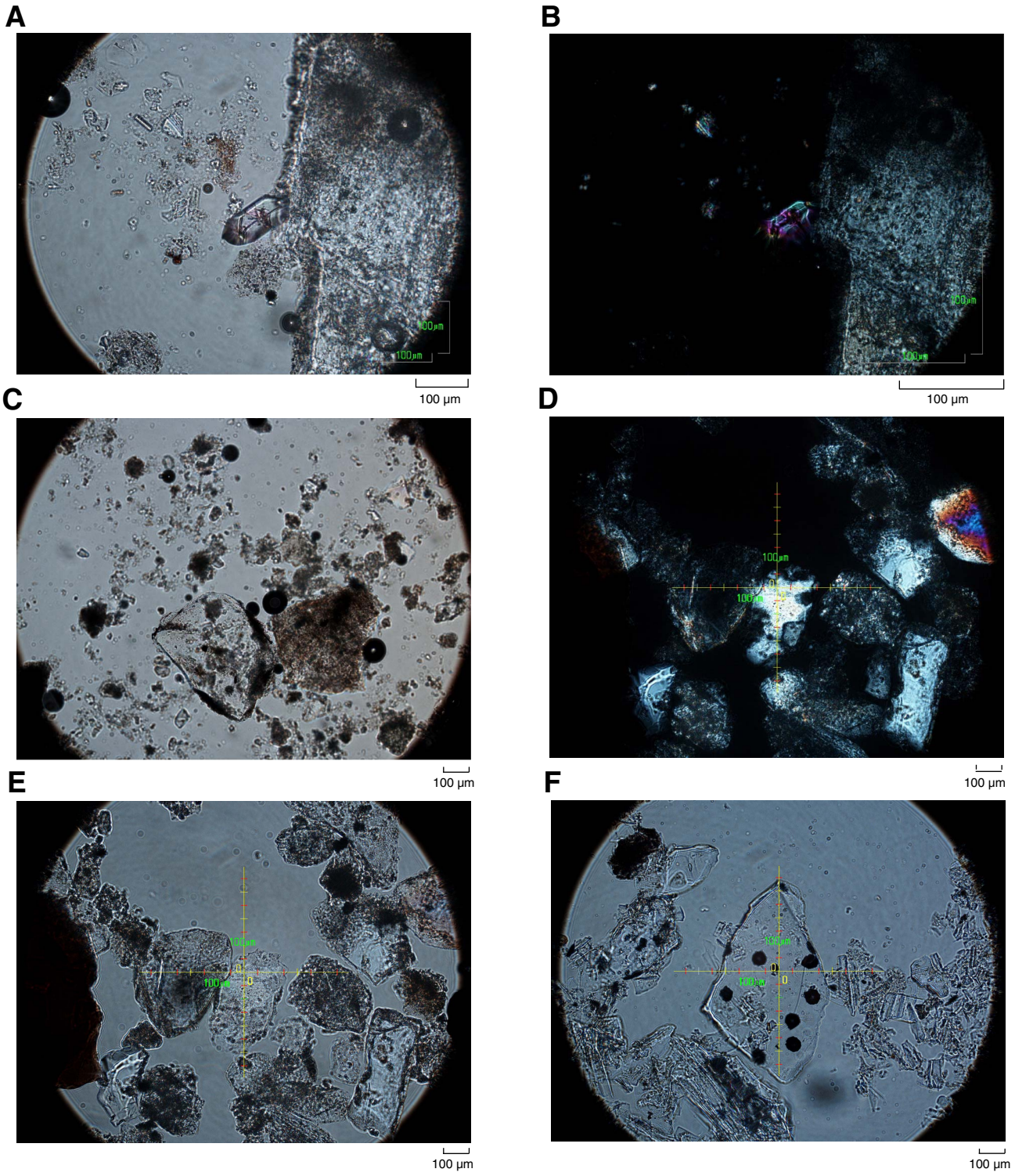

Figure F6 (continued). G. Garnet in sandstone of Unit V (Section 322-C0012A-45R-1, 45 cm). **H.** Same as G under crossed nicols. **I.** Calcareous nannofossils in silty claystone (Section 322-C0012A-34R-2, 62 cm). **J.** Same as I under crossed nicols.

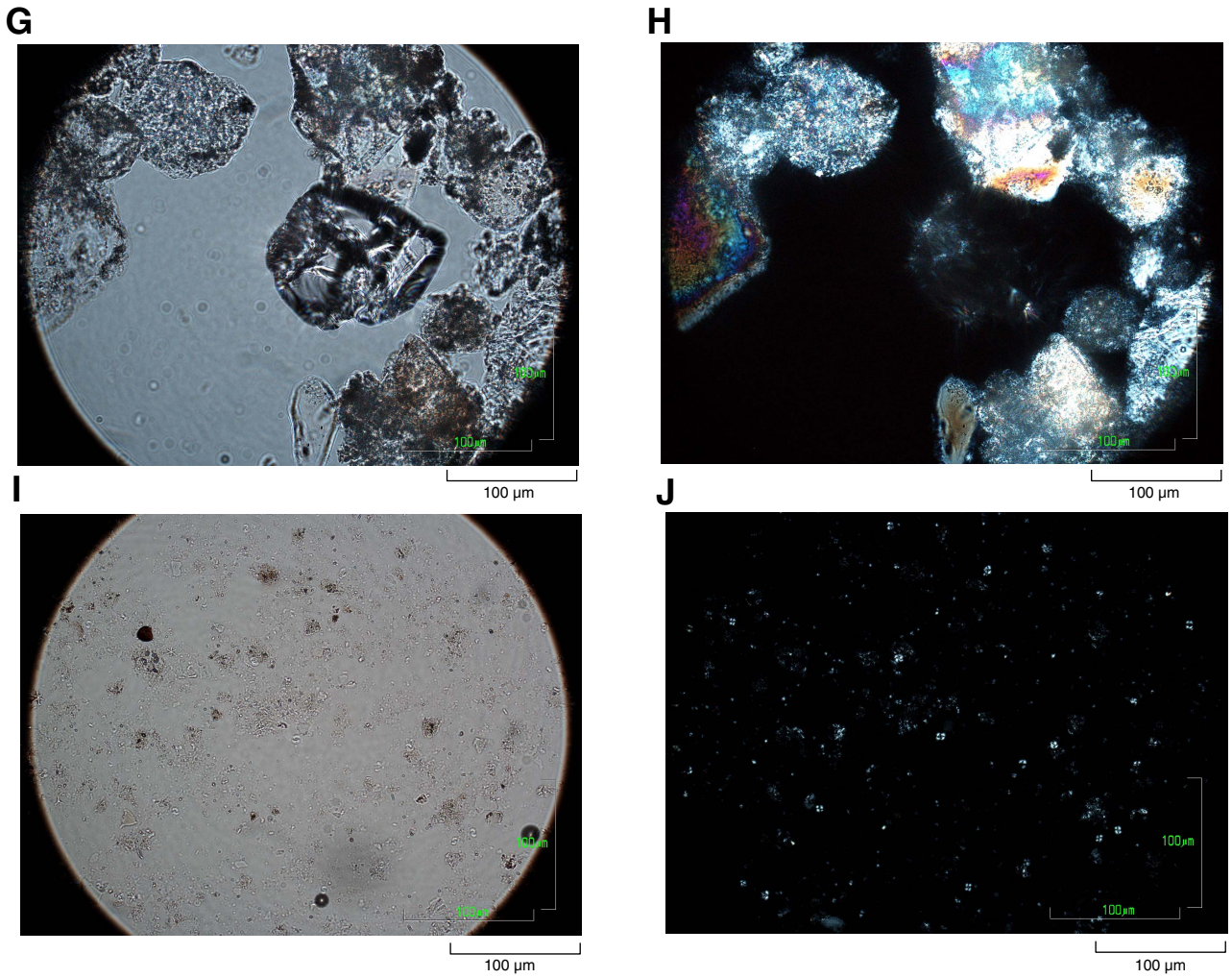

Figure F7. Representative steeply inclined bedding in Unit III, typically at 40°–45° (Sample 322-C0012A-22R-3, 92–107 cm).

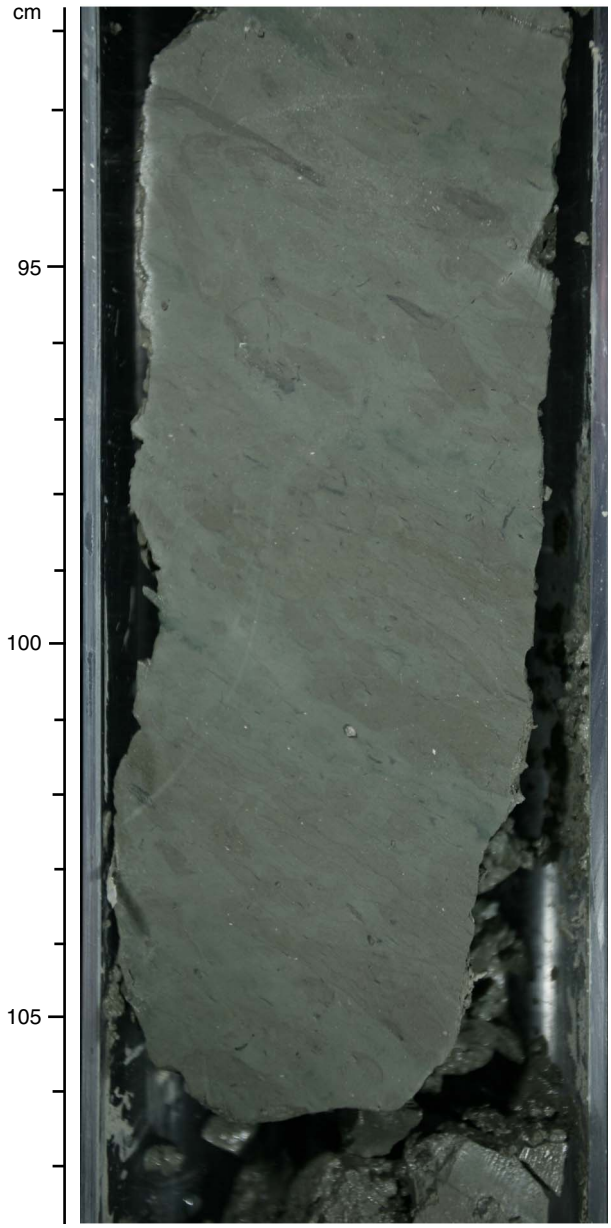

Figure F8. Lime mudstone correlation. **A.** Cemented yellowish carbonate layer at 115–122 cm (interval 322-C0012A-20R-4, 111–127 cm). We tentatively correlate this to a similar carbonate layer (**B**) at 132–137 cm, Site C0011 (interval 322-C0011B-19R-5, 124–136 cm).

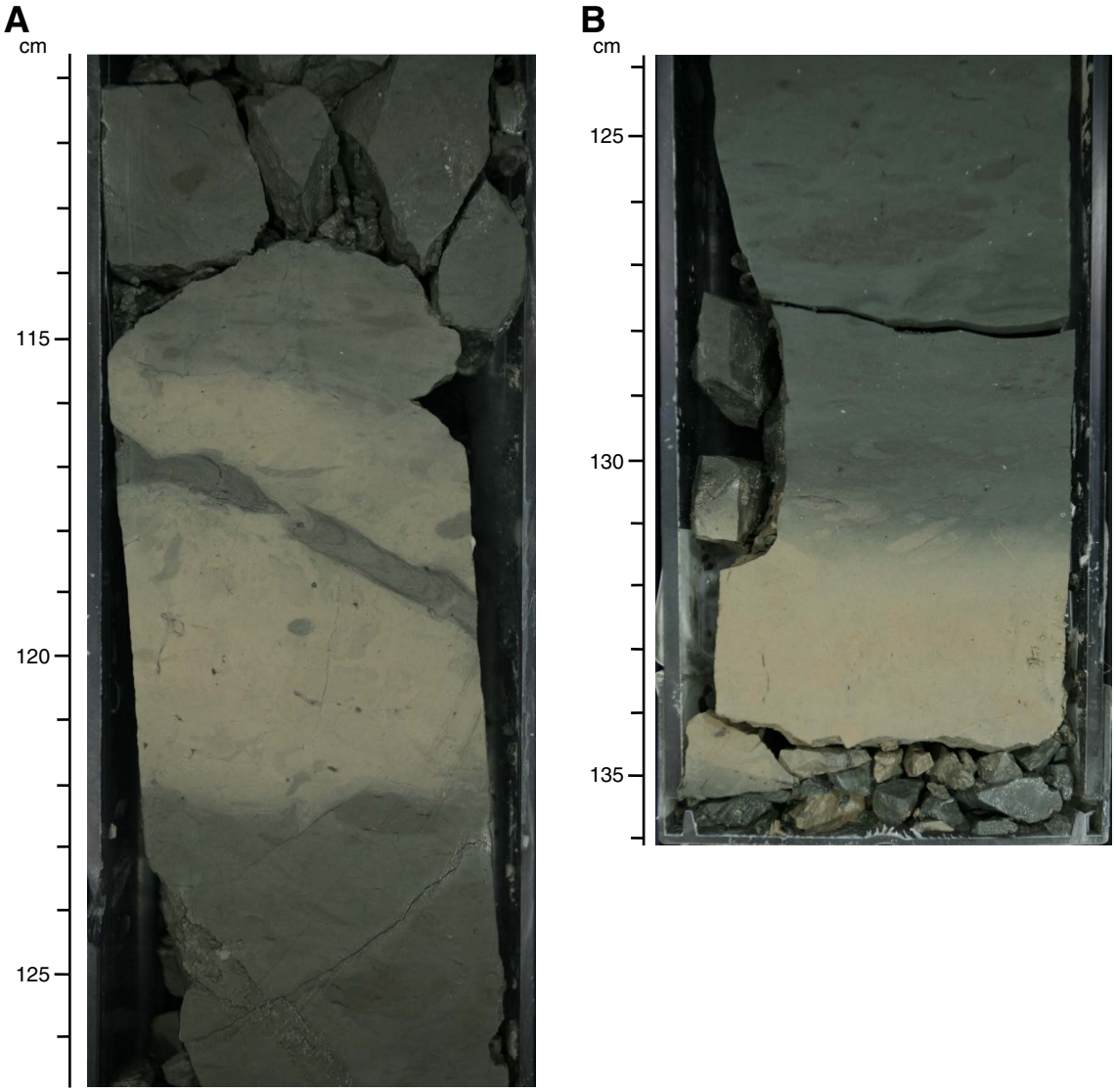

Figure F9. A. Laminated volcaniclastic siltstone sandstone showing normal grading, plane-parallel lamination, and load structures (interval 322-C0012A-43R-5, 30–56 cm). **B.** Volcaniclastic sandy siltstones showing current-ripple lamination (interval 322-C0012A-45R-4, 0–15 cm). **C.** Chaotic deposit of laminated volcaniclastic sandstones involved in an ~50 cm thick interval (interval 322-C0012A-45R-1, 71–105 cm), showing isoclinal folding, attenuation of beds, and sandstone injections. (Continued on next page.)

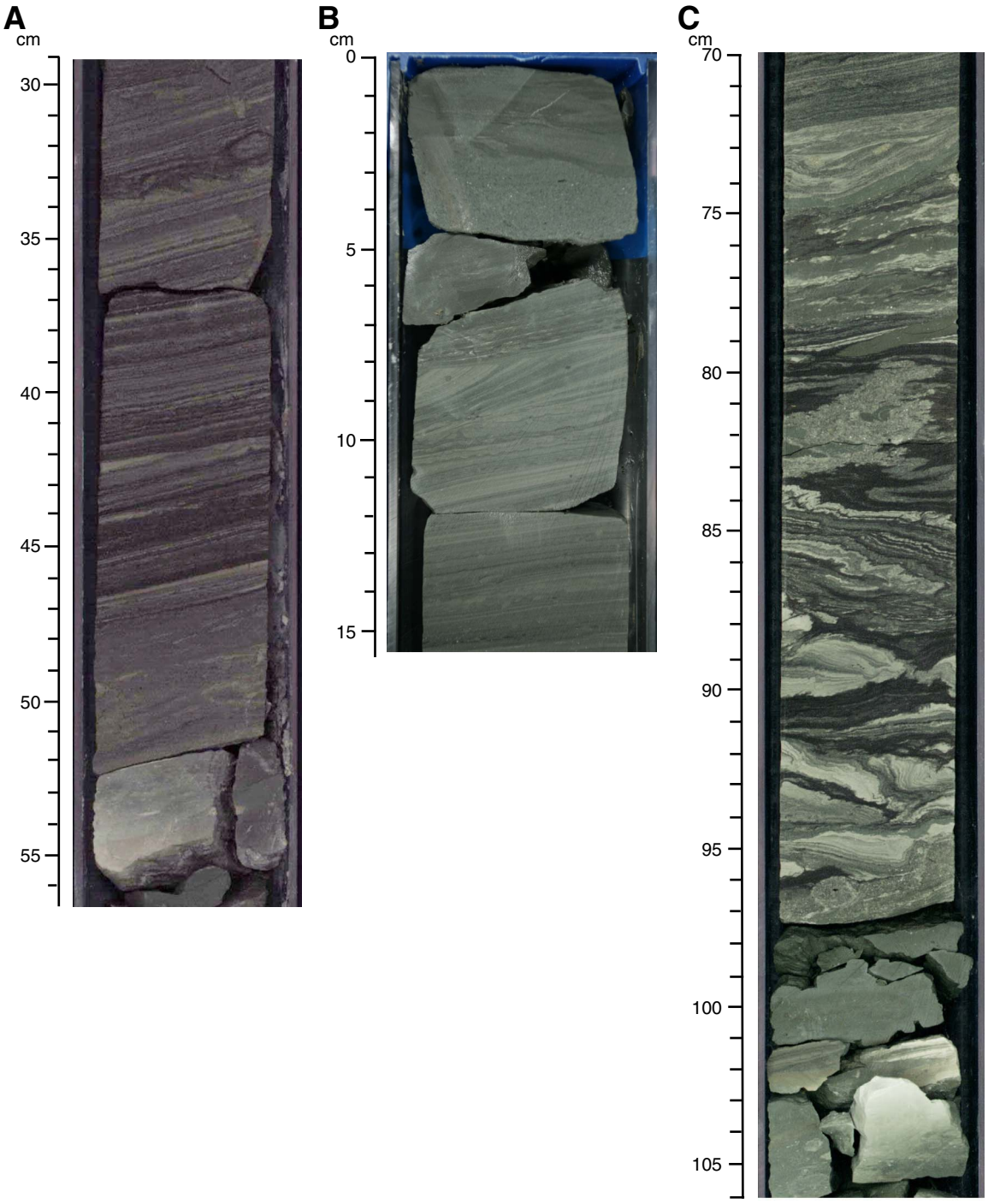

Figure F9 (continued). D. Digital photomicrograph of sandstone with imbricated volcanic glass shards (dark color). **E.** Thin section image of deformed glass shards (red-brown in color). **F.** Very coarse grained volcaniclastic sandstones with large angular clasts of green-gray silty claystone (bioturbated) >6 cm in length structures (interval 322-C0012A-45R-1, 0–26 cm).

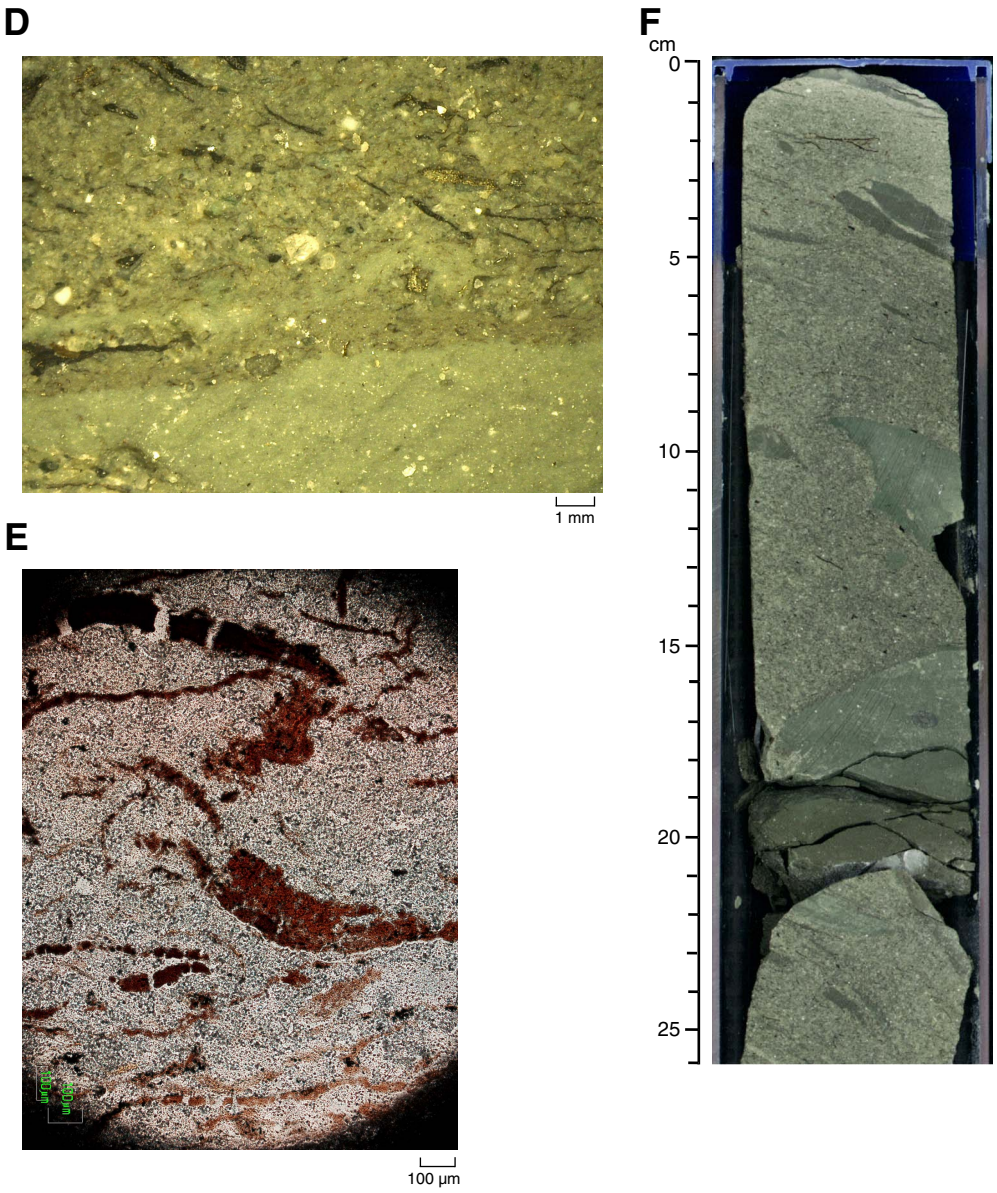

Figure F10. Smear slide data for sandstones of Unit V at Site C0012 versus depth. **A.** Quartz to total mineral ratio. **B.** Ratio of feldspar to total mineral content. **C.** Sedimentary lithic grains. **D.** Total volcaniclastic component. **E.** Heavy minerals to total mineral ratio. **F.** Glass versus total lithic grain content.

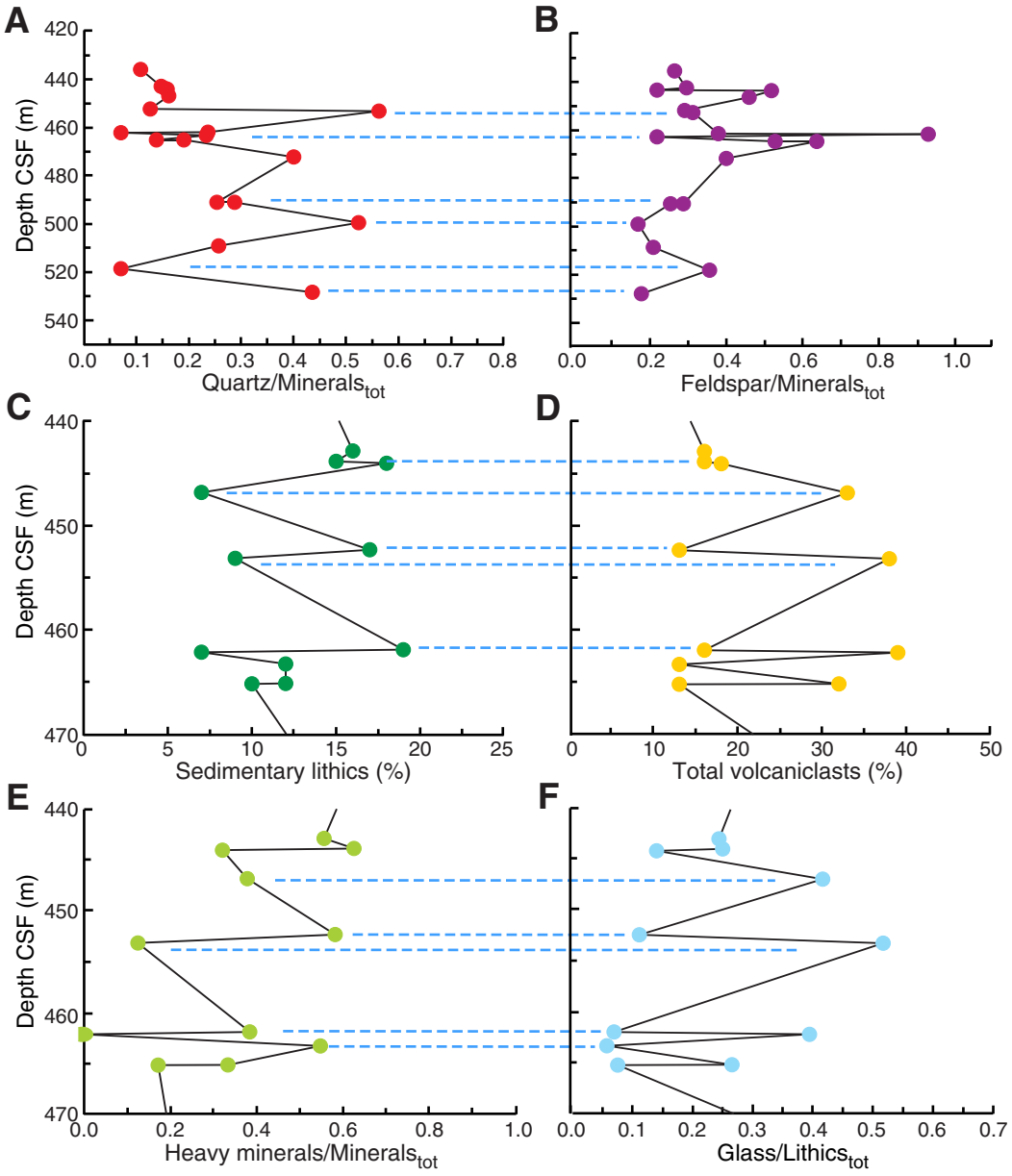

Figure F11. Red calcareous claystone overlying basalt basement (interval 322-C0012A-53R-1, 20–35 cm).

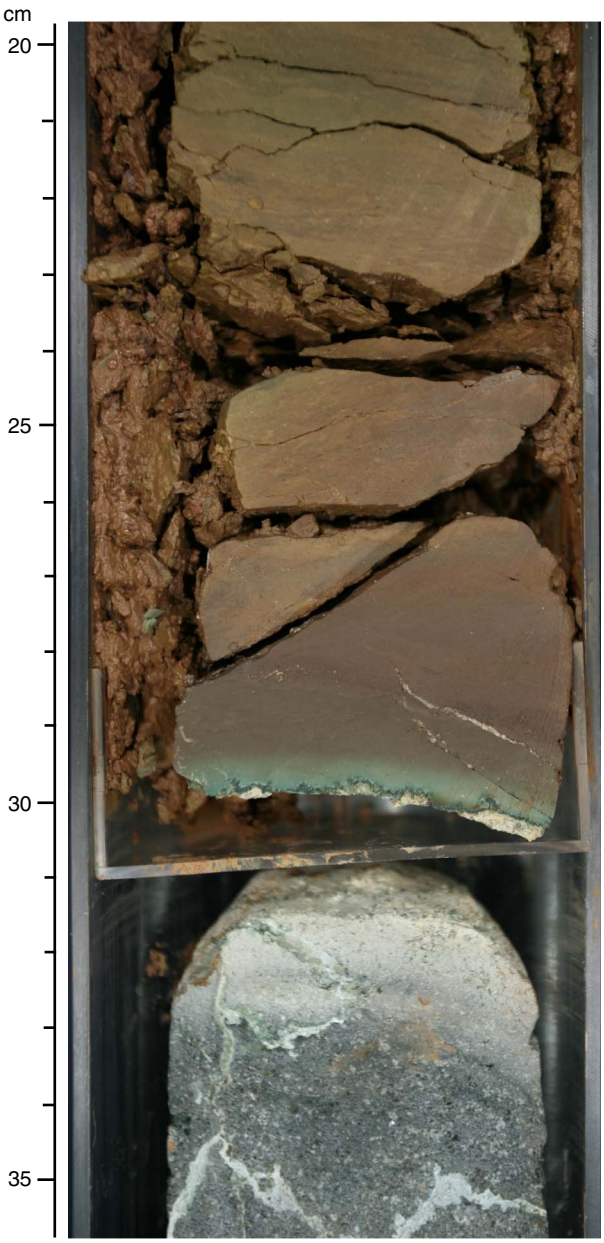

Figure F12. Close-up photographs. **A.** Base of a pillow lava structured basalt (glassy rim at base of pillow and gradation of vesicles) (interval 322-C0012A-57R-1, 84–91 cm). **B.** Basalt with heterogeneous vesicles content (interval 322-C0012A-53R-2, 81–93 cm). **C.** Breccia filling a large fracture within the basalt (interval 322-C0012A-58R-1, 22–31 cm). **D.** Mixed rubble caused by drilling disturbance (interval 322-C0012A-55R-CC, 34–45 cm).

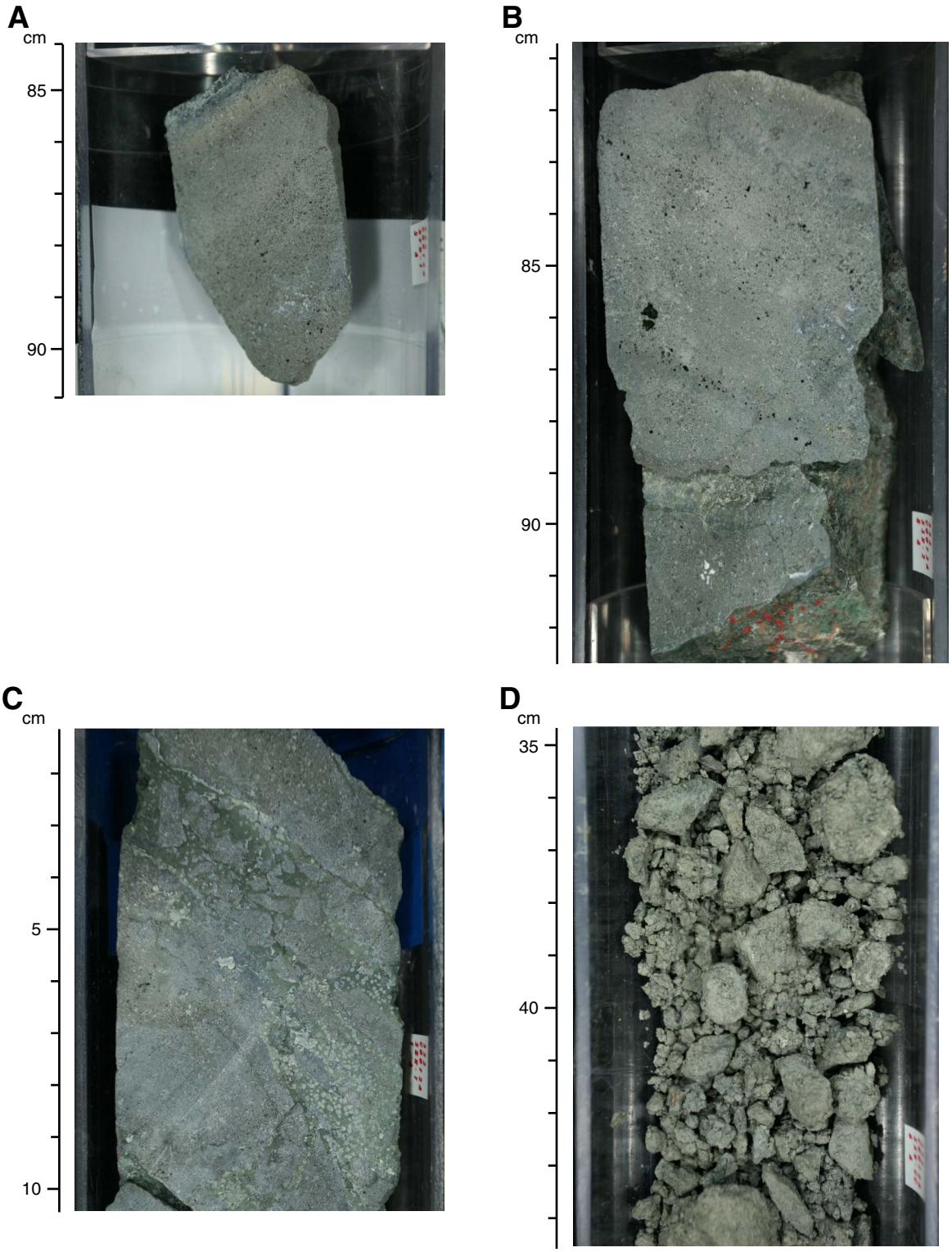

Figure F13. Photomicrographs of thin sections. **A.** Highly plagioclase–pyroxene phyric basalt with traces of iddingsite and celadonite-filled vesicles. **B.** Highly plagioclase–pyroxene phyric basalt including aggregates of pyrite. **C.** Diffuse limit between a highly phyric–sparsly vesicular basalt and a moderately phyric–highly vesicular basalt. **D.** Close-up photograph of heterogeneous basalt (interval 322-C0012A-55R-CC, 27–32 cm).

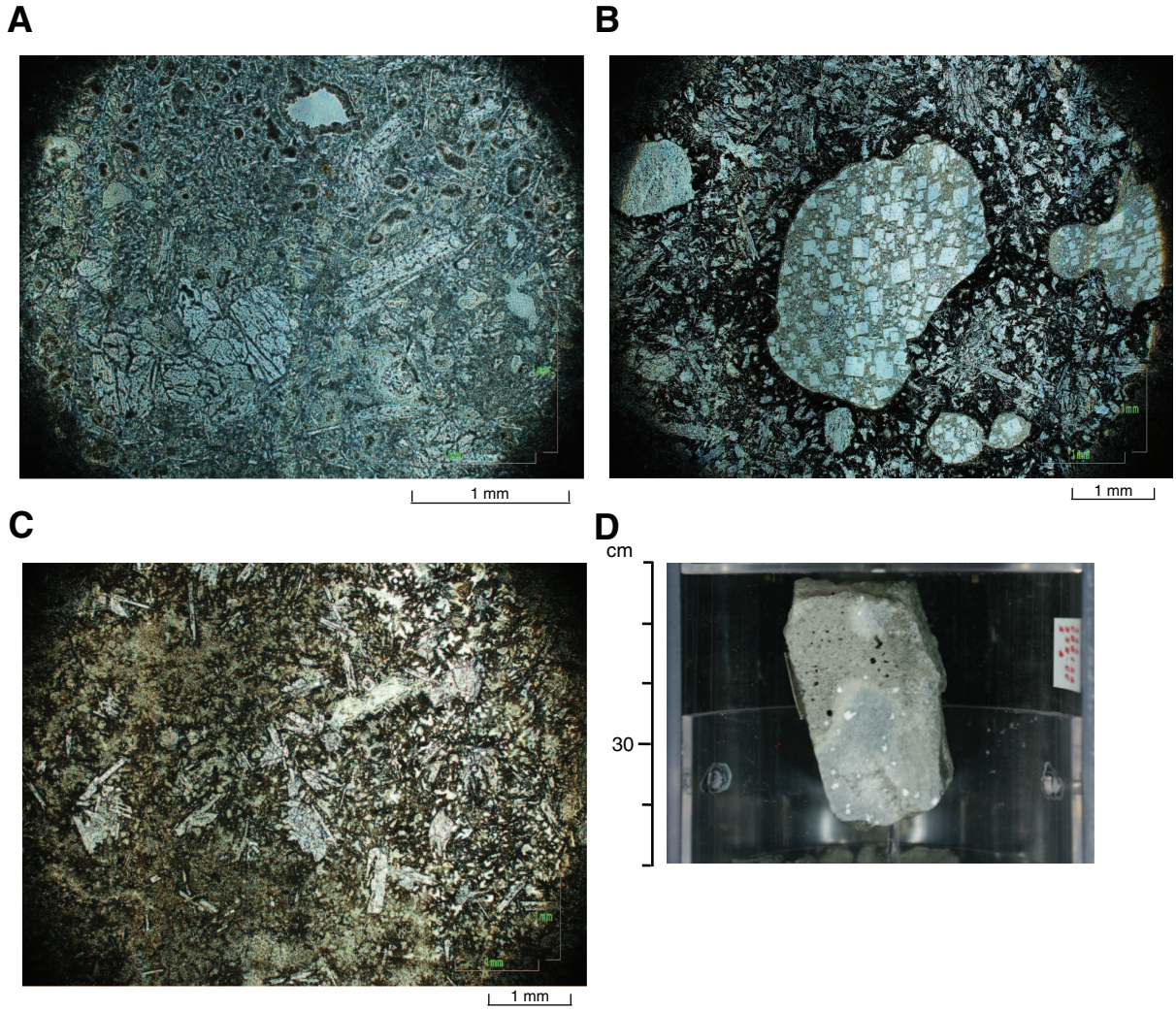

Figure F14. A, B. Close-up photographs of heterogeneous pieces of basalts showing a mixture between two different types of basalts. **A.** Interval 322-C0012A-55R-1, 5–12 cm. **B.** Interval 322-C0012A-57R-CC, 14–22 cm. **C, D.** Photomicrographs of thin section (Sample 322-C0012A-53R-2 [Piece 1, 0–5 cm]) in plane-polarized light. Phenocryst proportion and size as well as vesicles content are considerably different from one type of basalt to the other. The limit between the two types is diffuse.

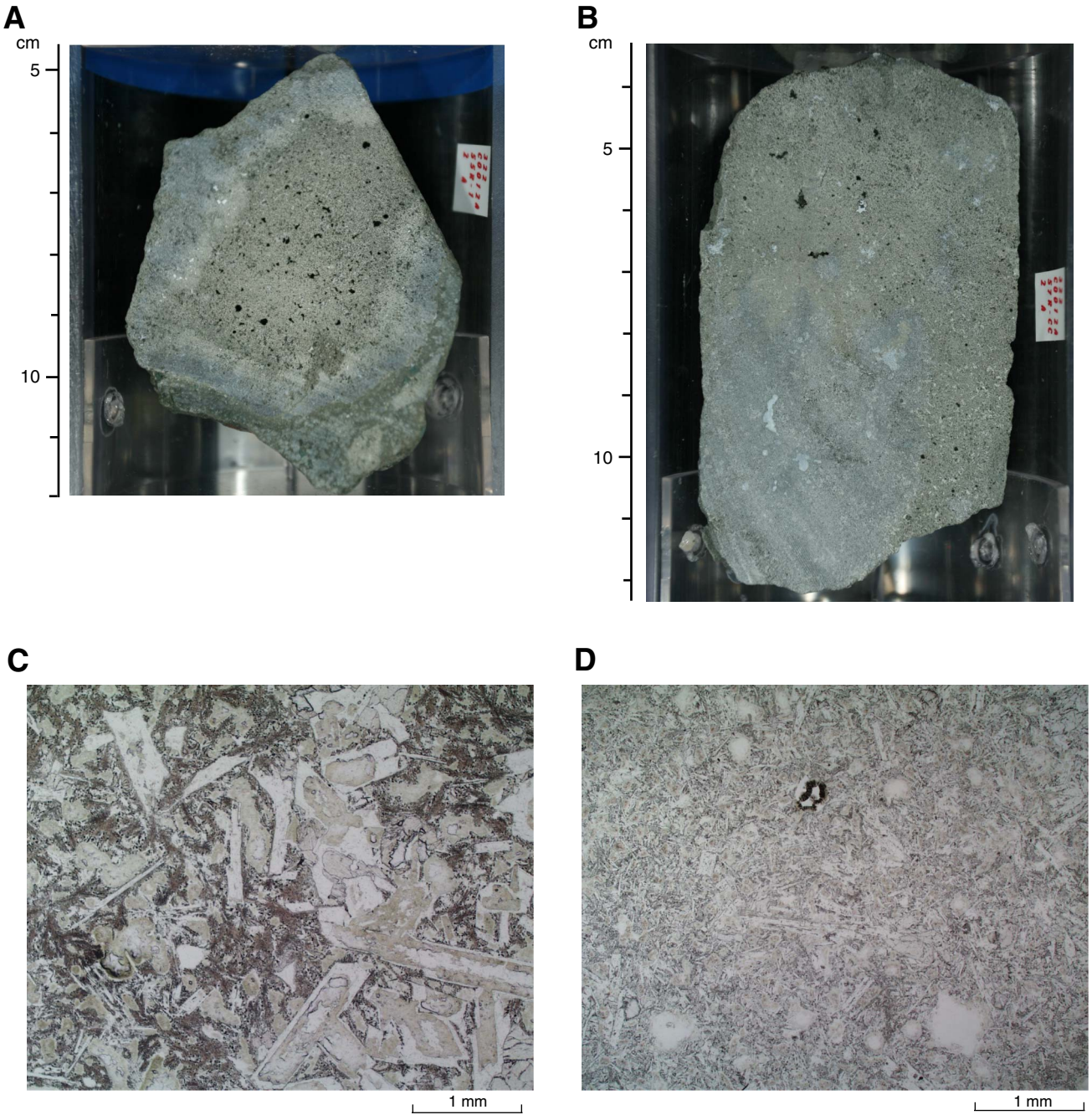

Figure F15. Photomicrographs of different alteration types. **A.** Interstitial groundmass replacement. **B.** Zeolite-filled vesicles. **C.** Celadonite-filled vesicles. **D.** Saponite and celadonite vein cutting a highly pyroxene–plagioclase phyric basalt.

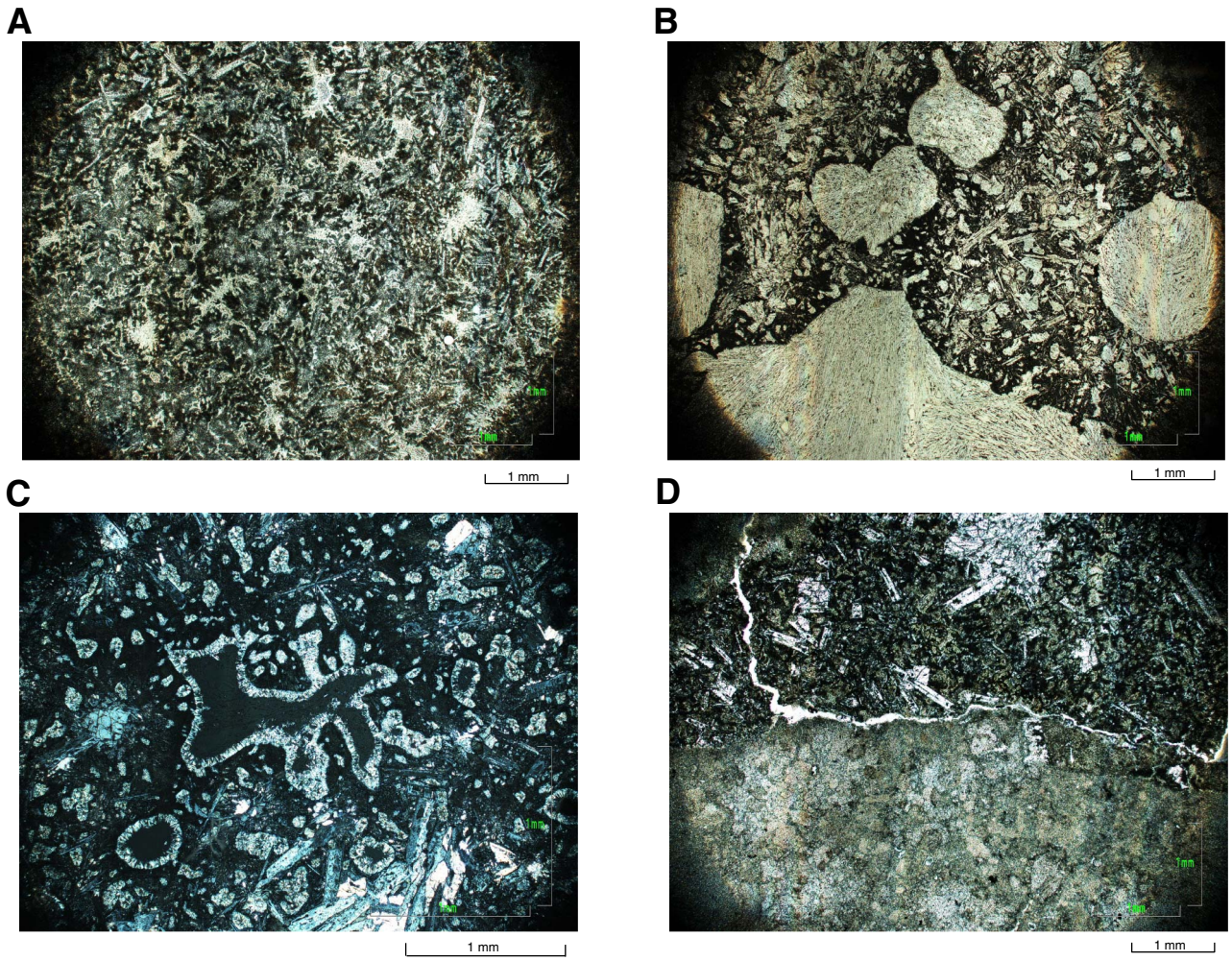

Figure F16. Photomicrographs of thin sections and close-up photographs of altered basalts. **A.** Saponite and celadonite replacing the groundmass (plane-polarized light). **B.** Saponite partly filling a vesicle (plane-polarized light). **C.** Celadonite filling a vein (interval 322-C0012A-53R-2, 6–16 cm). **D.** Saponite and celadonite filling a vein (cross-polarized light).

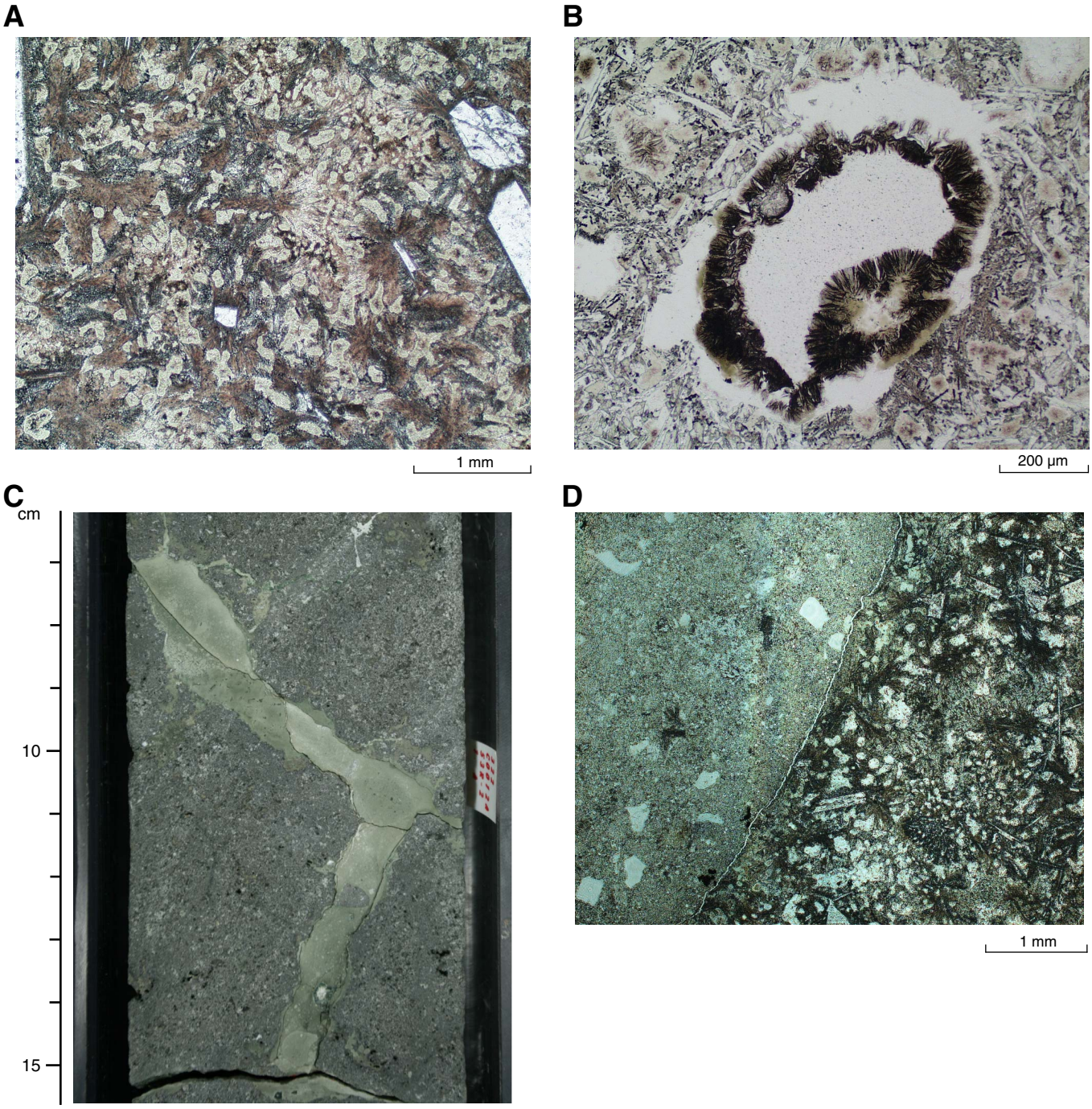

Figure F17. Photographs of different alteration types. **A.** Vesicles filled with both fibrous and isometric zeolites (plane-polarized light). **B.** Fibrous zeolite-filled vesicle (cross-polarized light). **C.** Vein filled by calcite (cross-polarized light).

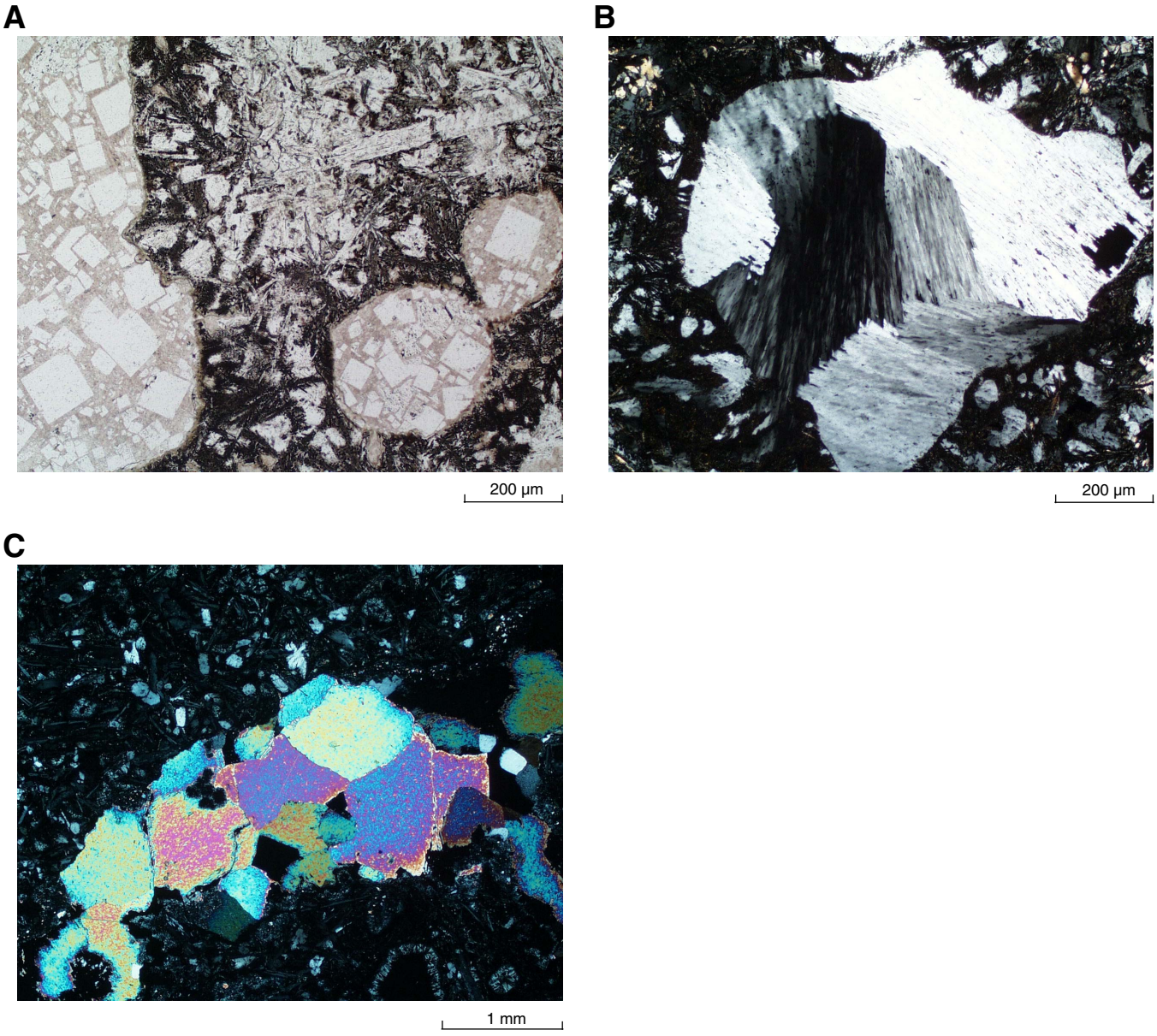

Figure F18. Major element contents of bulk rock samples in weight percent, measured by inductively coupled plasma–atomic emission spectroscopy. LOI = loss on ignition.

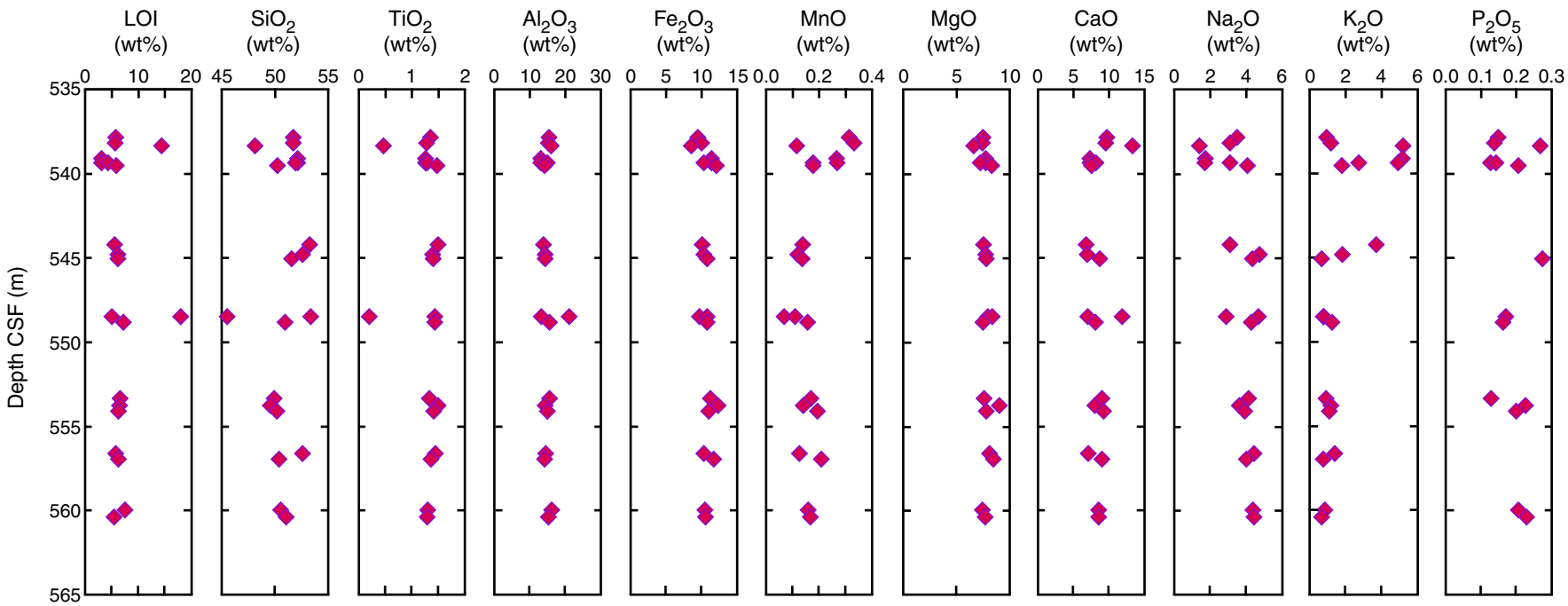

Figure F19. Bulk powder XRD analyses of sediment samples plotted against lithology, Site C0012, reported in relative weight percent. See text for explanation.

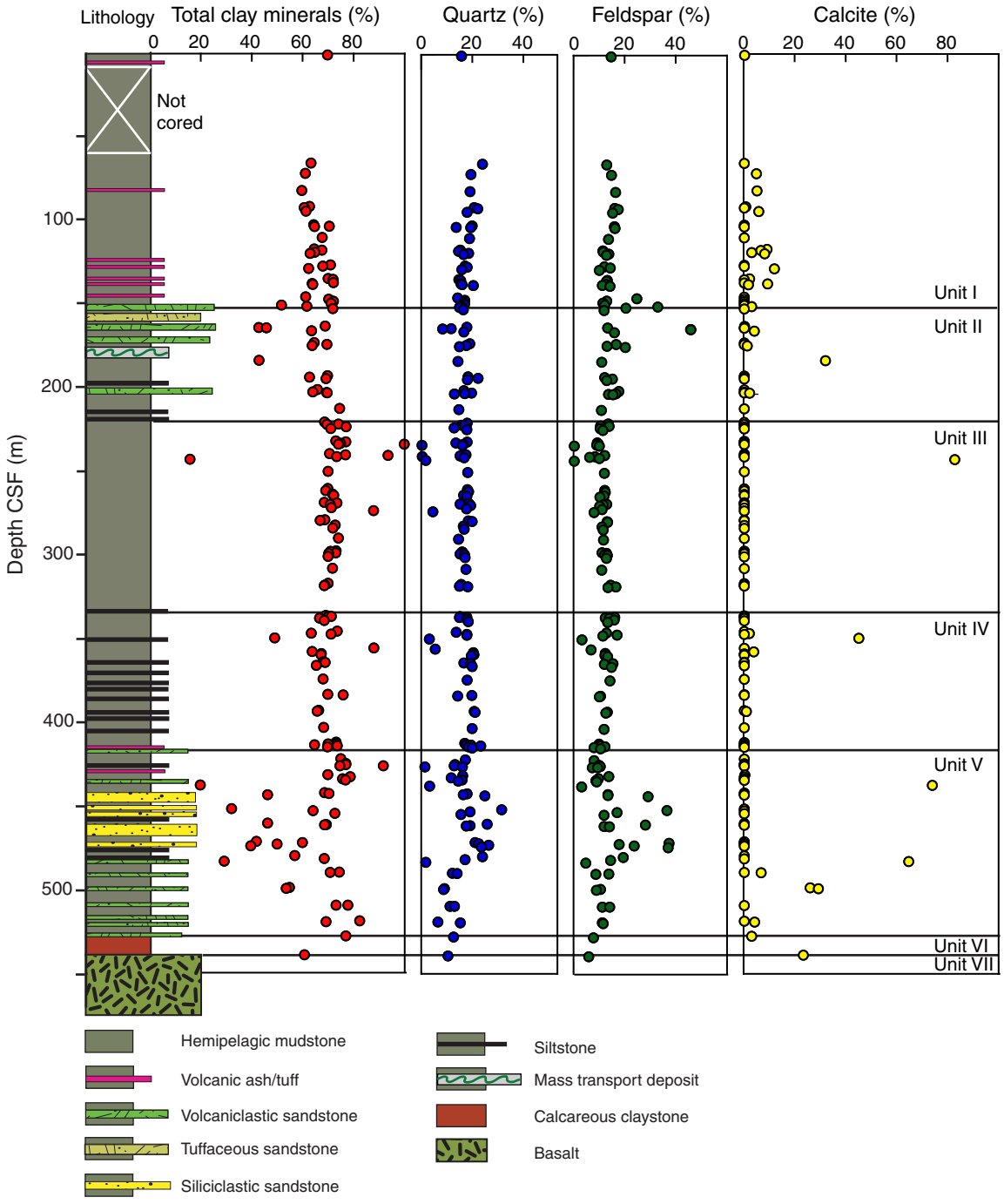

Figure F20. Major element content from XRF analysis plotted against lithology, Site C0012.

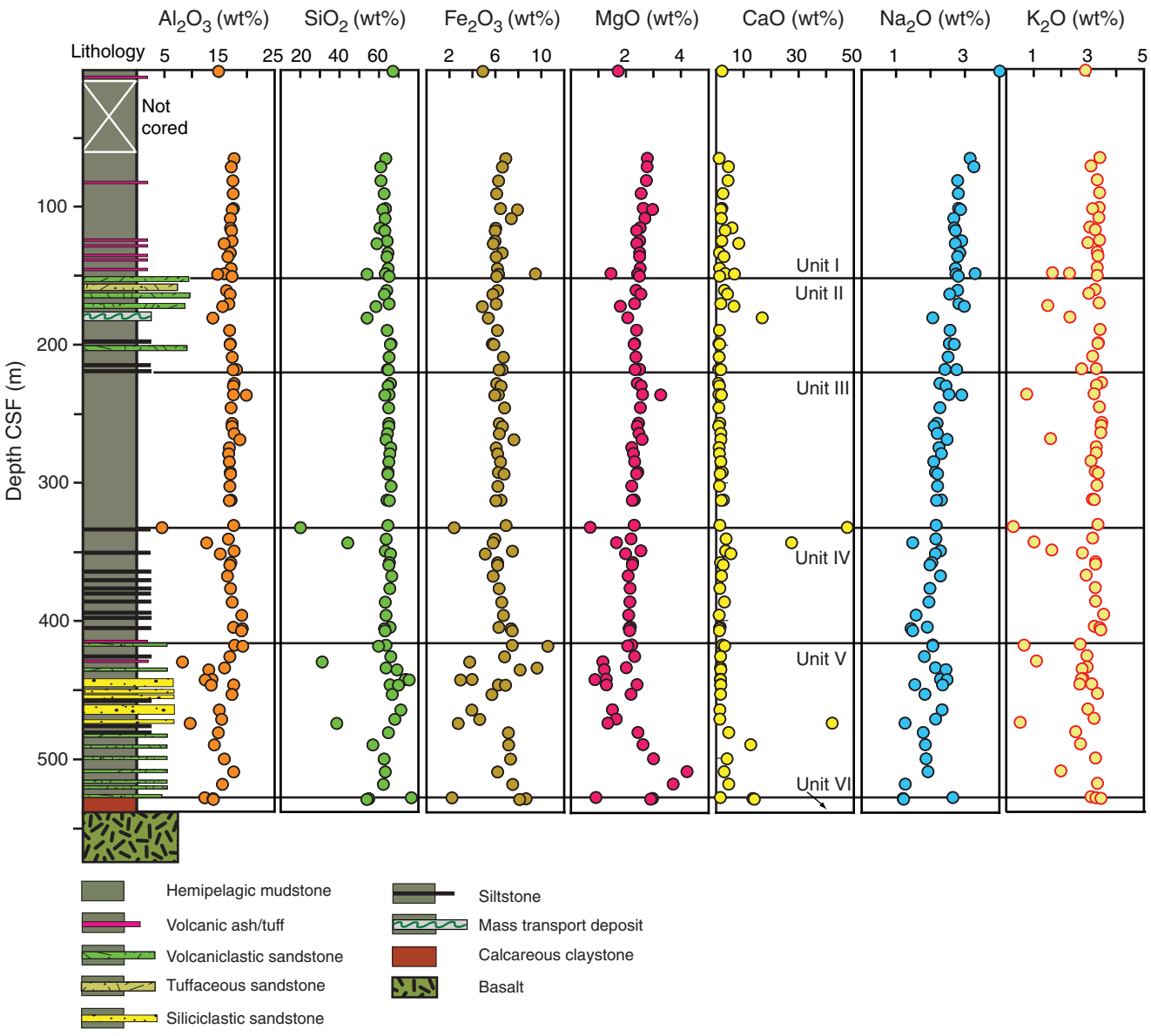

Figure F21. 3-D PSDM seismic reflection profile along In-line 95, Site C0012. **A.** Uninterpreted. **B.** Interpreted. Blue line = normal fault, VE = vertical exaggeration.

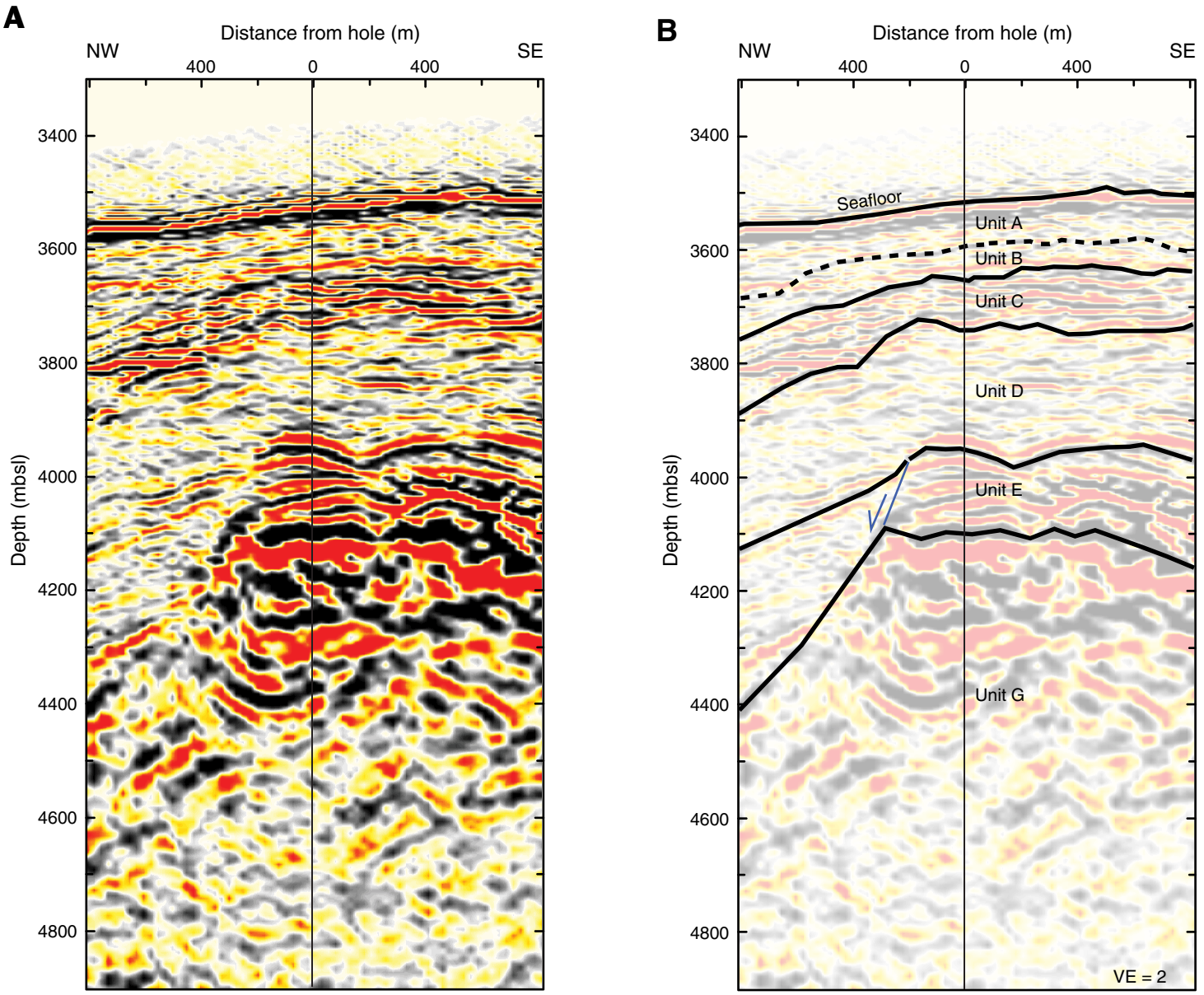

Figure F22. A. Ratio of turbidites to hemipelagites in each core versus core number. **B.** Cumulative thickness of turbidites (red line) and turbidite sediment accumulation rate versus cumulative thickness of hemipelagic sediments (blue line). **C.** Sediment accumulation rate for hemipelagites. See text for explanation.

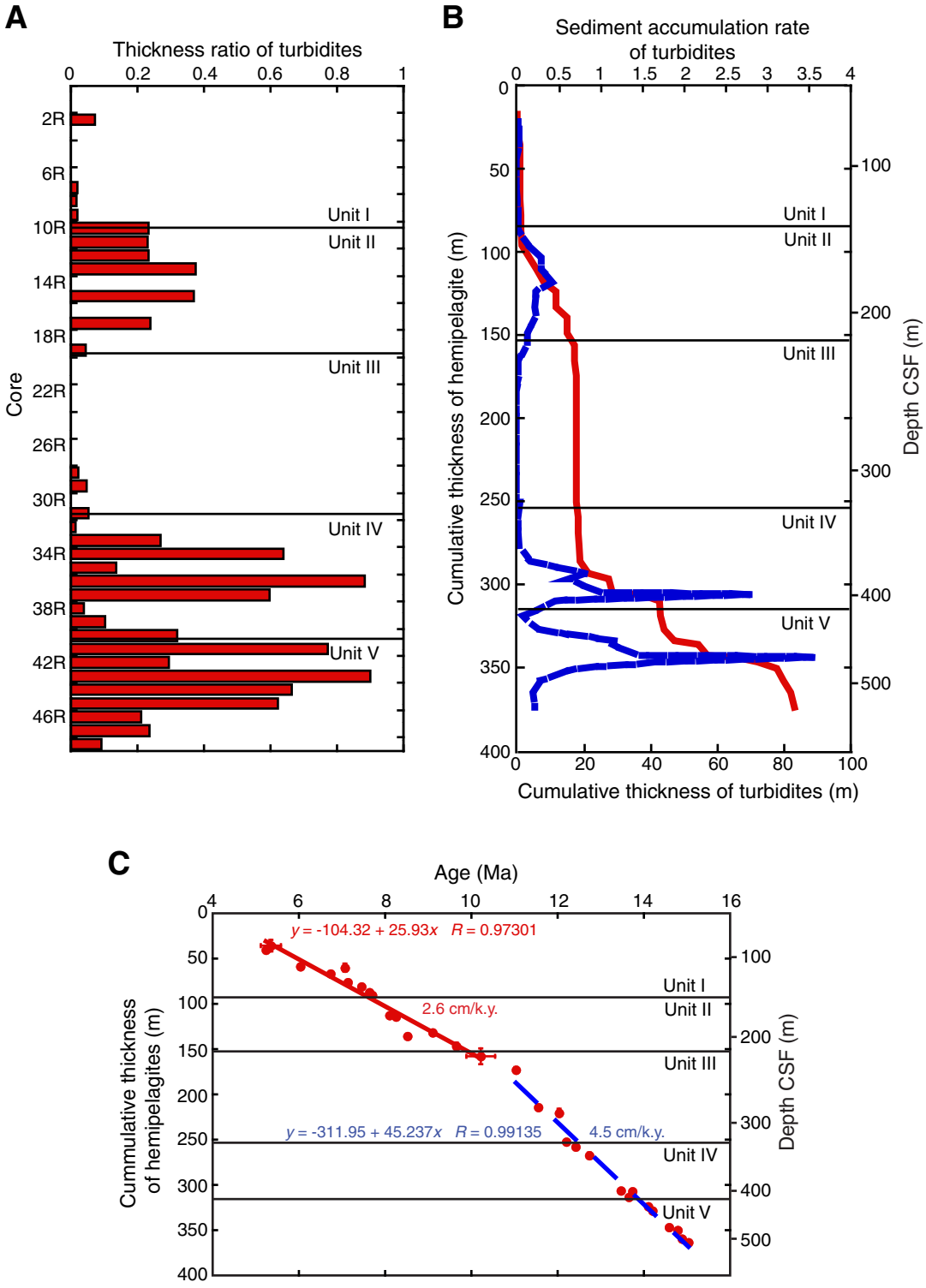

Figure F23. Depth profiles of total organic carbon (TOC)/total nitrogen (TN), Hole C0012A. Vertical dashed line = difference between generally terrigenous and marine sources for the organic carbon.

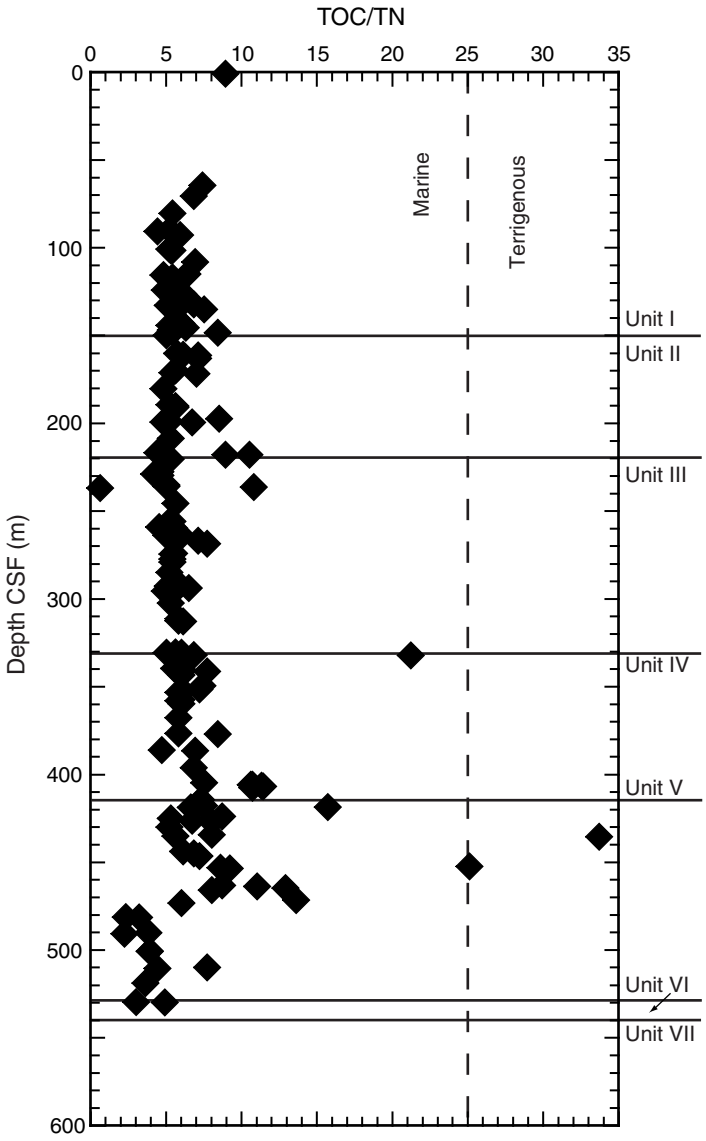

Figure F24. Dip angle variation of bedding and fault planes against depth. Yellow highlight = possible biostratigraphic hiatus (see **"Biostratigraphy"**).

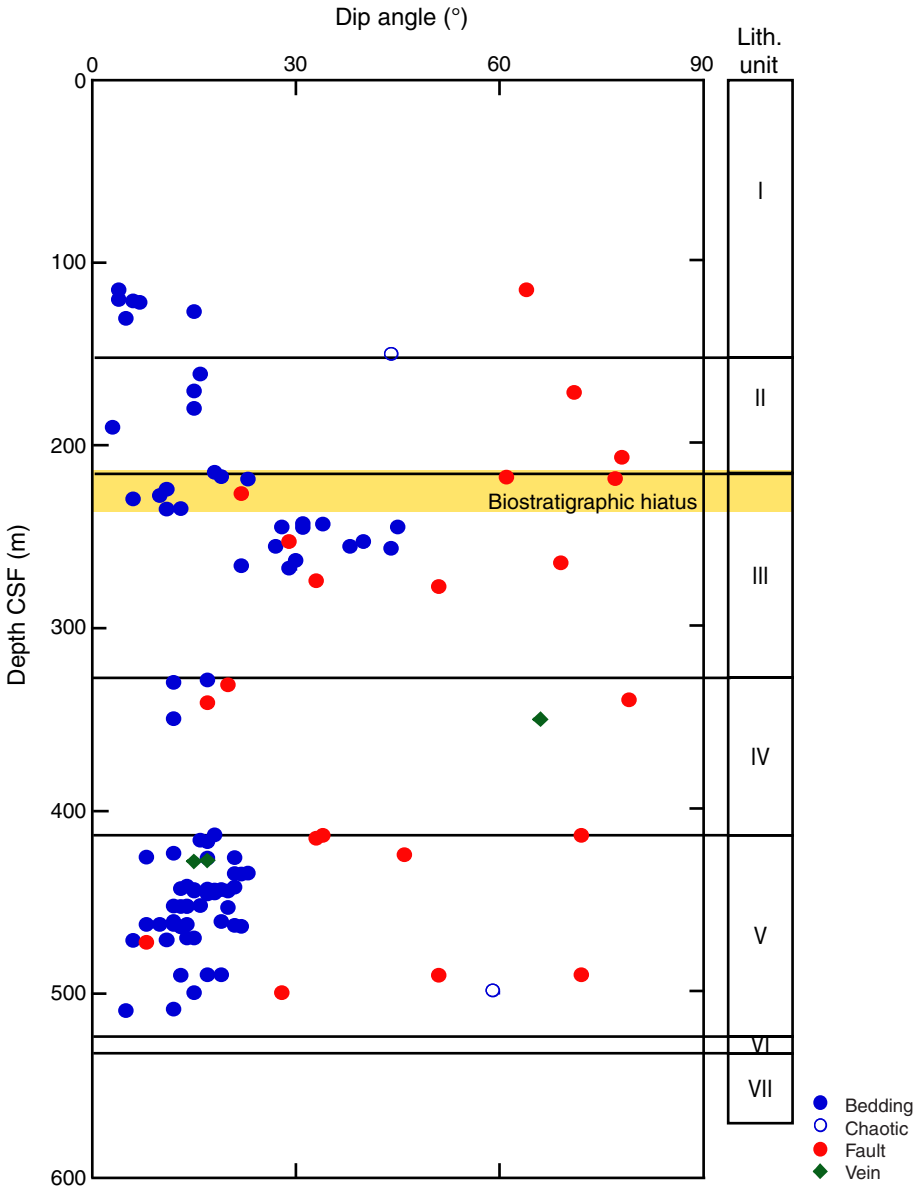

Figure F25. Stereo plots (lower hemisphere) of bedding plane and faults in Hole C0012A after paleomagnetic correction.

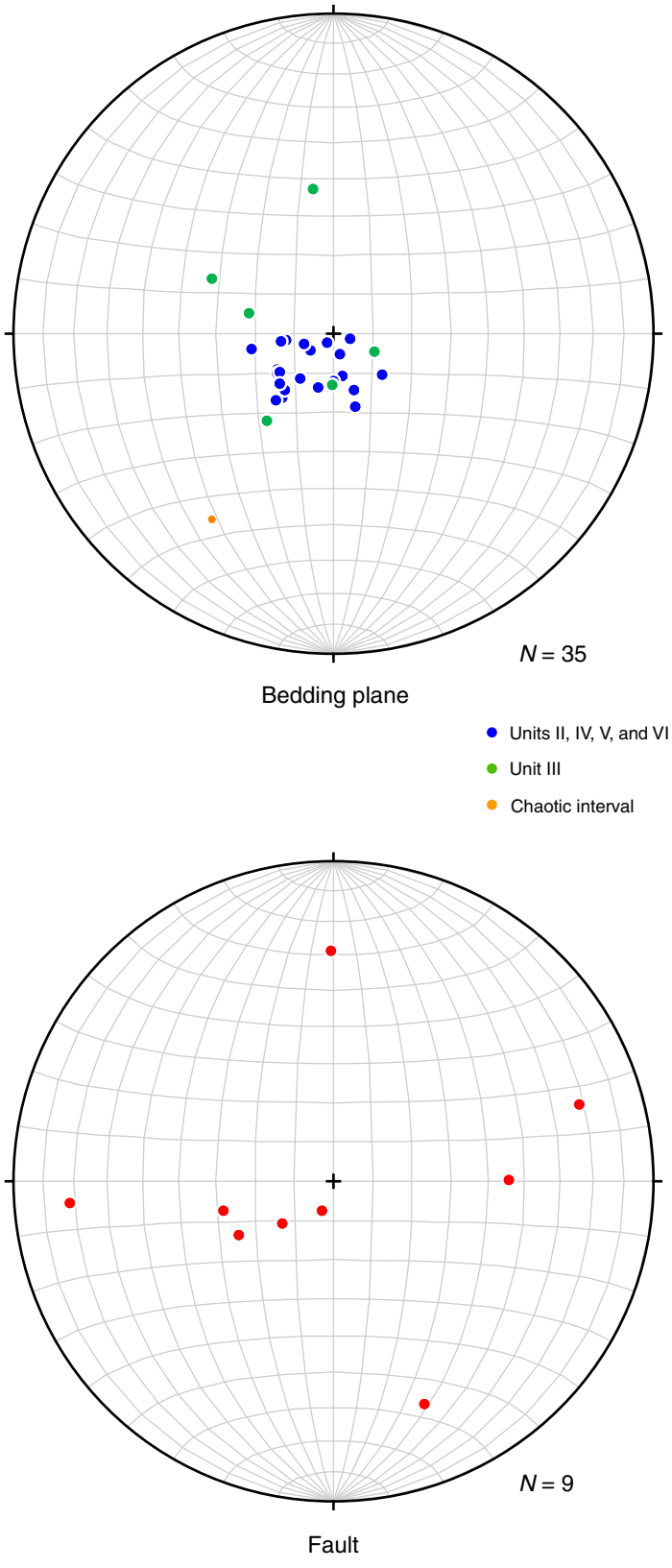

Figure F26. Layer-parallel faults. **A.** Interval 322-C0012A-25R-4, 105–120 cm. **B.** Interval 322-C0012A-32R-4, 28–37 cm.

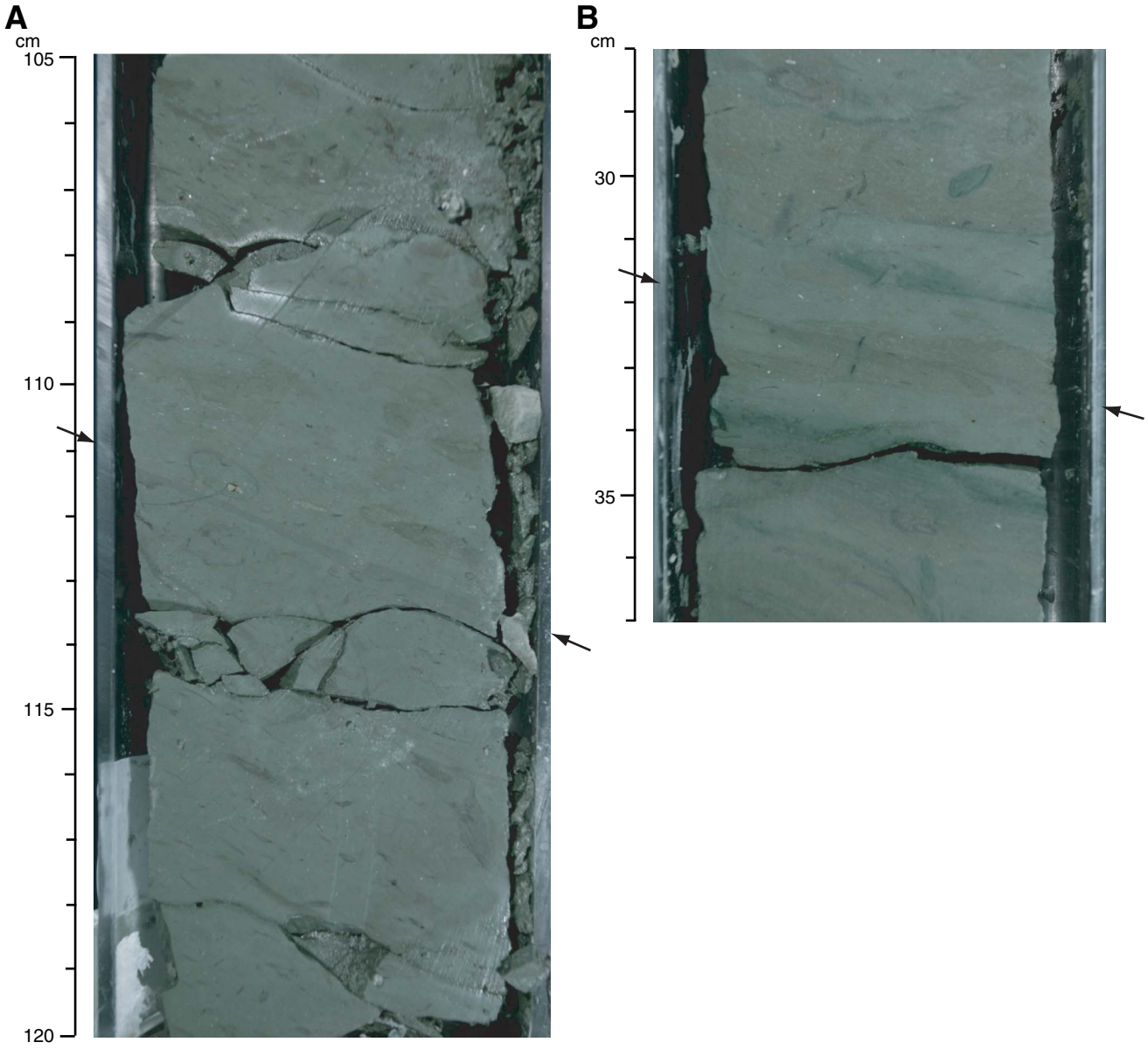

Figure F27. High-angle fault (interval 322-C0012A-14R-4, 10–42 cm). MSCL-I = photo image logger, CT = computed tomography.

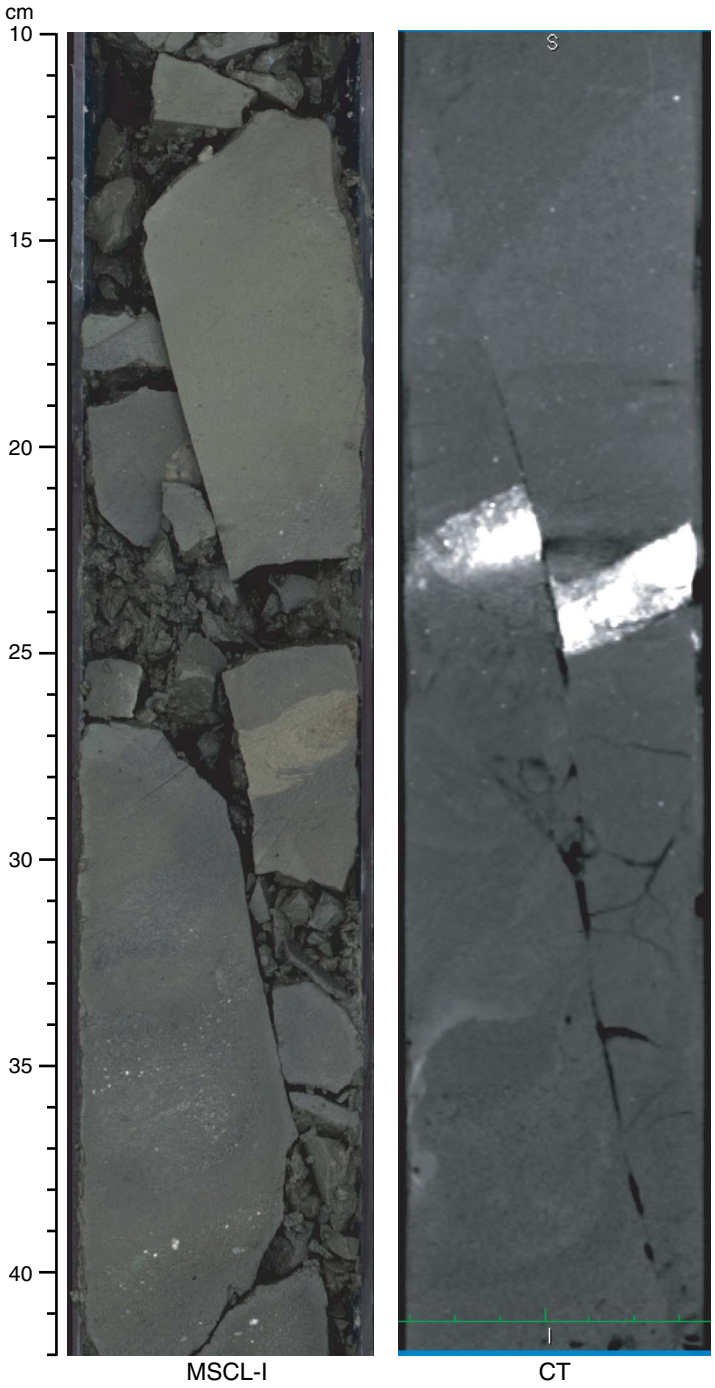

Figure F28. Bioturbated dark deformation band (interval 322-C0012A-25R-4, 0–12 cm).

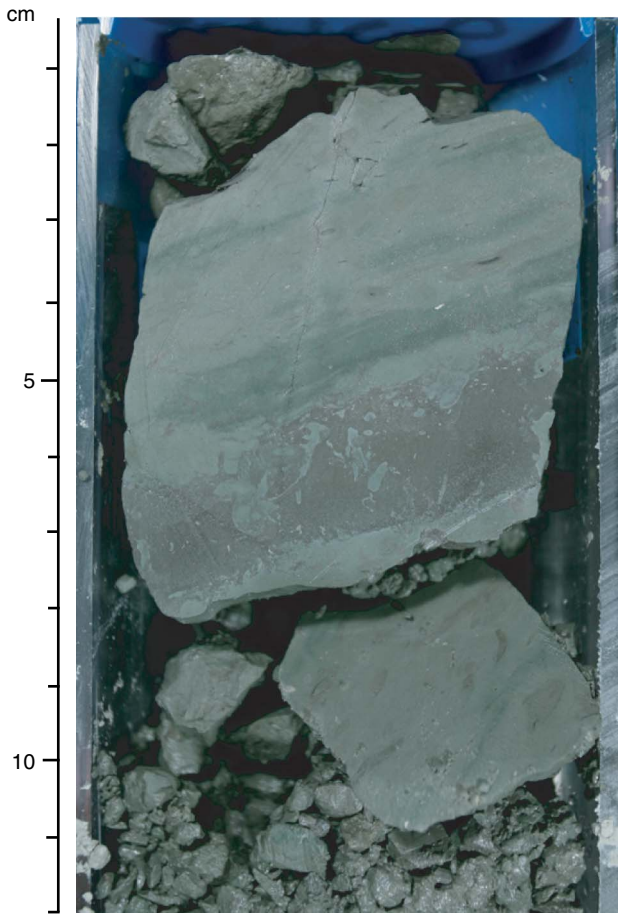

Figure F29. Mineral-filling vein and layer-parallel veins. **A.** Interval 322-C0012A-33R-4, 110–120 cm. **B.** Interval 322-C0012A-46R-3, 0–16 cm. Kinklike folding at 10–12 cm. **C.** Interval 322-C0012A-46R-1, 1–10 cm.

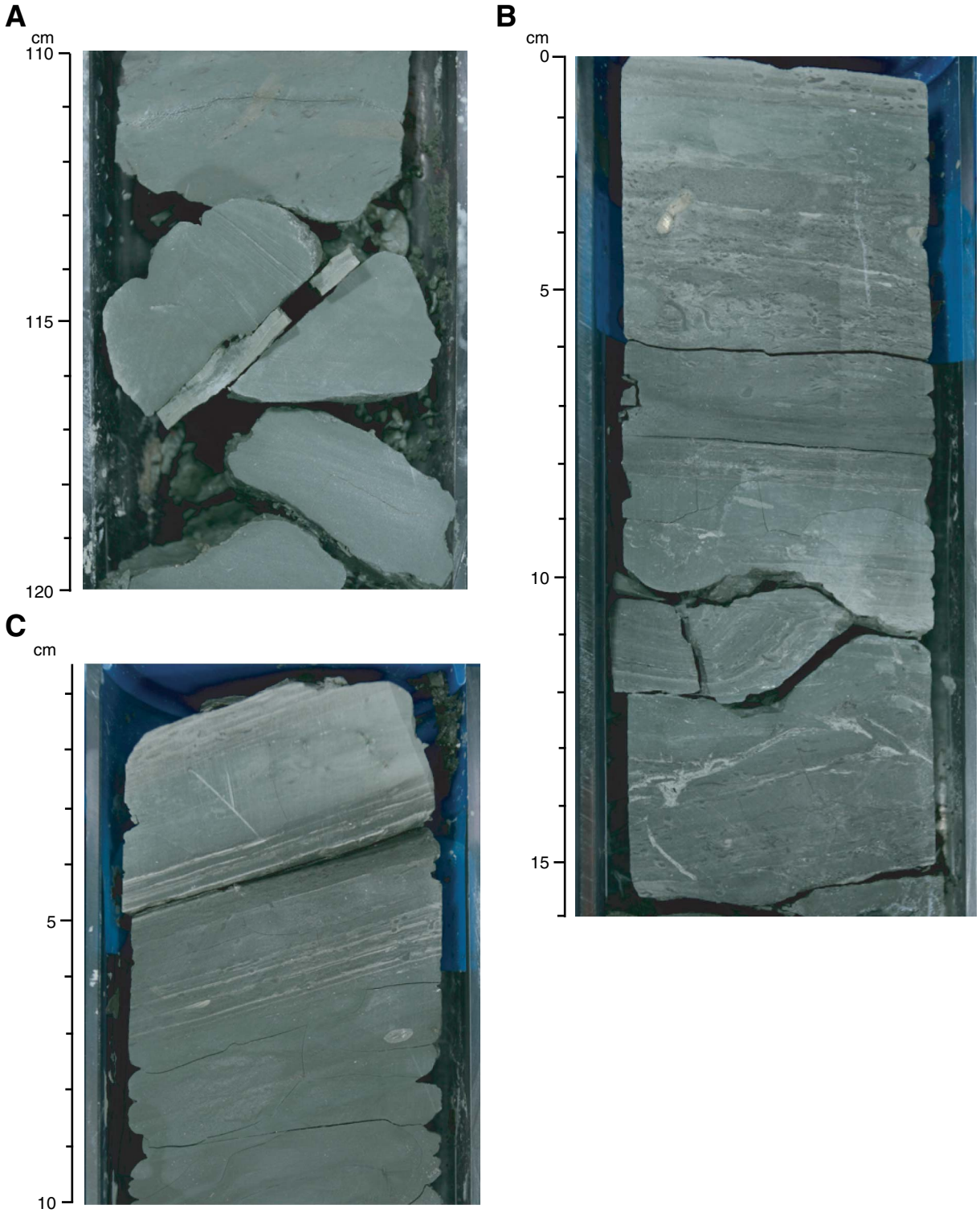

Figure F30. Sheath folding in laminated volcaniclastic sandstone (interval 322-C0012A-45R-1, 80–95 cm).

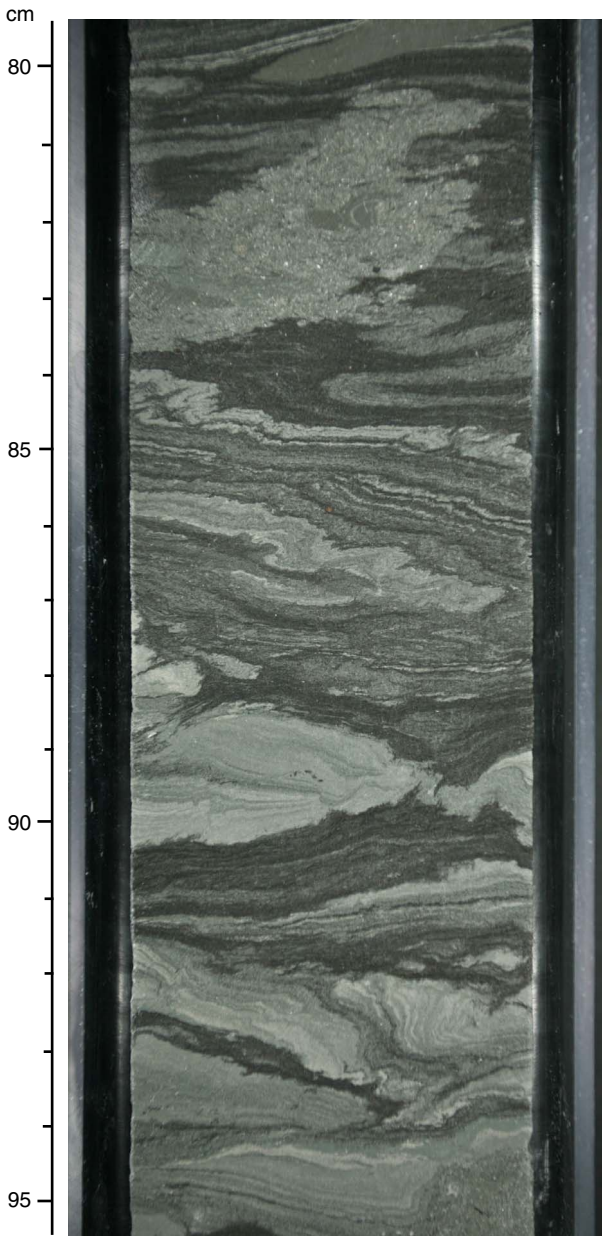

Figure F31. Schematic model showing a submarine slide event that could create the discrepancy between the biostratigraphic hiatus and the inclined bedding. **A.** Initial deposition. **B.** Sliding and surface redeposition. **C.** Unconformity formation. Core recovery together with intense drilling disturbance in Cores 322-C0012A-1R through 22R, however, precludes a more detailed understanding of the bedding dips in lower part of Unit III and upper part of Unit IV.

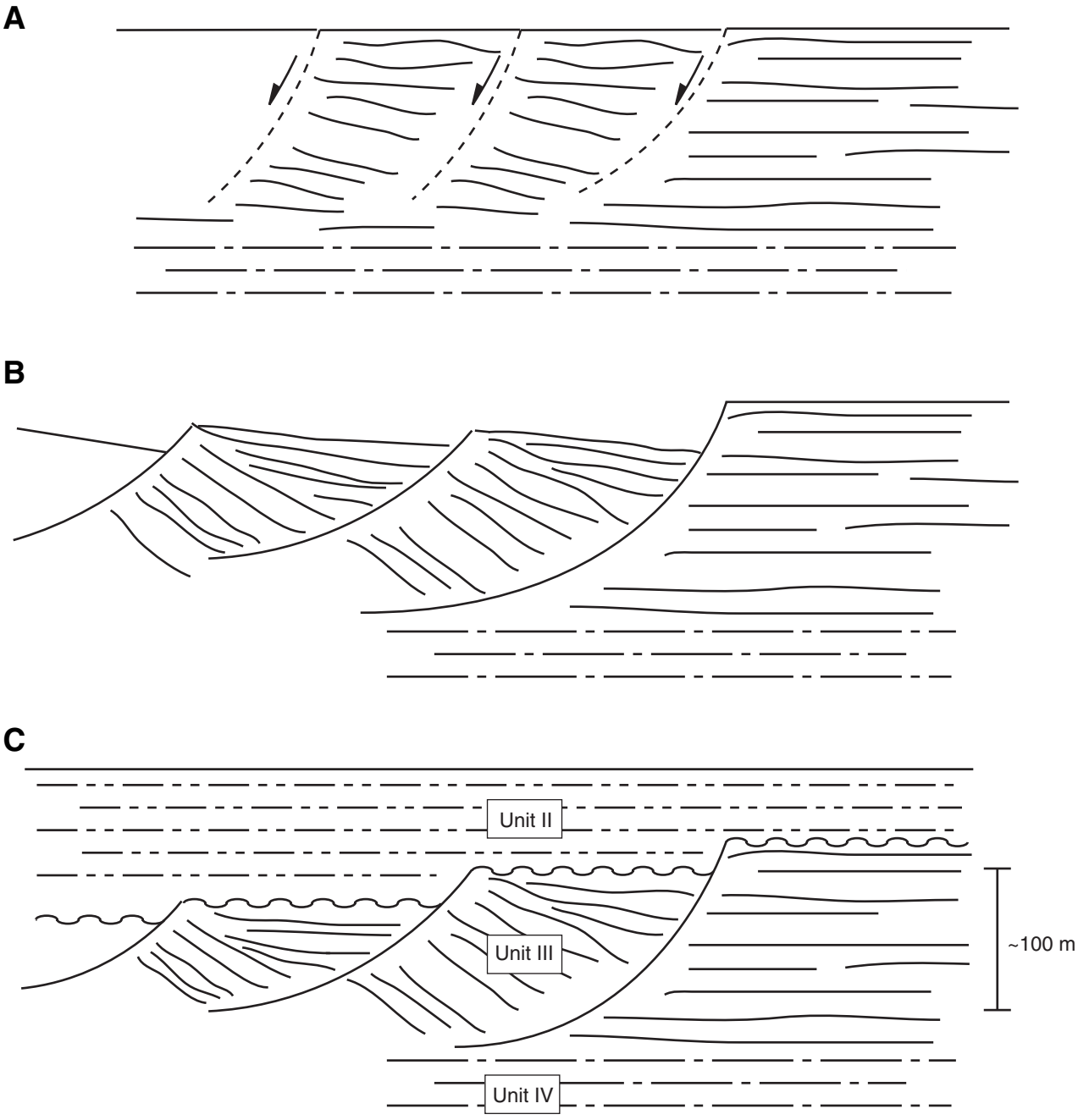

Figure F32. Chronostratigraphic correlation of Hole C0012A based on calcareous nannofossils and planktonic foraminifers. FO = first occurrence, LO = last occurrence, PE = paracme end, PB = paracme beginning.

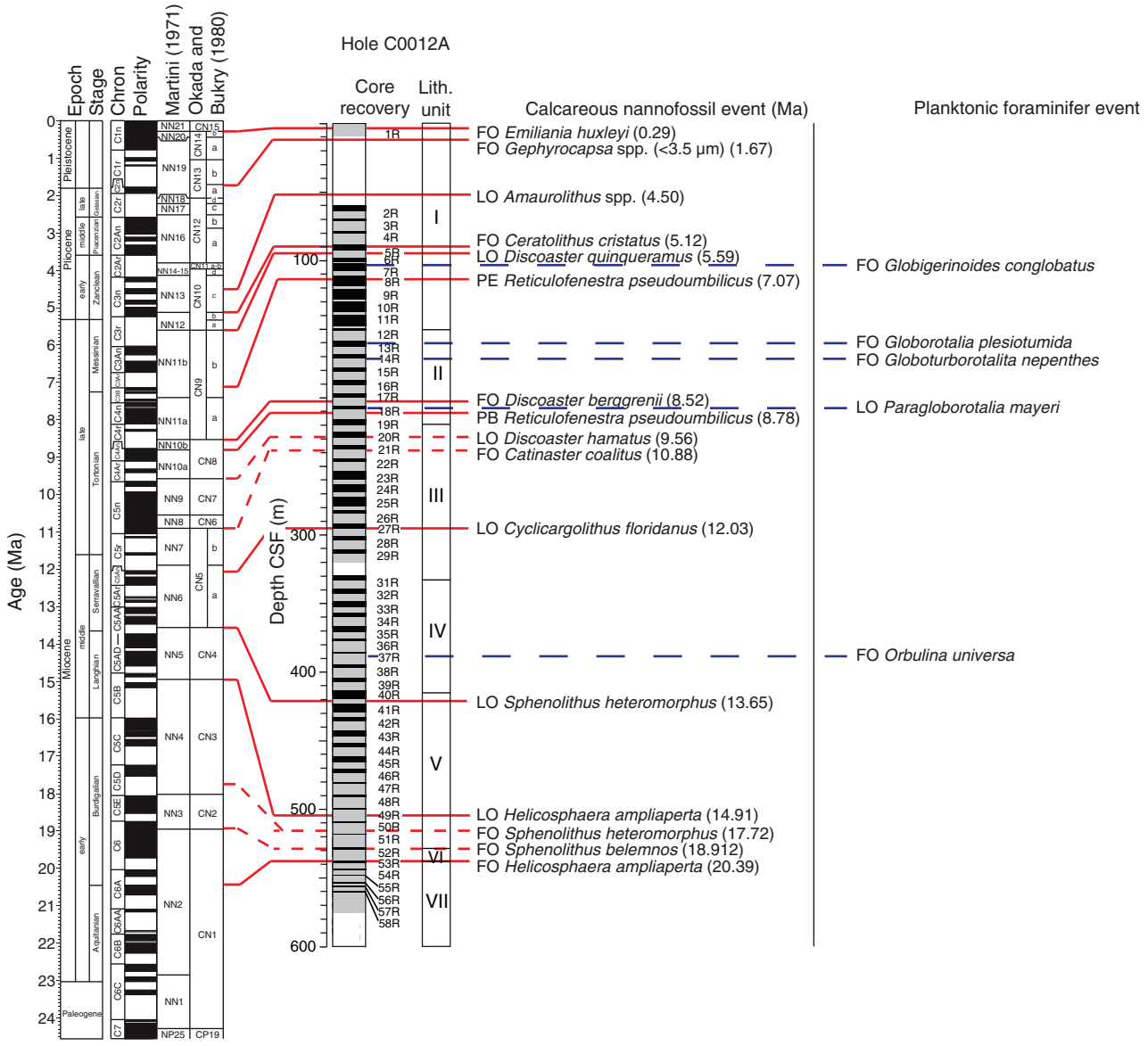

Figure F33. Deformed planktonic foraminifers.

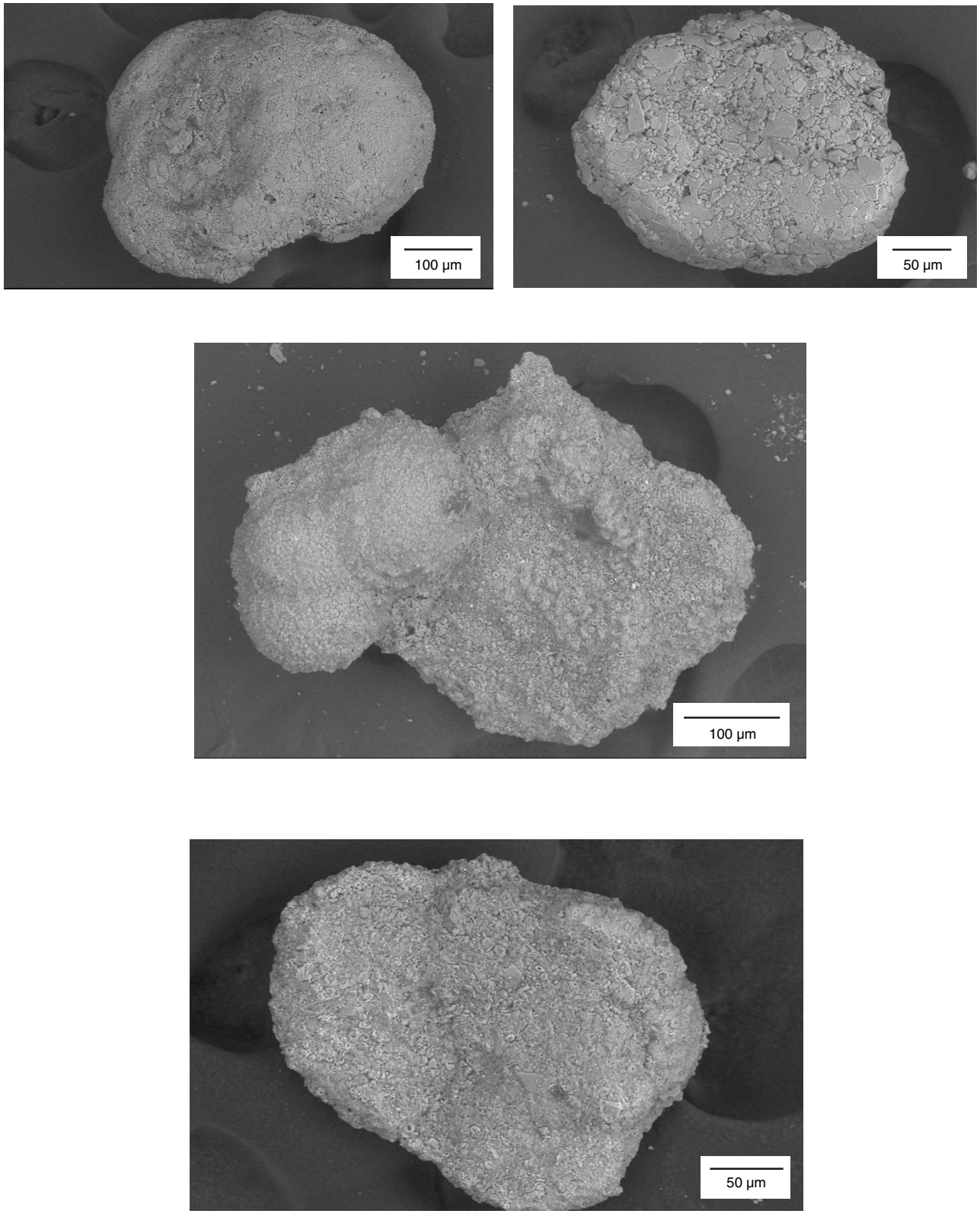

Figure F34. Sedimentation rates of Hole C0012A based on calcareous nannofossils.

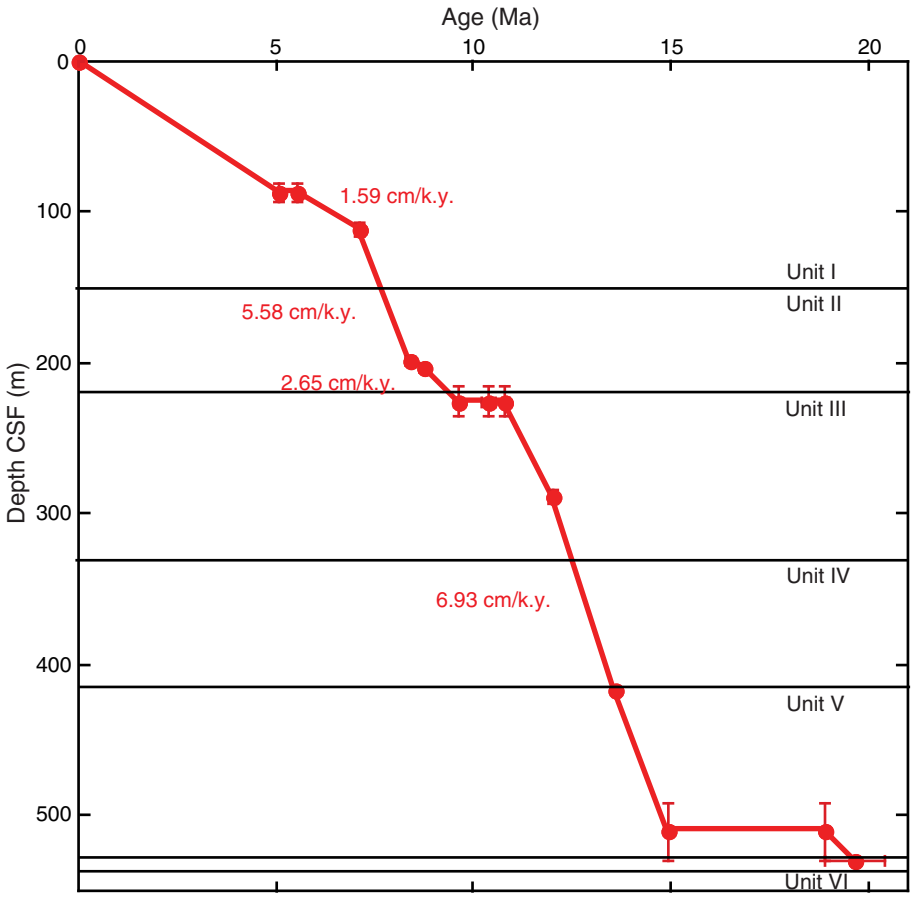

Figure F35. Results of paleomagnetic measurements on discrete samples plotted versus depth, Hole C0012A. From left to right, inclination (black = NRM before demagnetization, blue = linear regression fitting), magnetozones identified from this study (right = normal polarity, left = reversed polarity), magnetization intensity (black = NRM before demagnetization, red = after AF demagnetization at 10 mT), magnetic susceptibility, and *Q* ratios (blue = NRM_{0mT} – NRM_{10mT}, red = $NRM_{10\,mT}$; see text for details). Squares = tuffaceous sandstone, circles = volcanic sandstones.

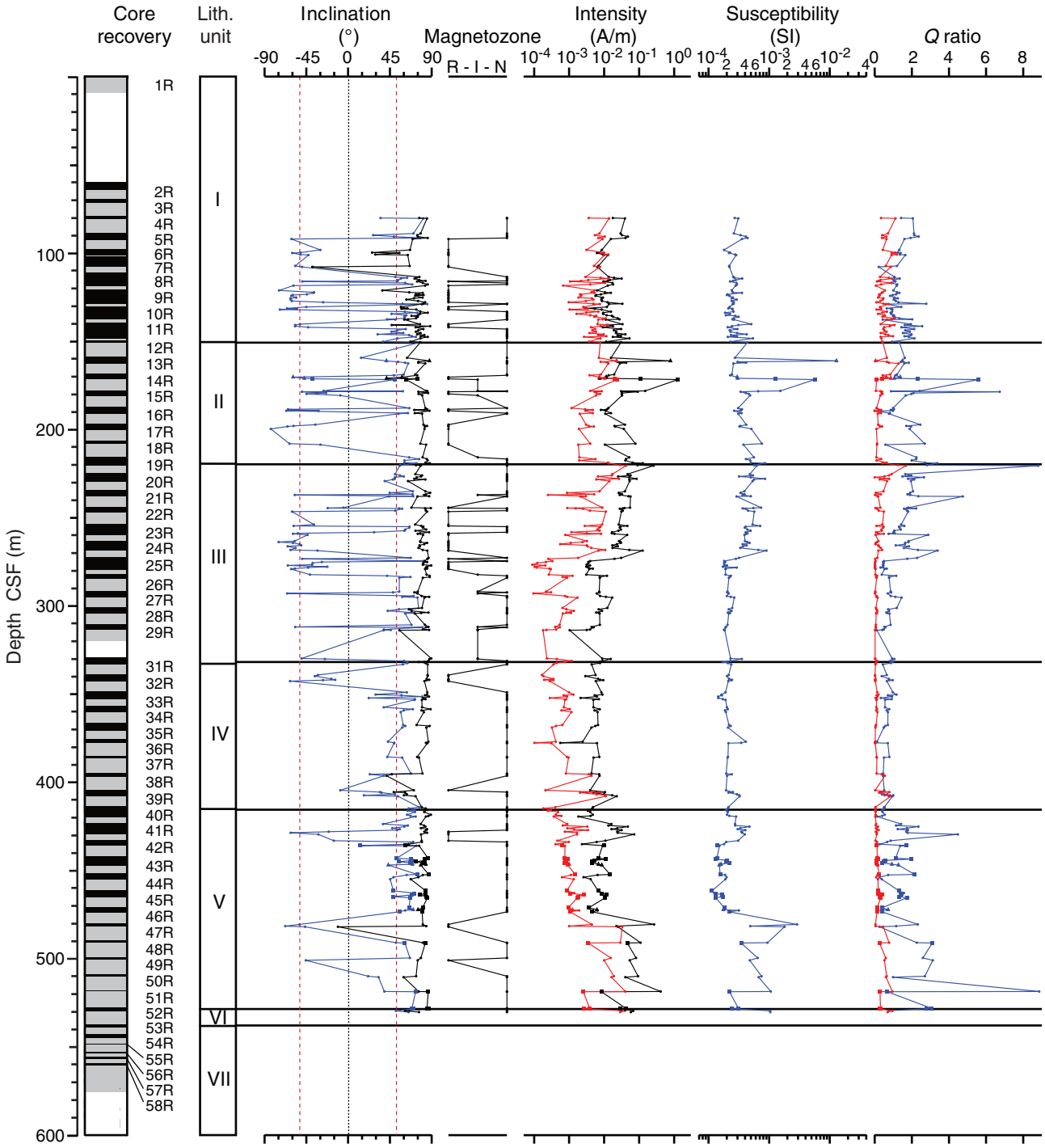

Figure F36. Histogram of inclinations isolated from the 269 discrete samples, Hole C0012A. Inclinations from these discrete samples are mostly concentrated at ±60° (positive and negative peaks). Red lines = inclination values theoretically predicted for the latitude of this site (±52.1°).

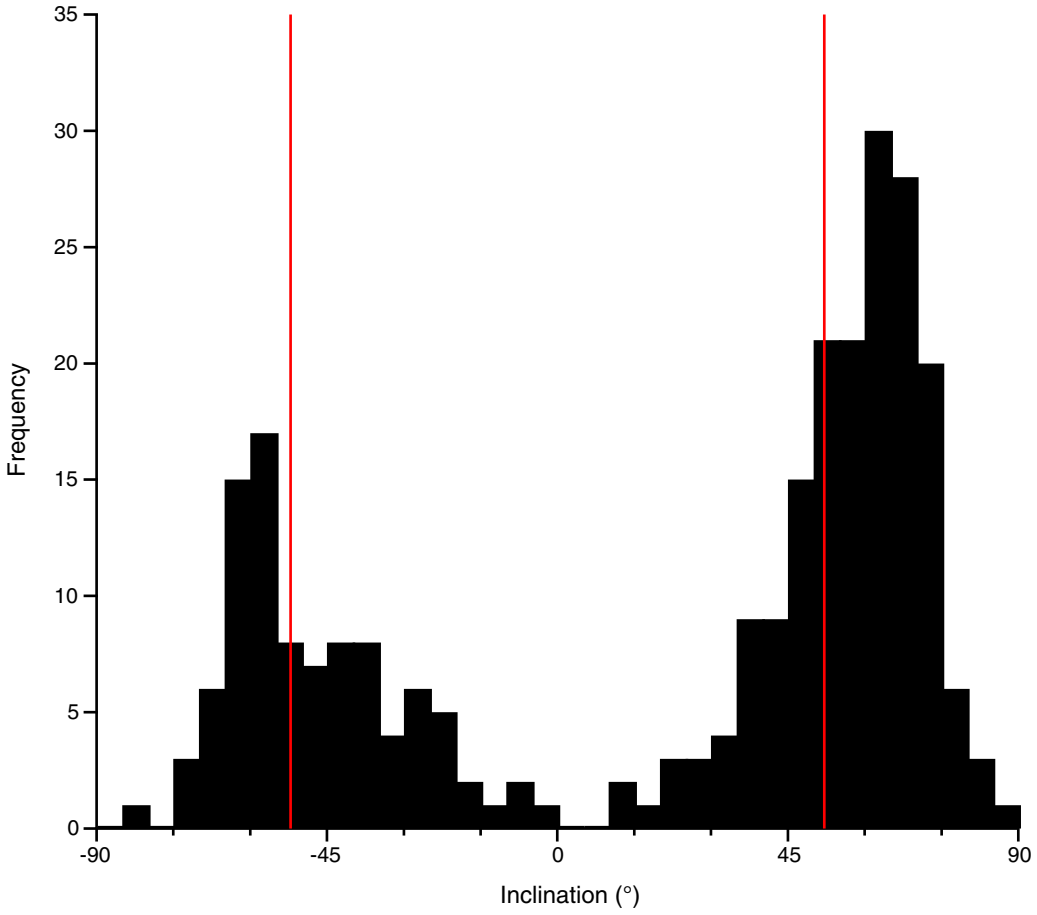

Figure F37. Representative vector endpoint diagrams of magnetization directions through stepwise AF demagnetization. **A.** Normal polarity Sample 322-C0012A-23R-4, 24–26 cm (from Unit III). **B.** Reversed polarity Sample 322-C0012A-24R-4, 4–6 cm (from Unit III). **C.** Reversed polarity Sample 322-C0012A-11R-1, 82–84 cm (from Unit II). **D.** Normal polarity Sample 322-C0012A-34R-1, 52–54 cm (from Unit IV). **E.** Normal polarity Sample 322-C0012A-39R-1, 107–109 cm (from Unit IV). **F.** Reversed polarity Sample 322-C0012A-6R-2, 37–39 cm (from Unit I). Open circles = projection of magnetization vector endpoints onto vertical planes, solid circles = projection of magnetization vector endpoints onto horizontal planes. NRM = natural remanent magnetization.

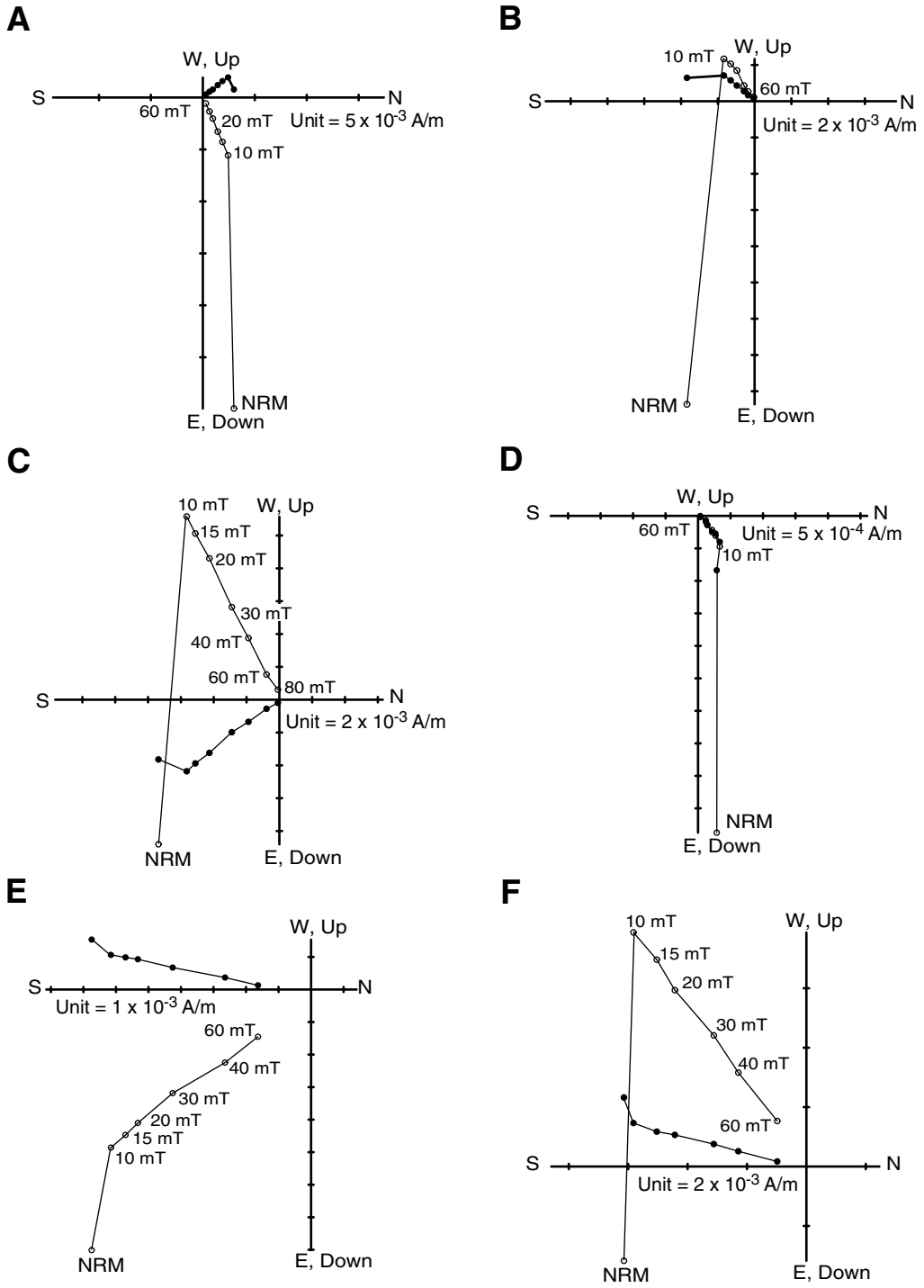

Figure F38. Age models, Hole C0012A. **A.** From top to 300 m CSF. Magnetozones identified from this study also shown (black = normal polarity, white = reversed polarity, gray = undetermined, red = no core recovery or no data). Depths of biostratigraphic and magnetostratigraphic datums listed in Tables T11 (Model A) and T6 (Model B) and plotted versus expected ages. Vertical bars = uncertainty of depth, horizontal error bars for nannofossil datum = uncertainty between oceans (Pacific/Atlantic/Mediterranean). For magnetostratigraphy, error bars represent uncertainty of polarity boundary recognition. Errors on astronomical tuning of ATNTS2004 (Lourens et al., 2004) for the age interval younger than 13 Ma are typically <0.2% (smaller than radius of circles). Sedimentation rates (green text) calculated from magnetostratigraphy age model with least squares fitting of linear regression line using the datum events with equal weight. Green (purple) ages on horizontal lines corresponding to unit boundary = boundary ages for age Model A (B) including errors of control points and line fitting. (Continued on next page.)

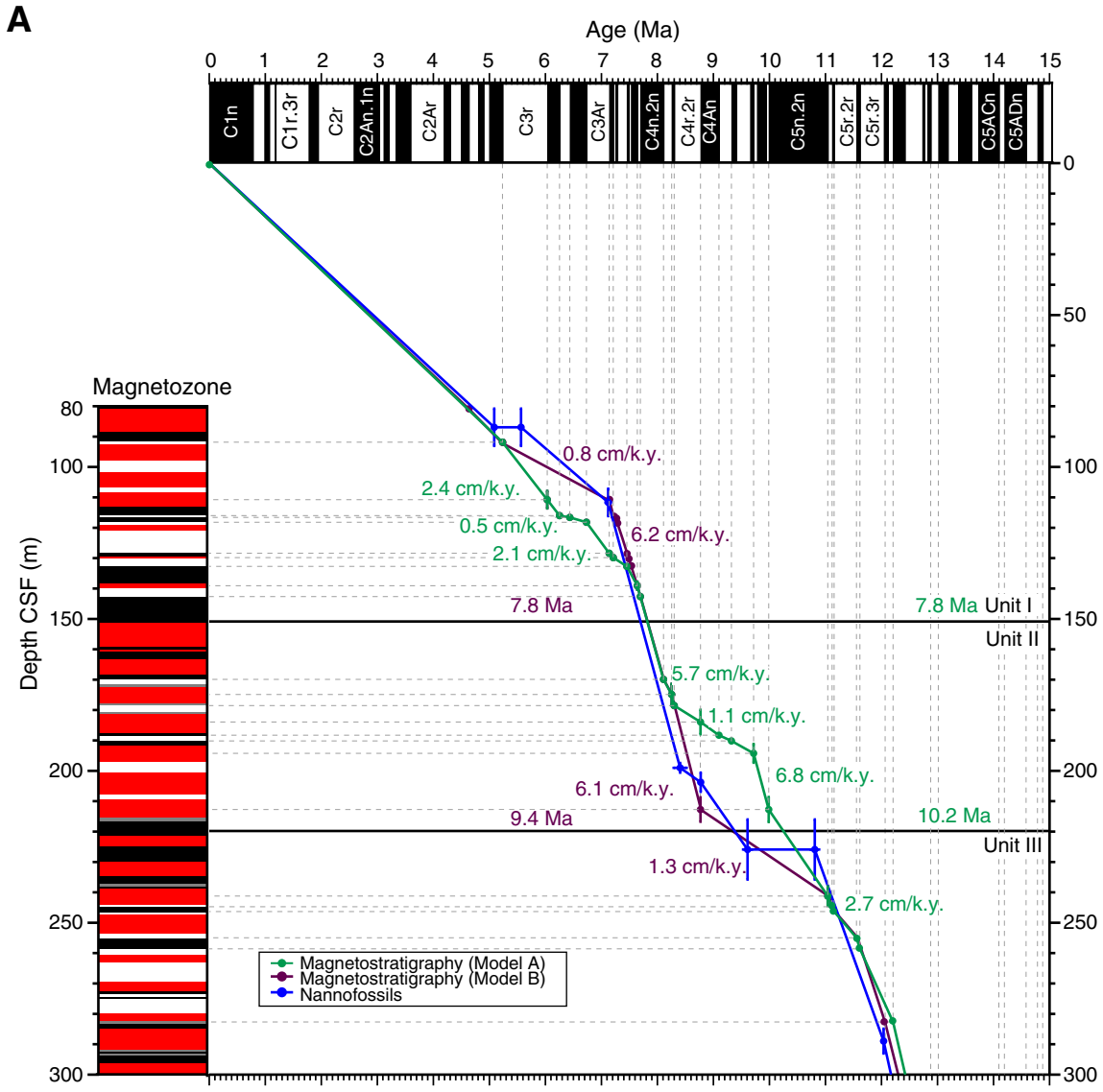

Figure F38 (continued). B. From top to bottom of hole. Error bar on oldest nannofossil datum (B; bottom blue circle) shows uncertainty that datum show the occurrence of the species just above basaltic basement (see "Biostratigraphy").

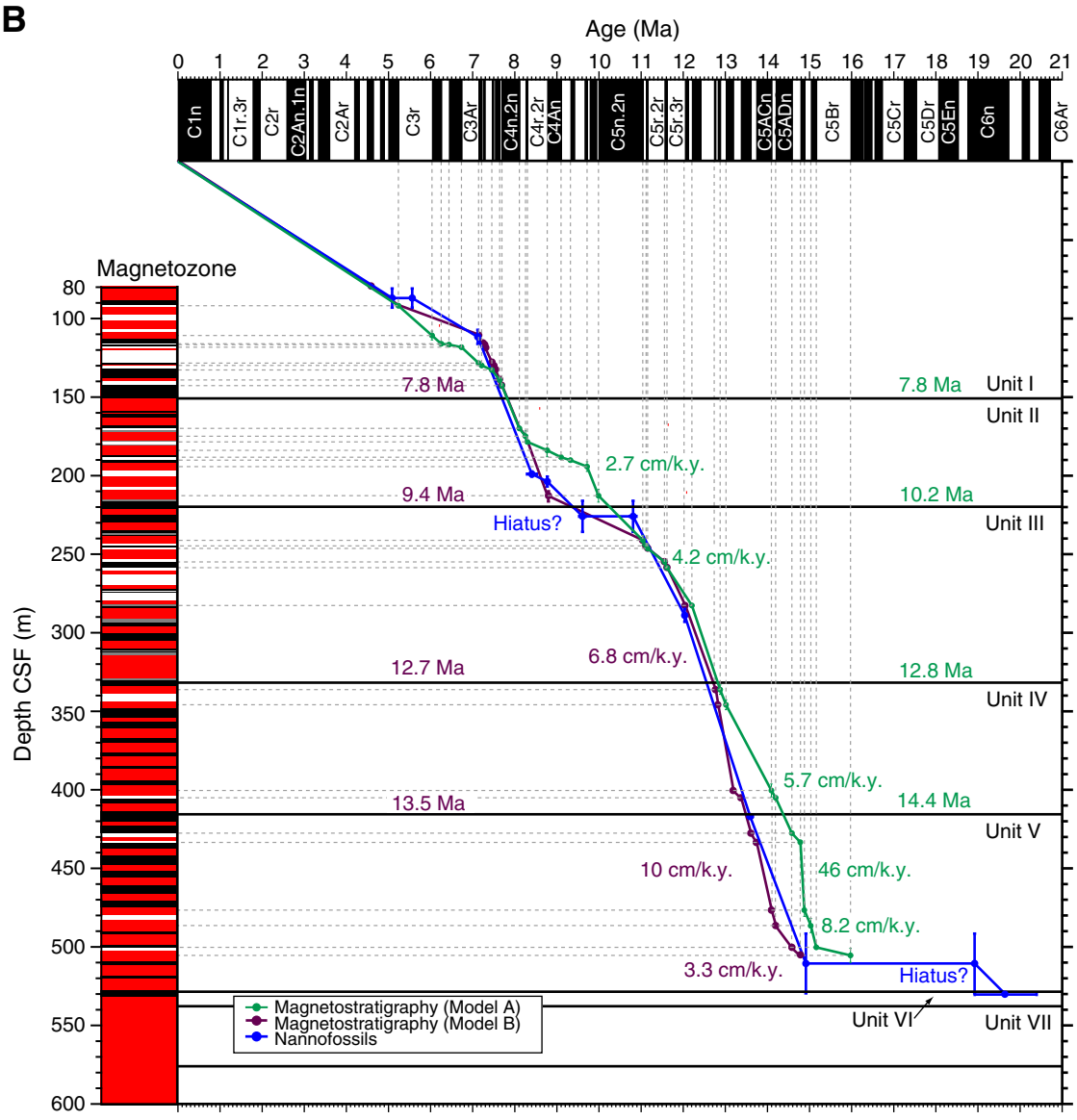

Figure F39. Example of vector endpoint diagrams of magnetization directions through stepwise AF and thermal demagnetization for basement basaltic rocks. **A.** Sample 322-C0012A-53R-2, 35–37 cm, demagnetized to 80 mT. **B.** Sister specimen of A taken as a fragment at the rim of core sample, measured postcruise with a cryogenic magnetometer to 80 mT. **C.** Sample 322-C0012A-54R-2, 77–79 cm, demagnetized to 50 mT. **D.** Enlargement of C below 23 mT AF demagnetization field. **E.** Sister specimen of C taken as a fragment of the rim of core sample, measured postcruise with a cryogenic magnetometer to 80 mT. **F.** Sister specimen of C taken between above two specimens, measured postcruise with a cryogenic magnetometer up to 600°C with a furnace. Open circles = projection of magnetization endpoints onto vertical plane, solid circles = projection of magnetization vector endpoints onto horizontal planes. NRM = natural remanent magnetization. (**Figure shown on next page.**)

Figure F39 (continued). (Caption shown on previous page.)

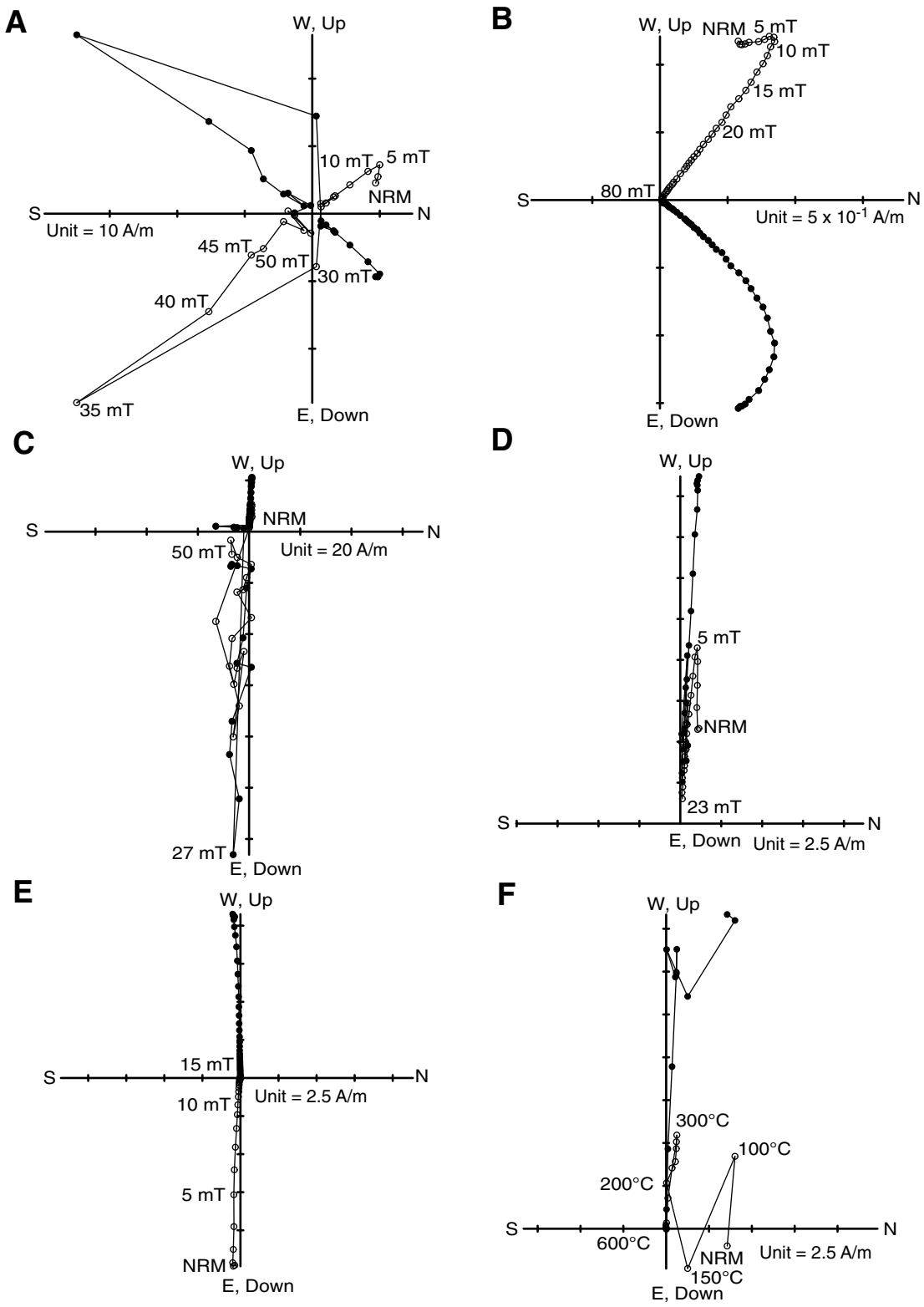

Figure F40. Downhole plot of parameters for AMS. **A.** K_{min} inclination. **B.** Anisotropy degree parameter (P′). **C.** Shape parameter (T).

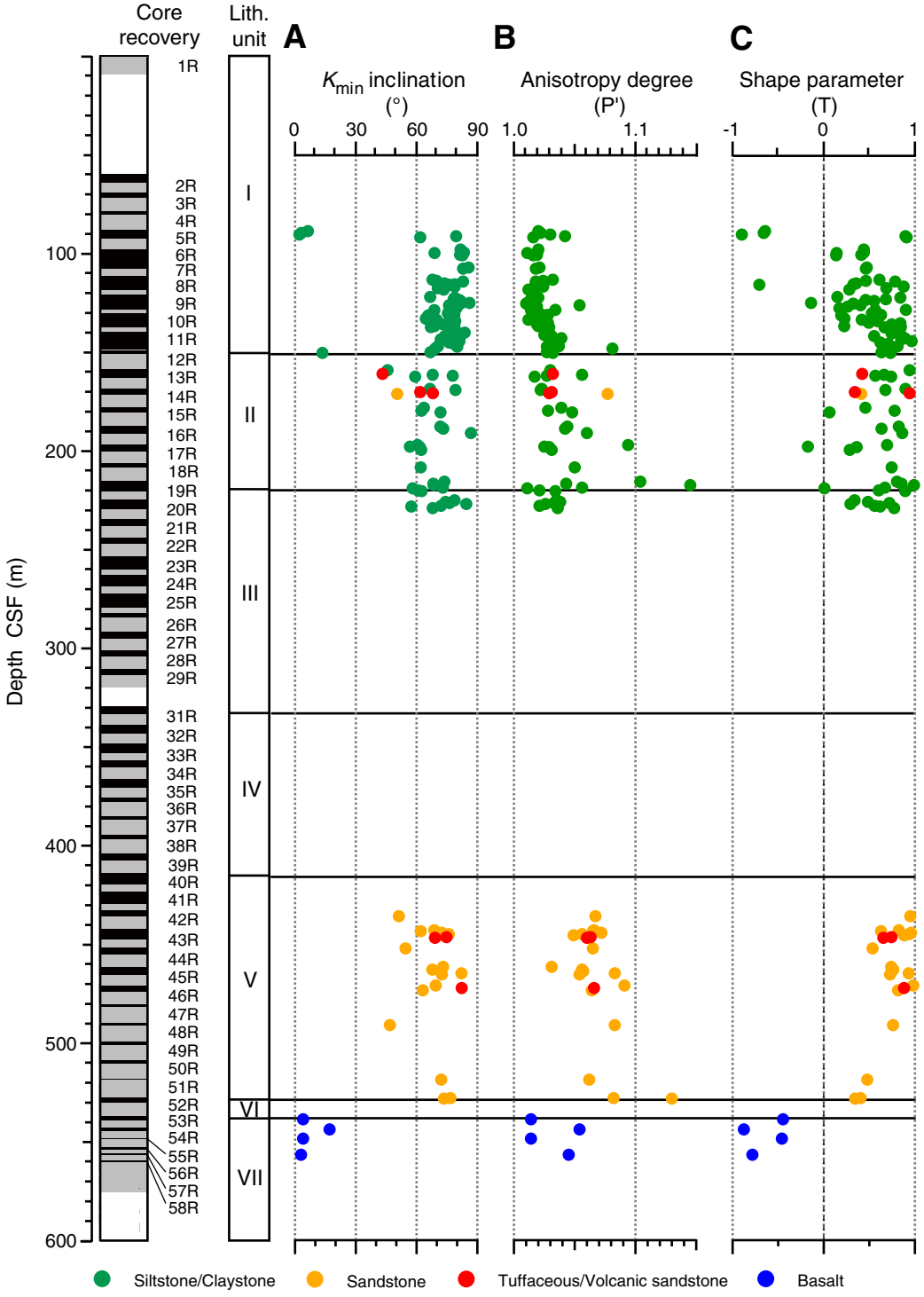

Figure F41. A. Gamma ray attenuation (GRA) density. **B.** Magnetic susceptibility. **C.** Noncontact electrical resistivity. **D.** Natural gamma radiation. Determined by MSCL-W. CMS = corrected volume magnetic susceptibility, cps = counts per second.

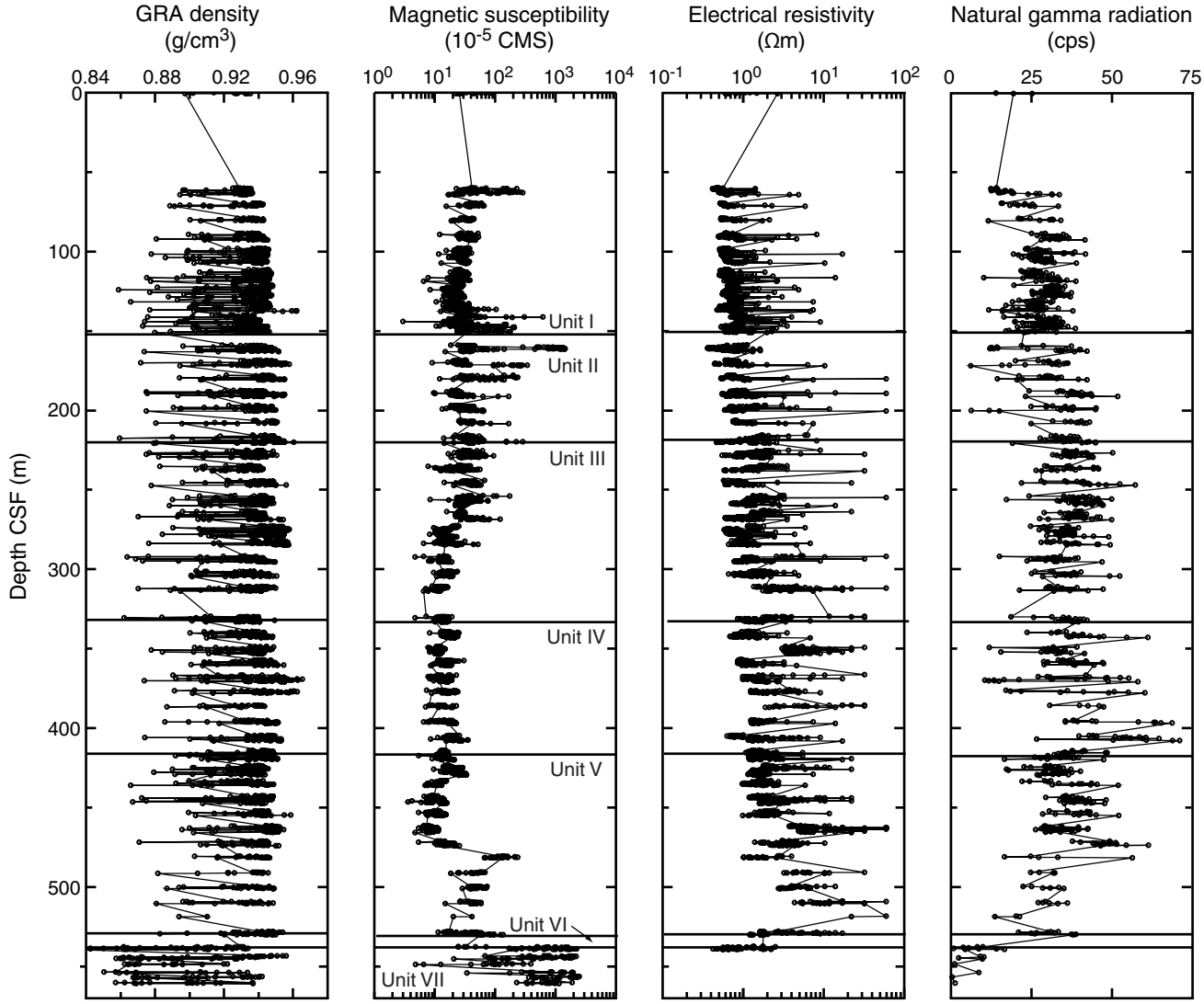

Figure F42. A. Bulk and grain density and (**B**) porosity of discrete mud(stone) and sand(stone) samples determined by MAD measurements. Solid line in B = modeled porosity-effective stress behavior assuming hydrostatic fluid pressure. **C.** *P*-wave velocity measurements on cube samples in the *x*-, *y*-, and *z*-direction of the core reference frame. Basalt velocities exceed 3000 m/s and are not plotted; data are available in Table **T17.** **D.** Thermal conductivity measurements on mud(stone) and sand(stone). Diamonds = half-space method, pluses = full-space method.

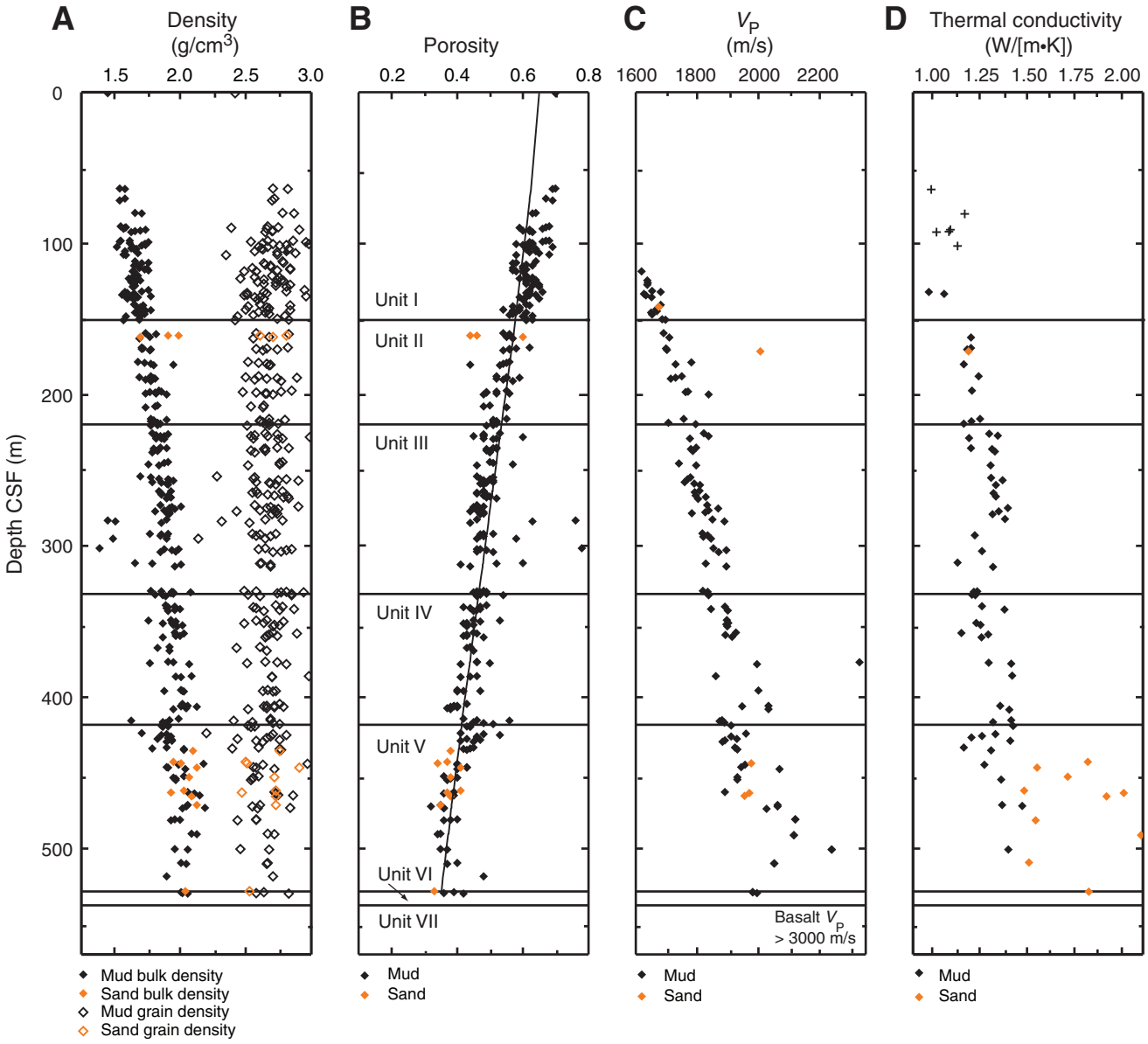

Figure F43. Undrained shear strength in the shallow section (<100 m CSF), Hole C0012A.

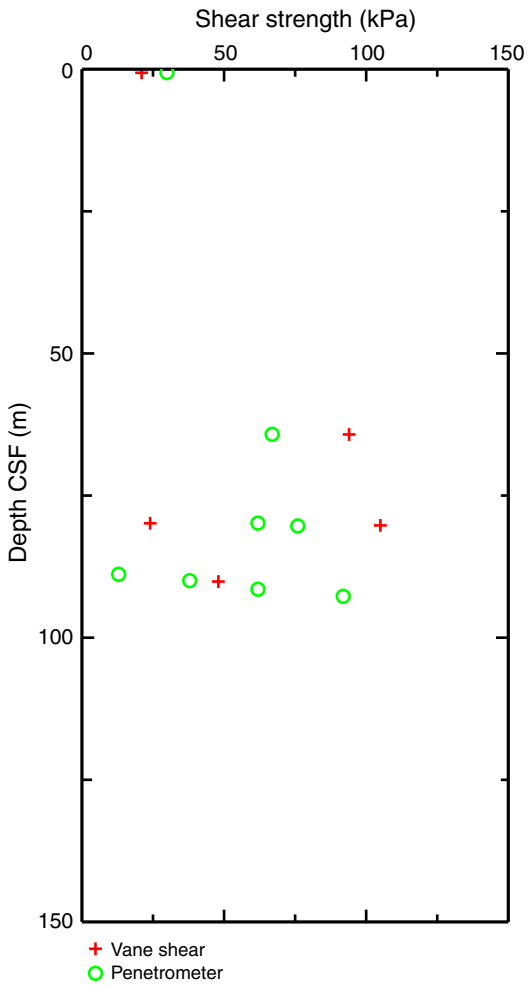

Figure F44. *P*-wave velocity, horizontal-plane anisotropy, and vertical-plane anisotropy on discrete cube samples, Hole C0012A. For vertical-plane anisotropy, positive values indicate horizontal V_P > vertical V_P. Basalt velocities exceed 3000 m/s and are not plotted; data are available in Table T17.

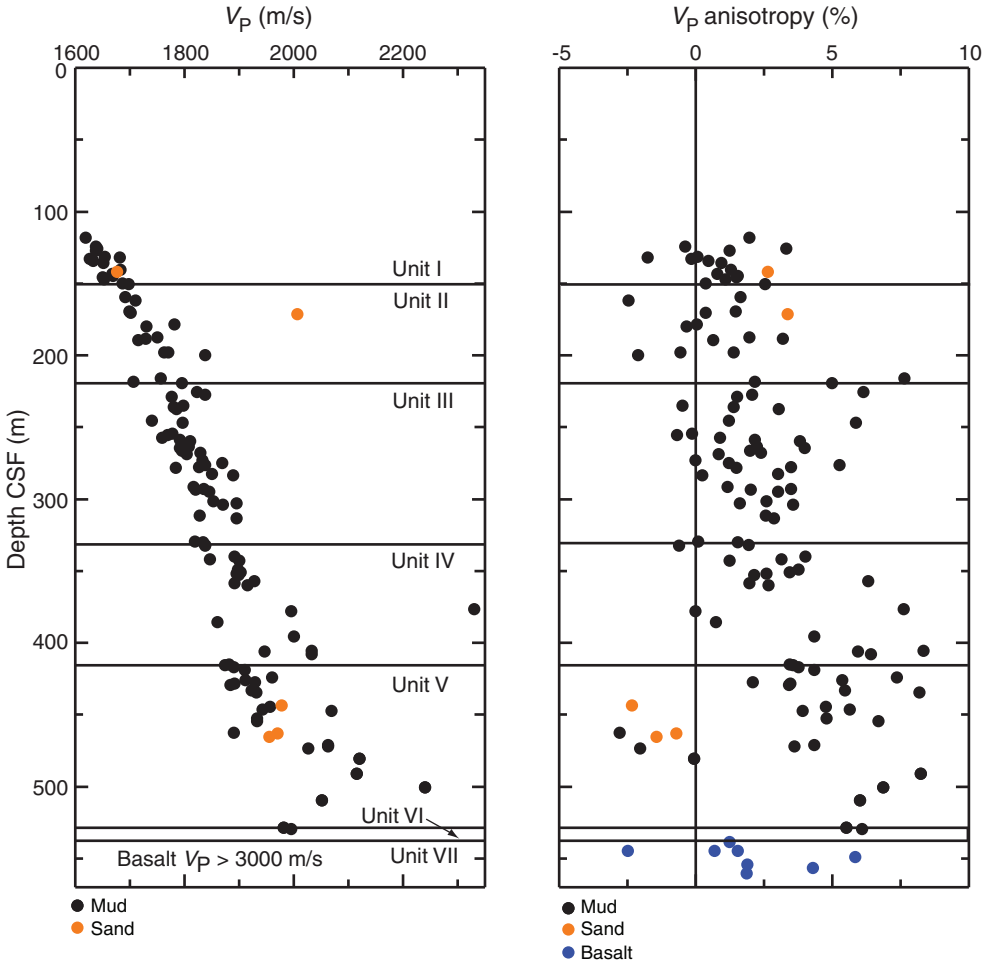

Figure F45. *P*-wave velocity versus porosity for discrete samples, Hole C0012A. Solid line = empirical trend for Shikoku Basin sediments defined by Hoffman and Tobin (2004), dashed lines = typical trends derived from global compilations (Erickson and Jarrard, 1998).

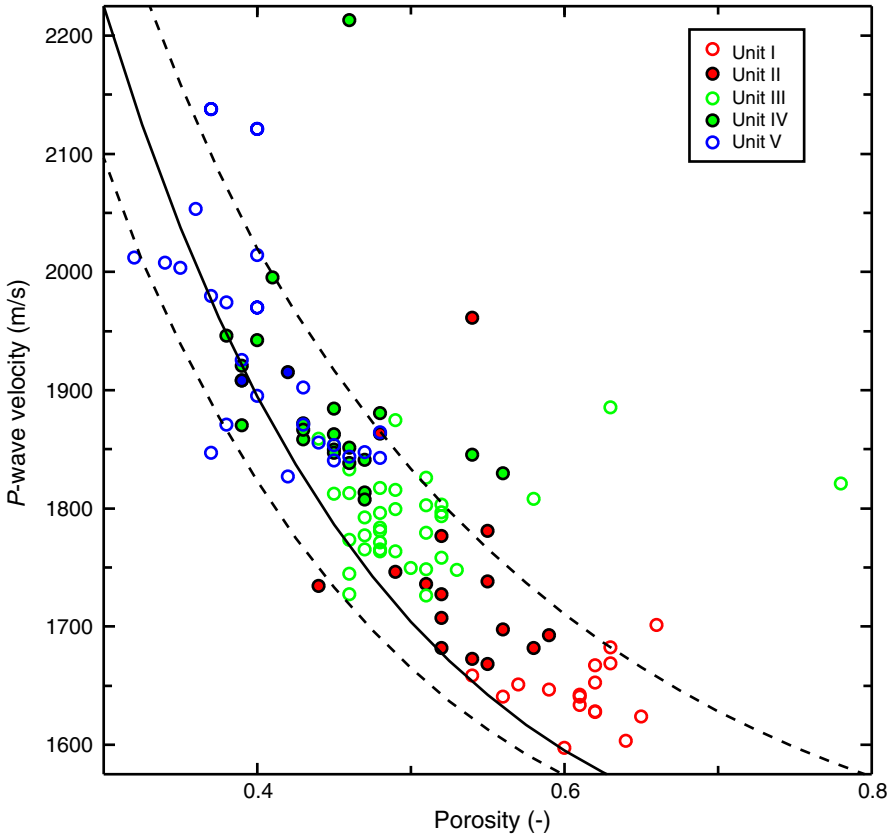

Figure F46. Electrical resistivity and vertical-plane anisotropy for discrete cube samples, Hole C0012A.

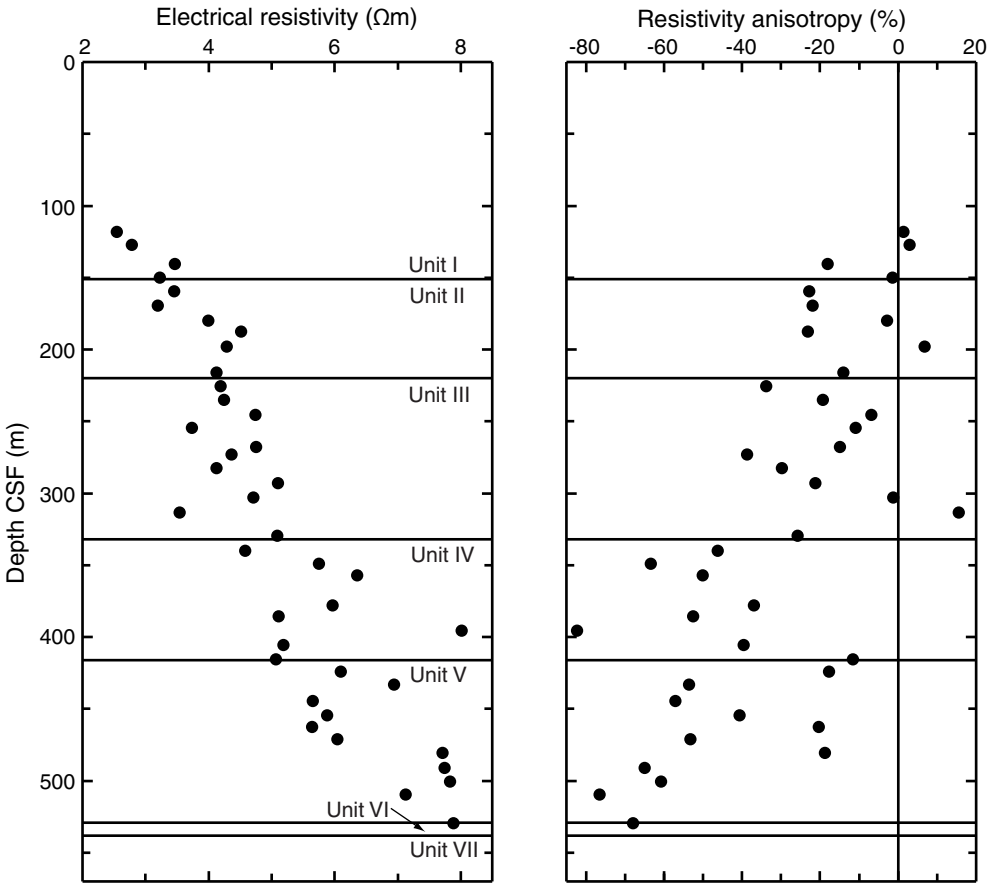

Figure F47. Porosity versus thermal conductivity, Hole C0012A. Lines = theoretical values for different grain thermal conductivities (k_s) based on a geometric mean mixing model.

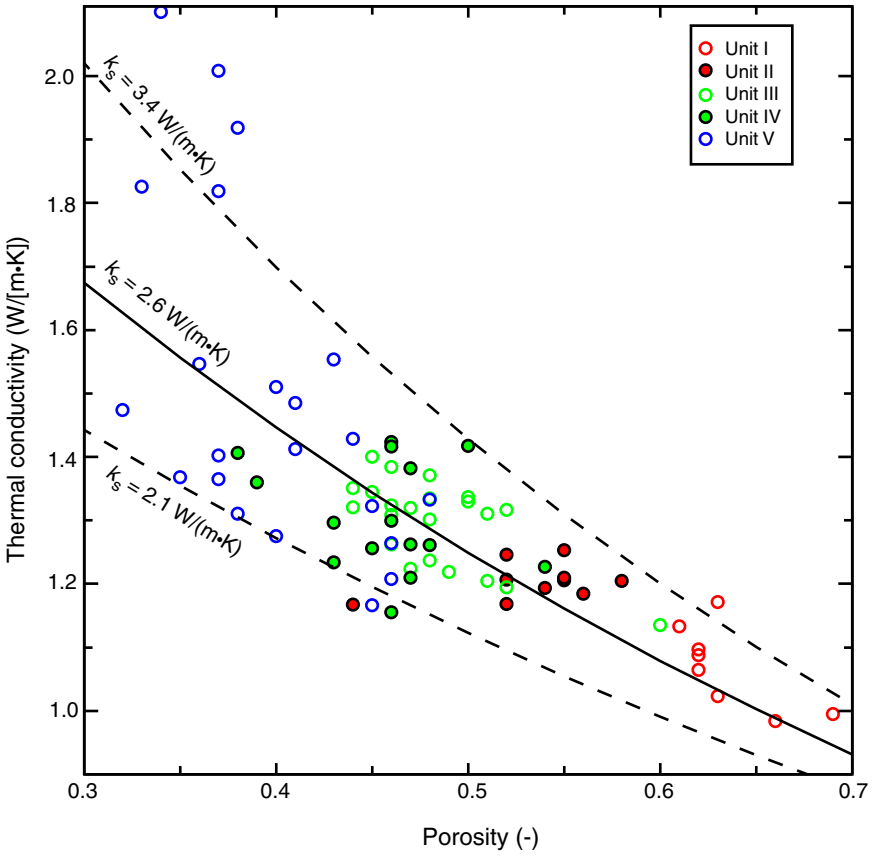

Figure F48. Volume of interstitial water recovered from whole-round sections, Hole C0012A.

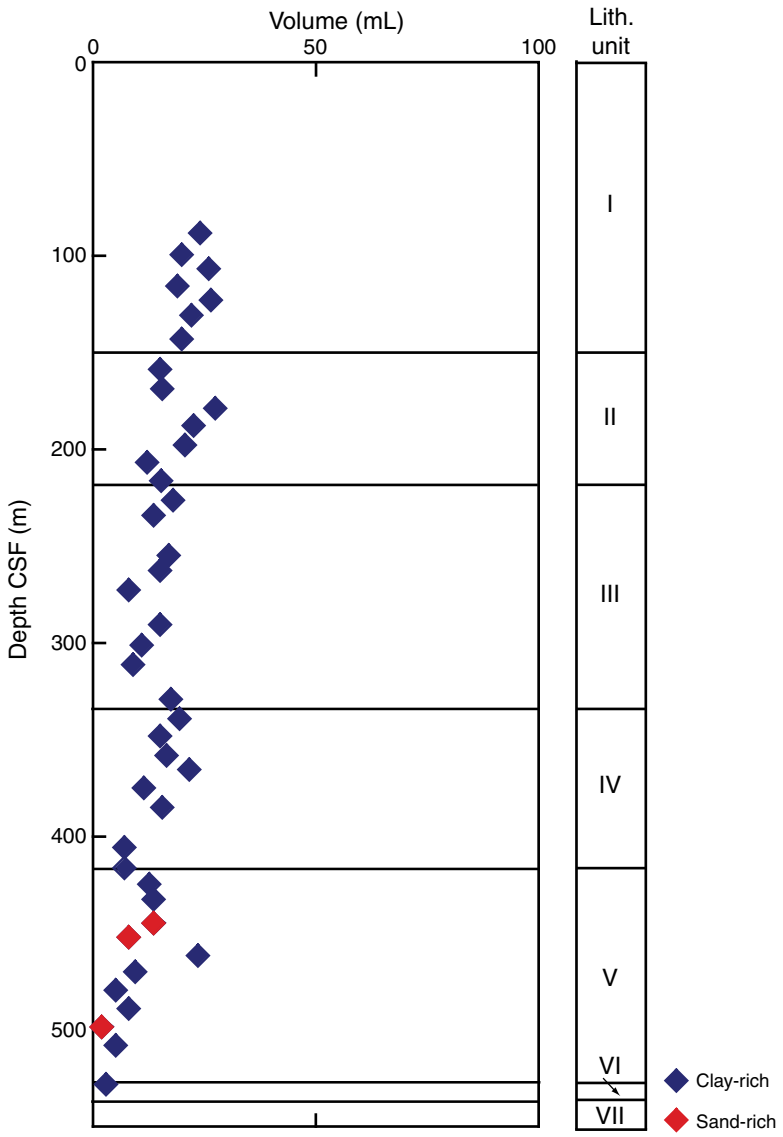

Figure F49. Interstitial water constituents (salinity, chlorinity, bromide, pH, alkalinity, sulfate, ammonium, hydrogen sulfide, and boron), Hole C0012A. Blue arrows = seawater concentrations.

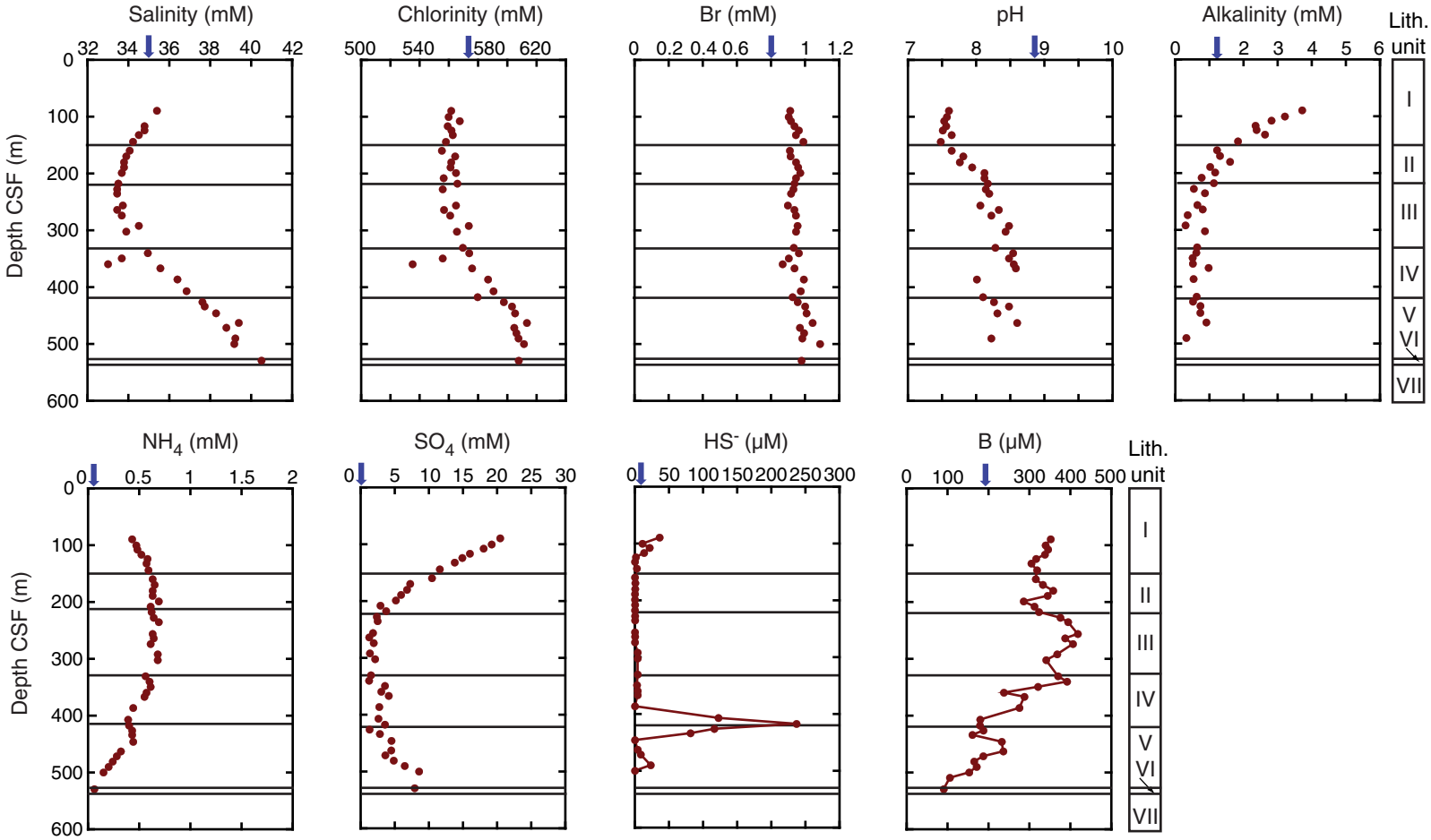

Figure F50. Interstitial water constituents (sodium, potassium, magnesium, calcium, silica, lithium, strontium, barium, and manganese), Hole C0012A. Blue arrows = seawater concentrations.

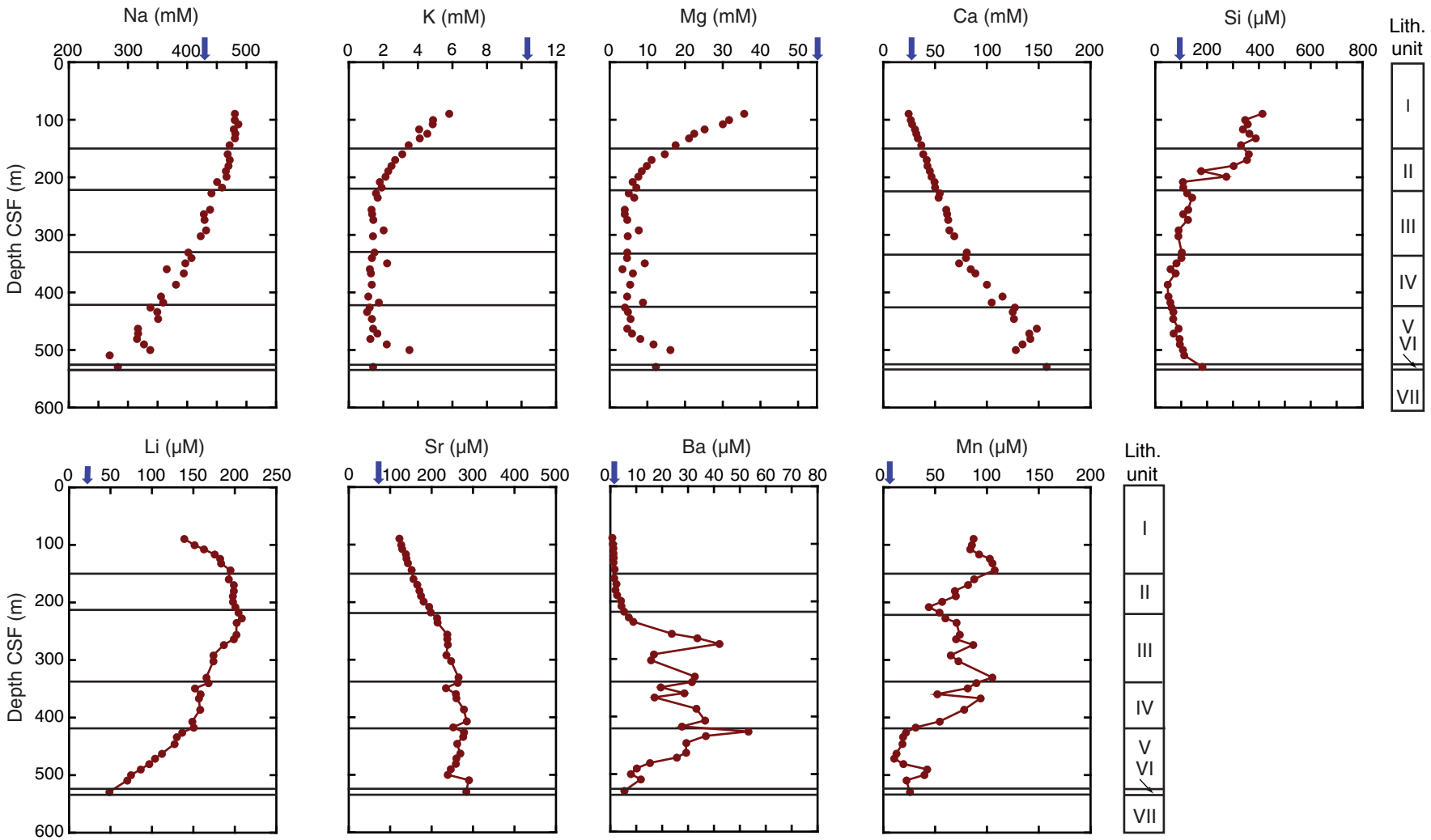

Figure F51. Interstitial water constituents (rubidium, zinc, uranium, lead, cesium, molybdenum, and vanadium), Hole C0012A.

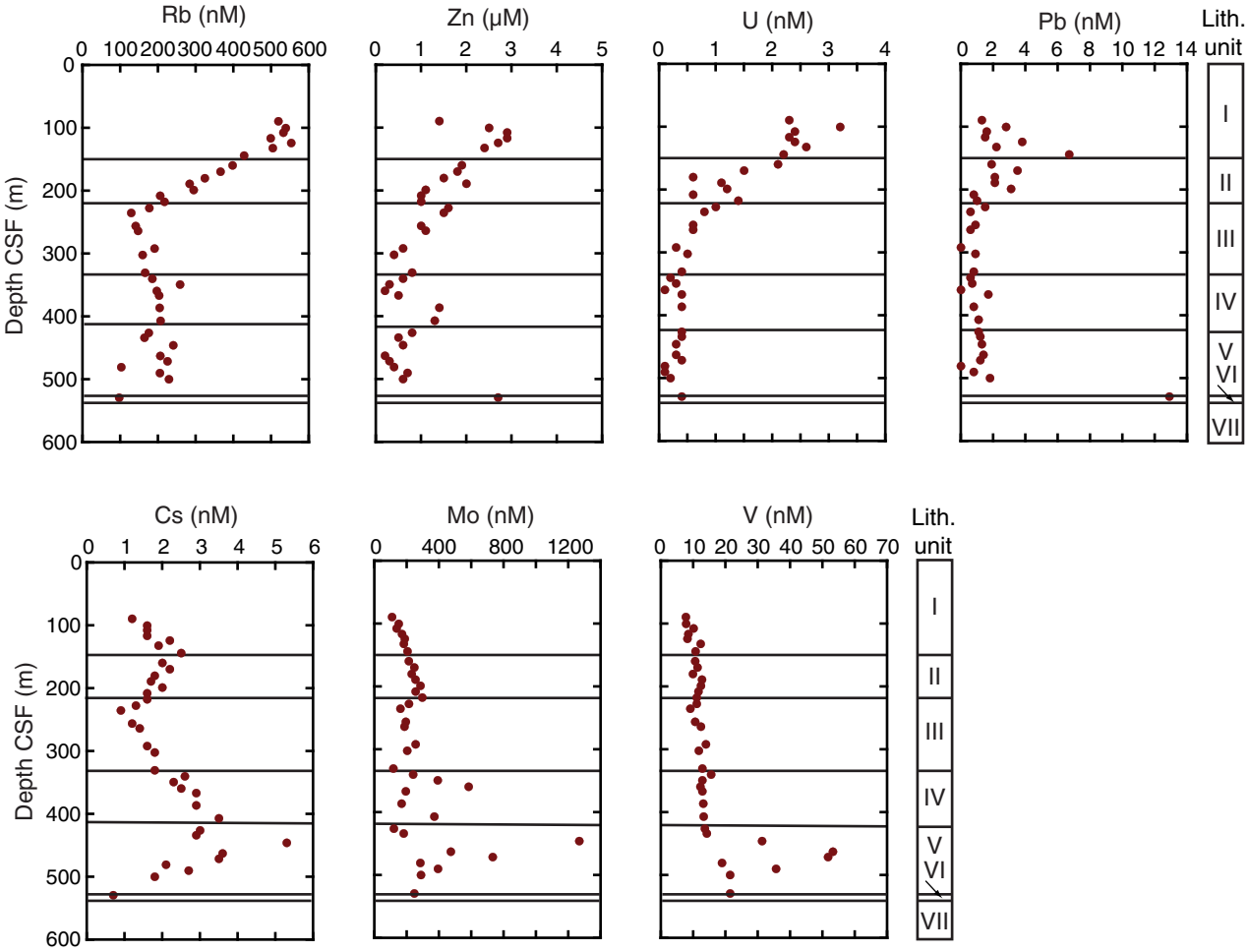

Figure F52. A. Comparison of sulfate distribution at Site C0012 (red) with profiles obtained from ODP Leg 190 Sites 1173 (blue), 1175 (green), and 1178 (black) drilled in this margin (Shipboard Scientific Party, 2001). **B.** Dissolved sulfate (red) and hydrogen sulfide (blue) superimposed on general methane distribution, Site C0012 (see **"Organic geochemistry"**). SW = seawater.

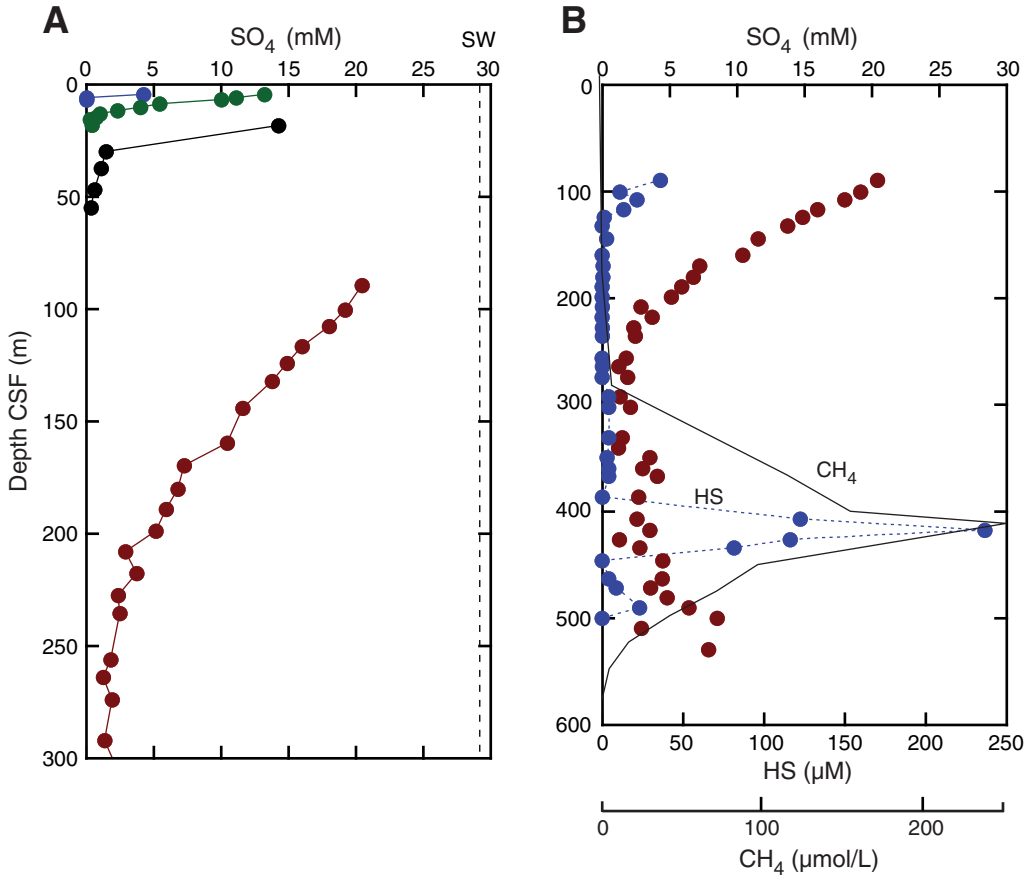

Figure F53. Depth distribution of saturation indexes estimated using pore fluid concentrations, pure end-member phases, and the PhreeqcI software package of Parkhurst and Appelo (1999). Calculations performed at 25°C (solid lines) and 5°C (dotted lines). **A.** Carbonates. **B.** Montmorillonites. **C.** Zeolites.

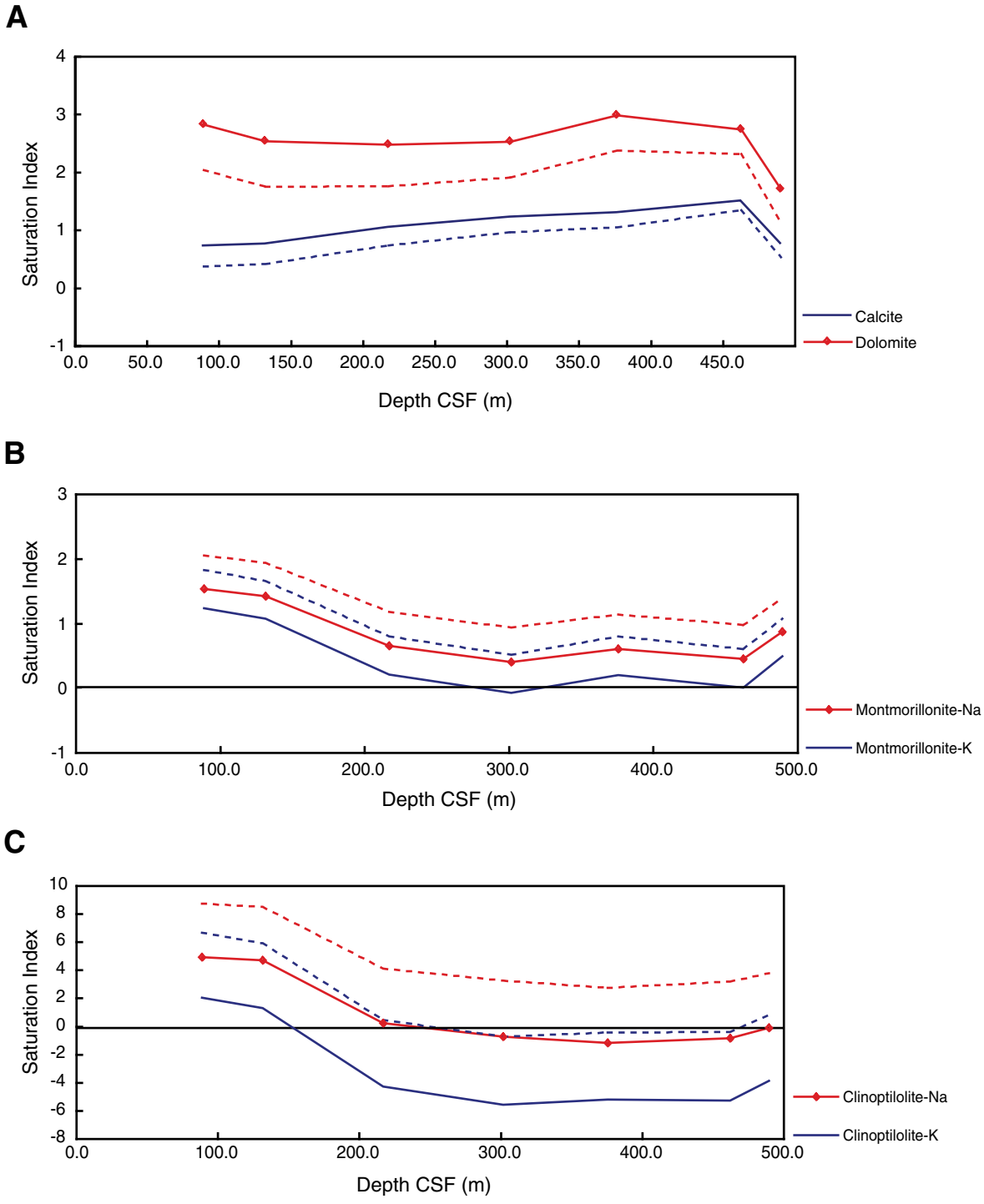

Figure F54. Depth profiles of methane, ethane, and C_1/C_2, Hole C0012A.

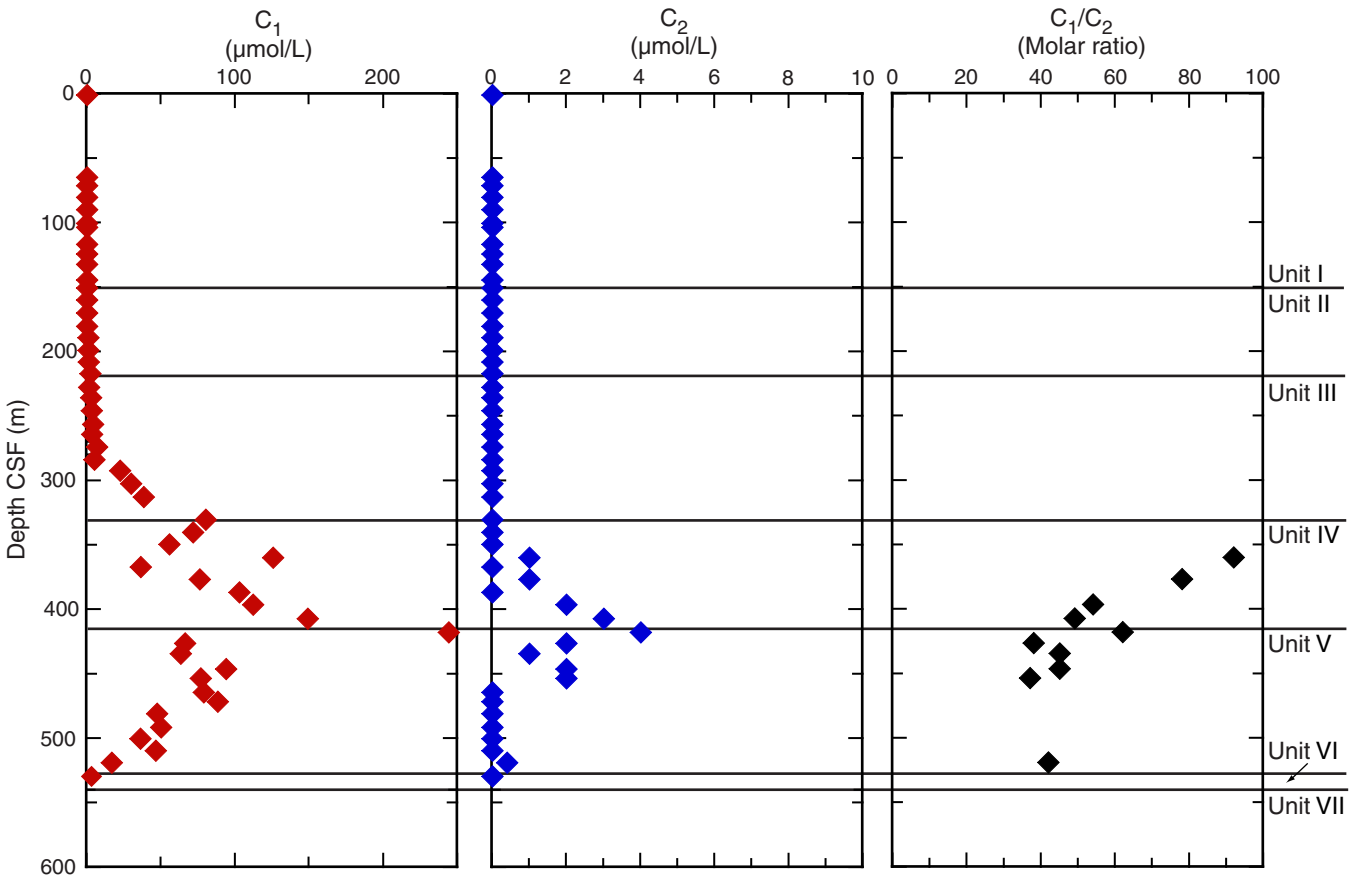

Figure F55. Depth profiles of inorganic carbon, total organic carbon, total nitrogen, and total sulfur in Hole C0012A.

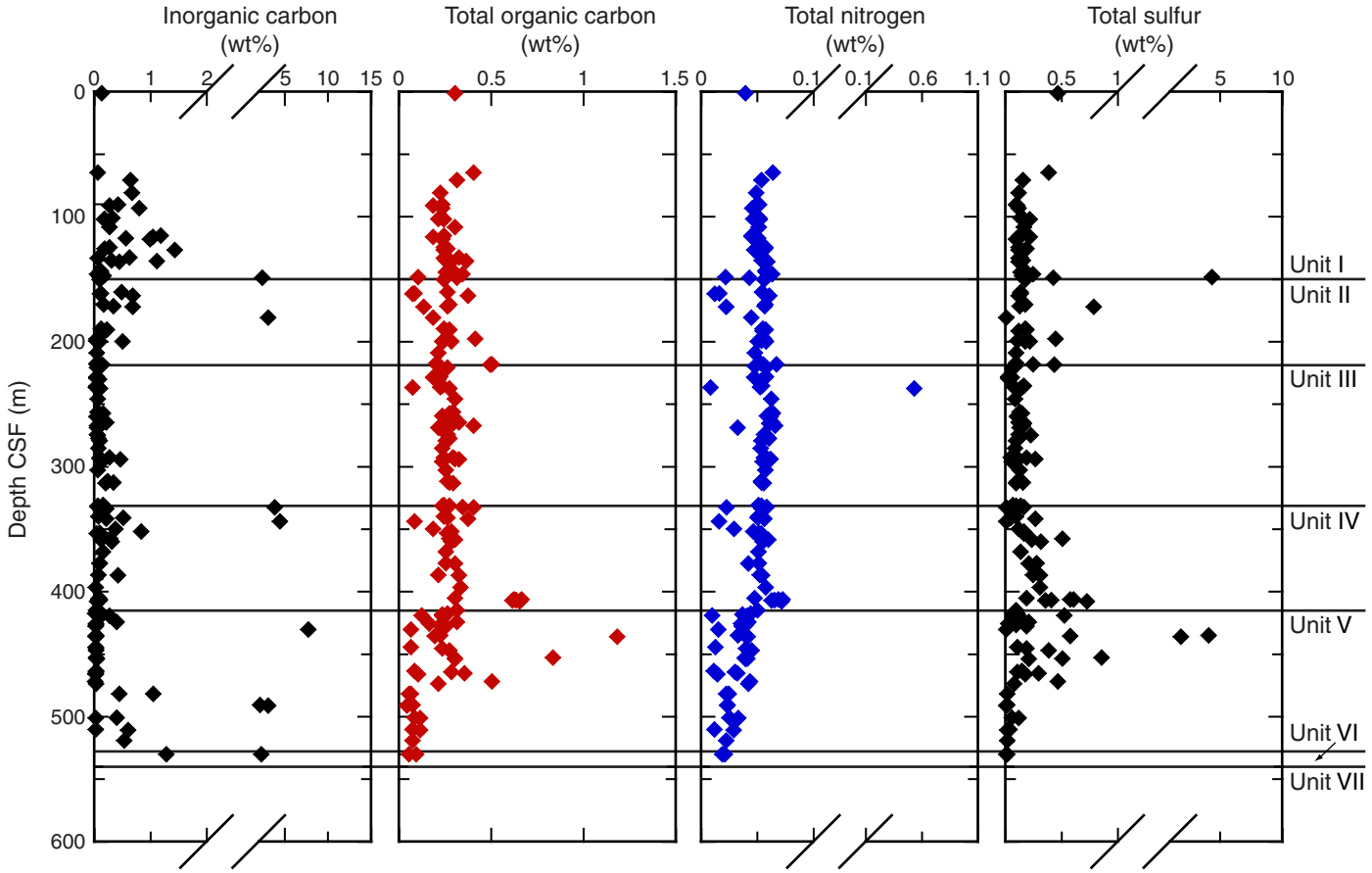

Figure F56. Plot of methane/ethane (C_1/C_2) molar ratios versus temperature, Hole C0012A. Temperature calculated using geothermal gradient of 0.056°C/m and bottom water temperature of 3°C. Modified from Pimmel and Claypool (2001). TOC = total organic carbon.

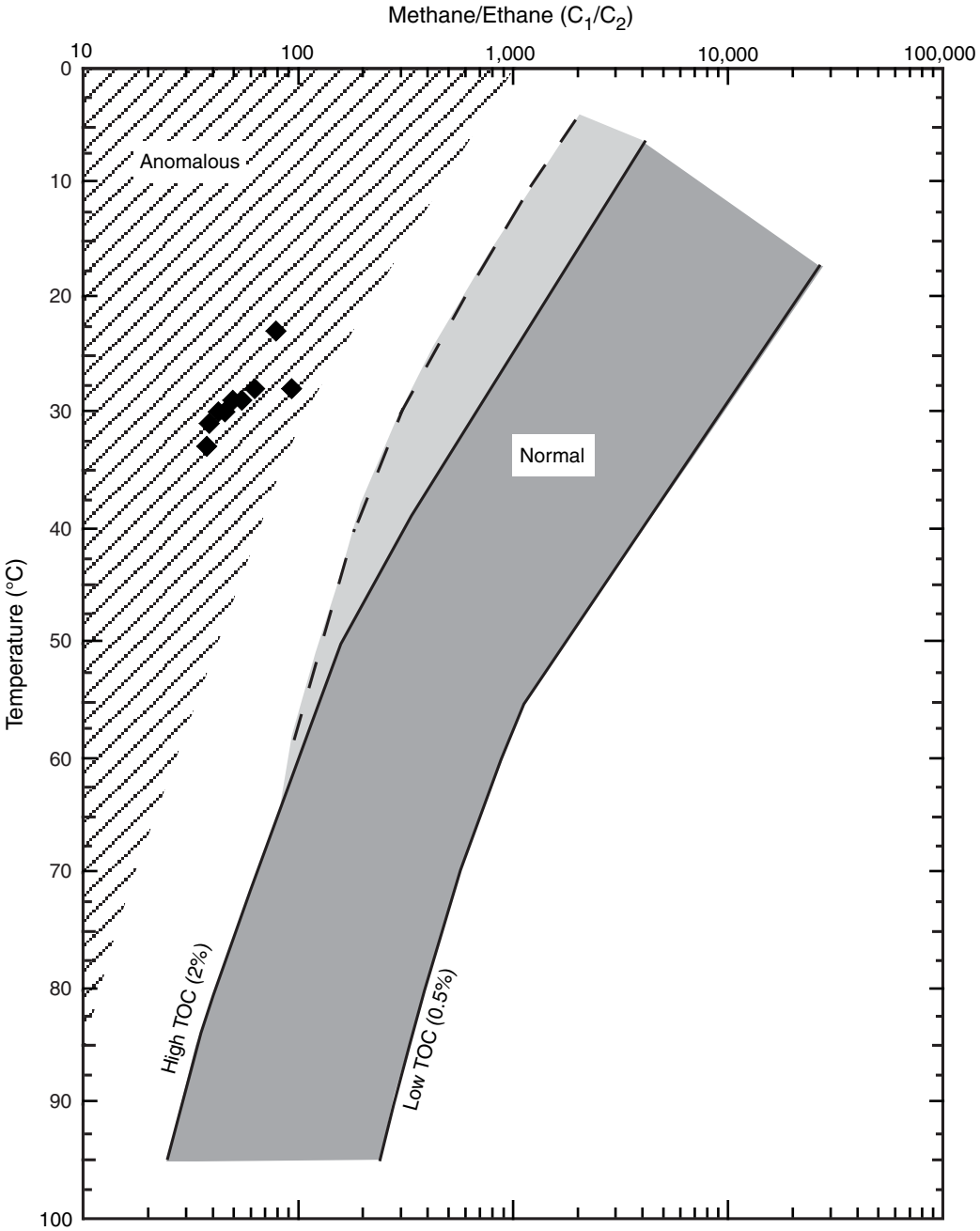

Figure F57. H_2 concentrations in sediment samples from Hole C0012A as a function of time from three replicable incubation experiments. **A.** Section 322-C0012A-7R-5. **B.** Section 322-C0012A-19R-2. **C.** Section 322-C0012A-22R-2. **D.** Section 322-C0012A-25R-2. **E.** Section 322-C0012A-29R-3. **F.** Section 322-C0012A-32R-2. **G.** Section 322-C0012A-35R-2. **H.** Section 322-C0012A-40R-4. **I.** Section 322-C0012A-45R-3. For information on samples and incubation temperature see Table T23. Note variable time of experiments.

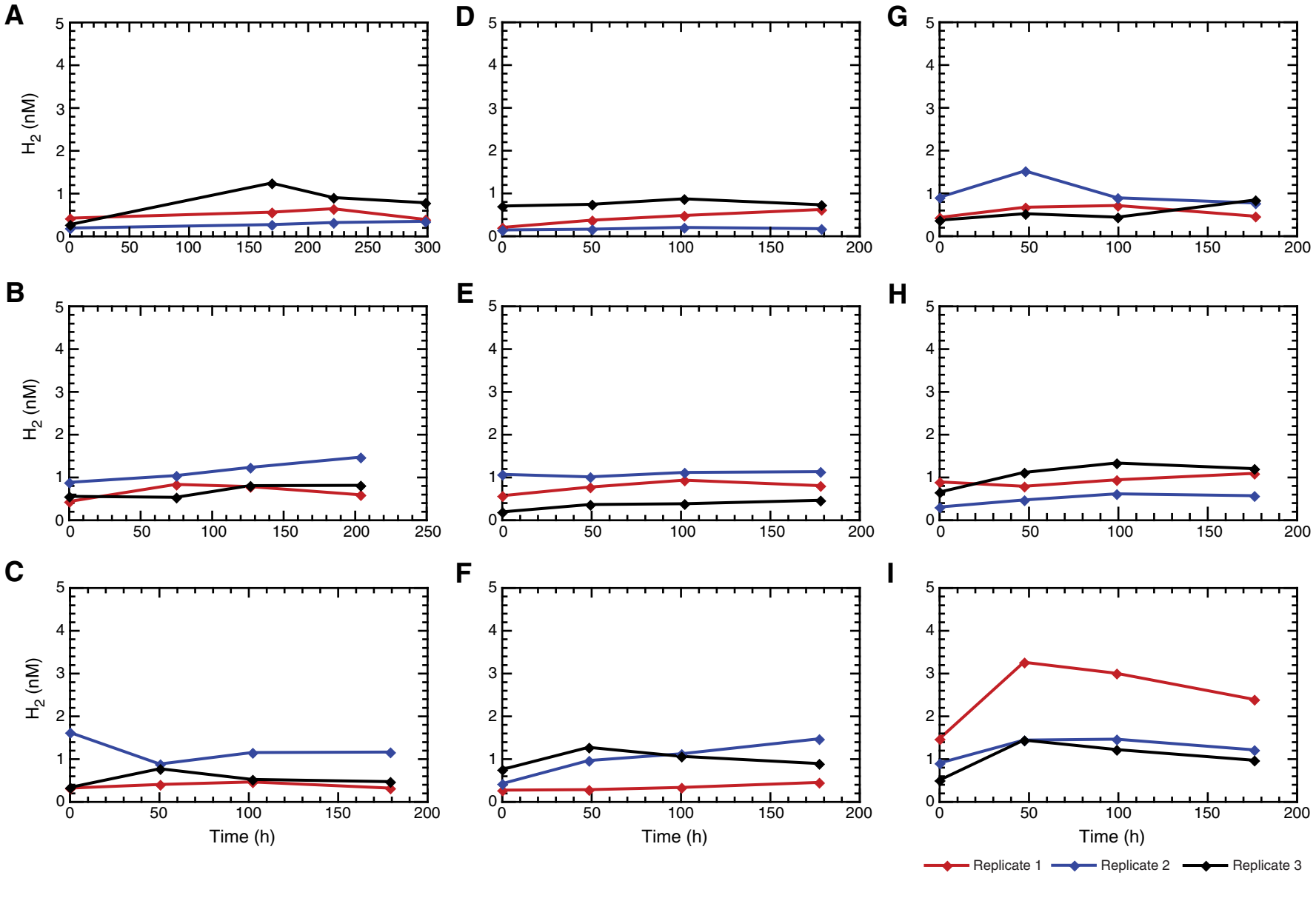

Figure F58. Depth profiles of the type and maturity of organic matter by Rock-Eval pyrolysis, Hole C0012A. T_{max} = temperature at which the maximum release of hydrocarbons from cracking of kerogen occurs during pyrolysis, S_2 = amount of hydrocarbons (HC) generated through thermal cracking of nonvolatile organic matter, S_3 = amount of CO_2 produced during pyrolysis of kerogen, HI = hydrogen index, OI = oxygen index, TOC = total organic carbon.

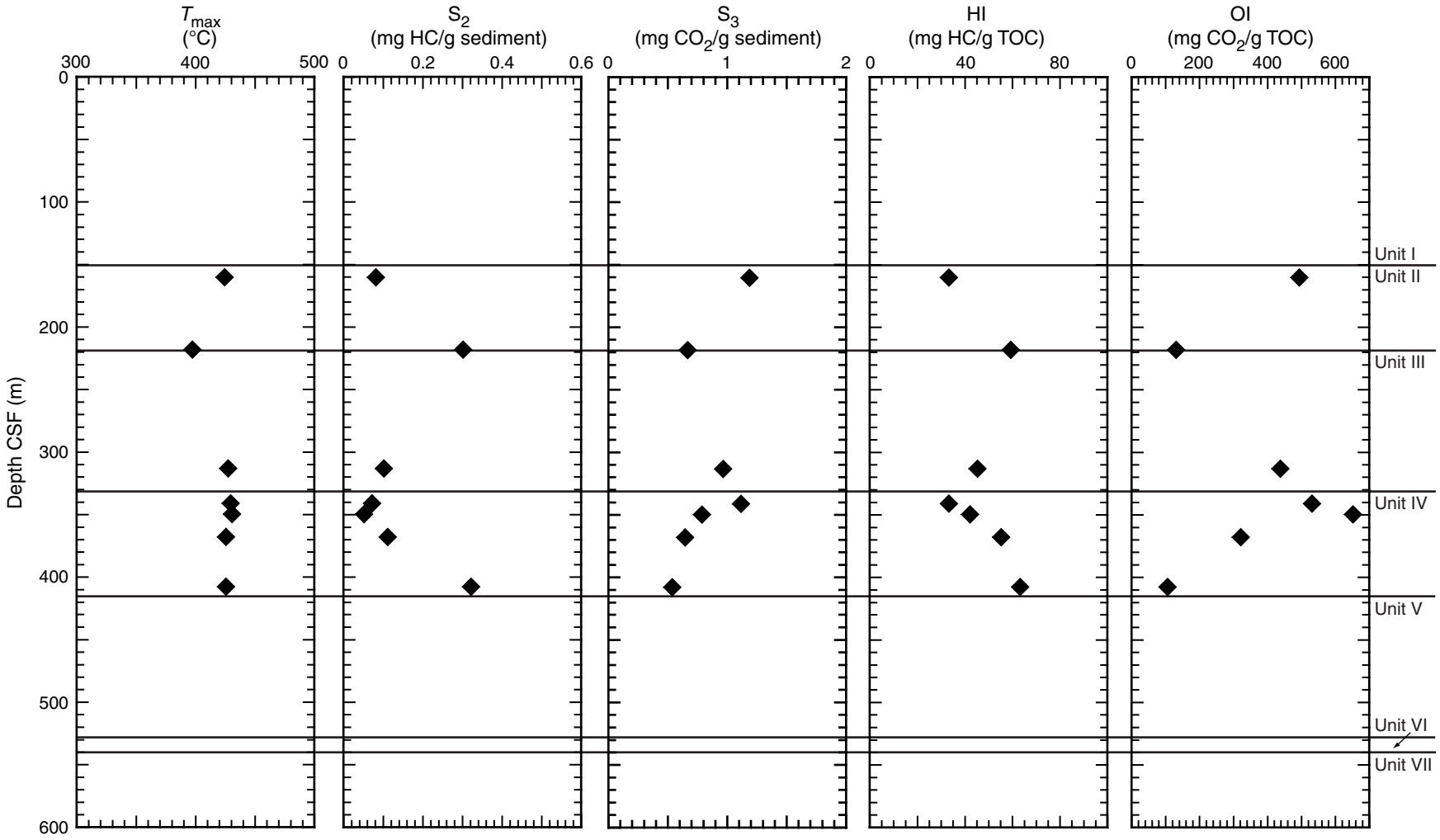

Figure F59. 3-D PSDM seismic reflection profile along Cross-line 435, Site C0012. **A.** Uninterpreted. **B.** Interpreted. VE = vertical exaggeration.

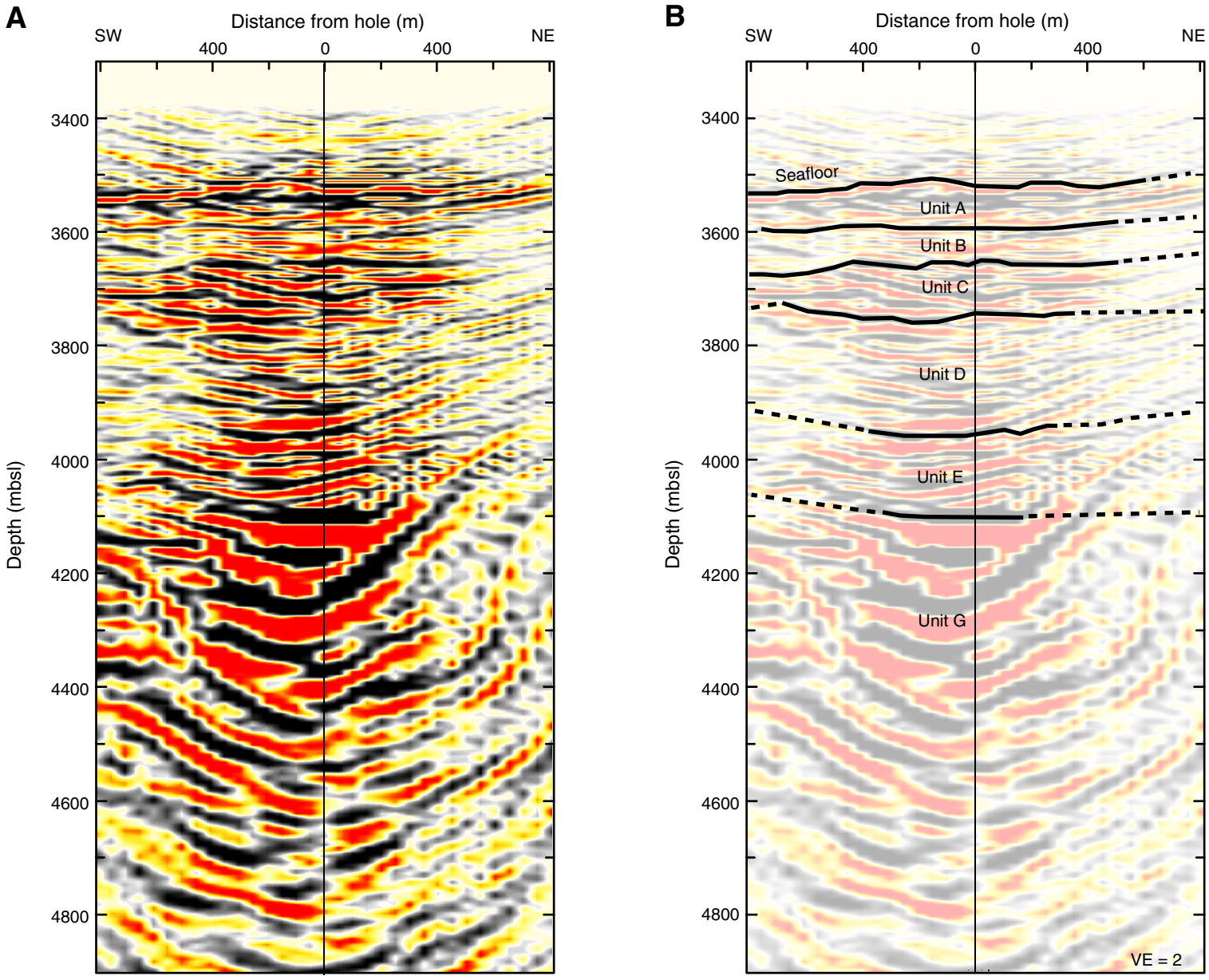

Table T1. Coring summary, Site C0012. (See table note.) (Continued on next page.)

Hole C0012A
Latitude: 32°44.888′N
Longitude: 136°55.024′E
Seafloor (DRF, m): 3539.0
Distance between rig floor and sea level (m): 28.3
Water depth (m): 3510.7
Total depth (DRF, m): 4115.0
Total penetration (CSF, m): 576.0
Total length of cored section (m): 576.0
Total core recovered (m): 206.95
Core recovery (%): 35.9
Total number of cores: 58

Hole C0012B
Latitude: 32°44.888′N
Longitude: 136°55.024′E
Seafloor (DRF, m): 3539.0
Distance between rig floor and sea level (m): 28.3
Water depth (m): 3510.7
Total depth (DRF, m): 4110.0
Total penetration (CSF, m): 571.0
Total length of cored section (m): 0
Total core recovered (m): NA
Core recovery (%): NA
Total number of cores: NA

Core	Date (2009)	Local time (h)	Depth DRF (m) Top	Depth DRF (m) Bottom	Depth CSF (m) Top	Depth CSF (m) Bottom	Advanced (m)	Recovered (m)	Recovery (%)
322-C0012A-									
1R	26 Sep	0020	3539.0	3599.0	0.0	60.0	60.0	0.84	1.4
2R	26 Sep	0315	3599.0	3608.5	60.0	69.5	9.5	4.40	46.3
3R	26 Sep	0540	3608.5	3618.0	69.5	79.0	9.5	2.32	24.4
4R	26 Sep	0809	3618.0	3627.5	79.0	88.5	9.5	1.82	19.2
5R	26 Sep	1018	3627.5	3637.0	88.5	98.0	9.5	4.54	47.8
6R	26 Sep	1232	3637.0	3641.0	98.0	102.0	4.0	3.82	95.5
7R	26 Sep	1500	3641.0	3650.5	102.0	111.5	9.5	5.94	62.5
8R	26 Sep	1710	3650.5	3660.0	111.5	121.0	9.5	7.54	79.4
9R	26 Sep	1910	3660.0	3669.5	121.0	130.5	9.5	8.00	84.2
10R	26 Sep	2145	3669.5	3679.0	130.5	140.0	9.5	7.29	76.7
11R	27 Sep	0016	3679.0	3688.5	140.0	149.5	9.5	8.75	92.1
12R	27 Sep	0248	3688.5	3698.0	149.5	159.0	9.5	1.73	18.2
13R	27 Sep	0511	3698.0	3707.5	159.0	168.5	9.5	4.22	44.4
14R	27 Sep	0747	3707.5	3717.0	168.5	178.0	9.5	3.58	37.7
15R	27 Sep	1010	3717.0	3726.5	178.0	187.5	9.5	3.09	32.5
16R	27 Sep	1231	3726.5	3736.0	187.5	197.0	9.5	4.01	42.2
17R	27 Sep	1443	3736.0	3745.5	197.0	206.5	9.5	3.60	37.9
18R	27 Sep	1650	3745.5	3754.7	206.5	215.7	9.2	2.14	23.3
19R	27 Sep	1915	3754.7	3764.2	215.7	225.2	9.5	5.00	52.6
20R	27 Sep	2127	3764.2	3773.7	225.2	234.7	9.5	4.63	48.7
21R	27 Sep	2354	3773.7	3783.2	234.7	244.2	9.5	3.58	37.7
22R	28 Sep	0302	3783.2	3792.7	244.2	253.7	9.5	3.21	33.8
23R	28 Sep	0528	3792.7	3802.2	253.7	263.2	9.5	6.41	67.5
24R	28 Sep	0802	3802.2	3811.7	263.2	272.7	9.5	5.84	61.5
25R	28 Sep	1038	3811.7	3821.2	272.7	282.2	9.5	7.20	75.8
26R	28 Sep	1332	3821.2	3830.7	282.2	291.7	9.5	2.65	27.9
27R	28 Sep	1622	3830.7	3840.2	291.7	301.2	9.5	3.89	40.9
28R	28 Sep	1847	3840.2	3849.7	301.2	310.7	9.5	3.53	37.2
29R	28 Sep	2145	3849.7	3859.2	310.7	320.2	9.5	3.24	34.1
30R	29 Sep	0048	3859.2	3868.7	320.2	329.7	9.5	0.00	0.0
31R	29 Sep	0400	3868.7	3878.2	329.7	339.2	9.5	3.66	38.5
32R	29 Sep	0651	3878.2	3887.7	339.2	348.7	9.5	4.23	44.5
33R	29 Sep	1109	3887.7	3896.0	348.7	357.0	8.3	4.78	57.6
34R	29 Sep	1410	3896.0	3905.5	357.0	366.5	9.5	3.63	38.2
35R	29 Sep	1654	3905.5	3915.0	366.5	376.0	9.5	4.54	47.8
36R	29 Sep	1943	3915.0	3924.5	376.0	385.5	9.5	3.95	41.6
37R	30 Sep	0004	3924.5	3934.0	385.5	395.0	9.5	1.45	15.3
38R	30 Sep	0346	3934.0	3943.5	395.0	404.5	9.5	2.27	23.9
39R	30 Sep	0707	3943.5	3953.0	404.5	414.0	9.5	3.63	38.2
40R	30 Sep	1005	3953.0	3962.5	414.0	423.5	9.5	6.01	63.3
41R	30 Sep	1318	3962.5	3972.0	423.5	433.0	9.5	6.28	66.1
42R	30 Sep	1626	3972.0	3981.5	433.0	442.5	9.5	3.32	34.9

Table T1 (continued).

Core	Date (2009)	Local time (h)	Depth DRF (m) Top	Depth DRF (m) Bottom	Depth CSF (m) Top	Depth CSF (m) Bottom	Advanced (m)	Recovered (m)	Recovery (%)
43R	30 Sep	1857	3981.5	3991.0	442.5	452.0	9.5	5.14	54.1
44R	30 Sep	2101	3991.0	4000.5	452.0	461.5	9.5	3.34	35.2
45R	1 Oct	0002	4000.5	4010.0	461.5	471.0	9.5	4.48	47.2
46R	1 Oct	0314	4010.0	4019.5	471.0	480.5	9.5	3.39	35.7
47R	1 Oct	0649	4019.5	4029.0	480.5	490.0	9.5	1.49	15.7
48R	1 Oct	1139	4029.0	4038.5	490.0	499.5	9.5	1.51	15.9
49R	1 Oct	1410	4038.5	4048.0	499.5	509.0	9.5	1.63	17.2
50R	1 Oct	1643	4048.0	4057.5	509.0	518.5	9.5	1.61	16.9
51R	1 Oct	2017	4057.5	4067.0	518.5	528.0	9.5	0.26	2.7
52R	1 Oct	2305	4067.0	4076.5	528.0	537.5	9.5	2.31	24.3
53R	2 Oct	0236	4076.5	4082.3	537.5	543.3	5.8	1.75	30.2
54R	2 Oct	0531	4082.3	4087.3	543.3	548.3	5.0	1.83	36.6
55R	2 Oct	0950	4087.3	4092.3	548.3	553.3	5.0	0.80	16.0
56R	2 Oct	1234	4092.3	4095.3	553.3	556.3	3.0	0.94	31.3
57R	2 Oct	1534	4095.3	4099.0	556.3	560.0	3.7	0.96	25.9
58R	3 Oct	0100	4099.0	4115.0	560.0	576.0	16.0	0.95	5.9

Note: DRF = drilling depth below rig floor, CSF = core depth below seafloor.

Table T2. Summary of lithologic units, Site C0012. (See table note.)

Unit	Unit name	Core, section, interval (cm) Top	Core, section, interval (cm) Bottom	Depth CSF (m) Top	Depth CSF (m) Bottom	Thickness (m)	Dominant lithology	Minor lithology
I	Upper Shikoku Basin	322-C0012A-1R-1, 0	322-C0012A-12R-2, 43	0.00	150.86	150.86	Silty clay(stone)	Ash
II	Middle Shikoku Basin	12R-2, 43	19R-4, 83	150.86	219.81	68.95	Silty claystone	Volcaniclastic sandstone Clayey siltstone
III	Lower Shikoku Basin hemipelagites	19R-4, 83	31R-4, 74	219.81	331.81	112.00	Silty claystone	Lime mudstone Calcareous claystone
IV	Lower Shikoku Basin turbidites	31R-4, 74	40R-2, 27	331.81	415.58	83.77	Silty claystone Clayey siltstone	Siltstone
V	Volcaniclastic-rich	40R-2, 27	52R-1, 51	415.58	528.51	112.93	Silty claystone Sandstone (incl. volcaniclastic)	Tuff
VI	Pelagic claystone	52R-1, 51	53R-1, 31	528.51	537.81	9.30	Red calcareous claystone	—
VII	Basement	53R-1, 31	58R-CC	537.81	576.00	38.19	Basalt	—

Note: — = not available.

Table T3. Results of bulk powder X-ray diffraction analysis, Site C0012. (See table note.) (Continued on next two pages.)

Core, section, interval (cm)	Depth CSF (m)	Measured values of X-ray diffraction peaks: Peak intensity (counts/step) Clay minerals	Quartz	Feldspar	Calcite	Integrated peak area (total counts) Clay minerals	Quartz	Feldspar	Calcite	Abundance calculated from SVD normalization factors: Absolute (wt%) Clay minerals	Quartz	Feldspar	Calcite	Total	Relative (wt%) Clay minerals	Quartz	Feldspar	Calcite
322-C0012A-																		
Unit I																		
1R-1, 62	0.62	35	462	86	42	3,584	16,920	7,493	2,265	40.2	9.1	8.4	0.1	57.8	70	16	15	Tr
2R-4, 28	64.13	46	888	142	26	4,495	34,080	9,591	1,052	49.9	18.9	10.2	0.1	79.1	63	24	13	Tr
3R-1, 72	70.22	44	738	117	130	3,908	25,901	9,684	5,831	44.7	14.2	10.9	3.6	73.4	61	19	15	5
3R-2, 25	80.26	55	707	134	159	4,153	28,126	11,512	6,520	48.4	15.4	13.2	4.2	81.2	60	19	16	5
5R-2, 25	89.68	49	800	138	77	4,529	31,325	11,815	4,115	52.1	17.2	13.4	0.6	83.3	63	21	16	1
5R-3, 42	90.31	40	548	129	25	3,770	29,049	11,082	1,814	44.1	16.0	12.7	0.1	72.9	60	22	17	Tr
5R-5, 18	92.49	40	519	119	143	4,309	26,434	10,843	6,957	49.6	14.4	12.3	4.7	81.0	61	18	15	6
6R-3, 10	100.45	56	786	154	59	4,906	31,872	12,312	2,798	56.1	17.4	13.9	0.1	87.6	64	20	16	Tr
6R-4, 66	101.34	57	600	141	40	5,955	24,799	13,321	2,212	67.5	13.1	15.4	0.1	96.1	70	14	16	Tr
6R-4, 71	101.39	55	779	158	45	5,040	31,477	12,730	1,806	57.7	17.2	14.5	0.1	89.5	65	19	16	Tr
7R-5, 108	107.84	55	683	127	50	5,057	28,859	10,337	2,963	56.3	15.7	11.3	0.1	83.5	67	19	14	Tr
8R-3, 30	114.62	55	714	122	251	5,422	26,241	9,832	10,388	60.0	14.2	10.6	8.4	93.2	64	15	11	9
8R-3, 108	115.40	53	713	137	237	5,857	25,921	10,186	9,027	64.5	13.9	11.0	6.3	95.7	67	15	11	7
8R-5, 0	116.62	57	859	138	150	5,168	30,441	11,123	6,104	58.1	16.6	12.3	2.8	89.8	65	19	14	3
8R-6, 47	117.33	69	761	113	255	4,874	26,381	10,051	9,111	54.7	14.3	11.1	7.1	87.2	63	16	13	8
9R-4, 0	124.03	70	835	131	64	6,240	30,585	10,844	2,900	68.3	16.5	11.6	0.1	96.6	71	17	12	0
9R-5, 59	124.86	63	811	144	44	5,700	31,013	12,143	2,272	63.9	16.8	13.5	0.1	94.3	68	18	14	0
9R-6, 30	125.98	53	716	109	255	4,958	25,378	8,315	11,665	54.4	13.8	8.7	10.5	87.4	62	16	10	12
10R-2, 41	132.03	56	711	135	150	5,853	25,521	11,039	5,824	65.0	13.6	12.2	2.1	92.9	70	15	13	2
10R-3, 44.5	132.62	60	807	136	25	6,781	29,826	12,152	1,850	74.6	15.9	13.3	0.1	103.9	72	15	13	Tr
10R-5, 35	134.39	64	756	127	59	6,190	27,281	10,924	2,825	68.0	14.6	11.9	0.1	94.6	72	15	13	Tr
10R-5, 92	134.96	56	772	125	273	5,333	27,146	9,711	10,549	59.0	14.7	10.4	8.7	92.8	64	16	11	9
10R-6, 0	135.44	51	697	141	79	4,295	28,025	9,729	4,431	48.4	15.4	10.7	1.4	76.0	64	20	14	2
11R-3, 24	142.89	66	752	314	31	5,512	30,517	22,769	1,824	69.8	16.1	28.2	0.1	114.1	61	14	25	Tr
11R-4, 0	144.03	66	857	130	29	6,340	31,450	11,793	1,948	69.9	17.0	12.8	0.1	99.8	70	17	13	Tr
11R-5, 107	145.37	69	859	143	25	6,568	30,681	10,607	1,445	71.3	16.5	11.2	0.1	99.2	72	17	11	Tr
11R-6, 113	146.64	56	794	118	49	6,205	29,830	10,804	2,208	68.0	16.1	11.6	0.1	95.7	71	17	12	Tr
11R-7, 79	147.69	33	818	337	29	3,231	27,352	24,154	1,215	48.3	14.5	30.9	0.1	93.8	51	15	33	Tr
11R-7, 132	148.22	38	480	133	85	3,165	17,434	10,533	3,992	38.3	9.3	12.7	2.0	62.3	62	15	20	3
12R-1, 31	149.81	72	834	132	28	6,618	30,551	11,145	1,597	72.2	16.4	11.9	0.1	100.7	72	16	12	Tr
														Average:	65	17	15	3
Unit II																		
13R-2, 25	159.89	57	792	133	91	5,479	28,922	10,753	4,272	60.9	15.7	11.8	0.3	88.6	69	18	13	Tr
13R-3, 68	160.81	42	1,172	1,251	40	3,115	37,932	57,656	2,420	71.1	19.3	76.4	0.1	166.9	43	12	46	Tr
13R-3, 88	161.01	31	763	888	61	3,187	25,598	51,143	3,330	67.7	12.4	68.0	0.1	148.2	46	8	46	Tr
13R-5, 28	162.77	59	743	200	161	5,079	28,277	12,778	6,761	58.5	15.3	14.7	3.7	92.2	63	17	16	4
14R-2, 0	169.69	60	761	149	42	4,982	30,982	12,905	2,700	57.3	16.9	14.8	0.1	89.1	64	19	17	Tr
14R-3, 85	170.83	60	645	138	65	5,652	29,045	10,735	3,954	62.5	15.7	11.7	0.1	90.1	69	17	13	Tr
14R-4, 22	171.52	36	494	337	64	3,537	18,692	11,228	3,408	42.4	10.0	13.5	0.9	66.7	64	15	20	1
15R-3, 0	180.09	38	551	103	301	3,054	21,914	8,257	23,239	36.2	12.1	9.3	27.1	84.7	43	14	11	32
16R-3, 0	189.03	66	894	140	26	6,358	33,460	11,346	2,048	69.7	18.2	12.1	0.1	100.1	70	18	12	Tr
16R-4, 68	189.99	46	413	100	32	3,722	27,226	9,198	1,724	42.3	15.0	10.2	0.1	67.7	63	22	15	Tr
16R-5, 12	190.85	63	776	136	53	5,815	30,911	11,099	2,755	64.3	16.8	12.1	0.1	93.2	69	18	13	Tr
17R-1, 28	197.28	57	628	126	28	4,874	26,488	12,982	1,442	56.5	14.2	15.1	0.1	86.0	66	17	18	Tr
17R-2, 45	198.65	59	899	175	25	5,347	34,596	13,867	1,610	61.4	18.9	15.8	0.1	96.3	64	20	16	Tr
17R-3, 27	199.09	66	831	150	27	6,116	30,871	12,119	2,088	68.0	16.7	13.4	0.1	98.1	69	17	14	Tr
17R-4, 17	199.28	56	533	133	127	5,496	22,006	11,937	5,553	62.3	11.6	13.7	2.1	89.6	69	13	15	2
18R-2, 48	208.38	78	770	124	29	6,882	27,592	10,246	1,681	74.3	14.7	10.7	0.1	99.9	74	15	11	Tr
19R-1, 79	216.49	80	959	146	24	6,322	33,879	12,559	1,423	70.2	18.4	13.8	0.1	102.4	69	18	13	Tr
19R-2, 51	217.56	74	774	119	22	6,649	28,361	9,807	848	71.6	15.2	10.2	0.1	97.1	74	16	10	Tr
19R-3, 12	217.70	64	788	134	35	6,091	30,394	12,152	1,684	67.8	16.4	13.5	0.1	97.7	69	17	14	Tr
19R-4, 17	219.15	80	689	111	38	7,548	25,650	10,421	2,431	81.2	13.4	10.9	0.1	105.6	77	13	10	Tr
														Average:	65	16	17	2
Unit III																		
19R-4, 122	220.20	66	585	116	28	6,136	30,675	10,132	1,713	66.7	16.6	10.7	0.1	94.1	71	18	11	Tr
20R-3, 0	227.50	69	918	126	23	6,861	32,980	9,373	1,142	73.2	17.9	9.3	0.1	100.5	73	18	9	Tr
20R-4, 16	228.00	87	717	108	25	7,115	25,363	9,354	1,548	76.1	13.4	9.6	0.1	99.1	77	14	10	Tr
20R-4, 100	228.84	72	878	115	22	7,292	31,355	9,373	1,613	77.6	16.9	9.2	0.1	103.8	75	16	9	Tr
20R-5, 14	229.38	110	53	47	34	14,697	1,941	3,316	1,780	147.8	0.1	0.2	0.1	148.2	100	0	0	Tr
20R-5, 20	229.44	67	807	110	24	6,629	28,897	9,434	1,629	71.2	15.5	9.6	0.1	96.4	74	16	10	Tr

Table T3 (continued). (Continued on next page.)

Core, section, interval (cm)	Depth CSF (m)	Measured values of X-ray diffraction peaks: Peak intensity (counts/step) Clay minerals	Quartz	Feldspar	Calcite	Integrated peak area (total counts) Clay minerals	Quartz	Feldspar	Calcite	Abundance calculated from SVD normalization factors: Absolute (wt%) Clay minerals	Quartz	Feldspar	Calcite	Total	Relative (wt%) Clay minerals	Quartz	Feldspar	Calcite
21R-1, 23	234.93	50	350	85	26	4,621	23,042	8,092	1,346	50.6	12.5	8.7	0.1	71.8	70	17	12	Tr
21R-2, 30	235.69	89	843	110	26	7,972	30,913	9,402	1,810	84.3	16.5	9.1	0.1	110.1	77	15	8	Tr
21R-3, 38	236.10	120	85	158	46	13,609	5,099	9,927	4,109	141.8	0.4	9.4	0.1	151.8	93	0	6	Tr
21R-3, 105	236.77	69	676	105	28	6,556	29,791	9,460	1,517	70.4	16.1	9.7	0.1	96.2	73	17	10	Tr
21R-CC, 20	238.29	22	87	9	1,562	1,608	3,340	292	78,363	19.3	2.0	0.1	101.1	122.4	16	2	0	83
22R-1, 109	245.29	58	637	121	30	5,583	29,095	9,820	1,385	61.1	15.8	10.5	0.1	87.4	70	18	12	Tr
23R-2, 45	255.52	73	729	123	35	6,418	33,322	11,381	1,913	70.3	18.1	12.2	0.1	100.6	70	18	12	Tr
23R-3, 45	256.55	72	848	143	35	6,116	33,251	11,279	2,325	67.3	18.1	12.1	0.1	97.6	69	19	12	Tr
23R-5, 91	258.75	75	852	146	28	6,647	30,821	11,284	1,320	72.6	16.6	12.1	0.1	101.4	72	16	12	Tr
23R-6, 43	259.51	70	731	124	24	6,258	30,508	9,330	1,633	67.3	16.5	9.5	0.1	93.5	72	18	10	Tr
24R-1, 48	263.68	58	622	112	21	4,805	26,574	9,214	1,130	53.0	14.5	10.0	0.1	77.6	68	19	13	Tr
24R-2, 0	263.93	86	785	110	49	6,880	28,868	10,986	3,040	74.8	15.4	11.7	0.1	102.1	73	15	11	Tr
24R-3, 48	264.76	60	669	124	28	6,073	32,579	9,218	1,631	65.3	17.8	9.3	0.1	92.6	71	19	10	Tr
24R-4, 98	266.67	74	754	129	29	6,474	32,096	10,506	1,706	70.3	17.4	11.0	0.1	98.8	71	18	11	Tr
24R-5, 132	268.36	84	331	95	28	9,885	12,348	9,352	2,024	104.1	5.3	9.4	0.1	118.9	88	4	8	Tr
25R-1, 110	273.80	70	815	168	26	6,559	35,576	12,657	2,051	72.5	19.3	13.8	0.1	105.7	69	18	13	Tr
25R-2, 25	274.17	71	786	158	26	6,057	36,627	12,365	1,573	67.3	20.0	13.5	0.1	100.9	67	20	13	Tr
25R-5, 22	276.99	71	869	144	30	7,031	31,750	11,060	1,819	76.2	17.1	11.6	0.1	105.0	73	16	11	Tr
25R-6, 57	278.70	72	795	138	29	6,751	31,703	11,087	2,007	73.5	17.1	11.7	0.1	102.4	72	17	11	Tr
26R-2, 100	284.61	69	762	129	31	7,634	30,773	12,202	1,846	83.1	16.4	13.1	0.1	112.6	74	15	12	Tr
27R-2, 0	292.04	72	739	122	53	6,638	29,229	10,456	3,428	72.1	15.7	11.0	0.1	98.9	73	16	11	Tr
27R-3, 8	292.45	76	737	130	22	6,686	31,421	12,226	1,294	73.6	16.9	13.3	0.1	104.0	71	16	13	Tr
27R-3, 88.5	293.26	71	741	122	27	6,552	27,724	11,005	1,722	71.6	14.8	11.9	0.1	98.4	73	15	12	Tr
27R-4, 16	293.62	69	799	129	107	6,418	31,545	12,170	4,564	71.1	17.0	13.3	0.1	101.5	70	17	13	Tr
27R-5, 48	295.30	71	819	130	32	6,506	32,541	12,089	1,926	71.7	17.6	13.1	0.1	102.6	70	17	13	Tr
28R-2, 10	302.26	72	886	127	22	6,905	33,637	10,958	1,909	74.8	18.2	11.4	0.1	104.5	72	17	11	Tr
29R-1, 49	311.19	65	764	158	61	6,585	30,575	13,560	3,219	73.7	16.4	15.2	0.1	105.4	70	16	14	Tr
29R-2, 13	312.23	63	776	158	73	6,242	29,033	14,790	3,943	71.3	15.5	17.1	0.1	104.0	69	15	16	Tr
29R-3, 0	312.57	61	910	155	55	6,212	33,599	12,347	2,687	69.0	18.2	13.5	0.1	100.9	68	18	13	Tr
31R-1, 40.5	330.11	70	700	181	48	6,520	30,325	15,019	2,951	74.1	16.2	17.3	0.1	107.7	69	15	16	Tr
31R-2, 38	330.54	82	819	140	40	6,801	34,758	12,182	2,358	74.6	18.8	13.1	0.1	106.6	70	18	12	Tr
31R-3, 0	330.59	81	758	152	34	6,902	30,208	13,456	1,653	76.7	16.1	15.0	0.1	107.9	71	15	14	Tr
31R-4, 64	331.71	59	773	155	33	5,680	31,718	13,497	2,057	64.6	17.2	15.4	0.1	97.2	66	18	16	Tr
														Average:	71	15	11	2
Unit IV																		
31R-5, 70	333.09	75	795	139	53	6,135	33,667	12,057	2,744	68.0	18.3	13.1	0.1	99.6	68	18	13	Tr
32R-1, 8	339.28	72	728	133	22	7,257	28,038	12,589	1,767	79.7	14.8	13.8	0.1	108.5	74	14	13	Tr
32R-2, 41	340.54	57	827	158	130	5,269	31,581	14,206	5,703	61.2	17.1	16.4	2.1	96.9	63	18	17	2
32R-3, 23	341.05	73	839	117	53	6,526	32,574	10,729	2,746	71.0	17.7	11.3	0.1	100.0	71	18	11	Tr
32R-CC, 8	343.22	50	172	51	521	4,668	6,512	3,684	38,238	50.2	3.1	3.2	46.2	102.7	49	3	3	45
33R-2, 0	349.21	82	339	74	108	8,945	12,811	7,558	4,038	93.6	5.8	7.2	0.1	106.6	88	5	7	Tr
33R-4, 26	351.28	59	802	119	159	5,468	35,260	10,933	6,989	60.7	19.4	11.7	3.6	95.4	64	20	12	4
33R-5, 12	352.39	69	869	125	27	6,209	37,984	11,686	1,760	68.2	20.8	12.4	0.1	101.6	67	21	12	Tr
33R-5, 80	353.07	68	886	143	28	6,261	36,940	12,656	2,256	69.5	20.2	13.8	0.1	103.6	67	19	13	Tr
34R-1, 23	357.23	64	737	144	48	5,810	29,873	13,068	2,120	65.7	16.1	14.8	0.1	96.7	68	17	15	Tr
34R-1, 72	357.72	61	877	132	32	5,875	33,080	10,560	2,228	64.4	18.1	11.2	0.1	93.7	69	19	12	Tr
34R-3, 0	359.54	61	790	136	74	5,536	34,892	12,769	3,423	62.6	19.1	14.2	0.1	96.0	65	20	15	Tr
35R-2, 65	367.46	59	758	149	39	6,144	33,452	13,000	2,327	68.8	18.1	14.5	0.1	101.5	68	18	14	Tr
36R-2, 34	376.51	63	684	105	26	5,783	32,361	9,192	1,286	62.4	17.7	9.4	0.1	89.6	70	20	10	Tr
36R-3, 29	376.82	67	610	112	34	6,976	26,381	9,571	2,539	74.9	14.0	9.8	0.1	98.8	76	14	10	Tr
37R-1, 44	385.94	66	929	139	28	5,455	34,317	11,086	1,671	60.5	18.8	12.0	0.1	91.4	66	21	13	Tr
37R-2, 0	386.30	57	749	133	93	5,066	32,682	9,998	4,573	56.1	18.0	10.7	0.9	85.6	66	21	12	1
38R-1, 95	395.95	62	848	127	26	5,752	33,546	10,398	1,692	63.0	18.4	11.0	0.1	92.4	68	20	12	Tr
39R-1, 2	404.52	72	841	101	36	6,702	30,886	9,636	2,095	72.0	16.7	9.8	0.1	98.5	73	17	10	Tr
39R-1, 107	405.57	69	719	94	21	6,219	29,413	8,521	905	66.4	15.9	8.5	0.1	90.9	73	18	9	Tr
39R-1, 118	405.68	59	716	98	28	5,524	30,367	8,822	2,063	59.7	16.6	9.0	0.1	85.5	70	19	11	Tr
39R-2, 37	406.23	63	959	136	25	5,256	37,650	10,385	1,712	57.9	20.9	10.9	0.1	89.7	64	23	12	Tr
39R-2, 73	406.59	70	788	82	32	6,054	29,604	7,304	2,312	63.9	16.1	6.8	0.1	87.0	73	19	8	Tr
39R-3, 35	407.25	63	748	92	28	5,446	30,707	8,626	1,384	58.8	16.8	8.8	0.1	84.5	70	20	10	Tr
40R-1, 21	414.21	74	848	101	22	7,234	32,302	8,493	2,336	76.3	17.5	8.0	0.1	101.9	75	17	8	Tr
														Average:	69	18	11	2
Unit V																		
40R-3, 26	416.98	66	609	121	31	7,212	25,092	9,684	1,959	77.3	13.2	10.0	0.1	100.6	77	13	10	Tr

Table T3 (continued).

Core, section, interval (cm)	Depth CSF (m)	Measured values of X-ray diffraction peaks: Peak intensity (counts/step)				Measured values of X-ray diffraction peaks: Integrated peak area (total counts)				Abundance calculated from SVD normalization factors: Absolute (wt%)					Abundance calculated from SVD normalization factors: Relative (wt%)			
		Clay minerals	Quartz	Feldspar	Calcite	Clay minerals	Quartz	Feldspar	Calcite	Clay minerals	Quartz	Feldspar	Calcite	Total	Clay minerals	Quartz	Feldspar	Calcite
40R-4, 30	417.71	62	398	88	38	6,440	22,022	8,924	2,463	69.3	11.5	9.3	0.1	90.3	77	13	10	Tr
40R-5, 24	418.34	70	93	98	48	9,007	5,163	7,508	4,687	94.5	1.3	7.4	0.1	103.4	91	1	7	Tr
40R-5, 45	418.55	65	699	104	77	6,629	28,423	8,848	3,678	70.9	15.3	8.9	0.1	95.1	75	16	9	Tr
41R-1, 23	423.73	65	713	130	101	5,795	27,957	11,437	4,571	64.5	15.0	12.7	0.4	92.7	70	16	14	Tr
41R-2, 0	424.88	73	590	108	27	7,977	24,327	10,242	1,696	85.3	12.6	10.6	0.1	108.6	79	12	10	Tr
41R-3, 0	426.07	68	755	107	27	7,286	30,276	8,979	2,016	77.3	16.3	8.8	0.1	102.4	75	16	9	Tr
41R-4, 38	426.89	82	738	107	32	7,792	29,374	9,699	1,956	82.9	15.6	9.6	0.1	108.2	77	14	9	Tr
41R-CC, 12	429.75	22	178	43	1,390	1,802	6,580	3,398	66,262	22.8	3.7	3.6	85.0	114.9	20	3	3	74
42R-2, 29	434.24	54	841	117	21	5,406	28,933	10,723	1,495	60.0	15.7	11.8	0.1	87.6	69	18	13	Tr
42R-3, 18	434.84	65	804	145	26	6,450	30,972	12,413	1,779	71.5	16.7	13.7	0.1	101.9	70	16	13	Tr
42R-3, 76	435.42	41	1,681	374	19	3,969	56,404	29,576	980	58.2	31.3	36.7	0.1	126.3	46	25	29	Tr
43R-1, 114	443.64	25	2,333	456	15	1,836	74,506	38,502	720	42.7	41.9	48.7	0.1	133.4	32	31	37	Tr
43R-2, 85	444.75	66	817	156	29	5,849	36,828	15,638	2,548	67.6	20.1	18.0	0.1	105.8	64	19	17	Tr
43R-4, 41	446.40	65	661	113	27	6,338	27,527	10,602	1,751	69.2	14.7	11.4	0.1	95.4	73	15	12	Tr
44R-1, 16	452.16	47	1,611	346	20	3,819	54,836	27,009	935	54.9	30.5	33.3	0.1	118.8	46	26	28	Tr
44R-1, 94	452.94	71	746	115	31	6,279	34,634	11,103	1,633	68.7	18.9	11.8	0.1	99.4	69	19	12	Tr
44R-2, 0	453.26	64	846	134	26	6,070	32,010	12,406	2,014	67.7	17.3	13.7	0.1	98.8	68	18	14	Tr
45R-2, 22	463.03	52	1,686	588	53	3,851	65,337	49,347	3,289	71.1	35.7	63.5	0.1	170.3	42	21	37	Tr
45R-2, 74	463.55	53	1,057	245	30	5,883	46,811	17,749	1,649	69.0	25.8	20.4	0.1	115.3	60	22	18	Tr
45R-3, 46	464.55	51	1,308	260	16	4,126	51,150	21,381	1,042	54.0	28.5	25.7	0.1	108.3	50	26	24	Tr
45R-4, 76	465.55	34	2,056	550	19	3,227	66,400	45,119	1,182	61.7	36.6	57.8	0.1	156.2	40	23	37	Tr
46R-2, 0	471.36	54	1,266	198	19	4,850	44,178	17,111	1,222	58.4	24.5	20.0	0.1	102.9	57	24	19	Tr
46R-3, 109	473.02	65	627	122	25	5,397	27,987	11,380	2,135	60.5	15.1	12.7	0.1	88.4	68	17	14	Tr
46R-CC, 37	474.45	35	88	126	1,077	3,051	4,181	5,251	63,934	36.5	2.0	5.9	81.0	125.3	29	2	5	65
47R-2, 30	481.07	79	523	150	111	7,265	25,197	13,241	5,076	80.6	13.1	14.8	0.1	108.6	74	12	14	Tr
47R-3, 10	481.22	66	740	91	272	6,944	27,520	9,151	10,289	74.5	14.7	9.2	7.1	105.6	71	14	9	7
48R-1, 10	490.10	51	420	105	577	4,968	17,501	9,535	23,993	56.3	9.2	10.7	26.8	103.0	55	9	10	26
48R-2, 0	490.52	49	380	84	567	4,357	14,934	7,342	23,396	48.7	7.8	8.0	26.6	91.2	53	9	9	29
49R-2, 37	500.30	64	525	101	103	6,730	20,426	9,868	4,535	73.0	10.5	10.6	0.1	94.2	77	11	11	Tr
49R-3, 22	500.54	67	509	116	27	5,944	22,303	11,296	1,835	66.1	11.7	12.7	0.1	90.6	73	13	14	Tr
50R-2, 40	509.69	70	249	101	38	7,313	13,156	9,873	2,255	79.0	6.2	10.8	0.1	96.1	82	6	11	Tr
50R-3, 50	510.21	52	472	85	130	5,105	23,017	8,720	6,303	56.0	12.4	9.4	3.4	81.2	69	15	12	4
51R-1, 10	518.60	64	538	87	158	6,511	21,348	7,191	6,430	68.9	11.2	6.9	2.7	89.8	77	13	8	3
														Average:	63	16	15	6
Unit VI																		
52R-2, 32	529.52	52	368	82	425	4,951	16,989	5,375	18,921	52.9	9.0	5.1	20.4	87.3	61	10	6	23

Note: SVD = singular value decomposition, Tr = trace.

Table T4. Results of XRF analysis, Hole C0012A. (See table note.) (Continued on next page.)

Core, section, interval (cm)	Depth CSF (m)	Oxide abundance (wt%)											
		SiO_2	Al_2O_3	Fe_2O_3	Na_2O	MgO	CaO	K_2O	MnO	Ti_2O	P_2O_5	LOI	Total
322-C0012A-													
1R-1, 62	0.62	67.03	14.78	4.88	4.09	1.70	2.04	2.87	0.093	0.520	0.082	7.03	98.07
2R-4, 28	64.13	63.26	17.60	6.88	3.14	2.77	0.97	3.39	0.059	0.732	0.102	6.63	98.91
3R-1, 72	70.22	60.76	17.08	6.59	3.25	2.76	4.33	3.07	0.117	0.744	0.100	8.42	98.80
4R-2, 25	80.26	60.80	17.38	6.25	2.78	2.73	4.17	3.29	0.187	0.725	0.082	8.09	98.39
5R-2, 25	89.68	62.41	17.40	6.10	2.80	2.54	2.37	3.38	0.437	0.713	0.099	7.07	98.24
6R-3, 10	100.45	63.25	17.44	6.43	2.81	2.62	2.00	3.36	0.262	0.689	0.087	6.62	98.94
6R-4, 66	101.34	61.85	17.26	7.89	2.87	2.96	1.62	3.13	0.237	0.720	0.087	6.76	98.62
7R-5, 108	107.84	62.93	16.93	7.37	2.67	2.68	1.79	3.35	0.205	0.685	0.086	6.28	98.69
8R-3, 30	114.62	60.42	16.97	6.01	2.68	2.50	5.66	3.02	0.257	0.688	0.102	8.80	98.30
8R-5, 0	116.62	62.79	17.12	5.98	2.72	2.37	3.22	3.22	0.291	0.691	0.095	7.22	98.50
9R-4, 0	124.03	64.02	17.21	5.96	2.90	2.49	1.98	3.38	0.116	0.714	0.081	6.45	98.86
9R-6, 30	125.98	58.82	15.77	5.81	2.71	2.38	8.16	2.96	0.559	0.639	0.253	10.54	98.06
10R-3, 45	132.62	64.35	16.90	6.57	2.84	2.49	1.05	3.29	0.149	0.700	0.082	5.69	98.42
10R-6, 0	135.44	63.86	16.47	6.04	2.78	2.49	2.71	3.32	0.281	0.688	0.083	6.77	98.71
11R-4, 0	144.03	64.50	17.04	6.16	2.72	2.50	1.21	3.29	0.245	0.724	0.090	5.61	98.47
11R-7, 79	147.69	62.96	15.82	9.47	3.29	1.45	3.15	1.67	0.059	0.567	0.096	6.05	98.53
11R-7, 132	148.22	53.85	14.62	6.25	2.73	2.41	6.53	2.29	8.708	0.583	0.274	13.26	98.24
12R-1, 31	149.81	64.91	17.17	6.11	2.80	2.48	1.22	3.29	0.124	0.739	0.079	10.76	98.92
13R-2, 25	159.89	63.76	16.23	6.17	2.78	2.36	2.92	3.21	0.520	0.686	0.095	19.75	98.73
13R-5, 28	162.77	62.50	16.85	5.77	2.55	2.53	4.06	2.99	0.159	0.637	0.089	7.63	98.13
14R-2, 0	169.69	65.07	16.66	6.04	2.82	2.30	1.55	3.36	0.099	0.669	0.082	5.62	98.65
14R-4, 22	171.52	58.35	15.51	4.85	2.97	1.79	6.35	1.49	0.371	0.643	0.423	5.84	92.74
15R-3, 0	180.09	53.76	13.70	5.37	2.06	2.06	16.60	2.30	1.531	0.554	0.359	15.22	98.29
16R-3, 0	189.03	64.05	16.76	6.16	2.56	2.37	1.01	3.40	0.286	0.694	0.089	5.78	97.37
17R-2, 45	198.65	66.03	16.91	5.71	2.54	2.30	0.92	3.34	0.067	0.693	0.078	6.14	98.57
17R-3, 27	199.09	65.63	16.84	5.85	2.68	2.29	1.18	3.32	0.072	0.672	0.080	5.09	98.61
18R-2, 48	208.38	65.08	17.26	6.68	2.50	2.35	0.99	3.13	0.074	0.713	0.082	5.15	98.85
19R-2, 51	217.56	64.13	18.03	6.57	2.41	2.49	0.84	3.26	0.077	0.702	0.083	2.92	98.57
19R-3, 12	217.70	64.56	17.40	6.31	2.75	2.32	1.55	2.73	0.083	0.695	0.080	5.93	98.47
20R-3, 0	227.50	65.71	17.62	6.11	2.27	2.40	0.77	3.45	0.094	0.752	0.088	5.01	99.27
20R-5, 20	229.44	64.54	17.45	6.47	2.44	2.54	1.12	3.27	0.168	0.685	0.093	4.90	98.78
21R-2, 30	235.69	64.94	17.46	6.24	2.53	2.59	0.89	3.18	0.079	0.664	0.083	4.96	98.66
21R-3, 38	236.10	62.76	19.82	5.93	2.90	3.25	1.80	0.74	0.128	0.176	0.064	6.60	97.58
22R-1, 109	245.29	64.75	17.04	6.78	2.27	2.51	0.90	3.37	0.165	0.710	0.089	5.08	98.59
23R-3, 45	256.55	64.83	17.27	6.33	2.18	2.44	1.27	3.46	0.149	0.731	0.083	5.24	98.73
23R-5, 91	258.75	64.78	17.21	6.60	2.10	2.40	0.82	3.44	0.124	0.722	0.077	4.66	98.27
24R-2, 0	263.93	64.17	17.62	6.32	2.19	2.46	1.60	3.42	0.187	0.725	0.086	5.50	98.78
24R-5, 132	268.36	63.37	18.65	7.60	2.47	2.57	1.60	1.60	0.107	0.709	0.053	5.90	98.74
25R-2, 25	274.17	65.84	16.71	6.05	2.24	2.20	0.94	3.26	0.097	0.709	0.085	4.71	98.13
25R-6, 57	278.70	65.38	16.59	6.18	2.31	2.26	1.07	3.26	0.273	0.709	0.095	4.95	98.13
26R-2, 81	284.42	64.79	16.71	6.42	2.09	2.30	1.61	3.07	0.155	0.735	0.080	5.29	97.97
27R-2, 0	292.04	64.47	16.93	6.23	2.13	2.42	2.14	3.22	0.231	0.687	0.088	5.83	98.54
27R-3, 89	293.26	64.44	16.97	6.73	2.20	2.37	1.34	3.33	0.156	0.711	0.093	5.56	98.33
28R-2, 10	302.26	65.95	16.81	6.19	2.20	2.20	1.01	3.28	0.177	0.720	0.082	4.86	98.61
29R-2, 13	312.23	63.86	17.05	6.47	2.31	2.29	2.58	3.12	0.134	0.690	0.092	5.76	98.59
29R-3, 0	312.57	65.11	16.73	6.02	2.17	2.22	1.73	3.19	0.110	0.696	0.083	5.33	98.06
31R-3, 0	330.59	64.37	17.48	6.90	2.16	2.29	1.24	3.32	0.150	0.779	0.081	4.89	98.76
31R-4, 105	332.12	19.84	4.48	2.38	0.83	0.69	47.49	0.24	4.573	0.185	19.872	17.09	100.57
32R-2, 41	340.54	63.48	16.58	5.92	2.15	2.17	3.52	3.13	0.146	0.706	0.111	6.60	97.92
32R-CC, 8	343.22	43.99	12.58	5.79	1.48	1.65	27.27	1.00	3.427	0.508	1.420	20.28	99.11
33R-2, 0	349.21	63.02	17.60	7.48	2.28	2.53	3.39	1.65	0.169	0.707	0.068	7.94	98.89
33R-4, 26	351.28	65.71	15.07	5.10	2.13	1.97	5.32	2.76	0.209	0.610	0.190	7.91	99.06
34R-1, 72	357.72	65.14	17.00	6.17	2.03	2.23	1.53	3.24	0.141	0.721	0.100	5.44	98.28
34R-3, 0	359.54	64.83	16.79	6.17	1.98	2.22	2.47	3.24	0.139	0.710	0.082	6.28	98.62
35R-2, 65	367.46	66.38	16.39	5.78	2.28	2.07	1.89	2.90	0.117	0.724	0.094	5.48	98.62
36R-2, 34	376.51	65.33	16.96	6.31	1.98	2.14	1.24	3.22	0.271	0.708	0.113	5.48	98.26
37R-2, 0	386.30	63.11	17.27	6.52	1.95	2.13	2.91	3.24	0.089	0.752	0.120	6.68	98.09
38R-1, 95	395.95	63.37	19.01	6.67	1.57	2.09	1.00	3.53	0.052	0.826	0.114	5.59	98.22
39R-1, 2	404.52	65.50	17.45	6.29	1.90	2.15	1.35	3.19	0.091	0.759	0.083	5.12	98.77
39R-1, 107	405.57	62.71	19.07	7.34	1.43	2.10	1.10	3.39	0.064	0.837	0.085	6.74	98.12
39R-3, 35	407.25	62.83	18.96	7.45	1.48	2.12	1.06	3.42	0.059	0.823	0.099	6.46	98.31
40R-4, 30	417.71	63.45	17.69	7.46	2.06	2.20	2.19	2.67	0.067	0.677	0.077	5.93	98.54
40R-5, 24	418.34	59.68	19.15	10.55	2.06	2.05	3.00	0.64	0.066	0.419	0.049	7.99	97.65
41R-3, 0	426.07	65.76	16.80	6.78	1.82	2.30	1.53	2.92	0.077	0.727	0.101	5.08	98.82
41R-CC, 12	429.75	30.87	8.25	3.74	0.90	1.15	50.32	1.09	4.369	0.331	0.143	29.78	101.16
42R-2, 29	434.24	63.40	15.87	9.62	2.13	2.00	1.53	2.93	0.080	0.658	0.107	6.65	98.30
42R-3, 96	435.62	69.02	12.97	8.14	2.44	1.20	1.58	2.75	0.079	0.554	0.064	12.15	98.79

Table T4 (continued).

Core, section, interval (cm)	Depth CSF (m)	Oxide abundance (wt%)											
		SiO_2	Al_2O_3	Fe_2O_3	Na_2O	MgO	CaO	K_2O	MnO	Ti_2O	P_2O_5	LOI	Total
43R-1, 7	442.57	73.26	13.57	3.95	2.28	1.27	1.39	2.78	0.048	0.503	0.071	4.05	99.12
43R-1, 32	442.82	75.15	12.32	2.95	2.48	0.86	1.53	2.72	0.032	0.370	0.057	2.52	98.45
43R-4, 41	446.40	65.49	17.50	6.23	1.54	2.39	1.51	3.09	0.077	0.660	0.075	5.60	98.57
43R-5, 23	446.65	69.73	13.44	6.86	2.34	1.28	1.55	2.66	0.065	0.600	0.069	10.13	98.59
44R-2, 0	453.26	66.59	17.23	5.68	1.83	2.17	1.54	3.31	0.070	0.757	0.118	4.87	99.31
45R-3, 46	464.55	71.00	14.91	3.91	2.33	1.49	1.28	2.96	0.047	0.650	0.087	3.66	98.66
46R-2, 0	471.36	67.93	15.33	4.62	2.14	1.63	1.24	3.18	0.055	0.717	0.092	4.51	96.92
46R-CC, 37	474.45	38.38	9.64	2.73	1.25	1.33	42.12	0.50	2.875	0.292	0.131	27.20	99.24
47R-2, 30	481.07	64.64	14.71	7.12	1.78	2.43	4.44	2.51	0.147	0.623	0.144	6.59	98.54
48R-1, 10	490.10	56.75	13.97	7.13	1.84	2.61	12.46	2.69	0.509	0.643	0.113	12.31	98.71
49R-2, 37	500.30	62.47	15.80	7.30	1.87	2.99	3.90	3.24	0.235	0.707	0.151	6.75	98.66
50R-2, 40	509.69	63.09	17.50	6.17	1.92	4.20	2.79	1.97	0.274	0.551	0.080	8.32	98.54
51R-1, 10	518.60	61.99	15.49	7.49	1.26	3.70	4.41	3.31	0.209	0.591	0.140	8.39	98.59
52R-1, 39	528.39	76.25	12.24	2.19	2.64	0.90	1.45	3.07	0.057	0.416	0.047	2.31	99.25
52R-1, 114	529.14	54.64	13.80	8.66	1.20	2.96	13.20	3.25	0.277	0.528	0.184	12.74	98.70
52R-2, 32	529.52	53.69	13.83	8.09	1.21	2.88	13.74	3.43	0.331	0.583	0.220	13.21	98.00

Note: LOI = loss on ignition.

Table T5. Summary of stratigraphic relations at Site C0012 and correlation with equivalent units in ODP sites and IODP Site C0011. (See table note.)

Unit	Unit name	Core, section, interval (cm) Top	Core, section, interval (cm) Bottom	Depth CSF (m) Top	Depth CSF (m) Bottom	Thickness (m)	Stratigraphic age	Lithologic description	Processes of formation	Stratigraphic correlation Site 808	Site 1173	Site 1174	Site 1177	Site C0011
I	Upper Shikoku Basin	322-C0012A-1R-1, 0	322-C0012A-12R-2, 43	0.00	150.86	150.86	Pleistocene–late Miocene (0 to 7.8 Ma)	Silty claystone and ash layers	Hemipelagic and air fall pyroclastic deposition	Subunit IVa	Unit II	Unit III	Unit I	Unit I
II	Middle Shikoku Basin	12R-2, 43	19R-4, 83	150.86	219.81	68.95	late Miocene (7.8–9.4 Ma)	Silty claystone and volcaniclastic sandstone	Hemipelagic settling and volcaniclastic turbidity currents in submarine fan system	NA	NA	NA	NA	Unit II
III	Lower Shikoku Basin hemipelagites	19R-4, 83	31R-4, 74	219.81	331.81	112.00	late–middle Miocene (9.4–12.7 Ma)	Silty claystone and lime mudstone	Hemipelagic settling	Subunit IVb	Unit III	Unit IV	Unit II	Unit III
IV	Lower Shikoku Basin turbidites	31R-4, 74	40R-2, 27	331.81	418.29	86.48	middle Miocene (12.7–13.5 Ma)	Silty claystone, clayey siltstone, and siltstone	Hemipelagic settling and terrigenous turbidity currents in submarine fan system	NA	NA	NA	Unit III	Unit IV
V	Volcaniclastic-rich	40R-2, 27	52R-1, 51	415.58	528.51	112.93	middle Miocene (13.5 to ≥18.9 Ma)	Silty claystone, sandstone (incl. volcaniclastic sandstone), and tuff	Hemipelagic settling, turbidity currents, and air fall pyroclastic deposition	Unit V	Unit IV	Unit V	Unit IV	Unit V
VI	Pelagic claystone	52R-1, 51	53R-1, 31	528.51	537.81	9.30	middle–early Miocene (≥18.9 Ma)	Red calcareous claystone	Pelagic settling	Unit VI	Unit V	NA	NA	NA
VII	Basement	53R-1, 31	58R-CC	537.81	576.00	38.19	early Miocene (>18.9 Ma)	Basalt	Igneous/Volcanic activity	Unit VI	Unit V	NA	Unit V	NA

Note: NA = not available.

Table T6. Paleomagnetic and biostratigraphic age datums, Hole C0012A (Model B). This table is available in an **oversized format.**

Table T7. Distribution of calcareous nannofossils, Site C0012. This table is available in an **oversized format.**

Table T8. Distribution of planktonic foraminifers, Hole C0012A. (See table notes.) (Continued on next page.)

Core, section, interval (cm)	Sample code	Depth CSF (m)	Abundance	Preservation	*Candeina nitida*	*Dentoglobigerina altispira*	*Dentoglobigerina altispira globosa*	*Globigerina connecta*	*Globigerina falconensis*	*Globigerina globularis*	*Globigerinella obesa*	*Globigerinita glutinata*	*Globigerinoides bollii*	*Globigerinoides bulloides*	*Globigerinoides conglobatus*	*Globigerinoides druryi*	*Globigerinoides elongatus*	*Globigerinoides immaturus*	*Globigerinoides kennetti*	*Globigerinoides quadrilobatus*	*Globigerinoides ruber*	*Globigerinoides sacculifer*	*Globigerinoides seigliei*	*Globigerinoides subquadratus*	*Globigerinoides triloba*	*Globigerinoita morugaensis*	*Globoconella* cf. *conoidea*	*Globoconella conomiozea*	*Globoquadrina dehiscens*	*Globoquadrina venezuelana*	*Globorotalia birnageae*	*Globorotalia continuosa*	*Globorotalia fohsi lobata*	*Globorotalia fohsi periphroronda*	*Globorotalia fohsi praefohsi*	*Globorotalia lenguaensis*	*Globorotalia mayeri*	*Globorotalia menardii "A"*	*Globorotalia merotumida*	*Globorotalia miozea*	*Globorotalia plesiotumida*	*Globorotalia praemenardii*	*Globorotalia praescitula*	*Globorotalia scitula*
322-C0012A-																																											
1R-CC, 2–7	PAL	0.71	R	G										+							+																						
2R-CC, 0–5	PAL	64.41	R	G								+																															
3R-CC, 0–5	PAL	71.69	R	G	+	+								+											+			+															
4R-CC, 14–19	PAL	80.79	C	G		+						+		+	+										+																	
6R-CC, 10.5–15.5	PAL	101.84	R	G										+	+																											
7R-CC, 10–15	PAL	107.95	C	G		+					+	+	+	+					+		+						+												+			
8R-CC, 10.5–15.5	PAL	119.02	R	G								+	+												+																+	
9R-CC, 0–5	PAL	131.36	R	G								+	+																												+	
10R-CC, 7.5–12.5	PAL	137.79	R	G								+	+												+													+			+	
11R-CC, 19–24	PAL	148.77	R	G		+							+	+											+																+	
12R-CC, 15–20	PAL	151.19	C	G							+	+	+									+			+		+													+	
13R-CC, 11–16	PAL	163.17	A	G			R															R			R															+	
14R-CC, 16–21	PAL	172.04	C	M		+						+		+											+														+			
15R-CC, 18.5–23.5	PAL	181.12	R	M			+		+					+						+					+		+		+					+					+		
17R-CC, 10.5–15.5	PAL	200.62	R	M						+	+		+	+									+		+														+		
19R-CC, 0–5	PAL	220.67	R	G						+		+		+											+				+		+			+	+	+					
23R-CC, 17–22	PAL	260.16	R	G			+							+										+				+			+										
24R-CC, 16.5–21.5	PAL	269.05	A	G								+	+	+			R							R	A			+			A		+				+			+	
25R-CC, 17–22	PAL	279.92	R	M			+										+							+																	
27R-CC, 4.5–9.5	PAL	295.54	R	M								+		+						+													+								
28R-CC, 15.5–20.5	PAL	304.73	R	M									+	+										+																	
29R-CC, 10–15	PAL	313.99	C	G			+		+		+	R	R	+		+		+						+	+				+			+		+	+	+			+	
31R-CC, 2–7	PAL	333.32	R	G			+					+		+						+					+				+	+			+		+	+				+	
32R-CC, 20–25	PAL	343.36	C	G							+	+						+		+			+	+	+	+			+	+		+			+					
33R-CC, 18.5–23.5	PAL	353.46	R	G												+															+										
34R-4, 63–68	PALW	360.63	R	G																			+		+																
35R-CC, 10–15	PAL	371.04	R	G			+					+												+	+	+					+	+	+							+	
36R-CC, 0–1	PAL	378.04	R	M								+	+			+				+						+					+	+									
37R-CC, 0–5	PAL	386.91	R	M													+																								
38R-CC, 14.5–19.5	PAL	397.22	R	M								+								+						+													+		
40R-CC, 4–9	PAL	419.93	R	P																									+										+		
48R-CC, 11–16	PAL	491.51	R	P		+		+								+										+			+												
49R-CC, 8.5–13.5	PAL	501.15	R	P				+																		+															
52R-CC, 7–12	PAL	530.32	R	P												+										+						+									

Notes: PAL = paleontologic sample, PALW = whole-round paleontologic sample. Abundance: A = abundant, C = common, R = rare, + = present. Preservation: G = good, M = medium, P = poor. Barren: 322-C0012A-5R-CC, 17.5–20.5 cm; 16R-CC, 16–21 cm; 18R-CC, 15–20 cm; 20R-CC, 6–11 cm; 21R-CC, 12–17 cm; 22R-CC, 20–25 cm; 26R-CC, 4–9 cm; 39R-CC, 5–10 cm; 41R-CC, 16–21 cm; 42R-CC, 15.5–20.5 cm; 43R-CC, 0–5 cm; 44R-CC, 12–17 cm; 45R-CC, 5–10 cm; 46R-CC, 0–5 cm; 47R-CC, 18–23 cm. No samples: 30R-CC; 50R-CC; 51R-CC.

Table T8 (continued).

Core, section, interval (cm)	Sample code	Depth CSF (m)	Abundance	Preservation	*Globorotalia siakensis*	*Globoturborotalita decoraperta*	*Globoturborotalita extremus*	*Globoturborotalita nepenthes*	*Globoturborotalita obliquus*	*Globoturborotalita woodi*	*Hastigerina praesiphonifera*	*Hirsutella margaritae*	*Menardella miocenica*	*Menardella pseudomiocenica*	*Neogloboquadrina acostaensis*	*Neogloboquadrina dutertrei*	*Neogloboquadrina humerosa*	*Neogloboquadrina pachyderma* dextral form	*Orbulina bilobata*	*Orbulina suturalis*	*Orbulina universa*	*Praeorbulina glomerosa curva*	*Sphaeroidinellopsis disjuncta*	*Sphaeroidinellopsis seminulina*	*Truncorotalia quinqueloba*
322-C0012A-																									
1R-CC, 2–7	PAL	0.71	R	G												+					+				
2R-CC, 0–5	PAL	64.41	R	G					+						+			+			+			+	
3R-CC, 0–5	PAL	71.69	R	G																				+	
4R-CC, 14–19	PAL	80.79	C	G			+					+		+		+	+	+		+	+			+	+
6R-CC, 10.5–15.5	PAL	101.84	R	G					+											+	+				
7R-CC, 10–15	PAL	107.95	C	G					+	+		+							+	+	+			+	
8R-CC, 10.5–15.5	PAL	119.02	R	G		+		+		+														+	
9R-CC, 0–5	PAL	131.36	R	G					+															+	
10R-CC, 7.5–12.5	PAL	137.79	R	G		+		+							+						+				
11R-CC, 19–24	PAL	148.77	R	G					+						+		+								
12R-CC, 15–20	PAL	151.19	C	G		+			+	+					+		+				+				
13R-CC, 11–16	PAL	163.17	A	G				+	R	+			+		+						+			+	
14R-CC, 16–21	PAL	172.04	C	M					+	+															
15R-CC, 18.5–23.5	PAL	181.12	R	M						+											+				
17R-CC, 10.5–15.5	PAL	200.62	R	M						+											+				
19R-CC, 0–5	PAL	220.67	R	G																				+	
23R-CC, 17–22	PAL	260.16	R	G						+										+		+			
24R-CC, 16.5–21.5	PAL	269.05	A	G	+					+									+	+	+			+	
25R-CC, 17–22	PAL	279.92	R	M																					
27R-CC, 4.5–9.5	PAL	295.54	R	M																					
28R-CC, 15.5–20.5	PAL	304.73	R	M						+															
29R-CC, 10–15	PAL	313.99	C	G	+					R								+		+	+	+			
31R-CC, 2–7	PAL	333.32	R	G						+									+					+	
32R-CC, 20–25	PAL	343.36	C	G	+														+	+					+
33R-CC, 18.5–23.5	PAL	353.46	R	G																	+				
34R-4, 63–68	PALW	360.63	R	G																					
35R-CC, 10–15	PAL	371.04	R	G	+																				
36R-CC, 0–1	PAL	378.04	R	M																+	+				
37R-CC, 0–5	PAL	386.91	R	M																			+		
38R-CC, 14.5–19.5	PAL	397.22	R	M					+																
40R-CC, 4–9	PAL	419.93	R	P							+														
48R-CC, 11–16	PAL	491.51	R	P																					
49R-CC, 8.5–13.5	PAL	501.15	R	P																					
52R-CC, 7–12	PAL	530.32	R	P																					

Table T9. Calcareous nannofossil events and absolute age, Hole C0012A. (See table notes.)

Nannofossil zone	Calcareous nannofossil event	Age (Ma)				Core, section, interval (cm)		Depth CSF (m)			Error (m)
		Upper	Lower	Middle	Error	Top	Bottom	Top	Bottom	Middle	
						322-C0012A-	322-C0012A-				
NN13/NN12	FO *Ceratolithus cristatus*	5.054	5.12	5.087	0.033	4R-CC, 14–19	5R-CC, 17.5–22.5	80.79	93.05	86.92	6.13
NN12/NN11b	LO *Discoaster quinqueramus*	5.54	5.59	5.565	0.025	4R-CC, 14–19	5R-CC, 17.5–22.5	80.79	93.05	86.92	6.13
PE *R. pseudoumbilicus*	PE *Reticulofenestra pseudoumbilicus*	7.077	7.167	7.122	0.045	7R-5, 40–42	8R-4, 45	107.165	116.175	111.67	4.505
NN11a/NN10b	FO *Discoaster berggrenii*	8.29	8.52	8.405	0.115	17R-1, 41–43	17R-CC, 10.5–15.5	197.42	200.625	199.0225	1.6025
NN10a/NN10b	PB *Reticulofenestra pseudoumbilicus* (>7 µm)	8.761	8.785	8.773	0.012	17R-CC, 10.5–15.5	18R-1, 40–41	200.625	206.905	203.765	3.14
LO *D. hamatus*	LO *Discoaster hamatus*	9.53	9.687	9.6085	0.0785	19R-1, 32–34	21R-3, 7	216.03	235.765	225.8975	9.8675
NN8/NN9	FO *Discoaster hamatus*	10.184	10.549	10.3665	0.1825	21R-3, 7	26R-CC, 4–9	216.03	235.765	225.8975	9.8675
NN8/NN7	FO *Catinaster coalitus*	10.733	10.886	10.8095	0.0765	21R-3, 7	26R-CC, 4–9	216.03	235.765	225.8975	9.8675
LO *C. floridanus*	LO *Cyclicargolithus floridanus*	12.037	12.037	12.037	0	26R-CC, 4–9	27R-3, 67	284.86	293.04	288.95	4.09
NN6/NN5	LO *Sphenolithus heteromorphus*	13.53	13.65	13.59	0.06	40R-2, 61	40R-5, 16	415.915	418.255	417.085	1.17
NN5/NN4	LO *Helicosphaera ampliaperta*	14.914	14.914	14.914	0	48R-CC, 11–16	52R-1, 67	491.515	529.59	510.5525	19.0375
NN3/NN2	FO *Sphenolithus belemnos*	18.921	18.921	18.921	0	48R-CC, 11–16	52R-1, 67	491.515	529.59	510.5525	19.0375
FO *H. ampliaperta*	FO *Helicosphaera ampliaperta*	18.921	20.393	19.657	0.736	52R-1, 67	52R-CC, 7–12	528.67	530.325	529.4975	0.8275

Notes: Age based on Raffi et al. (2006). PE = paracme end, LO = last occurrence, FO = first occurrence, PB = paracme beginning.

Table T10. Planktonic foraminifer events and absolute age, Hole C0012A. (See table notes.)

Planktonic foraminifer event	Core, section, interval (cm)		Depth CSF (m)			Error (m)
	Top	Bottom	Top	Bottom	Middle	
	322-C0012A-	322-C0012A-				
FO *Globigerinoides conglobatus*	6R-CC, 10.5–15.5	7R-CC, 10–15	101.845	107.165	104.505	2.66
FO *Globorotalia plesiotumida*	12R-CC, 15–20	13R-CC, 11–16	151.19	163.175	157.1825	5.9925
FO *Globoturborotalita nepenthes*	13R-CC, 11–16	14R-CC, 16–21	163.175	172.045	167.61	4.435
LO *Paragloborotalia mayeri*	17R-CC, 10.5–15.5	19R-CC, 0–5	200.625	220.695	210.66	10.035
FO *Orbulina universa*	36R-CC, 0–1	37R-CC, 0–5	378.05	386.94	382.495	4.445

Notes: Age based on Lourens et al. (2004). FO = first occurrence, LO = last occurrence.

Table T11. Paleomagnetic and biostratigraphic age datums, Hole C0012A (Model A). This table is available in an oversized format.

Table T12. Paleomagnetic directions used for reorientation of coherent blocks, Site C0012. (See table note.)

Core, section, interval (cm)	Depth CSF (m)	Lithologic unit	Lithology	Characteristic remanent magnetization		
				Declination (°)	Inclination (°)	Maximum angular deviation (°)
322-C0012A-						
8R-4, 43–45	116.17	I	Clay	137.3	–49.4	4.3
9R-2, 106–108	123.47		Clay	90.7	–44.5	4.5
10R-6, 72–74	136.17		Clay	–108.3	60.7	1.6
13R-4, 70–72	162.25	II	Clay	110.4	61.4	2.1
16R-5, 44–46	191.18		Clay	–170.2	54.2	5.2
19R-3, 131–133	218.90		Clay	94.7	60.7	2.6
20R-1, 90–92	226.11	III	Clay	7.5	55.8	1.4
21R-3, 26–28	235.99		Clay	30.2	44.8	8.6
21R-3, 108–110	236.81		Clay	21.5	69.4	2.4
22R-1, 74–76	244.95		Clay	173.6	58.1	6.2
22R-3, 82–84	246.63		Clay	37.1	–60.4	1.1
23R-1, 21–23	253.92		Clay	–84.1	–36.9	3.5
23R-4, 24–26	256.79		Clay	–38.1	61.6	0.9
24R-4, 4–6	265.74		Clay	–140.7	–50.5	3.6
24R-5, 127–129	268.32		Clay	117.5	–62.0	2.9
31R-4, 73–75	331.81		Clay	122.7	63.6	11.3
41R-2, 22–24	425.11	V	Clay	102.5	60.5	5.1
41R-4, 5–7	426.57		Clay	–19.8	55.6	4.6
41R-4, 61–63	427.13		Clay	–41.2	52.7	2.5
41R-5, 71–73	428.66		Clay	126.5	–61.9	4.1
42R-4, 8–10	436.04		Clay	–12.9	73.5	11.8
43R-1, 50–52	443.01		Clay	38.2	52.4	8.9
43R-2, 39–41	444.30		Clay	177.2	68.2	8.4
43R-5, 8–10	446.51		Volcaniclastic sand	9.1	69.4	3.6
44R-3, 10–12	453.81		Clay	35.1	48.9	10.9
45R-2, 96–98	463.78		Sand	–119.2	69.0	3.6
45R-4, 62–64	465.42		Sand	–45.4	66.6	4.8
46R-4, 10–12	473.45		Sand	–104.8	55.2	6.8
48R-2, 41–43	490.94		Clay	–71.7	51.5	0.8
48R-2, 55–57	491.08		Sand	109.2	61.1	12.0
49R-1, 6–8	499.57		Clay	–108.3	66.5	0.9
49R-3, 60–62	500.93		Clay	117.7	–45.6	1.7
50R-3, 77–79	510.49		Clay	129.1	32.7	0.7

Note: Maximum angular deviation calculated from Kirschvink (1980).

Table T13. Paleomagnetic results for basaltic samples. (See table notes.)

Core, section, interval (cm)	Depth CSF (m)	Specimen	Position	Measurement	Treatment	NRM intensity (A/m)	Declination (°)	Inclination (°)	Maximum angular deviation (°)
322-C0012A-									
53R-2, 35–37	538.77	A	Center	Onboard	AFD	1.40E+01	42.4	–28.0	1.8
		B	Rim	Onshore	AFD	2.02E+00	40.5	–44.2	1.8
54R-1, 77–79	543.88	A	Center	Onboard	AFD	2.20E+01	–87.0	–27.1	11.5
		B	Middle	Onshore	ThD	1.87E+01	–87.7	–18.3	1.5
		C	Rim	Onshore	AFD	1.62E+01	–92.2	0.2	1.4
55R-1, 23–25	548.54	A	Center	Onshore	AFD	6.30E+01	–125.5	–32.6	5.5
		B	Rim	Onshore	ThD	3.62E+01	–149.8	–36.9	11.9
57R-1, 44–46	556.75	A	Center	Onshore	AFD	1.13E+01	102.5	–53.5	0.7
		B	Rim	Onshore	ThD	2.68E+01	104.0	–35.0	2.0

Notes: Maximum angular deviation calculated from Kirschvink (1980). AFD = alternating-field demagnetization, ThD = thermal demagnetization.

Table T14. Mudstone MAD data, Hole C0012A. (Continued on next four pages.)

Core, section, interval (cm)	Depth CSF (m)	W_c Wet	W_c Dry	Porosity	Void ratio	Density (g/cm^3) Bulk	Density (g/cm^3) Dry	Density (g/cm^3) Grain
322-C0012A-								
1R-1, 63–64	0.64	0.49	0.97	0.70	2.28	1.45	0.74	2.42
2R-3, 79.5–80.5	63.63	0.46	0.87	0.70	2.30	1.54	0.82	2.71
2R-4, 29–30	64.14	0.45	0.81	0.69	2.24	1.58	0.87	2.82
3R-1, 75–76	70.26	0.44	0.78	0.67	2.06	1.58	0.89	2.72
3R-3, 21–22	71.60	0.46	0.86	0.69	2.27	1.54	0.83	2.70
4R-1, 81–82	79.82	0.39	0.65	0.64	1.76	1.66	1.01	2.78
4R-2, 25–26	80.26	0.38	0.60	0.63	1.69	1.71	1.07	2.87
5R-1, 25–26	88.76	0.45	0.83	0.68	2.15	1.55	0.85	2.67
5R-1, 85–86	89.36	0.43	0.77	0.67	2.06	1.59	0.90	2.75
5R-2, 25–27	89.69	0.38	0.63	0.59	1.46	1.58	0.97	2.39
5R-3, 42–44	90.32	0.43	0.76	0.66	1.97	1.57	0.89	2.66
5R-3, 100–102	90.90	0.37	0.58	0.62	1.64	1.74	1.10	2.91
5R-4, 25–27	91.55	0.36	0.56	0.60	1.48	1.70	1.09	2.71
5R-4, 72–73	92.02	0.38	0.62	0.62	1.64	1.66	1.02	2.70
5R-5, 18–20	92.50	0.39	0.65	0.63	1.67	1.63	0.99	2.65
6R-1, 21–22	98.22	0.43	0.74	0.67	2.07	1.62	0.93	2.86
6R-1, 25–26	98.26	0.45	0.81	0.68	2.10	1.55	0.86	2.67
6R-1, 97–99	98.98	0.44	0.78	0.66	1.92	1.54	0.87	2.54
6R-1, 126–127	99.27	0.36	0.56	0.62	1.61	1.76	1.13	2.96
6R-2, 24–26	99.66	0.40	0.67	0.63	1.72	1.62	0.97	2.63
6R-2, 87–89	100.29	0.35	0.53	0.58	1.40	1.73	1.13	2.71
6R-3, 10–12	100.46	0.37	0.59	0.63	1.73	1.74	1.09	2.98
6R-4, 29–31	100.98	0.35	0.55	0.60	1.50	1.74	1.12	2.81
6R-4, 71–73	101.40	0.36	0.57	0.61	1.53	1.71	1.09	2.76
7R-1, 26–28	102.27	0.39	0.63	0.62	1.66	1.64	1.01	2.67
7R-1, 26–28	102.27	0.46	0.87	0.69	2.20	1.52	0.81	2.60
7R-1, 118–120	103.19	0.39	0.64	0.62	1.63	1.63	0.99	2.62
7R-2, 19–21	103.66	0.39	0.65	0.64	1.80	1.67	1.01	2.83
7R-3, 9–11	104.05	0.38	0.62	0.61	1.59	1.65	1.02	2.63
7R-3, 113–115	105.09	0.41	0.70	0.64	1.75	1.58	0.93	2.57
7R-4, 30–32	105.66	0.38	0.61	0.62	1.63	2.81	0.73	2.74
7R-4, 99–101	106.35	0.39	0.65	0.65	1.82	1.68	1.02	2.88
7R-5, 52–53	107.28	0.44	0.80	0.68	2.14	1.57	0.87	2.74
7R-5, 108–110	107.85	0.37	0.59	0.58	1.36	1.59	1.00	2.35
8R-1, 17–19	111.68	0.39	0.65	0.64	1.76	1.66	1.01	2.78
8R-1, 125–127	112.76	0.34	0.52	0.58	1.41	1.76	1.16	2.79
8R-2, 21–23	113.13	0.34	0.52	0.57	1.34	1.71	1.13	2.64
8R-2, 107–109	113.99	0.37	0.59	0.61	1.53	1.67	1.05	2.65
8R-3, 30–32	114.63	0.39	0.64	0.63	1.67	1.65	1.01	2.69
8R-3, 108–110	115.41	0.37	0.58	0.60	1.53	1.69	1.07	2.69
8R-4, 38–40	116.12	0.34	0.52	0.57	1.30	1.69	1.11	2.55
8R-5, 0–3	116.64	0.35	0.54	0.60	1.51	1.75	1.13	2.84
8R-6, 47–49	117.34	0.36	0.57	0.61	1.59	1.73	1.10	2.84
8R-6, 93–95	117.80	0.33	0.50	0.57	1.32	1.76	1.18	2.74
8R-7, 19–21	118.47	0.38	0.61	0.60	1.53	1.64	1.02	2.58
8R-7, 29–30	118.56	0.36	0.56	0.58	1.36	1.65	1.06	2.49
9R-1, 25–26	121.26	0.37	0.59	0.61	1.55	1.68	1.06	2.70
9R-1, 115–116	122.16	0.38	0.61	0.61	1.53	1.64	1.02	2.57
9R-2, 16–17	122.57	0.39	0.64	0.63	1.74	1.66	1.01	2.76
9R-2, 97–98	123.38	0.38	0.60	0.59	1.44	1.61	1.00	2.46
9R-3, 22–23	123.84	0.37	0.60	0.61	1.55	1.66	1.04	2.64
9R-4, 0–2	124.04	0.40	0.66	0.64	1.78	1.64	0.99	2.74
9R-5, 20–21	124.48	0.37	0.58	0.61	1.56	1.70	1.08	2.77
9R-5, 59–61	124.87	0.39	0.63	0.63	1.72	1.67	1.02	2.79
9R-5, 120–121	125.48	0.38	0.62	0.61	1.57	1.63	1.01	2.59
9R-6, 30–32	125.99	0.40	0.67	0.64	1.78	1.64	0.98	2.73
9R-6, 110–111	126.78	0.38	0.61	0.61	1.56	1.65	1.03	2.64
9R-7, 24–25	127.34	0.41	0.68	0.65	1.90	1.65	0.98	2.84
9R-7, 90–91	128.00	0.39	0.63	0.63	1.67	1.66	1.02	2.73
9R-8, 10–11	128.62	0.41	0.69	0.65	1.88	1.64	0.97	2.81
10R-1, 25–26	130.76	0.36	0.56	0.62	1.61	1.76	1.13	2.95
10R-2, 15–16	131.77	0.37	0.59	0.62	1.62	1.71	1.07	2.81
10R-2, 41–43	132.04	0.42	0.74	0.66	1.90	1.58	0.91	2.64
10R-3, 44.5–46.5	132.63	0.39	0.64	0.61	1.56	1.60	0.98	2.51
10R-4, 50–51	133.14	0.38	0.62	0.62	1.62	1.65	1.02	2.66
10R-4, 124–125	133.88	0.42	0.72	0.64	1.76	1.56	0.91	2.51
10R-5, 35–37	134.40	0.40	0.68	0.62	1.65	1.58	0.94	2.49

Table T14 (continued). (Continued on next page.)

Core, section, interval (cm)	Depth CSF (m)	W_c		Porosity	Void ratio	Density (g/cm^3)		
		Wet	Dry			Bulk	Dry	Grain
10R-5, 92–94	134.97	0.35	0.54	0.61	1.57	1.78	1.15	2.96
10R-6, 0–2	135.45	0.36	0.56	0.59	1.42	1.68	1.08	2.61
10R-6, 27–28	135.72	0.38	0.61	0.61	1.54	1.63	1.01	2.57
10R-6, 110–111	136.55	0.41	0.71	0.65	1.82	1.60	0.94	2.64
10R-7, 29–30	137.15	0.37	0.60	0.60	1.51	1.65	1.03	2.59
11R-1, 21–22	140.22	0.38	0.61	0.61	1.56	1.65	1.02	2.61
11R-1, 100–101	141.01	0.37	0.58	0.62	1.61	1.72	1.08	2.84
11R-2, 20–21	141.45	0.35	0.54	0.57	1.34	1.67	1.08	2.52
11R-2, 103–104	142.28	0.35	0.54	0.59	1.41	1.70	1.10	2.66
11R-3, 24–26	142.90	0.36	0.55	0.59	1.45	1.70	1.09	2.68
11R-3, 103–104	143.69	0.32	0.48	0.54	1.17	1.70	1.15	2.50
11R-4, 0–2	144.04	0.34	0.51	0.59	1.41	1.78	1.18	2.84
11R-5, 16–17	144.46	0.33	0.50	0.57	1.31	1.74	1.16	2.67
11R-5, 107–109	145.38	0.35	0.54	0.58	1.38	1.69	1.09	2.60
11R-6, 25–26	145.77	0.38	0.60	0.61	1.56	1.66	1.04	2.65
11R-6, 113–115	146.65	0.34	0.51	0.57	1.33	1.73	1.15	2.68
11R-7, 25–26	147.15	0.33	0.50	0.56	1.25	1.71	1.14	2.56
11R-7, 100–101	147.90	0.38	0.61	0.63	1.67	1.69	1.05	2.80
11R-8, 26–28	148.35	0.39	0.63	0.60	1.50	1.59	0.98	2.44
12R-1, 25–26	149.76	0.37	0.59	0.61	1.59	1.69	1.06	2.74
12R-1, 86–87	150.37	0.38	0.61	0.63	1.69	1.69	1.05	2.83
12R-2, 50–51	150.93	0.40	0.66	0.61	1.55	1.57	0.95	2.42
13R-1, 36–37	159.37	0.32	0.46	0.54	1.17	1.74	1.19	2.58
13R-2, 25–27	159.90	0.32	0.46	0.56	1.28	1.82	1.24	2.83
13R-4, 46–47	162.00	0.32	0.46	0.55	1.21	1.77	1.21	2.68
13R-5, 16–17	162.66	0.34	0.52	0.57	1.31	1.69	1.11	2.56
14R-1, 30–31	168.81	0.37	0.59	0.62	1.63	1.71	1.08	2.82
14R-1, 102–103	169.53	0.34	0.52	0.58	1.36	1.72	1.13	2.66
14R-2, 0–2	169.70	0.33	0.50	0.56	1.26	1.71	1.14	2.58
14R-3, 25–26	170.23	0.32	0.48	0.56	1.28	1.78	1.20	2.74
14R-3, 85–87	170.84	0.31	0.45	0.54	1.17	1.77	1.22	2.63
15R-1, 25–26	178.26	0.34	0.52	0.56	1.27	1.68	1.11	2.52
15R-1, 98–99	178.99	0.33	0.48	0.55	1.23	1.73	1.17	2.60
15R-2, 25–26	179.66	0.31	0.45	0.54	1.17	1.78	1.23	2.66
15R-3, 0–2	180.10	0.23	0.30	0.44	0.80	1.95	1.50	2.69
15R-4, 20–21	180.58	0.30	0.44	0.53	1.14	1.80	1.25	2.68
16R-1, 25–26	187.76	0.30	0.43	0.52	1.09	1.78	1.24	2.60
16R-1, 87–88	188.38	0.34	0.51	0.55	1.24	1.69	1.12	2.50
16R-2, 25–26	188.68	0.34	0.52	0.59	1.47	1.78	1.17	2.89
16R-3, 0–2	189.04	0.31	0.45	0.55	1.21	1.80	1.24	2.74
16R-4, 16–17	189.47	0.30	0.42	0.52	1.09	1.81	1.27	2.66
16R-4, 68–70	190.00	0.32	0.46	0.54	1.16	1.74	1.19	2.57
16R-5, 12–14.5	190.86	0.33	0.49	0.57	1.31	1.78	1.20	2.77
17R-1, 28–30	197.29	0.31	0.44	0.55	1.23	1.84	1.28	2.85
17R-1, 100–101	198.01	0.29	0.40	0.52	1.09	1.86	1.32	2.77
17R-2, 9–10	198.30	0.28	0.40	0.49	0.96	1.77	1.27	2.48
17R-2, 45–47	198.66	0.28	0.39	0.49	0.97	1.81	1.31	2.58
17R-3, 27–29	199.10	0.29	0.41	0.52	1.06	1.82	1.29	2.66
17R-4, 17–19	199.29	0.33	0.49	0.56	1.26	1.74	1.17	2.65
17R-4, 72–73	199.83	0.26	0.35	0.48	0.94	1.90	1.40	2.71
18R-1, 59–60	207.10	0.28	0.39	0.50	1.02	1.83	1.31	2.64
18R-1, 124–125	207.75	0.27	0.38	0.48	0.93	1.81	1.31	2.54
18R-2, 48–50	208.39	0.33	0.48	0.55	1.24	1.74	1.18	2.63
19R-1, 25–26	215.96	0.31	0.46	0.55	1.20	1.78	1.22	2.68
19R-1, 79–81	216.50	0.27	0.37	0.51	1.02	1.90	1.39	2.80
19R-1, 132–133	217.03	0.29	0.41	0.51	1.04	1.80	0.97	2.61
19R-2, 51–53	217.57	0.30	0.43	0.52	1.09	1.78	1.25	2.61
19R-3, 12–15	217.72	0.29	0.42	0.52	1.07	1.79	1.26	2.61
19R-3, 50–51	218.09	0.29	0.40	0.51	1.04	1.81	1.29	2.63
19R-3, 97–98	218.56	0.29	0.41	0.52	1.07	1.83	1.30	2.68
19R-4, 17–19	219.16	0.29	0.41	0.52	1.09	1.85	1.32	2.75
19R-4, 42–43	219.41	0.28	0.40	0.51	1.03	1.83	1.31	2.65
19R-4, 122–124	220.21	0.29	0.41	0.51	1.06	1.83	1.30	2.68
19R-5, 20–21	220.50	0.28	0.40	0.49	0.97	1.78	1.27	2.51
20R-1, 25–26	225.46	0.31	0.44	0.53	1.14	1.79	1.24	2.65
20R-1, 106–107	226.27	0.26	0.35	0.48	0.93	1.91	1.42	2.74
20R-2, 17–18	226.78	0.27	0.37	0.48	0.93	1.82	1.33	2.57
20R-2, 79–80	227.40	0.25	0.34	0.45	0.83	1.85	1.39	2.54
20R-3, 0–2	227.51	0.26	0.36	0.48	0.93	1.88	1.39	2.67

Table T14 (continued). (Continued on next page.)

Core, section, interval (cm)	Depth CSF (m)	W_c Wet	W_c Dry	Porosity	Void ratio	Density (g/cm^3) Bulk	Density (g/cm^3) Dry	Density (g/cm^3) Grain
20R-4, 16–18	228.01	0.34	0.51	0.60	1.49	1.82	1.20	2.99
20R-4, 100–102	228.85	0.29	0.40	0.52	1.10	1.86	1.32	2.78
20R-4, 128–129	229.12	0.27	0.37	0.48	0.92	1.82	1.33	2.56
20R-5, 20–22	229.45	0.28	0.38	0.51	1.03	1.88	1.36	2.75
21R-1, 23–25	234.94	0.29	0.40	0.52	1.08	1.85	1.32	2.74
21R-1, 62–63	235.33	0.28	0.38	0.51	1.05	1.90	1.38	2.83
21R-2, 30–33	235.70	0.30	0.42	0.52	1.09	1.80	1.27	2.65
21R-3, 23–24	235.95	0.27	0.38	0.49	0.97	1.84	1.34	2.64
21R-3, 105–107	236.78	0.28	0.39	0.49	0.96	1.80	1.30	2.54
21R-4, 25–26	237.30	0.28	0.39	0.50	1.02	1.83	1.32	2.65
21R-4, 100–101	238.05	0.29	0.40	0.50	1.01	1.79	1.28	2.57
22R-1, 24–25	244.45	0.27	0.36	0.50	0.99	1.91	1.40	2.78
22R-1, 109–111	245.30	0.27	0.38	0.51	1.02	1.88	1.37	2.76
22R-3, 20–22	246.01	0.33	0.50	0.57	1.34	1.76	1.18	2.76
22R-3, 101–102	246.82	0.25	0.34	0.46	0.84	1.84	1.37	2.52
23R-1, 25–26	253.96	0.28	0.38	0.46	0.85	1.70	1.24	2.28
23R-1, 96–97	254.67	0.29	0.42	0.51	1.05	1.78	1.26	2.57
23R-2, 45–47	255.53	0.26	0.35	0.47	0.87	1.84	1.37	2.56
23R-2, 99–100	256.06	0.27	0.37	0.50	1.00	1.91	1.40	2.81
23R-3, 41.5–43.5	256.53	0.26	0.35	0.48	0.94	1.92	1.42	2.75
23R-4, 21–22	256.75	0.27	0.37	0.51	1.03	1.95	1.43	2.90
23R-4, 116–117	257.70	0.29	0.41	0.51	1.03	1.79	1.27	2.58
23R-5, 26–28	258.11	0.27	0.37	0.49	0.98	1.86	1.36	2.68
23R-5, 91–93	258.76	0.25	0.34	0.47	0.90	1.90	1.42	2.69
23R-6, 43–45	259.52	0.26	0.35	0.48	0.93	1.91	1.41	2.73
24R-1, 48–50	263.69	0.27	0.36	0.48	0.91	1.84	1.35	2.58
24R-2, 0–2	263.94	0.25	0.34	0.48	0.93	1.93	1.44	2.78
24R-3, 48–50	264.77	0.25	0.34	0.46	0.85	1.85	1.38	2.55
24R-3, 97–98	265.26	0.26	0.34	0.46	0.87	1.86	1.39	2.59
24R-4, 23–24	265.92	0.27	0.37	0.49	0.97	1.86	1.36	2.67
24R-4, 98–100	266.68	0.26	0.35	0.48	0.92	1.91	1.42	2.72
24R-5, 25–26	267.29	0.27	0.36	0.50	0.99	1.92	1.41	2.82
24R-5, 100–101	268.04	0.26	0.35	0.49	0.95	1.93	1.43	2.79
24R-6, 9–10	268.54	0.28	0.39	0.52	1.07	1.90	1.37	2.83
25R-1, 25–26	272.96	0.25	0.34	0.46	0.86	1.85	1.38	2.57
25R-1, 110–112	273.81	0.24	0.32	0.48	0.91	2.01	1.52	2.90
25R-2, 25–27	274.18	0.24	0.31	0.45	0.82	1.94	1.48	2.69
25R-3, 26–27	274.77	0.24	0.31	0.45	0.81	1.92	1.47	2.66
25R-3, 98–99	275.49	0.24	0.31	0.46	0.84	1.96	1.50	2.75
25R-4, 23–24	275.79	0.25	0.34	0.47	0.90	1.92	1.43	2.72
25R-4, 99–100	276.55	0.25	0.34	0.46	0.86	1.88	1.41	2.61
25R-5, 22–24	277.00	0.25	0.33	0.44	0.79	1.81	1.36	2.43
25R-5, 96–97	277.73	0.25	0.34	0.48	0.91	1.92	1.43	2.73
25R-6, 57–59	278.71	0.26	0.34	0.48	0.92	1.92	1.43	2.74
25R-7, 25–26	279.16	0.25	0.34	0.47	0.89	1.91	1.43	2.70
26R-1, 20–21	282.41	0.25	0.34	0.46	0.87	1.90	1.42	2.65
26R-1, 99–100	283.20	0.53	1.14	0.76	3.09	1.45	0.68	2.78
26R-2, 21–22	283.83	0.42	0.73	0.63	1.67	1.51	0.87	2.32
26R-2, 100–102	284.62	0.24	0.32	0.44	0.79	1.86	1.41	2.53
27R-1, 15–16	291.86	0.30	0.42	0.51	1.05	1.77	1.24	2.55
27R-2, 0–2	292.05	0.26	0.34	0.48	0.92	1.91	1.42	2.73
27R-3, 8–11	292.47	0.26	0.35	0.47	0.89	1.86	1.38	2.61
27R-3, 88.5–91	293.27	0.26	0.35	0.47	0.89	1.85	1.36	2.58
27R-4, 16–18	293.63	0.26	0.35	0.48	0.91	1.90	1.41	2.69
27R-5, 24–25	295.06	0.40	0.66	0.58	1.38	1.49	0.90	2.14
27R-5, 48–50	295.31	0.25	0.33	0.46	0.86	1.90	1.43	2.65
28R-1, 24–25	301.45	0.57	1.33	0.78	3.45	1.39	0.60	2.65
28R-1, 89–90	302.10	0.25	0.33	0.46	0.85	1.88	1.41	2.60
28R-2, 10–12	302.27	0.24	0.32	0.47	0.88	1.99	1.51	2.85
28R-3, 19–20	302.81	0.26	0.35	0.49	0.95	1.94	1.44	2.81
28R-3, 100–101	303.62	0.24	0.31	0.46	0.84	1.97	1.50	2.77
28R-4, 15–16	304.17	0.28	0.39	0.51	1.04	1.85	1.33	2.71
29R-1, 49–52	311.21	0.37	0.59	0.60	1.51	1.66	1.05	2.62
29R-1, 97–98	311.68	0.30	0.42	0.52	1.07	1.79	1.26	2.61
29R-2, 13–15	312.24	0.21	0.26	0.41	0.70	2.01	1.59	2.69
29R-4, 22–23	313.48	0.23	0.30	0.44	0.78	1.96	1.51	2.69
31R-1, 9–10	329.80	0.28	0.38	0.48	0.93	1.78	1.29	2.49
31R-1, 40.5–45.5	330.13	0.25	0.34	0.46	0.86	1.86	1.39	2.58
31R-2, 13–14	330.29	0.26	0.35	0.49	0.95	1.94	1.44	2.81

Table T14 (continued). (Continued on next page.)

Core, section, interval (cm)	Depth CSF (m)	W_c Wet	W_c Dry	Porosity	Void ratio	Density (g/cm^3) Bulk	Density (g/cm^3) Dry	Density (g/cm^3) Grain
31R-2, 38–43	330.56	0.25	0.33	0.47	0.89	1.95	1.47	2.77
31R-3, 0–3	330.60	0.22	0.28	0.45	0.81	2.08	1.62	2.94
31R-4, 25–26	331.33	0.25	0.33	0.47	0.89	1.93	1.45	2.74
31R-4, 64–67	331.73	0.26	0.35	0.49	0.97	1.95	1.45	2.85
31R-4, 111–112	332.19	0.27	0.36	0.47	0.89	1.81	1.33	2.52
31R-5, 20–21	332.60	0.29	0.41	0.54	1.15	1.87	1.32	2.85
31R-5, 70–72	333.10	0.25	0.33	0.46	0.84	1.89	1.42	2.61
32R-1, 8–11	339.30	0.27	0.36	0.49	0.97	1.89	1.39	2.73
32R-1, 89–90	340.10	0.25	0.33	0.47	0.88	1.96	1.48	2.78
32R-2, 41–43.5	340.55	0.23	0.29	0.42	0.74	1.91	1.48	2.56
32R-3, 23–25	341.06	0.23	0.31	0.44	0.77	1.90	1.46	2.58
32R-3, 101–102	341.83	0.24	0.32	0.47	0.89	2.00	1.52	2.87
32R-4, 21–22	342.30	0.24	0.32	0.46	0.85	1.96	1.49	2.76
32R-4, 75–76	342.84	0.24	0.32	0.45	0.83	1.91	1.44	2.64
33R-1, 25–26	348.96	0.24	0.31	0.45	0.81	1.93	1.47	2.66
33R-2, 0–2	349.22	0.31	0.45	0.53	1.12	1.76	1.21	2.58
33R-3, 25–26	349.99	0.24	0.32	0.47	0.87	1.97	1.49	2.79
33R-3, 104–105	350.78	0.23	0.30	0.43	0.76	1.94	1.50	2.64
33R-4, 26–28	351.29	0.23	0.30	0.42	0.73	1.87	1.44	2.49
33R-4, 103–104	352.06	0.24	0.31	0.45	0.82	1.95	1.49	2.72
33R-5, 12–14	352.40	0.22	0.28	0.43	0.74	2.02	1.58	2.76
33R-5, 80–82	353.08	0.22	0.29	0.43	0.76	1.98	1.54	2.71
34R-1, 23–25	357.24	0.23	0.30	0.45	0.81	1.96	1.50	2.71
34R-1, 72–75	357.74	0.23	0.30	0.46	0.85	2.03	1.56	2.89
34R-2, 17–18	358.52	0.22	0.28	0.43	0.74	1.97	1.54	2.68
34R-2, 101–102	359.36	0.22	0.29	0.43	0.77	2.00	1.55	2.74
34R-3, 0–2	359.55	0.22	0.29	0.42	0.73	1.97	1.54	2.66
34R-4, 48–49	360.47	0.27	0.36	0.48	0.94	1.87	1.37	2.65
35R-1, 21–22	366.72	0.23	0.30	0.44	0.78	1.92	1.47	2.61
35R-2, 65–67	367.47	0.24	0.31	0.43	0.74	1.83	1.40	2.43
35R-4, 25–26	369.14	0.24	0.32	0.45	0.83	1.92	1.45	2.66
36R-2, 34–36	376.52	0.24	0.32	0.46	0.84	1.91	1.44	2.65
36R-3, 32–33	376.86	0.24	0.32	0.46	0.86	1.95	1.47	2.74
36R-3, 105–106	377.59	0.29	0.41	0.50	0.99	1.77	1.26	2.51
36R-4, 26–27	378.00	0.20	0.26	0.41	0.70	2.07	1.65	2.81
37R-1, 43–44	385.94	0.22	0.29	0.46	0.84	2.09	1.62	2.98
37R-2, 0–2	386.31	0.23	0.29	0.44	0.77	1.97	1.53	2.70
37R-3, 13–14	386.83	0.21	0.27	0.41	0.71	2.01	1.58	2.70
38R-1, 38–39	395.39	0.20	0.26	0.40	0.67	2.01	1.60	2.67
38R-1, 82–84	395.83	0.25	0.34	0.47	0.87	1.88	1.40	2.63
38R-1, 98–99	395.99	0.21	0.27	0.42	0.72	2.02	1.59	2.73
38R-2, 22–23	396.33	0.20	0.26	0.40	0.68	2.03	1.61	2.71
39R-1, 6–7	404.57	0.22	0.28	0.43	0.74	2.02	1.58	2.76
39R-1, 104–105	405.55	0.20	0.25	0.40	0.66	2.01	1.61	2.66
39R-1, 118–121	405.70	0.20	0.24	0.39	0.65	2.06	1.65	2.72
39R-2, 13–14	405.99	0.20	0.25	0.39	0.65	2.01	1.60	2.64
39R-2, 37–40	406.24	0.18	0.22	0.38	0.60	2.13	1.74	2.79
39R-2, 73–75	406.60	0.20	0.25	0.40	0.66	2.04	1.63	2.72
39R-3, 35–37	407.26	0.19	0.23	0.37	0.60	2.05	1.67	2.66
39R-4, 59–60	407.98	0.20	0.25	0.38	0.62	1.95	1.55	2.52
40R-1, 21–23	414.22	0.22	0.28	0.42	0.73	1.99	1.55	2.69
40R-1, 119–120	415.20	0.25	0.33	0.46	0.86	1.92	1.44	2.69
40R-2, 25–26	415.56	0.35	0.54	0.56	1.28	1.63	1.06	2.41
40R-2, 115–116	416.46	0.25	0.33	0.45	0.81	1.87	1.41	2.55
40R-3, 26–28	416.99	0.26	0.35	0.48	0.94	1.89	1.40	2.71
40R-4, 30–33	417.72	0.28	0.38	0.51	1.03	1.88	1.36	2.76
40R-5, 45–47	418.56	0.24	0.32	0.44	0.79	1.86	1.41	2.52
40R-6, 0–2	419.32	0.23	0.30	0.43	0.75	1.91	1.47	2.57
40R-6, 35–36	419.66	0.24	0.32	0.44	0.79	1.87	1.42	2.54
41R-1, 23–25	423.74	0.25	0.33	0.41	0.70	1.71	1.29	2.20
41R-1, 99–101	424.50	0.26	0.35	0.48	0.93	1.90	1.41	2.71
41R-2, 0–2	424.89	0.30	0.42	0.53	1.15	1.86	1.31	2.81
41R-2, 95–96	425.84	0.24	0.32	0.46	0.84	1.93	1.46	2.69
41R-4, 38–40	426.90	0.24	0.32	0.46	0.84	1.91	1.45	2.66
41R-4, 100–101	427.51	0.24	0.32	0.43	0.75	1.83	1.39	2.44
41R-5, 14–15	428.09	0.25	0.33	0.47	0.90	1.94	1.45	2.76
41R-5, 98–99	428.93	0.22	0.28	0.41	0.70	1.94	1.52	2.58
41R-6, 25–26	429.46	0.24	0.32	0.45	0.83	1.90	1.44	2.63
42R-1, 25–26	433.26	0.24	0.32	0.45	0.81	1.90	1.44	2.60

Table T14 (continued).

Core, section, interval (cm)	Depth CSF (m)	W_c		Porosity	Void ratio	Density (g/cm^3)		
		Wet	Dry			Bulk	Dry	Grain
42R-1, 80–81	433.81	0.25	0.34	0.44	0.80	1.79	1.34	2.40
42R-2, 29–31	434.25	0.21	0.27	0.42	0.74	2.03	1.59	2.76
42R-3, 18–20	434.85	0.22	0.28	0.43	0.75	2.03	1.59	2.77
43R-2, 22–23	444.13	0.19	0.23	0.40	0.68	2.18	1.77	2.97
43R-2, 85–87	444.76	0.21	0.26	0.40	0.66	1.99	1.58	2.63
43R-4, 28–29	446.28	0.23	0.30	0.43	0.76	1.90	1.46	2.56
43R-4, 41–43	446.41	0.23	0.30	0.43	0.75	1.91	1.47	2.58
43R-5, 101–102	447.44	0.20	0.25	0.40	0.66	2.04	1.64	2.72
44R-1, 16–18	452.17	0.18	0.23	0.36	0.57	2.03	1.65	2.60
44R-2, 0–2	453.27	0.21	0.27	0.40	0.67	1.95	1.54	2.56
44R-3, 24–25	453.94	0.20	0.25	0.38	0.62	1.97	1.58	2.55
44R-3, 95–96	454.65	0.19	0.24	0.37	0.60	1.97	1.59	2.54
45R-1, 107–108	462.58	0.19	0.24	0.39	0.63	2.06	1.67	2.72
45R-2, 74–77	463.56	0.18	0.21	0.36	0.57	2.11	1.74	2.73
45R-3, 46–48	464.56	0.19	0.23	0.38	0.61	2.10	1.71	2.75
45R-4, 10–11	464.90	0.19	0.23	0.39	0.64	2.15	1.75	2.86
46R-1, 25–26	471.26	0.18	0.21	0.35	0.54	2.06	1.70	2.61
46R-3, 25–26	472.18	0.16	0.19	0.32	0.48	2.05	1.72	2.55
46R-3, 109–113	473.04	0.17	0.20	0.36	0.56	2.19	1.82	2.84
46R-4, 25–26	473.59	0.18	0.22	0.36	0.57	2.02	1.65	2.59
47R-1, 14–15	480.65	0.21	0.26	0.40	0.66	1.96	1.55	2.58
47R-2, 30–35	481.10	0.19	0.24	0.38	0.60	2.00	1.61	2.58
47R-3, 24–25	481.37	0.19	0.24	0.36	0.57	1.93	1.56	2.44
48R-1, 10–12	490.11	0.17	0.21	0.35	0.54	2.09	1.73	2.67
48R-2, 0–2	490.53	0.17	0.20	0.34	0.53	2.13	1.78	2.72
49R-2, 37–39	500.31	0.18	0.23	0.35	0.54	1.96	1.60	2.46
49R-3, 22–24	500.55	0.19	0.23	0.37	0.60	2.06	1.67	2.68
50R-2, 40–42	509.70	0.21	0.26	0.40	0.68	2.01	1.59	2.67
50R-3, 50–52	510.22	0.18	0.23	0.37	0.59	2.05	1.68	2.66
51R-1, 5–6	518.56	0.26	0.35	0.48	0.93	1.90	1.41	2.71
52R-1, 90–91	528.91	0.20	0.24	0.39	0.63	2.01	1.62	2.64
52R-2, 32–34	529.53	0.18	0.22	0.36	0.56	2.02	1.66	2.58
52R-3, 13–14	529.68	0.21	0.27	0.42	0.73	2.06	1.63	2.83

Table T15. Sandstone MAD data, Hole C0012A.

Core, section, interval (cm)	Depth CSF (m)	W_c		Porosity	Void ratio	Density (g/cm^3)		
		Wet	Dry			Bulk	Dry	Grain
322-C0012A-								
13R-3, 68–70	160.82	0.23	0.31	0.44	0.78	1.91	1.46	2.61
13R-3, 88–91	161.02	0.24	0.31	0.46	0.85	1.99	1.52	2.81
13R-4, 25–26	161.79	0.36	0.57	0.60	1.51	1.70	1.08	2.71
42R-3, 76–78	435.43	0.19	0.23	0.38	0.62	2.10	1.71	2.76
43R-1, 22–23	442.73	0.19	0.24	0.37	0.59	1.95	1.57	2.50
43R-1, 114–116	443.65	0.17	0.21	0.34	0.52	2.01	1.66	2.51
43R-5, 27–28	446.70	0.20	0.25	0.41	0.70	2.13	1.71	2.91
44R-1, 94–96	452.95	0.19	0.23	0.38	0.62	2.07	1.68	2.72
45R-1, 24–25	461.75	0.21	0.26	0.41	0.70	2.03	1.61	2.73
45R-2, 22–25	463.04	0.20	0.24	0.37	0.59	1.93	1.55	2.47
45R-4, 76–79	465.57	0.19	0.23	0.38	0.61	2.09	1.70	2.73
46R-2, 0–3	471.37	0.17	0.20	0.35	0.54	2.13	1.77	2.73
52R-1, 37–38	528.38	0.17	0.20	0.33	0.49	2.04	1.70	2.53

Table T16. Shear strength data, Hole C0012A.

Core, section, interval (cm)	Depth CSF (m)	Shear strength (kPa)	
		Vane	Penetrometer
322-C0012A-			
1R-1, 58–58	0.58	21	
1R-1, 60.5–62.5	0.62		30
2R-4, 33–33	64.19	94	
2R-4, 34.5–36.5	64.20		67
4R-1, 85–85	79.85	24	
4R-1, 87–89	79.88		62
4R-2, 29–29	80.30	105	
4R-2, 31–33	80.33		76
5R-1, 38–41	88.90		13
5R-3, 10–11	89.99		38
5R-3, 18–18	90.07	48	
5R-4, 19–20	91.49		62
5R-5, 48–50	92.80		92

Table T17. *P*-wave velocity, Hole C0012A. (**Continued on next page.**)

Core, section, interval (cm)	Depth (mbsf)	V_P (m/s)			Anisotropy (%)		Comments
		x	*y*	*z*	Horizontal	Vertical	
322-C0012A-							
8R-7, 20	118.47	1633	1626	1597	0.45	1.98	
9R-5, 30	124.57	1657	1615	1642	2.55	–0.38	
9R-6, 25	125.93	1650	1665	1603	–0.90	3.32	
9R-7, 26	127.35	1658	1631	1624	1.60	1.25	
10R-1, 109	131.59	1645	1663	1652	–1.09	0.08	
10R-2, 52	132.14	1674	1669	1701	0.26	–1.75	
10R-4, 60	133.24	1642	1610	1628	1.93	–0.14	
10R-5, 41	134.45	1636	1635	1628	0.06	0.48	
10R-6, 26	135.70	1654	1658	1641	–0.24	0.95	
11R-1, 67	140.67	1682	1696	1667	–0.81	1.30	
11R-2, 69	141.93	1687	1694	1646	–0.45	2.65	Sand
11R-3, 72	143.37	1674	1669	1658	0.30	0.81	
11R-5, 60	144.90	1669	1684	1651	–0.89	1.55	
11R-6, 11	145.62	1660	1656	1633	0.22	1.51	
11R-7, 23	147.13	1651	1666	1640	–0.92	1.11	
12R-1, 66	150.16	1694	1683	1682	0.67	0.38	
12R-2, 10	150.53	1722	1701	1669	1.25	2.54	
13R-1, 40	159.40	1696	1705	1672	–0.55	1.66	
13R-4, 50	162.04	1696	1696	1738	–0.04	–2.45	
14R-1, 96	169.46	1715	1698	1682	1.00	1.47	
14R-3, 50	170.48	1704	1703	1697	0.08	0.37	
14R-4, 19	171.49	2037	2020	1961	0.81	3.38	Sand
15R-1, 67	178.67	1781	1783	1781	–0.15	0.06	
15R-2, 55	179.96	1733	1724	1734	0.56	–0.34	
16R-1, 31	187.81	1754	1769	1727	–0.85	1.98	
16R-2, 28	188.70	1733	1762	1692	–1.62	3.21	
16R-4, 16	189.47	1693	1743	1707	–2.91	0.66	
17R-1, 102	198.02	1764	1769	1776	–0.30	–0.55	
17R-2, 11	198.31	1774	1769	1746	0.28	1.41	
17R-4, 71	199.82	1831	1817	1863	0.79	–2.11	
19R-1, 24	215.94	1809	1793	1668	0.93	7.65	
19R-3, 99	218.57	1708	1730	1682	–1.28	2.18	
19R-4, 41	219.39	1807	1842	1736	–1.95	4.99	
20R-1, 24	225.44	1857	1861	1748	–0.23	6.15	
20R-2, 78	227.38	1851	1850	1812	0.04	2.07	
20R-4, 105	228.89	1801	1770	1758	1.74	1.51	
21R-1, 27	234.97	1796	1793	1803	0.19	–0.48	
21R-3, 22	235.94	1787	1790	1764	–0.13	1.40	
21R-4, 26	237.30	1798	1809	1749	–0.61	3.05	
22R-1, 127	245.47	1748	1747	1726	0.04	1.23	
22R-3, 106	246.86	1844	1819	1727	1.33	5.87	
23R-1, 107	254.77	1778	1776	1779	0.09	–0.12	
23R-2, 72	255.79	1775	1755	1777	1.17	–0.68	
23R-4, 113	257.67	1763	1766	1748	–0.19	0.91	
23R-5, 95	258.79	1805	1803	1765	0.09	2.18	
23R-6, 53	259.61	1827	1838	1764	–0.58	3.84	
24R-1, 29	263.49	1825	1817	1781	0.44	2.24	
24R-3, 26	264.54	1811	1820	1744	–0.53	4.00	
24R-4, 102	266.71	1800	1814	1771	–0.81	2.01	
24R-5, 70	267.74	1824	1862	1799	–2.04	2.41	
24R-6, 38	268.83	1790	1827	1793	–2.06	0.85	
25R-1, 37	273.07	1832	1833	1833	–0.05	0.01	
25R-3, 61	275.12	1868	1884	1853	–0.89	1.22	
25R-4, 87	276.43	1865	1873	1773	–0.46	5.27	
25R-5, 100	277.77	1828	1867	1784	–2.13	3.51	
25R-6, 40	278.53	1796	1788	1765	0.46	1.51	
26R-1, 19	282.39	1843	1894	1813	–2.73	3.03	
26R-2, 19	283.80	1874	1906	1885	–1.68	0.24	
27R-1, 13	291.83	1810	1838	1802	–1.54	1.18	
27R-3, 49	292.86	1837	1874	1792	–2.01	3.49	
27R-4, 31	293.77	1821	1844	1796	–1.27	2.02	
27R-5, 31	295.13	1868	1858	1808	0.54	3.03	
28R-1, 26	301.46	1855	1883	1821	–1.52	2.61	
28R-3, 21	302.82	1886	1925	1874	–2.05	1.63	
28R-4, 13	304.15	1871	1914	1826	–2.25	3.59	
29R-1, 92	311.62	1849	1837	1797	0.65	2.56	
29R-4, 19	313.45	1913	1914	1859	–0.07	2.88	

Table T17 (continued).

Core, section, interval (cm)	Depth (mbsf)	V_P (m/s)			Anisotropy (%)		Comments
		x	*y*	*z*	Horizontal	Vertical	
31R-1, 11	329.81	1835	1803	1817	1.72	0.11	
31R-2, 16	330.32	1855	1832	1815	1.27	1.55	
31R-4, 109	332.16	1849	1849	1813	–0.02	1.96	
31R-5, 23	332.62	1844	1825	1845	1.00	–0.59	
32R-1, 84	340.04	1916	1917	1841	–0.02	4.02	
32R-3, 99	341.81	1865	1865	1807	0.00	3.14	
32R-4, 73	342.82	1916	1900	1884	0.84	1.25	
33R-1, 29	348.99	1907	1934	1850	–1.39	3.77	
33R-3, 114	350.87	1911	1936	1858	–1.28	3.45	
33R-4, 77	351.79	1889	1934	1863	–2.35	2.59	
33R-5, 76	353.03	1905	1920	1872	–0.80	2.15	
34R-1, 38	357.38	1999	1936	1847	3.20	6.32	
34R-2, 46	358.80	1879	1929	1867	–2.64	1.97	
34R-4, 17	360.15	1931	1933	1881	–0.12	2.68	
36R-3, 34	376.87	2445	2331	2213	4.76	7.61	
36R-4, 29	378.02	2022	1969	1995	2.64	0.00	
37R-1, 42	385.92	1894	1837	1851	3.06	0.76	
38R-1, 46	395.46	2009	2048	1942	–1.91	4.35	
39R-1, 116.5	405.67	2067	2108	1921	–1.96	8.34	
39R-2, 11	405.97	2032	1938	1870	4.75	5.96	
39R-4, 58	407.97	2089	2062	1946	1.32	6.43	
40R-1, 129	415.29	1874	1931	1838	–2.98	3.46	
40R-2, 50	415.81	1898	1894	1829	0.25	3.58	
40R-3, 21	416.93	1911	1916	1842	–0.24	3.78	
40R-5, 70	418.80	1927	1948	1855	–1.10	4.34	
41R-1, 65	424.15	2003	2011	1864	–0.43	7.37	
41R-2, 99	425.87	1949	1942	1844	0.33	5.37	
41R-4, 102	427.53	1936	1949	1902	–0.70	2.11	
41R-5, 47	428.41	1907	1918	1847	–0.61	3.47	
41R-6, 29	429.49	1889	1920	1841	–1.63	3.43	
42R-1, 34	433.34	1948	1967	1853	–0.97	5.47	
42R-2, 59	434.54	1994	1971	1827	1.18	8.19	
43R-1, 108	443.58	1965	1958	2008	0.37	–2.32	Sand
43R-2, 59	444.49	1991	1984	1895	0.32	4.76	
43R-4, 32	446.31	1971	1988	1871	–0.84	5.65	
43R-5, 100	447.42	2117	2073	2014	2.12	3.93	
44R-1, 91	452.91	1996	1929	1871	3.43	4.80	
44R-3, 80	454.50	1946	2003	1847	–2.87	6.70	
45R-1, 104	462.54	1939	1807	1925	7.03	–2.76	
45R-2, 38	463.19	1975	1956	1980	0.98	–0.71	Sand
45R-4, 59	465.38	1950	1942	1974	0.45	–1.43	Sand
46R-1, 28	471.28	2130	2055	2003	3.57	4.36	
46R-3, 34	472.27	2056	2117	2012	–2.91	3.63	
46R-4, 41	473.75	1955	2070	2053	–5.72	–2.03	
47R-1, 17	480.67	2152	2088	2121	3.05	–0.05	
48R-2, 81	491.33	2181	2165	2001	0.71	8.26	
48R-2, 81	491.33	2181	2165	2001	0.71	8.26	
49R-3, 53	500.85	2248	2332	2138	–3.65	6.87	
50R-3, 3	509.74	2053	2132	1970	–3.78	6.01	
52R-1, 80	528.80	2031	2003	1908	1.40	5.53	
52R-3, 11	529.65	2051	2020	1915	1.52	6.10	
53R-2, 47.5	538.89	3811	3896	3805	–2.21	1.26	Basalt
54R-2, 24	544.67	4587	4713	4767	–2.72	–2.48	Basalt
54R-2, 38.5	544.81	3290	3635	3409	–9.98	1.55	Basalt
54R-2, 57	545.00	3083	3267	3153	–5.78	0.70	Basalt
55R-CC, 10.5	549.03	3699	3686	3483	0.36	5.84	Basalt
56R-CC, 12.5	554.26	3625	3662	3574	–1.02	1.91	Basalt
57R-1, 21	556.51	3636	4038	3675	–10.47	4.31	Basalt
58R-1, 38	560.38	3423	3357	3327	1.96	1.87	Basalt

Table T18. Electrical resistivity data, Hole C0012A.

Core, section, interval (cm)	Depth CSF (m)	Resistivity (Ωm)			Anisotropy (%)	
		x	*y*	*z*	Horizontal	Vertical
322-C0012A-						
8R-7, 20	118.47	2.56	2.56	2.52	0.04	1.52
9R-7, 26	127.35	2.83	2.79	2.73	1.38	2.96
11R-1, 67	140.67	3.30	3.19	3.88	3.57	–17.93
12R-1, 66	150.16	3.43	2.98	3.25	13.84	–1.38
13R-1, 40	159.40	3.32	3.03	3.99	9.10	–22.69
14R-1, 96	169.46	2.78	3.11	3.67	–11.33	–21.82
15R-2, 55	179.96	3.64	4.27	4.06	–16.01	–2.69
16R-1, 31	187.81	3.96	4.33	5.23	–8.85	–22.99
17R-1, 102	198.02	4.32	4.44	4.09	–2.63	6.84
19R-1, 24	215.94	4.83	3.02	4.52	46.10	–13.95
20R-1, 24	225.44	3.73	3.66	5.19	1.70	–33.68
21R-1, 27	234.97	3.95	3.98	4.80	–0.68	–19.14
22R-1, 127	245.47	4.89	4.37	4.96	11.08	–6.79
23R-1, 107	254.77	3.54	3.65	4.00	–3.30	–10.72
24R-5, 70	267.74	4.24	4.78	5.23	–11.96	–14.78
25R-1, 37	273.07	3.65	3.88	5.56	–5.92	–38.59
26R-1, 19	282.39	3.56	3.82	4.98	–7.09	–29.70
27R-3, 49	292.86	4.75	4.71	5.85	0.80	–21.11
28R-3, 21	302.82	4.63	4.75	4.75	–2.67	–1.13
29R-4, 19	313.45	3.73	3.72	3.18	0.23	15.55
31R-1, 11	329.81	4.86	4.41	6.00	9.85	–25.69
32R-1, 84	340.04	3.42	4.21	6.10	–20.92	–46.15
33R-1, 29	348.99	4.07	4.72	8.47	–14.81	–63.37
34R-1, 38	357.38	5.77	4.64	8.67	21.72	–49.98
36R-4, 29	378.02	4.91	5.46	7.53	–10.67	–36.89
37R-1, 42	385.92	4.45	3.81	7.06	15.53	–52.38
38R-1, 46	395.46	6.12	4.80	13.09	24.18	–82.27
39R-1, 116.5	405.67	3.42	5.48	6.63	–46.44	–39.43
40R-2, 50	415.81	4.77	4.97	5.46	–4.03	–11.44
41R-1, 65	424.15	5.32	6.13	6.83	–14.04	–17.55
42R-1, 34	433.34	5.21	5.96	9.65	–13.41	–53.42
43R-2, 59	444.49	4.65	4.28	8.03	8.21	–57.02
44R-3, 80	454.50	5.09	4.95	7.58	2.73	–40.63
45R-1, 104	462.54	5.47	5.03	6.43	8.43	–20.18
46R-1, 28	471.28	4.86	4.87	8.39	–0.28	–53.12
47R-1, 17	480.67	7.79	6.63	8.70	16.21	–18.74
48R-2, 81	491.33	5.88	5.84	11.49	0.80	–64.91
49R-3, 53	500.85	6.06	6.09	11.35	–0.44	–60.60
50R-3, 3	509.74	5.14	4.95	11.29	3.65	–76.47
52R-3, 11	529.65	5.95	5.80	11.91	2.59	–67.89

Table T19. Thermal conductivity data, Hole C0012A.

Core, section, interval (cm)	Depth CSF (m)	Thermal conductivity (W/[m·K])	Comments
322-C0012A-			
2R-4, 30	64.15	0.995	
4R-2, 34	80.35	1.171	
5R-3, 85	90.74	1.097	
5R-4, 73	92.02	1.088	
5R-5, 15	92.46	1.023	
6R-4, 83	101.51	1.133	
10R-2, 46	132.08	0.984	
10R-4, 67	133.31	1.064	
13R-4, 51	162.05	1.206	
14R-1, 80	169.30	1.205	
14R-3, 5	170.03	1.184	
14R-4, 17	171.47	1.193	Sand
15R-2, 51	179.92	1.167	
16R-1, 31	187.81	1.246	
17R-1, 17	197.17	1.21	
19R-1, 17	215.87	1.253	
19R-3, 6	217.64	1.207	
19R-4, 30	219.28	1.168	
20R-1, 69	225.89	1.301	
20R-2, 60	227.20	1.345	
20R-4, 70	228.54	1.194	
21R-1, 53	235.23	1.205	
21R-3, 10	235.82	1.316	
21R-4, 50	237.54	1.33	
22R-3, 96	246.76	1.308	
23R-1, 132	255.02	1.31	
23R-4, 7	256.61	1.371	
23R-6, 62	259.70	1.335	
24R-3, 77	265.05	1.323	
24R-5, 31	267.35	1.337	
25R-3, 39	274.90	1.4	
25R-5, 47	277.24	1.351	
25R-7, 4	278.95	1.319	
26R-1, 11	282.31	1.384	
27R-3, 50	292.87	1.224	
28R-3, 88	303.49	1.262	
29R-1, 32	311.02	1.135	
29R-4, 45	313.71	1.32	
31R-1, 20	329.90	1.237	
31R-2, 16	330.32	1.219	
31R-4, 118	332.25	1.21	
31R-5, 18	332.57	1.227	
32R-1, 58	339.78	1.262	
32R-3, 120	342.02	1.382	
33R-3, 126	350.99	1.234	
33R-4, 101	352.03	1.256	
34R-1, 53	357.53	1.155	
34R-2, 28	358.62	1.296	
34R-4, 38	360.36	1.261	
36R-3, 62	377.15	1.299	
36R-4, 3	377.76	1.417	
37R-1, 34	385.84	1.423	
39R-1, 116	405.66	1.36	
39R-4, 37	407.76	1.406	
40R-1, 113	415.13	1.416	
40R-2, 128	416.59	1.322	
40R-5, 77	418.87	1.428	
41R-1, 85	424.35	1.333	
41R-2, 73	425.61	1.264	
41R-4, 6	426.57	1.208	
41R-5, 90	428.84	1.412	
42R-1, 33	433.33	1.166	
42R-3, 50	435.16	1.31	
43R-1, 16	442.66	1.819	Sand
43R-2, 60	444.50	1.275	
43R-5, 8	446.50	1.553	Sand
44R-1, 61	452.61	1.714	Sand
44R-3, 62	454.32	1.365	
45R-1, 12	461.62	1.485	Sand
45R-2, 44	463.25	2.008	Sand
45R-4, 70	465.49	1.918	Sand
46R-1, 30	471.30	1.368	
46R-3, 4	471.97	1.474	
47R-3, 40	481.52	1.546	Sand
48R-2, 59	491.11	2.101	Sand
49R-3, 49	500.81	1.402	
50R-1, 22	509.22	1.51	Sand
52R-1, 44	528.44	1.826	Sand

Table T20. Interstitial water geochemistry (raw data), Hole C0012A. (See table note.) (Continued on next page.)

Core, section	Depth CSF (m)	pH	Alkalinity (mM)	Salinity	Cl (mM)	Na (mM)	NH_4 (mM)	H_4SiO_4 (μM)	Ca (mM)	Mg (mM)	Sr (μM)	Li (μM)	K (mM)	PO_4 (μM)	SO_4 (mM)	Mn (μM)	Br (mM)	Ba (μM)
322-C0012A-																		
5R-2	89.43	7.600	3.72	35.4	561	480	0.43	413	24.4	35.7	122	139	5.8	3.23	20.45	87	0.91	0.7
6R-3	100.35	7.570	3.21	—	560	480	0.47	346	26.5	31.7	126	151	4.9	ND	19.18	85	0.90	0.9
7R-5	107.66	7.530	2.82	—	567	486	0.48	356	27.7	30.0	128	163	4.8	ND	18.01	84	0.92	1.1
8R-5	116.62	7.560	2.35	34.8	559	478	0.52	338	30.4	25.2	138	176	4.1	ND	15.99	92	0.94	1.2
9R-4	124.03	7.510	2.38	34.8	562	481	0.58	362	31.8	22.4	139	182	4.5	ND	14.88	103	0.96	1.3
10R-3	132.17	7.640	2.63	34.5	563	480	0.57	387	33.3	21.0	143	183	4.1	ND	13.77	105	0.95	1.2
11R-4	144.03	7.480	1.83	34.2	558	471	0.59	330	36.7	17.5	151	195	3.4	ND	11.58	107	0.99	1.6
13R-2	159.64	7.640	1.22	34.1	555	468	0.63	361	38.5	14.6	156	192	3.1	3.06	10.45	88	0.91	1.5
14R-2	169.69	7.810	1.31	33.9	564	471	0.65	353	41.9	11.1	165	198	2.7	ND	7.26	82	0.91	2.3
15R-3	180.09	7.760	1.60	33.8	561	469	0.63	302	42.5	9.8	170	198	2.5	ND	6.78	69	0.95	1.9
16R-3	189.03	7.940	1.02	33.8	561	465	0.63	177	44.8	8.5	174	197	2.3	ND	5.92	70	0.96	2.6
17R-3	198.82	8.120	1.17	33.7	565	466	0.69	274	46.5	7.6	180	198	2.1	ND	5.15	57	0.97	4.0
18R-2	207.90	8.120	0.77	—	556	450	0.61	106	49.4	6.1	194	201	1.8	ND	2.89	44	0.95	4.2
19R-2	217.58	8.170	1.13	33.5	566	458	0.62	108	49.9	7.1	198	204	1.9	ND	3.72	54	0.94	5.3
20R-3	227.50	8.140	0.54	33.4	556	441	0.64	123	54.4	5.0	213	208	1.6	ND	2.34	60	0.93	7.1
21R-2	235.39	8.190	0.87	33.4	—	—	0.69	142	53.2	6.5	214	202	1.7	ND	2.47	71	0.92	8.8
23R-3	256.10	8.060	0.64	33.7	565	438	0.63	126	60.7	4.0	237	202	1.3	ND	1.80	74	0.90	23.6
24R-2	263.93	8.330	0.80	33.4	557	428	0.64	107	61.5	4.0	237	198	1.3	ND	1.23	70	0.94	33.5
25R-2	273.92	8.220	0.36	33.7	561	429	0.61	126	62.6	4.6	239	187	1.4	ND	1.90	87	0.94	42.0
27R-2	292.04	8.480	0.30	34.5	573	432	0.68	90	63.7	7.7	235	174	2.0	ND	1.35	65	0.96	16.8
28R-2	302.16	8.430	0.87	33.9	565	423	0.68	89	68.5	4.8	246	174	1.4	ND	2.11	72	0.95	15.7
29R-3	312.57	8.380	0.66	33.8	557	419	0.56	77	66.8	7.9	237	160	1.9	ND	6.24	78	0.88	16.2
31R-3	330.59	8.280	0.64	—	570	402	0.56	102	80.4	4.6	265	166	1.5	ND	1.50	105	0.93	32.5
32R-2	340.13	8.540	0.61	34.9	574	407	0.60	100	79.7	4.6	263	168	1.3	ND	1.22	90	0.96	31.4
33R-2	349.21	8.480	0.51	33.7	556	397	0.61	81	73.0	9.3	234	152	2.2	ND	3.56	81	0.90	19.4
34R-3	359.54	8.550	0.51	33.0	535	365	0.57	58	84.3	3.4	258	158	1.2	ND	3.01	52	0.87	28.5
35R-2	366.81	8.580	0.97	35.6	576	394	0.55	78	88.8	6.1	259	157	1.3	ND	4.10	94	0.94	17.0
36R-2	376.20	8.360	1.04	34.8	562	385	0.42	73	82.8	11.6	239	139	2.2	ND	6.39	110	0.91	14.5
37R-2	386.30	8.010	0.54	36.4	587	381	0.44	47	99.9	5.4	278	158	1.3	ND	2.72	78	0.99	33.1
39R-3	406.90	—	—	36.8	590	355	0.39	50	114.9	4.6	285	149	1.1	ND	2.59	54	0.97	36.5
40R-4	417.40	8.100	0.62	36.4	580	359	0.40	58	104.6	8.8	252	150	1.7	ND	3.56	31	0.93	27.6
41R-3	426.10	8.260	0.52	37.6	597	338	0.43	62	126.9	4.0	278	136	1.2	ND	1.30	22	0.96	53.3
42R-2	433.90	8.480	0.73	37.7	603	349	0.43	69	124.8	4.8	276	130	1.1	ND	2.80	19	1.00	36.8
43R-4	446.00	8.310	0.73	38.3	605	350	0.44	69	126.0	5.5	261	127	1.3	ND	4.50	18	1.01	29.3
44R-2	453.30	8.560	1.30	37.7	589	340	0.30	86	123.2	8.3	248	113	1.3	ND	7.03	27	0.95	26.8
45R-3	462.80	8.600	0.91	39.4	613	316	0.32	89	148.0	4.6	269	112	1.4	ND	4.48	13	1.04	29.2
46R-2	471.30	—	—	38.8	605	317	0.28	70	140.8	5.9	259	103	1.7	ND	3.59	10	0.97	25.6
47R-2	480.70	—	—	—	606	315	0.24	93	141.8	8.1	258	97	1.2	ND	4.83	19	0.99	15.2
48R-1	490.00	8.220	0.32	39.2	607	327	0.20	94	134.3	11.6	246	86	2.2	ND	6.44	42	0.98	10.1
49R-2	499.90	—	—	39.2	611	337	0.15	106	127.8	16.1	239	75	3.5	ND	8.55	40	1.09	7.9
50R-2	509.30	—	—	41.3	627	269	0.11	111	175.8	6.1	290	70	0.9	ND	2.92	22	0.99	11.7
52R-2	529.20	—	—	40.5	608	282	0.06	181	157.6	12.2	283	48	1.4	ND	7.91	26	0.98	5.4

Note: — = not determined, ND = not detectable.

Table T20 (continued).

Core, section	Depth CSF (m)	B (µM)	HS (µM)	Fe (µM)	V (nM)	Zn (µM)	Rb (nM)	Mo (nM)	Cs (nM)	Pb (nM)	U (nM)
322-C0012A-											
5R-2	89.43	352	36.13	2.95	7.7	1.4	519.1	109.0	1.2	1.3	2.3
6R-3	100.35	339	10.95	1.35	7.8	2.5	538.8	150.5	1.6	2.8	3.2
7R-5	107.66	345	21.66	3.46	10.1	2.9	532.5	137.2	1.6	1.6	2.4
8R-5	116.62	338	13.43	1.65	8.5	2.9	498.9	170.5	1.6	1.5	2.3
9R-4	124.03	316	1.47	0.80	8.2	2.7	553.4	187.1	2.2	3.8	2.4
10R-3	132.17	304	0.00	0.61	12.3	2.4	504.1	181.7	1.9	2.2	2.6
11R-4	144.03	318	2.83	0.55	10.7	—	428.5	204.1	2.5	—	2.2
13R-2	159.64	315	0.00	0.53	10.6	1.9	397.8	212.2	2.0	1.9	2.1
14R-2	169.69	333	0.55	ND	11.3	1.8	365.8	246.5	2.2	3.5	1.5
15R-3	180.09	358	0.43	ND	9.9	1.5	324.1	230.0	1.8	2.1	0.6
16R-3	189.03	344	0.00	ND	12.7	2.0	283.8	253.7	1.7	2.1	1.1
17R-3	198.82	286	0.04	ND	12.4	1.1	294.6	284.2	2.0	3.1	1.2
18R-2	207.90	312	0.30	ND	11.6	1.0	205.6	255.1	1.6	0.8	0.6
19R-2	217.58	323	0.09	ND	11.1	1.0	217.1	296.2	1.6	1.0	1.4
20R-3	227.50	375	0.19	ND	11.1	1.6	176.8	212.9	1.3	1.5	1.0
21R-2	235.39	394	0.21	ND	9.1	1.5	128.9	160.6	0.9	0.6	0.8
23R-3	256.10	418	0.00	ND	10.6	1.0	140.7	194.3	1.2	0.9	0.6
24R-2	263.93	387	0.17	0.47	12.4	1.1	147.2	186.1	1.4	0.6	0.6
25R-2	273.92	406	0.00	0.46	—	—	—	—	—	—	—
27R-2	292.04	368	4.10	ND	13.9	0.6	190.9	254.8	1.6	ND	0.3
28R-2	302.16	341	4.04	0.44	11.7	0.4	159.1	202.8	1.8	0.9	0.5
29R-3	312.57	337	1.14	ND	12.2	0.3	193.8	205.3	2.0	0.7	0.3
31R-3	330.59	370	4.02	ND	12.8	0.8	165.8	116.9	1.8	0.8	0.4
32R-2	340.13	392	—	ND	15.5	0.6	184.8	239.8	2.6	0.6	0.2
33R-2	349.21	321	3.11	0.42	12.8	0.3	258.4	391.7	2.3	0.7	0.3
34R-3	359.54	237	4.03	ND	12.2	0.2	196.7	582.2	2.5	ND	0.1
35R-2	366.81	287	4.15	ND	12.8	0.5	202.9	193.6	2.9	1.7	0.4
36R-2	376.20	270	3.30	ND	—	—	—	—	—	—	—
37R-2	386.30	275	0.12	ND	13.1		204.2	167.4	2.9	0.8	0.4
39R-3	406.90	180	122.59	ND	13.2	1.3	206.6	370.7	3.5	1.1	1.4
40R-4	417.40	179	236.76	ND	—	—	—	—	—	—	—
41R-3	426.10	187	116.34	ND	13.6	0.8	175.3	120.7	3.0	1.1	0.4
42R-2	433.90	160	81.55	ND	14.2	0.5	164.1	180.4	2.9	1.2	0.4
43R-4	446.00	232	0.00	ND	31.3	0.6	240.3	1268.0	5.3	1.3	0.3
44R-2	453.30	202	0.00	ND	—	—	—	—	—	—	—
45R-3	462.80	236	4.16	0.61	53.2	0.2	206.1	472.9	3.6	1.4	0.3
46R-2	471.30	187	8.64	ND	51.7	0.3	225.1	732.1	3.5	1.2	0.4
47R-2	480.70	165	—	ND	18.9	0.4	102.5	283.6	2.1	ND	0.1
48R-1	490.00	171	23.22	ND	35.6	0.7	205.0	393.3	2.7	0.8	0.1
49R-2	499.90	153	0.00	ND	21.4	0.6	228.8	287.6	1.8	1.8	0.2
50R-2	509.30	106	—	ND	—	—	—	—	—	—	—
52R-2	529.20	90	—	ND	21.4	—	97.1	246.6	0.7	—	0.4

Table T21. Estimates of major ion concentrations expected at the pore fluid anomaly observed at 500 m CSF. (**See table notes.**)

	Formation fluid	Expected value	Observed value
Mg (mM)	5	15	16
Ca (mM)	157	128	127
Na (mM)	298	334	315
SO_4 (mM)	4	9.0	8.5
Cl (mM)	620	608	604

Notes: Formation fluid value estimated by interpolating the data from above and below the observed anomaly at 500 m CSF. Expected value assuming a 20% seawater component, based on the potassium data.

Table T22. Hydrocarbon gas composition in headspace samples of sediments, Hole C0012A. (See table note.)

Core, section, interval (cm)	Depth CSF (m)	Concentration in headspace (ppmv)					Concentration in interstitial water (μM)			
		Methane	Ethane	Propane	Isobutane	C_1/C_2	Methane	Ethane	Propane	Isobutane
322-C0012A-										
1R-1, 63–67	0.65	BD	BD	BD	BD	—	BD	BD	BD	BD
2R-4, 50–54	64.37	BD	BD	BD	BD	—	BD	BD	BD	BD
3R-1, 137–141	70.89	BD	BD	BD	BD	—	BD	BD	BD	BD
4R-1, 96.5–100.5	79.99	BD	BD	BD	BD	—	BD	BD	BD	BD
5R-1, 88.5–92.5	89.41	BD	BD	BD	BD	—	BD	BD	BD	BD
6R-2, 90–94	100.33	BD	BD	BD	BD	—	BD	BD	BD	BD
7R-1, 142–146	103.44	BD	BD	BD	BD	—	BD	BD	BD	BD
8R-4, 85.5–89.5	116.60	BD	BD	BD	BD	—	BD	BD	BD	BD
9R-3, 37.5–41.5	124.01	BD	BD	BD	BD	—	BD	BD	BD	BD
10R-2, 51.5–55.5	132.15	BD	BD	BD	BD	—	BD	BD	BD	BD
11R-3, 134–138	144.01	BD	BD	BD	BD	—	BD	BD	BD	BD
12R-1, 88.5–92.5	150.41	BD	BD	BD	BD	—	BD	BD	BD	BD
13R-1, 60–64	159.62	BD	BD	BD	BD	—	BD	BD	BD	BD
14R-1, 115–119	169.67	BD	BD	BD	BD	—	BD	BD	BD	BD
15R-2, 64–68	180.07	BD	BD	BD	BD	—	BD	BD	BD	BD
16R-2, 56.5–60.5	189.01	2.7	BD	BD	BD	—	0.9	BD	BD	BD
17R-2, 57.5–61.5	198.80	2.9	BD	BD	BD	—	0.9	BD	BD	BD
18R-1, 136–140	207.88	2.7	BD	BD	BD	—	1.1	BD	BD	BD
19R-1, 131–135	217.03	3.5	BD	BD	BD	—	2.3	BD	BD	BD
20R-2, 85.5–89.5	227.48	4.4	BD	BD	BD	—	1.5	BD	BD	BD
21R-1, 64.5–68.5	235.37	4.0	BD	BD	BD	—	2.7	BD	BD	BD
22R-1, 130–134	245.52	4.6	BD	BD	BD	—	3.4	BD	BD	BD
23R-2, 99.5–103.5	256.08	6.7	BD	BD	BD	—	4.2	BD	BD	BD
24R-1, 69–73	263.91	7.0	BD	BD	BD	—	3.5	BD	BD	BD
25R-1, 117.5–121.5	273.90	8.9	BD	BD	BD	—	6.7	BD	BD	BD
26R-1, 137–141	283.59	22.7	BD	BD	BD	—	5.0	BD	BD	BD
27R-1, 29.5–33.5	292.02	63.0	BD	BD	BD	—	22.4	BD	BD	BD
28R-1, 91.5–95.5	302.14	65.0	BD	BD	BD	—	29.8	BD	BD	BD
29R-2, 43.5–47.5	312.55	66.6	BD	BD	BD	—	38.3	BD	BD	BD
31R-1, 41.5–45.5	330.14	85.3	BD	BD	BD	—	80.1	BD	BD	BD
32R-1, 89–93	340.11	56.2	BD	BD	BD	—	71.5	BD	BD	BD
33R-1, 47–51	349.19	77.3	BD	BD	BD	—	55.6	BD	BD	BD
34R-2, 116–120	359.52	145	1.6	BD	BD	92	126	1.4	BD	BD
35R-1, 27–31	366.79	80.3	BD	BD	BD	—	36.3	BD	BD	BD
36R-3, 0–4	376.55	149	1.9	BD	BD	78	76.1	1.0	BD	BD
37R-1, 76–80	386.28	86.3	BD	BD	BD	—	103	BD	BD	BD
38R-1, 106.5–110.5	396.09	175	3.2	BD	BD	54	112	2.1	BD	BD
39R-2, 100.5–104.5	406.88	122	2.5	BD	BD	49	149	3.0	BD	BD
40R-3, 65–69	417.39	172	2.8	BD	BD	62	244	3.9	BD	BD
41R-2, 115–119	426.05	110	2.9	BD	BD	38	66.2	1.7	BD	BD
42R-1, 90.5–94.5	433.93	150	3.3	BD	BD	45	63.2	1.4	BD	BD
43R-3, 66–70	445.97	208	4.6	BD	BD	45	93.8	2.1	BD	BD
44R-1, 121.5–125.5	453.24	166	4.5	BD	BD	37	76.7	2.1	BD	BD
45R-2, 124–128	464.07	71.2	BD	BD	BD	—	78.8	BD	BD	BD
46R-1, 31.5–35.5	471.34	33.9	BD	BD	BD	—	88.2	BD	BD	BD
47R-1, 23–27	480.75	26.0	BD	BD	BD	—	47.2	BD	BD	BD
48R-2, 82–86	491.36	26.9	BD	BD	BD	—	50.1	BD	BD	BD
49R-1, 38.5–42.5	499.91	83.0	BD	BD	BD	—	36.0	BD	BD	BD
50R-1, 25–29	509.27	79.1	BD	BD	BD	—	46.3	BD	BD	BD
51R-1, 0–2	518.51	120	2.8	BD	BD	42	16.8	0.4	BD	BD
52R-2, 0–2	529.21	5.6	BD	BD	BD	—	3.0	BD	BD	BD

Note: BD = below detection, — = not applicable.

Table T23. H_2 concentration in sediment samples, determined by incubation method, Hole C0012A. (See table note.)

Core, section, interval (cm)	Depth CSF (m)	*T* (°C)	1/β	*t* (h)	Replicate 1		Replicate 2		Replicate 3	
					H_2 in headspace gas (ppmv)	H_2 in interstitial water (nM)	H_2 in headspace gas (ppmv)	H_2 in interstitial water (nM)	H_2 in headspace gas (ppmv)	H_2 in interstitial water (nM)
322-C0012A-										
7R-5, 80–90	107.60	15	62.96	0	0.28	0.19	0.40	0.27	0.62	0.42
				169.3	0.40	0.27	1.85	1.24	0.84	0.56
				221.1	0.48	0.32	1.34	0.90	0.96	0.64
				298.1	0.53	0.35	1.16	0.78	0.58	0.39
19R-2, 15–25	217.25	15	62.96	0	1.30	0.88	0.82	0.55	0.64	0.43
				74.9	1.55	1.04	0.79	0.53	1.24	0.83
				126.6	1.84	1.23	1.19	0.80	1.16	0.78
				203.7	2.19	1.47	1.21	0.81	0.88	0.59
22R-2, 12.5–26	245.73	15	62.96	0.0	2.42	1.62	0.49	0.33	0.47	0.32
				50.4	1.31	0.88	1.14	0.77	0.59	0.40
				102.1	1.71	1.15	0.77	0.52	0.69	0.46
				179.1	1.72	1.16	0.70	0.47	0.48	0.32
25R-2, 15–25	274.12	20	64.07	0.0	0.22	0.14	1.09	0.70	0.32	0.20
				50.2	0.24	0.16	1.15	0.74	0.58	0.37
				101.7	0.31	0.20	1.36	0.87	0.75	0.48
				178.5	0.26	0.17	1.14	0.73	0.97	0.62
29R-3, 58.5–68.5	313.21	20	64.07	0.0	1.66	1.07	0.30	0.19	0.89	0.57
				49.2	1.57	1.01	0.56	0.36	1.20	0.77
				101.9	1.73	1.11	0.60	0.38	1.45	0.93
				177.9	1.76	1.13	0.72	0.46	1.25	0.80
32R-2, 58.5–68.5	340.77	20	64.07	0.0	0.66	0.42	1.17	0.75	0.42	0.27
				48.5	1.50	0.96	1.98	1.27	0.44	0.28
				100.2	1.75	1.12	1.66	1.06	0.51	0.33
				177.2	2.30	1.47	1.38	0.89	0.71	0.45
35R-2, 15–25	367.01	25	66.68	0.0	1.48	0.90	0.60	0.37	0.70	0.43
				47.9	2.47	1.52	0.85	0.52	1.08	0.67
				99.6	1.45	0.89	0.72	0.44	1.16	0.71
				176.6	1.26	0.77	1.37	0.84	0.75	0.46
40R-4, 0–11	417.46	25	66.68	0.0	0.48	0.30	1.05	0.65	1.46	0.89
				47.3	0.77	0.47	1.81	1.11	1.28	0.79
				99.0	0.99	0.61	2.18	1.33	1.54	0.94
				176.0	0.92	0.57	1.95	1.20	1.77	1.09
45R-3, 48–56.5	464.60	30	68.07	0.0	1.53	0.90	0.84	0.50	2.49	1.47
				47.3	2.44	1.44	2.44	1.44	5.52	3.26
				99.0	2.47	1.46	2.07	1.22	5.07	3.00
				176.0	2.05	1.21	1.65	0.97	4.05	2.39

Note: *T* = incubation temperature, β = experimentally determined solubility constant corrected for temperature and salinity (Crozier and Yamamoto, 1974), *t* = duration of incubation.

Table T24. Total carbon, inorganic carbon, organic carbon, total nitrogen, and total sulfur contents in the solid phase of sediments, Hole C0012A. (See table note.) (Continued on next two pages.)

Core, section, interval (cm)	Depth CSF (m)	IC (wt%)	$CaCO_3$ (wt%)	TN (wt%)	TC (wt%)	TS (wt%)	TOC (wt%)	TOC/TN
322-C0012A-								
1R-1, 62–66	0.64	0.12	1.02	0.0388	0.42	0.46	0.30	8.9
2R-4, 28–33	64.15	0.05	0.44	0.0632	0.45	0.38	0.40	7.4
3R-1, 72–76	70.24	0.63	5.28	0.0528	0.94	0.15	0.31	6.8
4R-2, 25–30	80.28	0.66	5.48	0.0486	0.88	0.11	0.22	5.4
5R-2, 25–27	89.69	0.41	3.44	0.0510	0.64	0.09	0.23	5.2
5R-3, 42–44	90.32	0.26	2.14	0.0479	0.44	0.10	0.18	4.4
5R-5, 18–20	92.50	0.79	6.56	0.0450	1.01	0.11	0.23	5.9
6R-3, 10–12	100.46	0.31	2.62	0.0510	0.54	0.13	0.23	5.2
6R-4, 66–68	101.35	0.17	1.44	0.0456	0.38	0.16	0.21	5.3
6R-4, 71–73	101.40	0.16	1.33	0.0515	0.40	0.21	0.24	5.4
7R-5, 108–110	107.85	0.26	2.14	0.0505	0.56	0.16	0.30	6.9
8R-3, 30–32	114.63	1.17	9.71	0.0443	1.41	0.12	0.24	6.4
8R-3, 108–110	115.41	1.03	8.55	0.0445	1.21	0.21	0.18	4.8
8R-5, 0–3	116.64	0.55	4.58	0.0500	0.78	0.11	0.23	5.4
8R-6, 47–49	117.34	0.98	8.20	0.0489	1.21	0.09	0.23	5.4
9R-4, 0–2	124.04	0.26	2.19	0.0567	0.50	0.11	0.24	4.9
9R-5, 59–61	124.87	0.17	1.38	0.0561	0.43	0.18	0.26	5.4
9R-6, 30–32	125.99	1.42	11.9	0.0466	1.67	0.11	0.24	6.1
10R-2, 41–43	132.04	0.61	5.10	0.0542	0.93	0.13	0.32	6.8
10R-3, 44.5–46.5	132.63	0.05	0.40	0.0547	0.29	0.11	0.24	5.1
10R-5, 35–37	134.40	0.29	2.43	0.0533	0.54	0.15	0.25	5.4
10R-5, 92–94	134.97	1.10	9.16	0.0562	1.46	0.12	0.36	7.5
10R-6, 0–2	135.45	0.43	3.60	0.0582	0.71	0.11	0.28	5.6
11R-3, 24–26	142.90	0.10	0.83	0.0567	0.39	0.17	0.29	6.0
11R-4, 0–2	144.04	0.11	0.88	0.0571	0.36	0.13	0.25	5.2
11R-5, 107–109	145.38	0.04	0.34	0.0627	0.38	0.24	0.34	6.3
11R-6, 113–115	146.65	0.15	1.26	0.0587	0.42	0.14	0.26	5.3
11R-7, 79–81	147.70	0.08	0.70	0.0211	0.18	4.30	0.10	5.4
11R-7, 132–134	148.23	2.32	19.3	0.0423	2.62	0.42	0.31	8.4
12R-1, 31–33	149.82	0.08	0.69	0.0552	0.32	0.17	0.24	5.0
13R-2, 25–27	159.90	0.47	3.89	0.0535	0.73	0.13	0.26	5.7
13R-3, 68–70	160.82	0.11	0.93	0.0154	0.19	0.13	0.08	6.1
13R-3, 88–91	161.02	0.09	0.75	0.0116	0.16	0.13	0.07	7.1
13R-5, 28–30	162.78	0.67	5.60	0.0599	1.04	0.11	0.37	7.1
14R-2, 0–2	169.70	0.15	1.27	0.0563	0.42	0.17	0.27	5.6
14R-3, 85–87	170.84	0.33	2.78	0.0559	0.59	0.12	0.26	5.4
14R-4, 22–24	171.53	0.67	5.59	0.0217	0.80	0.78	0.13	7.0
15R-3, 0–2	180.10	3.01	25.0	0.0440	3.19	0.00	0.18	4.8
16R-3, 0–2	189.04	0.11	0.90	0.0541	0.35	0.17	0.24	5.2
16R-4, 68–70	190.00	0.21	1.75	0.0568	0.48	0.18	0.27	5.6
16R-5, 12–14.5	190.86	0.18	1.51	0.0541	0.44	0.11	0.26	5.6
17R-1, 28–30	197.29	0.03	0.21	0.0555	0.43	0.44	0.41	8.5
17R-2, 45–47	198.66	0.02	0.20	0.0528	0.26	0.10	0.24	5.2
17R-3, 27–29	199.10	0.08	0.71	0.0571	0.32	0.21	0.23	4.8
17R-4, 17–19	199.29	0.49	4.07	0.0499	0.77	0.17	0.28	6.7
18R-2, 48–50	208.39	0.03	0.22	0.0471	0.24	0.09	0.21	5.3
19R-1, 79–81	216.50	0.04	0.33	0.0522	0.23	0.09	0.20	4.4
19R-2, 51–53	217.57	0.03	0.23	0.0663	0.53	0.24	0.50	8.9
19R-3, 12–15	217.72	0.13	1.05	0.0548	0.62	0.43	0.49	10.5
19R-4, 17–19	219.16	0.09	0.77	0.0473	0.30	0.08	0.21	5.1
19R-4, 122–124	220.21	0.04	0.33	0.0571	0.30	0.06	0.26	5.3
20R-3, 0–2	227.51	0.03	0.25	0.0571	0.25	0.02	0.22	4.6
20R-4, 16–18	228.01	0.03	0.24	0.0466	0.21	0.05	0.18	4.5
20R-4, 100–102	228.85	0.03	0.22	0.0551	0.22	0.02	0.20	4.2
20R-5, 20–22	229.45	0.07	0.62	0.0541	0.29	0.03	0.21	4.6
21R-1, 23–25	234.94	0.03	0.26	0.0535	0.26	0.16	0.23	5.0
21R-2, 30–33	235.70	0.02	0.19	0.0518	0.25	0.07	0.22	5.0
21R-3, 38–40	236.11	0.02	0.17	0.0076	0.09	0.14	0.07	10.8
21R-3, 105–107	236.78	0.09	0.73	0.5239	0.36	0.13	0.27	0.6
22R-1, 109–111	245.30	0.05	0.44	0.0618	0.35	0.08	0.30	5.6
23R-2, 45–47	255.53	0.05	0.43	0.0619	0.34	0.12	0.29	5.4
23R-3, 45–47	256.56	0.14	1.16	0.0632	0.41	0.14	0.27	5.1
23R-5, 91–93	258.76	0.04	0.33	0.0580	0.27	0.10	0.23	4.5
23R-6, 43–45	259.52	0.03	0.26	0.0610	0.32	0.10	0.29	5.5
24R-1, 48–50	263.69	0.11	0.90	0.0619	0.37	0.15	0.26	5.0
24R-2, 0–2	263.94	0.20	1.63	0.0627	0.52	0.11	0.32	6.0

Table T24 (continued). (Continued on next page.)

Core, section, interval (cm)	Depth CSF (m)	IC (wt%)	$CaCO_3$ (wt%)	TN (wt%)	TC (wt%)	TS (wt%)	TOC (wt%)	TOC/TN
24R-3, 48–50	264.77	0.13	1.06	0.0598	0.42	0.16	0.29	5.7
24R-4, 98–100	266.68	0.04	0.32	0.0653	0.44	0.15	0.40	7.1
24R-5, 132–134	268.37	0.04	0.36	0.0317	0.25	0.12	0.21	7.7
25R-1, 110–112	273.81	0.04	0.35	0.0552	0.30	0.11	0.26	5.5
25R-2, 25–27	274.18	0.05	0.42	0.0571	0.31	0.22	0.26	5.4
25R-5, 22–24	277.00	0.06	0.46	0.0596	0.33	0.11	0.27	5.4
25R-6, 57–59	278.71	0.08	0.64	0.0531	0.32	0.09	0.25	5.4
26R-2, 100–102	284.62	0.06	0.47	0.0525	0.29	0.08	0.23	5.2
27R-2, 0–2	292.05	0.26	2.18	0.0570	0.55	0.04	0.29	5.9
27R-3, 8–11	292.47	0.08	0.68	0.0553	0.32	0.18	0.24	5.1
27R-3, 88.5–91	293.27	0.09	0.78	0.0613	0.39	0.26	0.30	5.6
27R-4, 16–18	293.63	0.45	3.77	0.0578	0.78	0.11	0.32	6.5
27R-5, 48–50	295.31	0.12	1.00	0.0540	0.35	0.05	0.23	4.9
28R-2, 10–12	302.27	0.05	0.42	0.0565	0.31	0.12	0.25	5.3
29R-1, 49–52	311.21	0.22	1.83	0.0527	0.48	0.10	0.26	5.8
29R-2, 13–15	312.24	0.33	2.71	0.0531	0.59	0.15	0.27	5.8
29R-3, 0–3	312.59	0.19	1.57	0.0551	0.48	0.09	0.29	6.1
31R-1, 40.5–45.5	330.13	0.14	1.20	0.0503	0.38	0.06	0.24	5.6
31R-2, 38–43	330.56	0.15	1.25	0.0530	0.42	0.09	0.27	6.0
31R-3, 0–3	330.60	0.05	0.42	0.0529	0.28	0.13	0.23	5.0
31R-4, 64–67	331.73	0.05	0.39	0.0577	0.38	0.16	0.34	6.8
31R-4, 105–107	332.13	3.76	31.3	0.0219	4.15	0.00	0.40	21.2
31R-5, 70–72	333.10	0.20	1.63	0.0534	0.45	0.05	0.25	5.5
32R-1, 8–11	339.30	0.06	0.49	0.0501	0.29	0.09	0.24	5.5
32R-2, 41–43.5	340.55	0.50	4.15	0.0499	0.76	0.04	0.26	6.1
32R-3, 23–25	341.06	0.20	1.67	0.0558	0.57	0.26	0.37	7.7
32R-CC, 8–10	343.23	4.38	36.5	0.0152	4.46	0.00	0.08	6.0
33R-2, 0–2	349.22	0.36	2.98	0.0285	0.54	0.11	0.18	7.4
33R-4, 26–28	351.29	0.82	6.82	0.0457	1.10	0.16	0.28	7.2
33R-5, 12–14	352.40	0.08	0.66	0.0507	0.34	0.16	0.26	6.1
33R-5, 80–82	353.08	0.03	0.23	0.0526	0.29	0.16	0.26	5.8
34R-1, 23–25	357.24	0.27	2.26	0.0527	0.54	0.50	0.27	6.0
34R-1, 72–75	357.74	0.11	0.88	0.0592	0.40	0.23	0.30	5.8
34R-3, 0–2	359.55	0.30	2.48	0.0542	0.58	0.31	0.28	6.0
35R-2, 65–67	367.47	0.14	1.15	0.0504	0.39	0.13	0.25	5.8
36R-2, 34–36	376.52	0.08	0.70	0.0509	0.34	0.27	0.25	5.8
36R-3, 29–32	376.84	0.08	0.66	0.0414	0.38	0.20	0.30	8.4
37R-1, 44–48	385.96	0.06	0.46	0.0515	0.26	0.24	0.21	4.7
37R-2, 0–2	386.31	0.41	3.45	0.0537	0.73	0.30	0.32	6.9
38R-1, 95–100	395.98	0.01	0.05	0.0568	0.34	0.30	0.33	6.8
39R-1, 2–5	404.54	0.07	0.60	0.0469	0.37	0.18	0.30	7.5
39R-1, 107–109	405.58	0.06	0.50	0.0720	0.72	0.57	0.66	10.7
39R-1, 118–121	405.70	0.08	0.68	0.0680	0.70	0.60	0.62	10.6
39R-2, 37–40	406.24	0.08	0.67	0.0647	0.71	0.40	0.63	11.3
39R-2, 73–75	406.60	0.07	0.59	0.0620	0.68	0.35	0.61	11.4
39R-3, 35–37	407.26	0.04	0.33	0.0711	0.69	0.72	0.65	10.7
40R-1, 21–23	414.22	0.02	0.17	0.0497	0.33	0.09	0.31	7.3
40R-3, 26–28	416.99	0.00	0.04	0.0434	0.26	0.10	0.26	7.0
40R-4, 30–33	417.72	0.13	1.07	0.0362	0.36	0.06	0.23	7.5
40R-5, 24–26	418.35	0.07	0.58	0.0091	0.19	0.52	0.12	15.7
40R-5, 45–47	418.56	0.26	2.16	0.0402	0.49	0.11	0.23	6.6
41R-1, 23–25	423.74	0.39	3.23	0.0415	0.70	0.20	0.31	8.7
41R-2, 0–2	424.89	0.02	0.15	0.0351	0.18	0.02	0.16	5.3
41R-3, 0–3	426.09	0.02	0.16	0.0390	0.24	0.09	0.22	6.7
41R-4, 38–40	426.90	0.01	0.07	0.0358	0.25	0.18	0.25	8.0
41R-CC, 12–14	429.76	7.63	63.6	0.0145	7.70	0.00	0.06	5.2
42R-2, 29–31	434.25	0.02	0.16	0.0320	0.24	4.04	0.22	8.0
42R-3, 18–20	434.85	0.02	0.18	0.0390	0.21	0.57	0.19	5.6
42R-3, 76–78	435.43	0.01	0.09	0.0408	1.19	1.83	1.18	33.7
43R-1, 114–116	443.65	0.01	0.05	0.0120	0.07	0.10	0.06	6.1
43R-2, 85–87	444.76	0.02	0.19	0.0395	0.25	0.18	0.23	6.8
43R-4, 41–43	446.41	0.02	0.16	0.0442	0.29	0.38	0.27	7.2
44R-1, 16–18	452.17	0.02	0.13	0.0386	0.85	0.85	0.83	25.1
44R-1, 94–96	452.95	0.03	0.22	0.0406	0.33	0.50	0.30	8.6
44R-2, 0–2	453.27	0.03	0.28	0.0387	0.34	0.20	0.30	9.2
45R-2, 22–25	463.04	0.02	0.14	0.0105	0.09	0.14	0.08	8.7
45R-2, 74–77	463.56	0.02	0.16	0.0295	0.30	0.10	0.28	11.0
45R-3, 46–48	464.56	0.01	0.06	0.0314	0.36	0.29	0.35	12.9
45R-4, 76–79	465.57	0.01	0.07	0.0139	0.10	0.17	0.10	8.0

Table T24 (continued).

Core, section, interval (cm)	Depth CSF (m)	IC (wt%)	$CaCO_3$ (wt%)	TN (wt%)	TC (wt%)	TS (wt%)	TOC (wt%)	TOC/TN
46R-2, 0–3	471.37	0.00	0.02	0.0430	0.50	0.46	0.50	13.6
46R-3, 109–113	473.04	0.02	0.19	0.0412	0.23	0.07	0.21	6.0
47R-2, 30–35	481.10	0.43	3.56	0.0239	0.47	0.01	0.05	2.3
47R-3, 10–13	481.24	1.04	8.70	0.0218	1.10	0.01	0.06	3.2
48R-1, 10–12	490.11	2.05	17.1	0.0229	2.12	0.01	0.07	3.8
48R-2, 0–2	490.53	3.02	25.2	0.0229	3.06	0.00	0.04	2.2
49R-2, 37–39	500.31	0.39	3.22	0.0246	0.47	0.05	0.08	3.9
49R-3, 22–24	500.55	0.01	0.12	0.0324	0.12	0.11	0.11	3.9
50R-2, 40–42	509.70	0.01	0.11	0.0111	0.09	0.03	0.07	7.7
50R-3, 50–52	510.22	0.59	4.88	0.0283	0.69	0.01	0.11	4.4
51R-1, 10–13	518.62	0.52	4.31	0.0216	0.58	0.01	0.07	3.6
52R-2, 32–34	529.53	2.21	18.4	0.0183	2.26	0.00	0.05	3.0
52R-3, 13–18	529.70	1.27	10.6	0.0206	1.35	0.01	0.09	4.9

Note: IC = inorganic carbon, TN = total nitrogen, TC = total carbon, TS = total sulfur, TOC = organic carbon.

Table T25. Characterization of the type and maturity of organic matter, Hole C0012A. (**See table notes.**)

Core, section, interval (cm)	Depth CSF (m)	S_1 (mg HC/g)	S_2 (mg HC/g)	S_3 (mg CO_2/g)	T_{max} (°C)	HI (mg HC/g TOC)	OI (mg CO_2/g TOC)	PI	PC (wt%)	RC (wt%)
322-C0012A-										
13R-2, 25–27	159.90	0.01	0.08	1.18	424	33	492	0.1	0.04	0.2
19R-2, 51–53	217.57	0.17	0.3	0.66	397	59	129	0.36	0.06	0.45
29R-3, 0–3	312.59	0.01	0.1	0.96	427	45	436	0.08	0.04	0.18
32R-2, 41–43.5	340.55	0	0.07	1.11	429	33	529	0.04	0.04	0.17
33R-2, 0–2	349.22	0	0.05	0.78	430	42	650	0.05	0.03	0.09
35R-2, 65–67	367.47	0.01	0.11	0.64	425	55	320	0.06	0.03	0.17
39R-3, 35–37	407.26	0.01	0.32	0.53	425	63	104	0.02	0.05	0.46

Notes: Determined by Rock Eval pyrolysis. S_1 = amount of free hydrocarbons, S_2 = amount of hydrocarbons generated through thermal cracking of nonvolatile organic matter, S_3 = amount of CO_2 produced during pyrolysis of kerogen, T_{max} = temperature at which the maximum release of hydrocarbons from cracking of kerogen occurs during pyrolysis, HI = hydrogen index, OI = oxygen index, PI = production index, PC = pyrolyzable carbon, RC = residual organic carbon.

Table T26. Depth and type distribution of sediment and interstitial water samples for microbiology, Hole C0012A. (See table notes.)

Core, section	Top depth CSF (m)	Cultivation studies	Cell counting and FISH studies	DNA/RNA phylogeny studies	Interstitial water sample
1R-1	0.00	5 cm WRC	2 cm^3 slurry	10 cm WRC	No
5R-2	89.43	5 cm WRC	2 cm^3 slurry	10 cm WRC	Yes
6R-3	100.35				Yes
7R-5	106.76	5 cm WRC	2 cm^3 slurry	10 cm WRC	Yes
8R-5	116.62				Yes
9R-4	124.03			10 cm^3 chip	Yes
9R-7	127.09			10 cm^3 chip	No
10R-3	132.17	5 cm WRC	2 cm^3 slurry	10 cm WRC	Yes
11R-4	144.03			10 cm^3 chip	Yes
13R-2	159.64	5 cm WRC	2 cm^3 slurry	10 cm WRC	Yes
14R-2	169.69			10 cm^3 chip	Yes
15R-3	180.09				Yes
16R-3	189.03				Yes
16R-4	189.31		2 cm^3 slurry	10 cm WRC	No
17R-3	198.82				Yes
18R-2	207.90				Yes
19R-2	217.05	5 cm WRC	2 cm^3 slurry	10 cm WRC	Yes
20R-3	227.50				Yes
21R-2	235.39				Yes
22R-2	245.54		2 cm^3 slurry	10 cm WRC	No
23R-3	256.10				Yes
24R-2	263.93				Yes
25R-2	273.92	5 cm WRC	2 cm^3 slurry	10 cm WRC	Yes
27R-2	292.04				Yes
28R-2	302.16				Yes
29R-3	312.57	5 cm WRC	2 cm^3 slurry	10 cm WRC	Yes
31R-3	330.59				Yes
32R-2	340.13	5 cm WRC	2 cm^3 slurry	10 cm WRC	Yes
33R-2	349.21				Yes
34R-3	359.54				Yes
35R-2	366.81	5 cm WRC	2 cm^3 slurry	10 cm WRC	Yes
36R-2	376.17				Yes
37R-2	386.30				Yes
39R-3	406.90			10 cm^3 chip	Yes
40R-4	417.41	5 cm WRC	2 cm^3 slurry	10 cm WRC	Yes
41R-3	426.07			10 cm^3 chip	Yes
42R-2	433.95	5 cm WRC	2 cm^3 slurry	10 cm WRC	Yes
43R-4	445.99			10 cm^3 chip	Yes
44R-2	453.26			10 cm^3 chip	Yes
45R-3	462.81	5 cm WRC	2 cm^3 slurry	10 cm WRC	Yes
46R-2	471.36				Yes
47R-2	481.12			10 cm^3 chip	No
48R-1	490.00			10 cm^3 chip	Yes
49R-2	499.93			10 cm^3 chip	Yes
50R-2	509.29			10 cm^3 chip	No
52R-1	528.00	5 cm WRC			No
52R-2	529.20			10 cm^3 chip	No
53R-1	537.50			20 cm^3 piece	No
53R-1	537.54			32.5 cm^3 piece	No
53R-1	537.68			27.5 cm^3 piece	No
53R-1	537.78			17.5 cm^3 piece	No
53R-1	537.81			40 cm^3 piece	No
53R-1	537.96			27.5 cm^3 piece	No
53R-1	538.02			75.5 cm^3 piece	No
53R-1	538.27			65 cm^3 piece	No
53R-2	539.05			70 cm^3 piece	No
54R-2	545.28			55 cm^3 piece	No
55R-1	548.30			25 cm^3 piece	No
55R-1	548.52			30 cm^3 piece	No
56R-3	554.02			30 cm^3 piece	No
56R-CC	554.37			35 cm^3 piece	No
57R-1	556.35			25 cm^3 piece	No
58R-CC	560.74			65 cm^3 piece	No

Notes: FISH = fluorescence in situ hybridization. WRC = whole-round core.